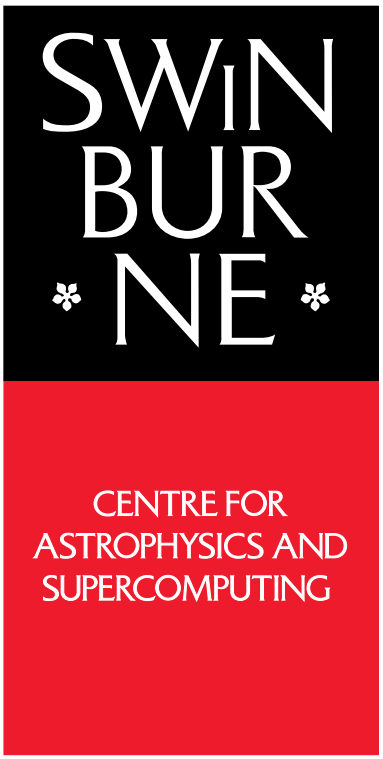

Timing properties across the pulsar population

Aditya Parthasarathy Madapusi

Presented in fulfillment of the requirements
of the degree of Doctor of Philosophy

January 2020

Faculty of Science, Engineering and Technology
Swinburne University

Abstract

The rotational stability of pulsars enables, through pulsar timing, a plethora of astrophysical studies from measuring neutron star equations of state to detecting the stochastic background of nHz-frequency gravitational waves permeating the Universe. However, intrinsic noise processes arising due to instabilities in the pulsar's rotation or stochastic properties of its emission can lead to biased measurements of pulsar parameters and/or limit the attainable timing precision. These noise processes can be categorised based on the timescales on which they manifest in pulse arrival times. Timing noise is a red-noise process that appears as low-frequency structures in pulsar timing residuals on time-scales of months to years. Although timing noise is widespread across the pulsar population, young and normal pulsars provide the most promising avenues for detailed studies. Timing noise is also thought to be related to glitches which are also more common in young pulsars. Pulse jitter, on the other hand, is an intrinsic, stochastic and an impulse-modulated noise process that manifests on time-scales of seconds to minutes. Only highly sensitive observations of the most stable millisecond pulsars provide the opportunity to characterise jitter. This thesis is divided into two parts, focused on characterising both long and short term intrinsic noise processes observed in pulsars.

In the first part of this thesis, we characterise timing noise over a time-span of ~ 15 years for a sample of 85 high-$\dot{E}$, young radio pulsars observed with the 64-m Parkes radio telescope. We apply a novel and improved Bayesian inference technique that enables a simultaneous modelling of stochastic and deterministic pulsar parameters thus accounting for the covariances between the timing model and the additional noise components. For our sample of pulsars, we measure the mean red-noise amplitude ($A_{\rm red}$) to be $-10.4^{+1.8}_{-1.7}$ yr$^{3/2}$ and the spectral index (β) to be $-5.2^{+3.0}_{-3.8}$ and show that the strength of timing noise scales proportionally to $\nu^{1}\dot{\nu}^{-0.6\pm0.1}$, where ν is the spin frequency of the pulsar and $\dot{\nu}$ is its spin-down rate. Using Bayesian evidences to select preferred timing models, we detect new proper motions for two pulsars and discuss the possibility of planetary companions. Although Bayesian pulsar timing techniques have been applied to precision timing of millisecond pulsars in the context of pulsar timing arrays, this is the first time that it has been applied to a large sample of young radio pulsars over such long time spans.

Young pulsars also offer a unique opportunity to study the long-term spin down processes by measuring their braking index (n). However, a major challenge associated with this measurement in young pulsars is the presence of timing noise and glitches which bias measurements of higher-order spin-frequency derivatives, affecting measurements of n. Using the Bayesian inference techniques discussed in this thesis, we detect significant braking

indices for 19 pulsars in our sample. Under the assumption that magnetic dipole braking is the only braking mechanism, we expect a braking index of 3. However, this assumption is imperfect since many young pulsars reside in dense plasma environments, undergo complex interactions between the neutron star crust and the superfluid core and are thought to show temporal evolution of the magnetic field strength and changes in the inclination angle between the rotation and magnetic axis. We detect values of n much larger than 3 and show that our measurements are consistent with the addition of substantial (> 4 years) archival data even in the presence of glitches. We introduce a glitch recovery model and use the Bayesian evidence to show that our measurements of n are unlikely to be due to an exponential glitch recovery from an unseen glitch in the past. Furthermore, we use glitch statistics and show that it is highly unlikely for these pulsars to have undergone large glitches to retain an exponential signal in our data set. We, therefore, conclude that the value of n can be significantly larger than 3, at least over decadal timescales. We develop a parameterization for the detectability of n and discuss the implications of these results on the long-term evolution of pulsars.

In the second part of this thesis, we characterise jitter in millisecond pulsars measured from very high signal-to-noise (S/N) observations using the SKA precursor, MeerKAT radio telescope in South Africa. We briefly describe the data analysis and reduction pipeline MEERPIPE, which was developed as part of this thesis and report jitter measurements for a sample of 25 MSPs. In 12 of these pulsars, we measure jitter for the first time. We report an implied jitter of ~ 4 ns in an hour for PSR J2241–5236, which is the lowest jitter level hitherto reported in a pulsar. To account for frequency-dependent profile evolution, we create wideband templates and characterize jitter as a function of frequency. In PSR J0437–4715 we detect time-dependent frequency evolution of the profile caused by the varying spectral index of single pulses, which places a fundamental limit on our ability to precisely measure the pulsar dispersion measure (DM). We present a detailed statistical analysis of single pulses for eight MSPs and discuss this in the context of jitter measurements. We find that the most precisely-timed MSP, PSR J1909–3744, shows clear evidence of pulse nulling. Finally, we discuss the role of MeerKAT in the context of the International Pulsar Timing Array (IPTA) and relevant optimizing strategies for precision pulsar timing.

Acknowledgements

The work presented in this thesis would not have been possible without the support and confidence from a lot of people that I have been fortunate enough to receive. This thesis represents a snapshot of various ongoing projects which has brought together many dedicated collaborators from Swinburne University of Technology, the Australian Telescope National Facility (ATNF), Auckland University of Technology, the South African Radio Astronomy Observatory (SARAO) and colleagues that are part of the international MeerTime collaboration. Most of this research was conducted with the pulsar group at the Centre for Astrophysics and Supercomputing at Swinburne and it has been an absolute pleasure working with them. The incredibly friendly and encouraging environment here has allowed me to grow as a scientist and has provided me with the tools to pave my way. I have relied heavily on the support of my family and friends both at home and at work. I have a lot of people to thank.

I cannot begin to acknowledge anyone without starting with my supervisors - Matthew Bailes, Simon Johnston, Willem van Straten, Stefan Oslowski and Ryan Shannon. It has been an absolute privilege to have worked with such an esteemed team of astronomers. Matthew's incredibly wide knowledge of the field and his grand futuristic visions have always inspired and helped me see the bigger picture. I'd like to thank him for the freedom that he provided, allowing me to explore various projects during the course of this PhD. He has been a great support to me to freely discuss professional and personal issues and I thank him for patiently guiding me through various difficult situations over the last four years. I will surely miss his frequent spurts of excitement that can be heard across the hallway and his enthusiasm for all things pulsars and science.

Working with Simon has been one of the most productive and fun experiences ever. I have spent many months working with him at ATNF and have learnt about so many things, from pulsars to cricket. His knowledge of pulsar emission mechanisms, slow pulsars, polarization has been an incredible treasure trove for me to learn from. One of the most important things that I continue to learn from him is the approach to writing scientific papers. I have enjoyed working with him and I hope that I continue to do so. Finally, I must note that although he has defeated me in almost every ping-pong match that we have played, I will always cherish the one match that I won!

Willem provided me with my first opportunity into the field of pulsar astronomy. I started my first project on pulsars with him over Skype around five years back and since then I have always been awestruck by the depth of understanding that he possesses. I

sincerely thank him for the incredible patience that he continues to show towards me and the initial opportunities that he provided to a naive but passionate engineering student willing to do astronomy. Without him, this thesis would not have been possible. My understanding of statistics and my approach to coding was fundamentally transformed after working with him. He is also one of the humblest and kindest people I have had the privilege of working with. Thank you, Willem, for everything and I look forward to continued collaborations.

Ryan has always amazed me with his understanding of such a diverse range of topics in transient astronomy and statistics. He has been a constant go-to person throughout my PhD and has been very patient with me over the last few years. I have learnt a great deal from him. He was one of the key persons who guided me towards using Bayesian statistics for my pulsar timing projects and I thank him for that.

Stefan is a supervisor, a mentor and a friend. He has been very supportive throughout my PhD and has given me valuable advice on both research and personal life. Without him, this journey would have been difficult. I continue to learn from his in-depth knowledge of pulsar software, Linux and HPC systems and I look forward to working with him further. He was also primarily responsible for introducing me to the amazing world of VIM editors!

Andrew Jameson and Chris Flynn - I thank them for being such supportive mentors. AJ is the backbone to most of the pulsar software infrastructure. Despite having so many responsibilities, he always took the time out in helping me install various pulsar software on OzStar and in providing useful advice in designing and developing code for MeerTime. I thank him for all the support. Chris has, more than anything, inspired me to become a better human being. Thank you. I also thank him for all the advice and extremely valuable feedback on my thesis.

I want to thank Lindley Lentati for being such a great collaborator and a friend. Despite not being involved directly in academia, he has been very kind in helping me out in understanding, using and developing TEMPONEST. He has always provided crucial and unique feedback on the techniques more than the astrophysics. I shall also always cherish our time at Disneyland and meeting Darth Vader!

Renee Spiewak and Wael Farah are my closest friends at work. They have provided incredible support and have allowed me to discuss everything from career choices to coding issues. Renee and I have worked together on many MeerKAT related projects and it has been an absolute pleasure. I thank Renee for always maintaining composure listening to my poor jokes and my childish mannerisms. We have had a lot of unanticipated adventures together and I am glad we have lived to tell the tale! Wael and I started our PhD together

and he has been a great colleague and friend ever since. Thanks for all the late evening chats, Wael.

Seldom does one make new friends who eventually become family. Vivek and Chandra are family. I am very fortunate to have met Chandra and to have had him as my flatmate. He has been there through very testing personal times and has gone above and beyond to provide immense strength and support. The last four years would have been very different if not for him. Thank you da naaye, for everything! Vivek - the original - is my 'pulsar brother'. He has been there as one of my closest friends ever since I moved to Australia and has guided me both professionally and personally. Thanks for all the support thambi, and in spite of all my whining, I enjoyed Maari! Manisha and Shivani have been great friends and we have shared many sweet memories. I hope I meet them more often.

My visits to ATNF were always more interesting because of George Hobbs, Lawrence Toomey and Dick Manchester. They have been excellent and supportive collaborators. I thank them for the fun ping-pong matches and the regular dinner gatherings which always led to very interesting anecdotes.

I have been very fortunate to have made good friends at my work place. Daniel Reardon has been a wonderful colleague and a good friend. He provided valuable support while developing software for MeerTime and has often guided me back to the bigger picture when I was too involved in coding. More importantly, I want to thank him for motivating me back into cycling and constantly helping me out in the process. I have had the most fun riding along the beautiful Melbourne bay. Marcus Lower has been the immediate person for me to discuss incomplete ideas, wild theories and new papers. I have grown to appreciate Bayesian statistics even more after many discussions with him. Fabian Jankowski and I used to have adjacent desks when I first started my PhD. I thank Fabian for the constant support that he provided when I was getting started and in helping me understand the various nuances of using supercomputers and pulsar software.

Vivek, Cherie, Rahul, Pravir, Debatri and Mohsen - they have been great colleagues and I thank them for all the support. I would like to thank the Swinburne OzGrav team for creating such a friendly and creative work atmosphere. I would also like to thank the Swinburne CAASTRO team for allowing me to attend various conferences and participating in various outreach events. The g2 and OzStar HPC systems have played a vital role in my thesis work and I thank the Swinburne HPC team for doing such a great job in maintaining these systems. I would like to thank everyone in the UTMOST collaboration for being so friendly and approachable. Finally, I would like to thank the SARAO team and the MeerTime collaboration for providing excellent opportunities to

be a part of the MeerKAT telescope commissioning efforts and in being supportive of my work. I would especially like to thank Sarah Buchner for all the help that she provided with MeerKAT commissioning and especially in being such a great host when I visited Cape Town.

A big shoutout to the OzGrav outreach team, especially to Lisa, Mark and Carl. I am so glad that I met Mark. I especially would like to thank him for introducing me to sailing and to tall ships. Sailing as a crew member on the Enterprise was one of the best experiences in my life. Lisa and Carl are one of the most lively people I have known. I thank Lisa for giving me wonderful opportunities to do science outreach and for baking delicious cakes on my birthdays. Carl has been a great inspiration for creative work. He has taught me a great deal in photography and art. It has been a pleasure knowing him.

I thank Ramesh Balasubramanyam for giving me my first opportunity in radio astronomy and for taking the time out to discuss history, art and science. I would also like to thank Avinash Deshpande for the long late-night discussions on pulsars, science outreach and for sharing historical anecdotes of Raman and Rad.

I would like to thank Jagdeesh for introducing me to astronomy and for sharing his enthusiasm for the subject. I also thank Pradeep and Sriram for being such great friends during my engineering and for sharing and supporting my interest in science. I thank Arvind anna for literally providing me with a second home in Sydney along with delicious food.

I would like to dedicate my thesis to Amma and Appa. They have given me immense freedom to pursue my interests and have trusted me with my decisions throughout. My friend for the last 25 years, Meher, has been there through everything in life. Thank you, Meher, for being there. Pikky, my dearest friend and loving partner - thank you for sharing this life with me.

Declaration

The work presented in this thesis has been carried out in the Centre for Astrophysics & Supercomputing at Swinburne University of Technology between 2016 and 2019. This thesis contains no material that has been accepted for the award of any other degree or diploma. To the best of my knowledge, this thesis contains no material previously published or written by another author, except where due reference is made in the text of the thesis. The content of the chapters listed below has appeared in refereed journals. Minor alterations have been made to the published papers in order to maintain argument continuity and consistency of spelling and style.

- Chapter 3 has been published in "Monthly Notices of the Royal Astronomical Society" as *Timing of young radio pulsars* I*: Timing noise, periodic modulation and proper motion* authored by A. Parthasarathy, R.M. Shannon, S. Johnston, L. Lentati, M. Bailes, S. Dai, M. Kerr, R.N. Manchester, S. Oslowski, C. Sobey, W. van Straten and P. Weltevrede.

  I led the project and did most of the software development and data analysis directly required for the manuscript. R.M. Shannon and S. Johnston were instrumental in providing valuable suggestions throughout the duration of the project. The Bayesian pulsar timing framework was originally developed by L. Lentati who has subsequently helped me develop it further as required, for the analysis presented here. I wrote most of the manuscript, with help from S. Johnston, R.M. Shannon, S. Oslowski, W. van Straten and suggestions from the various co-authors mentioned above. The comments from the anonymous reviewer during the publication phase were also helpful in improving the overall quality and presentation of the manuscript. Most of the co-authors also helped with the observations taken using the 64-m Parkes radio telescope.

- Chapter 4 has been submitted for publication in "Monthly Notices of the Royal Astronomical Society" as *Timing of young radio pulsars* II*. Braking indices and their interpretation* authored by A. Parthasarathy, S. Johnston, R.M. Shannon, L. Lentati, M. Bailes, S. Dai, M. Kerr, R.N. Manchester, S. Oslowski, C. Sobey, W. van Straten and P. Weltevrede.

  I led the project and did most of the software development and data analysis directly required for the manuscript. S. Johnston directly helped in implementing code for the glitch simulations using MCMC and provided valuable support while preparing

the manuscript. R.M. Shannon suggested in exploring the possibility of a wide-orbit companion for PSR J0857–4424 and directly helped with the mathematical formulation of the power spectral density of a braking index signal. L. Lentati provided crucial suggestions on the data analysis related to TEMPONEST. Useful comments while writing the manuscript were provided by the supervisory panel and the remaining co-authors.

- Chapter 5 will be submitted for publication in a peer-reviewed journal as *Jitter limits on 25 southern declination millisecond pulsars with the MeerKAT radio telescope* authored by A. Parthasarathy, M. Bailes, R.M. Shannon, S. Oslowski, W. van Straten, R. Spiewak, D. Reardon, S. Buchner, M. Keith and the MeerTime collaboration.

  I led the project and wrote all of the code relevant to the analysis presented here. I led the development of the data analysis pipeline (MEERPIPE) with important contributions from R. Spiewak and D. Reardon. A. Jameson developed code for the MeerKAT pulsar backend (PTUSE). M. Bailes is the P.I of MeerTime, the key science pulsar timing project with MeerKAT. M. Bailes, R.M. Shannon, S. Oslowski and W. van Straten provided valuable suggestions on the methodology for jitter measurements. M. Bailes helped in providing directions to the manuscript. S. Buchner and R. Spiewak helped in scheduling and observing pulsar observations with the MeerKAT radio telescope.

Aditya Parthasarathy Madapusi
Melbourne, Victoria, Australia
2019

To amma and appa, for everthing I have in life.

Contents

List of Figures

2

List of Tables

1 Introduction

"Astronomy is divided into 2 halves, the study of the Crab Nebula and the rest of the Universe" – Jan Oort

1.1 The Crab Nebula

The discovery of the Crab Nebula is widely credited to the French astronomer Charles Messier (Messier 1771). He independently discovered it 27 years after the little known discovery by an English physician, John Bevis, who observed the nebula in 1731. Charles Messier, renowned for finding comets, discovered the Crab Nebula while trying to find Halley's comet, which was predicted to appear in the constellation of Taurus. Noticing the stationary nature of the object, Messier concluded that it was not a comet and recorded it as M1 in his extensive catalogue of nebulae (Messier 1774).

The development of astronomical photography towards the end of the 18^{th} century was instrumental in revolutionizing our understanding of the Crab Nebula. Numerous photographs of the same object over many decades provided the opportunity to study the nebula over many timescales (Lockyer 1900; Lampland 1921). Measurements of changes in brightness and size of the nebulosity from various photographs of the nebula resulted in the discovery that the more conspicuous outer filaments of the nebula were moving in a generally outward direction from the centre. The fact emerged, in 1921, that the Crab Nebula is expanding (Duncan 1939). It was also during this time that Swedish astronomer Knut Lundmark, using material extracted from old Chinese chronicles, pointed out that the position of the Crab Nebula coincided with the recorded position of a 'guest star', first observed by the Chinese on July 4^{th}, 1054 (Lundmark 1921). The Chinese record discusses the appearance of a bright star in the constellation of Taurus and its disappearance over

six months.

In 1928, using the photographs of the Crab Nebula spaced many years apart, Edwin Hubble concluded that assuming a constant rate of expansion, the nebula must have taken $\sim$ 900 years to reach its measured physical dimensions (Hubble 1928). This strengthened the association of the Crab Nebula to the 'guest star' seen by the Chinese astronomers. Following this, spectroscopic observations revealed a Doppler shift in the spectral lines which was a clear consequence of the expansion of the nebula and finally, spectrographic measurements provided valuable information about the distance to the nebula, which was estimated to be $\sim$ 5000 light-years from Earth (Mayall 1937). The distance to the nebula combined with the brightness as recorded by the Chinese astronomers indicated that the 'guest star' was at least 100 times as luminous as an ordinary nova, making the Crab Nebula the first astronomical object to be associated with a supernova explosion.

Meanwhile, in Germany, when Walter Bothe and Herbert Becker used polonium to bombard beryllium with alpha particles (Bothe & Becker 1930), James Chadwick, a former research assistant of Ernest Rutherford, realized that this was evidence for the existence of a particle that he had hypothesized; the neutron, a nuclear particle with no electrical charge. Assisted by Norman Feather, they developed an apparatus to prove the existence of the neutron and in February 1932, Chadwick's letter to *Nature* titled "Possible Existence of a Neutron" (Chadwick 1932) later earned him the Nobel Prize in Physics.

Two years later, in 1934, Walter Baade and Fritz Zwicky published these remarkably visionary and insightful words; *"With all reserve, we advance the view that supernovae represent the transition from ordinary stars into neutron stars, which in their final stages consist of extremely closely packed neutrons"* (Baade & Zwicky 1934b). They coined the term 'super-nova' and conceived the concept of a 'neutron star' for the first time. Over the following years, the existence of neutrons and the idea of a neutron star stimulated an abundance of theoretical speculations regarding their mass, radii and associations with supernova remnants (Hess & Steinmaurer 1935; Landau 1938; Zwicky 1939; Oppenheimer & Volkoff 1939).

Closely following the end of the second world war, there were further scientific insights into the Crab Nebula and neutron stars. John Bolton and his colleagues, in 1949, discovered three discrete Galactic sources of radio emission using an aerial on a high cliff overlooking the sea in Sydney, Australia (Bolton et al. 1949). They identified that the position of one of the radio sources agrees with that of the Crab Nebula. It was then, only the second known compact astrophysical source, apart from the Sun, to have radio emis-

sion[1]. However, the estimates of its density and temperature as measured by Hermann Minkowski (Minkowski 1942) were insufficient to explain the observed radio emission by strictly invoking thermal processes. Also, the detection of X-ray emission from the Crab Nebula by a sub-orbital rocket in July 1964 (Bowyer et al. 1964) added to this great puzzle.

The observations of radio, millimetre and X-ray emissions from the Crab Nebula posed many questions to the prevailing understanding about the nature of the object. Iosif Shklovskii, in 1966, radically theorized that the wide range of electromagnetic emission ranging from radio to X-rays is not due to thermal radiation but due to relativistic particles gyrating in a magnetic field; synchrotron radiation (Shklovskii 1966). He also conjectured that since X-ray emitting electrons will lose energy rather quickly, they must be a continuous production of relativistic particles in a strong, sustained magnetic field to explain the observations. Shklovskii's theories were further reinforced by Franco Pacini, in November 1967, who proposed that a highly magnetized, rotating neutron star with an arbitrary angle between the magnetic field dipole and the angular momentum vector (oblique rotator) is likely to release energy due to rotational and magnetic energy loss (Pacini 1967). He postulated that such a release of energy from a central neutron star could be causing the outward acceleration of the Crab Nebula.

As Franco Pacini published these results on November 1967, a team of radio astronomers at the University of Cambridge were investigating a strange and potentially astronomical phenomenon that was noticed by a diligent graduate student, Jocelyn Bell.

1.2 The Discovery of Pulsars

The story begins in 1951 when it was observed that compact radio sources show temporal intensity variations due to the scattering and subsequent interference of radio waves propagating through the Earth's ionosphere (Hewish 1951). This phenomenon is called scintillation. Further observations of such radio sources showed that the scattering due to density variations in the solar wind could also cause scintillation (Hewish 1955). 'Interplanetary scintillation' could then be used to study the solar wind and the dynamics of the solar plasma. Antony Hewish constructed a radio telescope, called the 'Interplanetary Scintillation Array' (Hewish & Ryle 1955) to study these phenomena and used a novel strategy of sampling the radio waves with a high time resolution of 0.1s. This technique would also allow, for the first time, to study the recently discovered, energetic cores of distant galaxies known as quasars (Schmidt 1963). While studying quasars, Hewish's student

[1]In 1931, Karl Jansky discovered that the source of radio interference affecting his linear directional antenna was originating from the center of the Milky Way galaxy.

Jocelyn Bell discovered a signal that was periodic and which appeared to be astrophysical in origin.

The discovery of a bright periodic electromagnetic signal in 1968 by Jocelyn Bell and Antony Hewish during the high-time-resolution survey gave rise to speculations of oscillating or rotating compact stars like white dwarfs and neutron stars. After much speculation, Jocelyn Bell and her colleagues concluded that they had discovered a highly magnetised, rapidly rotating compact star with coherent beams of energetic emission. Since the rotation of the star appeared to observers as a pulsating beam they were named, 'pulsars' (Hewish et al. 1969). The discovery of a pulsar with a significantly shorter period (rotating at 33 ms) at the centre of the Crab Nebula made it unlikely for a pulsar to be a white dwarf (Staelin & Reifenstein 1968). It thus became evident that a pulsar was a rapidly rotating, highly magnetized neutron star, with beams of coherent emission radiating from its magnetic dipoles as Pacini had predicted.

The subsequent measurements of the spin-down of the Crab Pulsar and the loss of rotational energy in the form of a pulsar wind (Michel 1969b) were sufficient to explain the acceleration of particles in the Crab Nebula and the emissions across the electromagnetic spectrum due to synchrotron radiation. Thus, the study of the Crab Nebula over many decades laid the foundations of our understanding of neutron stars and hence, pulsars.

1.3 Pulsars

After more than five decades since their serendipitous discovery, pulsars and neutron stars have proven to be a fruitful ground for exploring the physics of matter at super-nuclear densities (Ashton et al. 2019; Demorest et al. 2010; Lattimer & Prakash 2007; Pines & Alpar 1985; Pandharipande et al. 1976), strong-field tests of gravity (Taylor & Weisberg 1982b; Burgay et al. 2003; Kramer et al. 2004), the nature of super-strong magnetic fields (Gavriil et al. 2002), measuring neutron star masses (Cromartie et al. 2020) and the study of the stochastic background of low-frequency gravitational waves (Aggarwal et al. 2019; Arzoumanian et al. 2018a; Shannon et al. 2015; Lentati et al. 2015b; Yunes & Siemens 2013; Manchester et al. 2013; Demorest et al. 2013; Hobbs et al. 2010a). Although an abundance of work has been published on various aspects of neutron stars and pulsars, there remains an assortment of fascinating problems in pulsar astronomy waiting to be solved (Shao et al. 2015; Keane et al. 2015; Tauris et al. 2015; Janssen et al. 2015; Lazio 2013; Cordes et al. 2004). A few such problems are discussed in this thesis.

Arthur Eddington, in 1926, indicated that once nucleosynthesis ceases at the core of a star, the internal pressure is overcome by gravity and the star starts to collapse (Eddington

1926). In the absence of any additional opposing pressure, this collapse would never stop[2]. However, the energy released during a stellar collapse ionizes the atoms, creating an electron gas. Ralph Fowler, in 1926, postulated that since electrons are fermions, they must obey Pauli's exclusion principle, which can prevent a continued stellar collapse and restore the balance between gravity and degeneracy pressure (Fowler 1926). The pressure generated by the degenerate electron gas balances the inward pressure due to gravity only in stars whose zero-age main sequence (ZAMS) mass is $< \sim 8.3 M_{\odot}$ (Belczynski et al. 2008). Such a star balanced by degenerate electron gas pressure is called a 'white dwarf'.

In scenarios where the initial mass of the star is $> \sim 8.3 M_{\odot}$, or if the mass of a white dwarf exceeds the Chandrashekar limit of $1.44 M_{\odot}$ (Chandrasekhar 1931; Landau 1932), the electron degeneracy pressure is insufficient to counteract the inward gravitational force and the stellar collapse continues. This causes the density of the stellar core to increase and once it is sufficiently high, the electrons cause an inverse β-decay of protons producing neutrons and neutrinos (Wick 1933; Alvarez 1937). The neutrinos, being weakly interactive, escape the stellar core carrying away thermal energy thus accelerating the collapse of the star. Neutrons also obey Pauli's exclusion principle and the degenerate neutrons provide additional pressure that balances the inward force of gravity. Such a star, sustained by neutron degeneracy pressure reaches a stable configuration and is called a 'neutron star'.

Neutron stars are thus born in spectacular and violent explosions of stars with initial masses of $8 M_{\odot} < M < \sim 25 M_{\odot}$ (Baade & Zwicky 1934b,a,c). Due to the conservation of angular momentum, the newly formed neutron star spins very rapidly, with the fastest observed spin frequency of 716 Hz (PSR J1748−2446ad) (Hessels et al. 2006). The highly dynamical collapse and the high electrical conductivity of the progenitor star also conserves the magnetic flux. Hence the magnetic field of the neutron star is of the order of 10^{12} G and is thought to co-rotate with the neutron star. Observations of neutron star radii, masses, temperatures and spin-periods can help constrain the precise 'Equation of State' (EOS) of the neutron star, which describes the relationship between the pressure supporting a star and its density (Lattimer 2004). The outermost layer of a neutron star contains ordinary atomic nuclei, mostly iron, due to its high binding energy per nucleon. Moving inwards, the pressure increases and so does the concentration of free neutrons. The strong nuclear forces are no longer able to sustain the neutrons in the cores of atoms, and thus the free neutrons form the neutron drip layer (Lattimer & Prakash 2004). Our understanding of physics is uncertain towards the centre of the neutron star, where matter exceeds nuclear

[2]The collapse will cease when the star reaches 'infinite' density.

densities (Collins & Perry 1975; Kaplan & Nelson 1986).

The rapid rotation of a neutron star, in the presence of a strong magnetic field, leads to the generation of an electric field which accelerates particles to very high energies. These accelerated particles travelling along the curved magnetic field lines, are thought to produce gamma rays and further decay into electron-positron pairs which are thought to produce the observed radio emission. The radio waves emerge in the form of a beam which is aligned tangentially to the open magnetic field lines at the height of emission. For an in-depth review of pulsar emission mechanisms, see Ginzburg & Zhelezniakov (1975).

1.3.1 Neutron stars as Pulsars

Pulsars are rapidly rotating neutron stars, with beams of coherent emission that are swept through our line of sight, thus producing a pulsating signal, analogous to a lighthouse (Gold 1968; Pacini 1968). Numerous theories have been put forth to explain the physical processes that result in the radio emission from pulsars and to understand the structure of the pulsar magnetosphere (Melrose 1995; Asseo 1996; Asseo & Porzio 2006). The currently accepted model is due to Goldreich & Julian (1969). In this model, the pulsar is a rapidly rotating neutron star, rotating about an axis (R), which is inclined to a dipolar magnetic field axis (μ), subtending an inclination angle (α) as seen in Figure 1.1. The magnetic field of the neutron star is thought to be anchored to its surface and the co-rotation induces an electric field that drives the electrons on the surface of the neutron star to form a plasma. This plasma and the magnetic field forms the pulsar's magnetosphere. An imaginary boundary termed the 'light cylinder' marks the extent of the closed magnetosphere, where the co-rotation velocity is equal to the speed of light (c). The magnetic field lines are closed within the 'light cylinder' and become open beyond that. The emission mechanism is not well understood but is speculated to be a consequence of particles being accelerated by the electric field along the open magnetic field lines emitting curvature radiation in the form of γ-ray photons. These photons subsequently undergo pair-production after interacting with the magnetic field, resulting in electron-positron pairs leading to the production of more photons. Thus, a particle cascade develops, which results in the production of the radio emission in the form of a coherent beam (an emission cone) aligned tangentially to the open magnetic field lines. If this radio beam sweeps across the line of sight to Earth, we see the pulsation with the observed intensity of the beam varying with the pulse phase as the beam enters and exits our view. A number of these periodic pulses accumulate to form a 'pulse profile', which is an average measure of the flux density of the pulsar as a function of pulse phase.

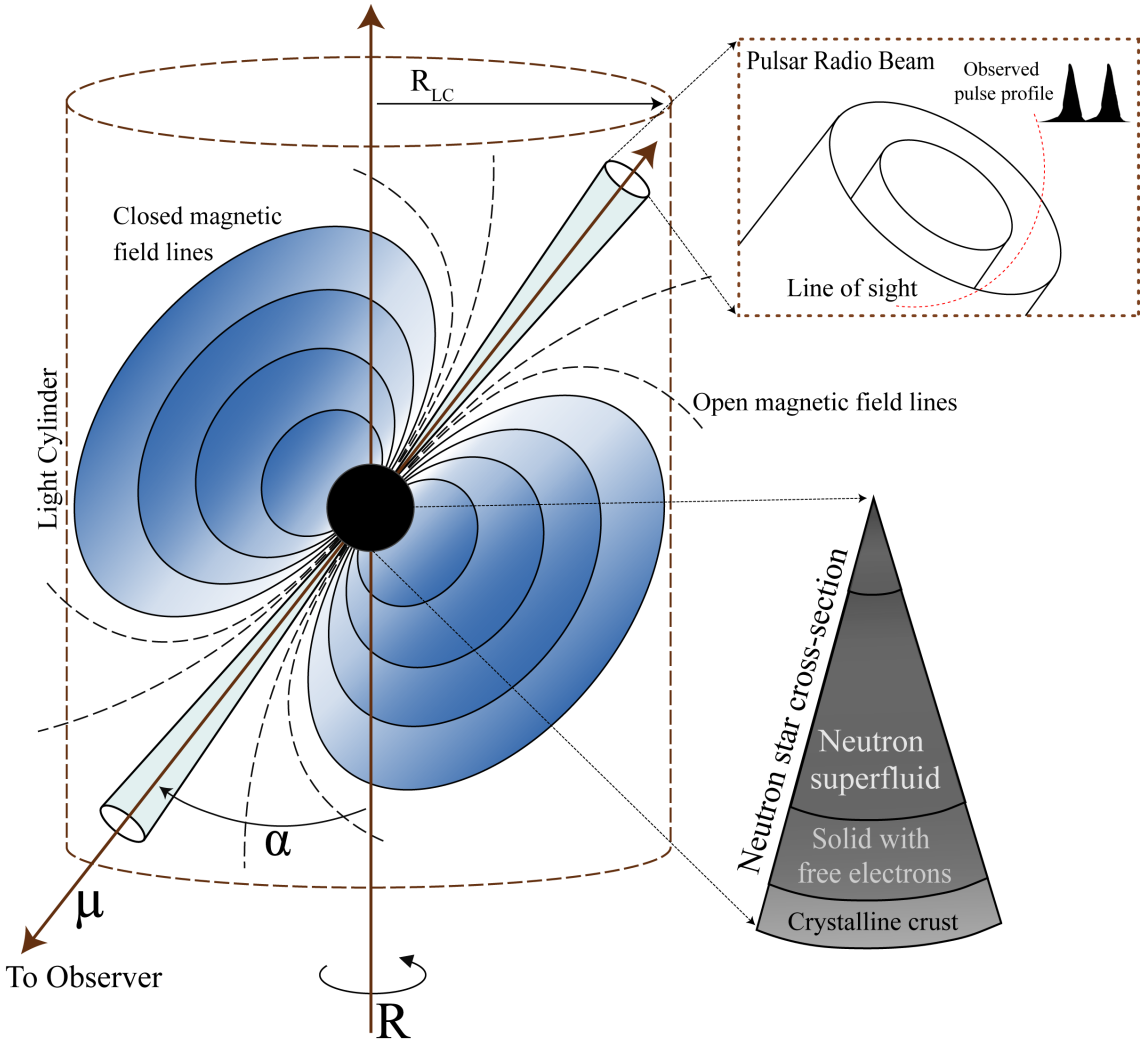

Figure 1.1 A diagram representing our idea of the pulsar 'lighthouse' model. The compact neutron star (black) rotates about an axis (R), with its magnetic axis (μ) aligned with respect to the rotation axis at an angle (α). The pulsar's magnetosphere is represented as the blue gradient traversing across the closed magnetic field lines and extending up to the light cylinder radius ($R_{\rm LC}$). Coherent emission is produced by relativistic charged particles accelerating along the open magnetic field lines (black dashed line) towards the observer. The observed pulse profile is a result of our line of sight (red dashed line) cutting across the pulsar's radio beam. The structure of the neutron star is also indicated as a cross-sectional image (grey wedge).

1.3.2 Pulsar Properties

When a massive star collapses to form a neutron star, angular momentum is conserved. Thus any rotation of the progenitor star will be translated into a rapid rotation of the compact neutron star. Also, the magnetic field of the progenitor star is amplified due to magnetic flux conservation, thus producing a very strong magnetic field. Thus, rapid spin periods and strong magnetic fields are two fundamental properties of a neutron star. Soon after the discovery of pulsars, Gold (1968) predicted that the pulse period should increase with time, which was observationally confirmed in 1969 (Boynton et al. 1969). The rotation period of the pulsar increases due to energy loss in the form of dipolar radiation, pulsar winds and high energy emission. This energy loss ($\dot{E}$), also known as spin-down luminosity, is defined as,

$$\dot{E} = -I\Omega\dot{\Omega} = 4\pi^2 \frac{\dot{P}}{P^3} I, \tag{1.1}$$

where I is the moment of inertia of the pulsar, $\Omega = 2\pi/P$ is the angular velocity of the pulsar, $\dot{\Omega}$ is its derivative, P is the pulsar spin-period and $\dot{P}$ is its derivative.

The power radiated as an electromagnetic wave by a rotating magnet with a magnetic dipole moment is given by (Jackson 1975),

$$\dot{E}_{\rm dipole} = \frac{2|\mathbf{m}|^2\Omega^4}{3c^3} \sin\alpha. \tag{1.2}$$

By comparing $\dot{E}_{\rm dipole}$ with the spin-down luminosity ($\dot{E}$), and by assuming that the spin-down luminosity is dominated by magnetic dipole radiation, we get,

$$\dot{\Omega} = -\left(\frac{2|\mathbf{m}|^2 \sin^2\alpha}{3Ic^3}\right)\Omega^3, \tag{1.3}$$

which can be expressed as a power-law and in terms of the rotational frequency $\nu = 1/P$ and its derivative ($\dot{\nu}$) as,

$$\dot{\nu} = -K\nu^n, \tag{1.4}$$

where K is generally assumed to be a constant and n is defined as the braking index of the pulsar. Assuming that the spin-down of the pulsar is dominated by magnetic dipole braking, then $n = 3$. The braking index describes the relationship between the braking torque acting on a pulsar and its spin frequency; therefore it is fundamental in our understanding of pulsar electrodynamics. Computing the derivative of Equation 1.4 and solving for n, we obtain,

$$n = \frac{\ddot{\nu}\nu}{\dot{\nu}^2}, \tag{1.5}$$

where $\ddot{\nu}$, is the second derivative of the spin frequency.

If there are other dissipation mechanisms that dominate the spin-down luminosity, then the value of n will differ from 3. For instance, gravitational radiation or magnetic quadrupole radiation results in $n = 5$ (Ferrari & Ruffini 1969), while if rotational energy is lost due to mass loss, then $n = 1$ (Michel 1969a). However, the value of n is also sensitive to variations in the moment of inertia, the strength of the pulsar's magnetic field and/or variations in the inclination angle, α. Verification of the spin-down law as stated in Equation 1.4 can be obtained by measuring higher order spin-down terms, like $\dddot{\nu}$. However, measurements of the intrinsic $\ddot{\nu}$ and $\dddot{\nu}$ are challenging both because they are very small quantities and they are contaminated by other physical effects present in the pulsar data. Techniques to measure unbiased values of higher order spin-down terms and new measurements of pulsar braking indices are discussed in Chapters 3 and 4 of this thesis.

Integrating Equation 1.4 can give us an estimate of the age (t) of the pulsar,

$$t = -\frac{\nu}{(n-1)\dot{\nu}}\left(1 - \frac{\nu^{n-1}}{\nu_i^{n-1}}\right) \tag{1.6}$$

where ν_i is the spin frequency of the pulsar at birth. If the pulsar was born spinning much faster than its current spin-period ($\nu_i \gg \nu$), and $n = 3$, then Equation 1.6 simplifies to the characteristic age (τ_c) of the pulsar,

$$\tau_c = -\frac{1}{2}\frac{\nu}{\dot{\nu}}. \tag{1.7}$$

If there is an independent estimate of the age of the pulsar, for example, from a historical supernova association, Equation 1.6 can be used to estimate the birth spin frequency of the pulsar. Such a measurement can be computed for the Crab pulsar, as we know that it is associated with the historical supernova event of 1054 A.D. as described in Section 1.1. The birth period of the Crab Pulsar is estimated to be ~ 19 ms (Manchester & Taylor 1977). It must be noted here that for most pulsars, τ_c is just an order-of-magnitude estimate of the true age of the pulsar.

Retaining the assumption that $n = 3$ and by relating the magnetic field strength (B), to the magnetic moment (m) as $B \approx |m|/r^3$, we can obtain an expression for the surface magnetic field strength ($B_{\rm S}$) of the pulsar,

$$B_{\rm S} \equiv B(r = R) = \sqrt{\frac{3c^3}{8\pi^2}\frac{I}{R^6 \sin^2\alpha} P\dot{P}}. \tag{1.8}$$

Observed values of the above pulsar parameters are typically highly uncertain, especially due to the uncertainties associated with the measurement of the braking index and the initial spin frequency of the pulsar (ν_i). Also, the initial strength of the magnetic field is not very well known but is often assumed to be between $10^{11}G \leq B \leq 10^{13}G$.

1.3.3 Categorizing Pulsars

Pulsars are typically categorized based on their spin periods and spin-down rates as represented graphically in the standard P-$\dot{P}$ diagram shown in Figure 1.2. This is a natural way to classify pulsars as P and $\dot{P}$ are easy to measure and using the relationships described in Section 1.3.2, the magnetic field strength and the characteristic age can be computed, which are represented as lines of constant slope in Figure 1.2. There are currently 2702 known pulsars plotted as obtained from the ATNF pulsar catalogue[3] (Manchester et al. 2005) at the time of writing. These can be classified into a few distinct categories, providing us with insights into their birth and evolutionary characteristics.

Pulsars are born in the upper left region of the P-$\dot{P}$ diagram, where they have short periods and high spin-down rates. Many of these 'younger' pulsars have known or suspected associations with supernova remnants (SNRs) which reinforces the theory of the formation of neutron stars from the deaths of massive stars. As they age, they lose rotational energy, thereby slowing down and moving to the cluster of 'normal' radio pulsars with spin periods of ~ 0.5 s. Few pulsars (~ 50) are seen with spin-periods longer than several seconds. It is assumed that a significant amount of pair plasma is required for radio-emission (following Goldreich & Julian 1969), which may not be produced for long spin-periods, thus leading to a theoretical 'death-line' as shown (grey shaded region) in the figure (Rudak & Ritter 1994). However, pulsars discovered past this death-line highlight the uncertainties in our understanding (Young et al. 1999). The top right hand corner of the figure depicts pulsars with long spin periods and large magnetic fields, known as the 'magnetars'[4] (Duncan & Thompson 1992). These pulsars are believed to be powered mainly by the decay of their magnetic fields rather than by rotation (Kaspi 2007). A detailed review of these objects is provided in Kaspi & Beloborodov (2017). The bottom-left corner of the figure shows pulsars with the fastest rotation rates, high characteristic ages, relatively weak magnetic fields and mostly in binary systems. These are the 'millisecond

[3] http://www.atnf.csiro.au/research/pulsar/psrcat/
[4] http://www.physics.mcgill.ca/~pulsar/magnetar/main.html

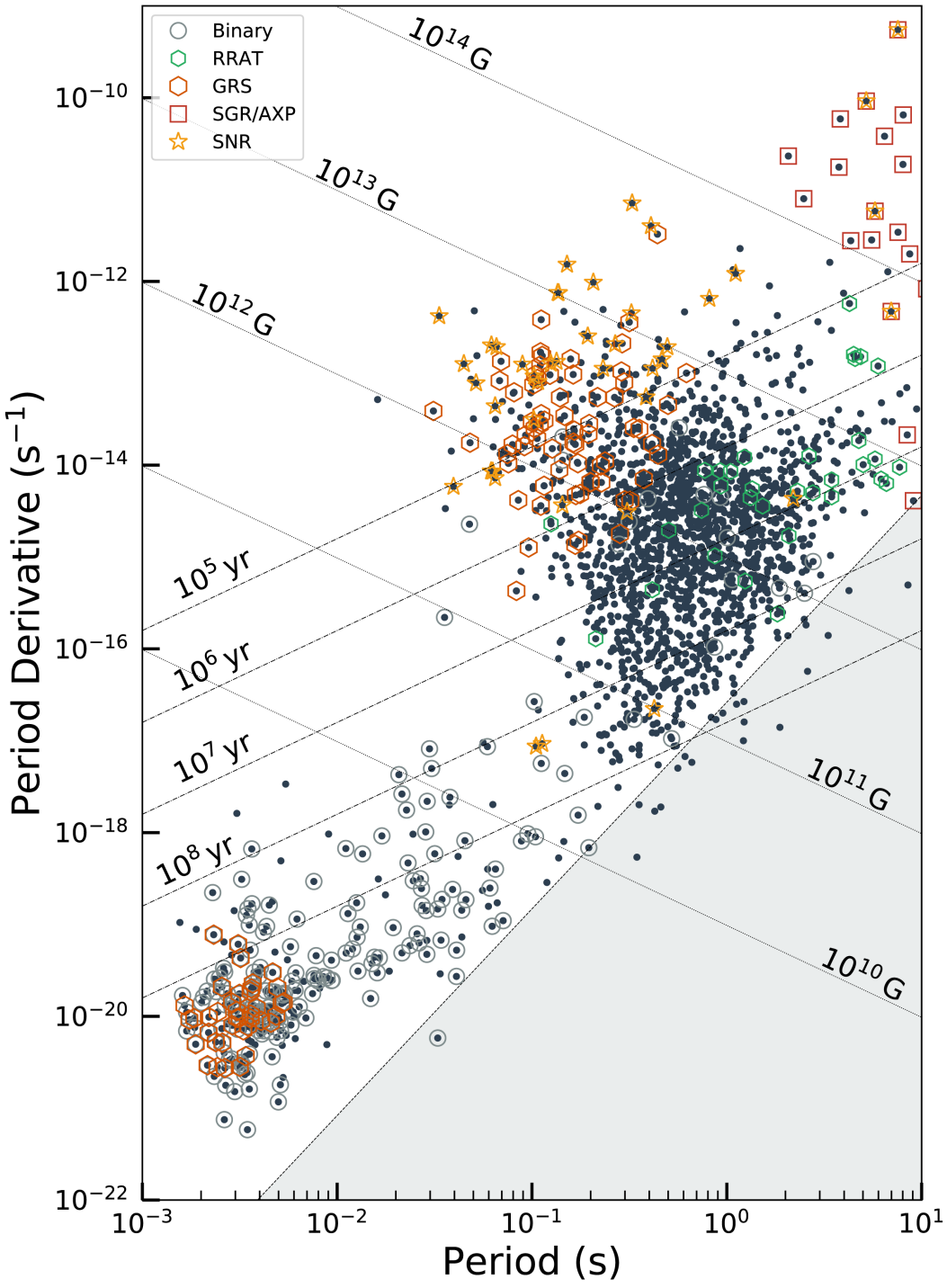

Figure 1.2 The known pulsar population of $\sim$ 2700 pulsars are shown here. Different types of pulsars, including rotating radio transients (RRAT), gamma-ray sources (GRS), anomalous X-ray pulsars (AXP) and associations with supernova remnants (SNR), are represented symbolically as noted in the legend. The grey shaded area towards the bottom-right represents the one possible theoretical 'death-line' beyond which pair-production in neutron stars is thought to cease.

pulsars' (MSPs). These pulsars have different evolutionary tracks than the rest of the pulsar population as they are thought to evolve from normal pulsars through accretion of material from binary companion stars in a process called 'recycling' (Radhakrishnan & Srinivasan 1982). Apart from the above-mentioned classes of pulsars, a growing number of pulsars are being discovered that appear to pulsate sporadically. We can classify such pulsars as 'sporadic' emitters. These include pulsars that are in the 'off' state (nulls) for many pulse periods termed as 'nulling pulsars' (Backer 1970c; Ritchings 1976; Wang et al. 2007) and pulsars that are characterized by solitary pulsations every ~ 100 rotation periods known as 'Rotating Radio Transients' (RRATs) (McLaughlin et al. 2006).

This thesis focuses largely on 'young pulsars' and 'millisecond pulsars', which are further discussed below.

Young Pulsars

In the context of the billion-year old recycled millisecond pulsars, 'young' pulsars have a median age of 10^5 years. Neutron stars, as stated previously, are born in violent supernova explosions and are hence surrounded by the nebulous remnant for tens of thousands of years unless the pulsar was imparted with a high kick velocity at birth that allowed it to escape its parent remnant (Frail et al. 1994; Johnston et al. 2005; Spruit & Phinney 1998). Studying young neutron stars and their associations with supernova remnants aids in our understanding of birthrate statistics (Keane & Kramer 2008). Young pulsars owing to their stronger magnetic field strengths also emit high energy radiation. The high-energy emission from neutron stars offers insights into the dynamics of the pulsar magnetosphere and radio emission mechanisms (Abdo et al. 2013) and finally, young neutron stars are the only class of pulsars that enable a comprehensive study of the spin-down mechanisms. Owing to their rapid spin-down rate, young pulsars provide the most promising avenue for the measurement of braking indices on relatively short timescales (~ 50 years) (Hobbs et al. 2004; Livingstone et al. 2007; Lyne et al. 2015a) in addition to the measurement of higher order spin frequency derivatives that can assist in distinguishing between various spin-down models. Young pulsars also experience frequent 'glitches', which are sudden increases in the spin frequency of the pulsar. Glitches provide a window into the physics of neutron star interiors and the dynamics between the core and the crust components of the neutron star (Ashton et al. 2019; Yu et al. 2013; Espinoza et al. 2011b; Shannon et al. 2016b). The majority of young pulsars also exhibit long-term stochastic wandering of their pulse phase, which manifest as low-frequency noise in pulsar timing datasets over year long timescales (Cordes 1980; Cordes & Shannon 2010; Hobbs et al. 2010b). This is

termed as 'timing noise', which along with glitches make it complex to obtain an unbiased measurement of the higher order spin frequency terms and the braking index. Timing noise and glitches are further discussed in Section 1.7.

Millisecond Pulsars

During the supernova of a massive star in a binary system, if the explosion does not impart a high kick velocity to the stellar neutron star remnant or if the mass loss is not too high, a pulsar may be born orbiting a main-sequence stellar companion. At some point, the companion star grows massive enough to enter into the red giant phase of its evolution and fill the Roche-lobe of the neutron star, leading to mass transfer via Roche-lobe overflow. This process of 'recycling' can last up to a few million years, leading to the formation of pulsars with spin-periods of a few milliseconds (Heuvel 2011; Tauris et al. 2017). The infalling plasma during accretion transfers angular momentum to the neutron star, thus spinning it up, and dampening its magnetic field. Pulsars reborn through such a process are called 'recycled pulsars' and have masses in the range of $1.2 \leq M_{\rm p} \leq 2M_{\odot}$. Millisecond pulsars are recycled pulsars characterized by extremely slow spin-down rates, very high spin periods and low inferred magnetic field strengths, thus placing them in the lower left-hand corner of the P-$\dot{P}$ diagram. As a consequence of their evolutionary tracks, $\sim$ 80% of MSPs are found in binary systems with the majority of them having a white dwarf (WD) companion star. The first millisecond pulsar was discovered in 1982 (Backer et al. 1982). It remains one of the fastest known pulsars, with a spin frequency of 642 Hz. We currently know of about 200 MSPs [5] (Manchester et al. 2005).

1.4 Effects of the Ionised Interstellar Medium

The interstellar medium refers to the region between the stars in the Galaxy. This matter includes gas in ionized, atomic, and molecular form, as well as dust and cosmic rays. It is composed primarily of hydrogen, followed by helium with trace amounts of carbon, oxygen, and nitrogen and other elements. The interstellar medium can be distinguished into different phases, depending on the temperature and density of the matter. The three-phase model proposed by McKee & Ostriker (1977), models the ISM as a cold neutral medium (CNM), a warm ionised medium (WIM) and a hot ionised medium (HIM). The ionised interstellar medium (IISM), which refers to magnetised plasma with typical electron densities of $n_e \sim 0.1\text{cm}^{-3}$ in the spiral arms of the Milky Way galaxy, interacts

[5] https://www.atnf.csiro.au/people/pulsar/psrcat/

with the radio waves from compact sources like pulsars leading to various propagation effects. These include frequency dispersion, Faraday rotation, scattering and scintillation, which are briefly described below.

1.4.1 Frequency dispersion

The ionised interstellar medium (IISM) introduces a frequency-dependent time delay of the pulse arrival times. This was first noted in the pulsar discovery paper, Hewish et al. (1969), that higher frequency radio waves arrived earlier than their lower frequency counterparts. This delay arises due to perturbations of the free electrons in the IISM which oscillate at the 'plasma frequency', $f_p \simeq 8.5\mathrm{kHz}\sqrt{\mathrm{n_e/cm^{-3}}}$ (Lorimer & Kramer 2004). Radio waves at a frequency $f > f_p$, will thus experience a reduction in their group velocity $v_g(f) = c\mu(f)$, where the index of refraction $\mu(f) = \sqrt{1-(f_p/f)^2}$. This effect introduces a frequency-dependent time delay relative to a wave of infinite frequency, given by

$$\Delta t_{\mathrm{DM}} = \left(\mathcal{D}\oint \frac{ds}{v_g(f)}\right) - \frac{\mathcal{D}}{c} \tag{1.9}$$

where the integration is performed over the fractional distance s from the pulsar ($s = 0$) to the observer ($s = 1$). For radio observations, typically at MHz to GHz frequencies, the time-delay in the arrival time between two pulses with frequencies f_1 and f_2 ($f_2 > f_1$) is defined as,

$$\Delta t_{\mathrm{DM}} = \mathrm{DM}\left(\frac{\mathcal{D}}{f_1^2} - \frac{\mathcal{D}}{f_2^2}\right), \tag{1.10}$$

where $\mathcal{D} = e^2/(2\pi m_e c)$ and DM (dispersion measure) is the total electron content along the line-of-sight to the pulsar, expressed in units of $\mathrm{cm^{-3}pc}$,

$$\mathrm{DM} = \mathcal{D}\oint n_e ds. \tag{1.11}$$

The delay in the arrival time can be estimated if a pulse is detected over a finite bandwidth. Using an electron density model of the IISM, one can estimate the distance to the pulsar by measuring its DM. The first electron density model was published by Manchester & Taylor (1981), followed by other models like the LMT85 (Lyne et al. 1985) and TC93 (Taylor & Cordes 1993) models. The NE2001 model (Cordes & Lazio 2002), has been the standard model for more than a decade. Very recently, a new model named YMW16 (Yao et al. 2017) was published, which uses over 1800 HII regions across the Galaxy.

1.4.2 Scattering

Soon after the realization that pulsar signals are dispersed by the free electrons in the IISM, it was also noted that fluctuations in electron density led to scattering of pulses (Rickett 1990; Narayan 1992). These fluctuations cause a continuous change in the instantaneous refractive index of the IISM. The turbulent and in-homogeneous nature of the IISM also causes multi-path propagation of radiation (Armstrong et al. 1995). This results in the wavefronts becoming deflected from their original paths, i.e, the same pulse is detected multiple times but with different time delays, causing an exponential pulse tail for an infinite thin screen model. This pulse-broadening is typically modelled as the convolution of the true 'intrinsic' pulse shape with an exponential decay function with a time constant known as the scattering timescale (τ_s). Scattering is inherently a spatial effect, but is manifested as a time varying effect in pulse intensity. Thus the observed timescale τ can be related to a spatial scale S using an effective velocity $S = V_{\rm eff}\tau$. We now know that the scattering due to Kolmogorov turbulence is diffractive in nature but this diffractive process is strongly modulated by refraction on larger scales. As a result of two different spatial scales, there are two temporal scales for diffractive ($\tau_{\rm diff}$) and refractive ($\tau_{\rm ref}$) effects. Typically, $\tau_{\rm diff}$ is minutes to hours, while $\tau_{\rm ref}$ is days to months. The scattering timescale (τ_s) is also highly dependent on the observing frequency (ν), as $\tau_s \propto \nu^{-4}$, which has been observed in a number of pulsars.

1.4.3 Scintillation

Another observational consequence of the scattering of the radio waves due to irregularities of the IISM is scintillation. Interference between different scattered wavefronts produces a spatial pattern of intensity variations (Lyne & Rickett 1968). An analogous phenomenon is the twinkling of stars in the night sky due to the scattering of light in the Earth's atmosphere. The scintillation timescales, however, for pulsars are much longer and the scattering medium as discussed in the previous section is the inhomogenous, turbulent plasma. The diffractive scattering on shorter timescales, leads to stronger scintillation while the refractive scattering on longer timescales leads to weaker scintillation. In practice, the interference pattern is sampled as a function of time and frequency across the bandwidth of the receiver. This interference pattern is represented in the 'dynamic spectrum' of a pulsar from which one can measure the scintillation timescale and bandwidth. An example dynamic spectrum is shown in Figure 1.3 .

In addition to dispersion, scintillation and scattering, the radio waves from the pulsar also undergo Faraday rotation. The magnetised component of the IISM is responsible for

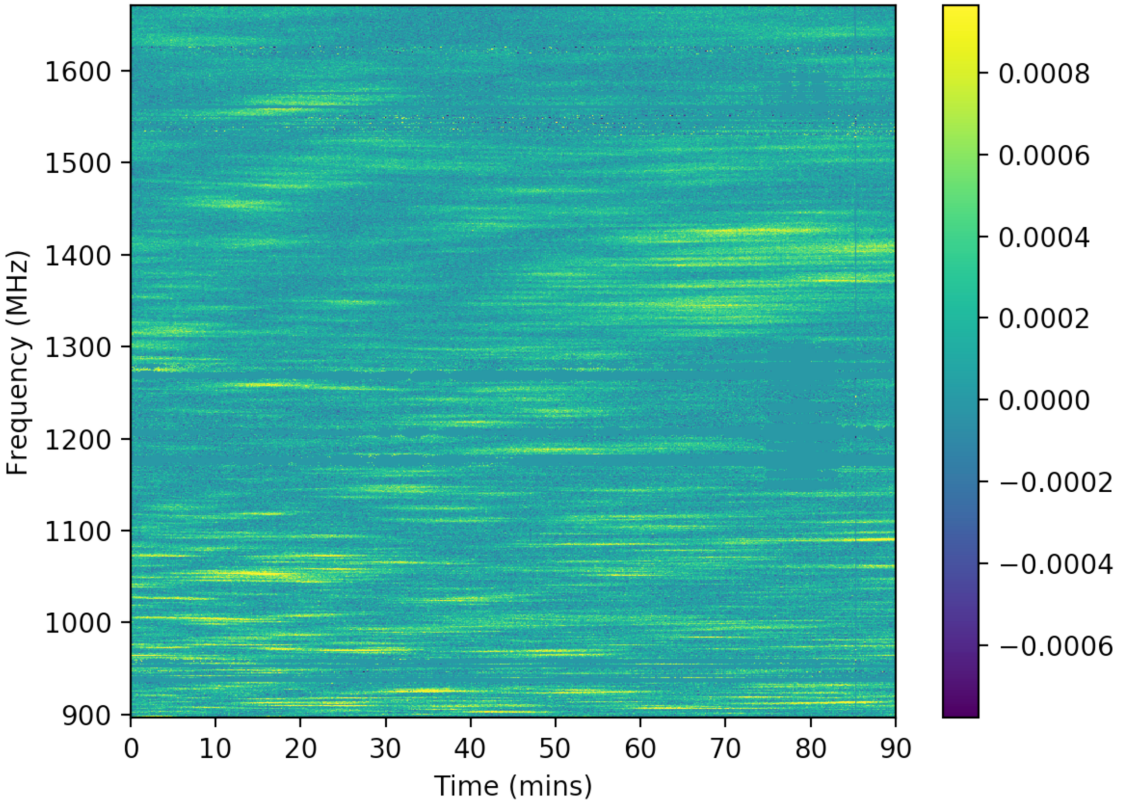

Figure 1.3 Dynamic spectrum observations of the binary pulsar PSR J1757–5322 observed with the MeerKAT radio telescope for $\sim$ 90 minutes. The observing bandwidth is 775.75 MHz. The color in the dynamic spectrum represents the normalized flux after subtracting the mean. The striations seen are due to the diffractive scintillation due to the IISM as the pulsar and Earth move relative to each other. Observations like these provide strong constraints on the turbulence of the IISM and in precision timing of binary orbit parameters.

Faraday rotation, which is observed as a change to the position angle of the polarisation of an electromagnetic wave and is proportional to the strength of the magnetic field in the direction of propagation, the path length and the square of the wavelength. We refer the reader to an excellent review by Rickett (1990) for more details.

1.5 Pulsar Timing

Pulsars are remarkably stable 'celestial clocks'. The beamed emission from pulsars is observed as a series of pulses separated by the pulsar's rotation period. Figure 1.4 depicts the propagation of the signal from the pulsar to the telescope and the various processing stages that lead to the measurement of a pulse time-of-arrival (ToA) and timing residuals, which are the difference between the ToAs and the best-fit timing model. ToAs form the fundamental data product for pulsar timing and in conjunction with the predictions made by a 'timing model', enable the computation of pulsar timing residuals. Much of the scientific applications of pulsars is through the precise measurement and study of pulsar timing residuals.

1.5.1 The Signal Path

The lighthouse model suggests that the radio emission from pulsars arrives as a series of pulses propagating through the IISM. These pulses are frequency dispersed and scattered when they arrive at the telescope, where they are focused at the receiver feed by a parabolic surface. In practice, individual pulses are often averaged over many rotations of the pulsar to form a stable 'pulse profile'. Pulsar timing typically is not performed on individual pulses because it has been shown that the pulse-to-pulse emission is not perfectly stable and that single pulses exhibit stochastic variations in pulse shape, amplitude and phase (Cordes & Downs 1985; D'Alessandro et al. 1993b; Jenet et al. 2001b; Osłowski et al. 2011; Shannon et al. 2014b). Such stochasticity on short timescales fundamentally limits the precision with which we can time pulsars, and this will be further discussed in Section 1.7 and in Chapter 5. Averaging over many pulses also reduces the contribution of the radiometer noise. The ratio of the pulsar signal strength to that of the noise introduced by the observing system electronics is defined as,

$$\mathrm{S/N} = \sqrt{N_\mathrm{p} B t}\left(\frac{G S_\mathrm{peak}}{T_\mathrm{sys}}\right)\sqrt{\frac{P-W}{W}}, \tag{1.12}$$

where S/N is the signal-to-noise ratio, N_p is the number of polarizations recorded, B is the bandwidth, t is the integration time, S_peak is the peak brightness of the pulsar, T_sys is

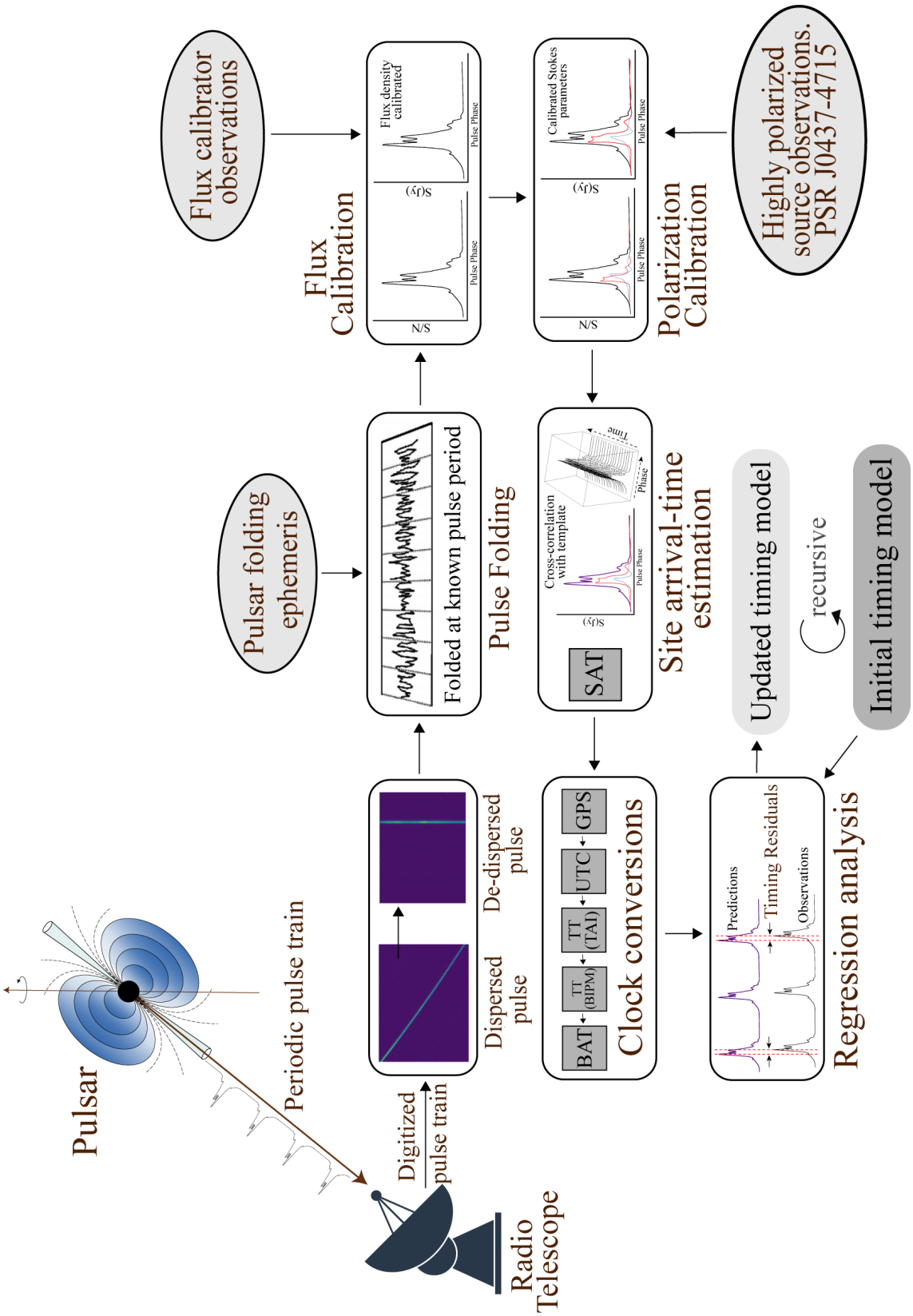

Figure 1.4 A schematic diagram outlining the various stages involved in observing and data processing for pulsar timing.

the system temperature, P is the pulse period, W is the width of the on-pulse region and $G = \eta_A A/(2k_B)$ is the telescope gain based on the aperture efficiency η_A, the telescope aperture A and Boltzmann's constant k_B. Equation 1.12 quantitatively explains that an ideal telescope would have a large collecting area (large G) and a cooled receiver (low noise, small T_{sys}) with a wide observing bandwidth (large B). The optimal observing frequency range is highly dependent on the characteristics of the pulsar, however some generalizations can be made based on the dependence of the flux density spectra and the effects of the IISM on pulsar observations. Pulsars typically have steep flux density spectra such that they are brighter at lower frequencies with a $\hat{S} \propto f^{-1.60\pm0.54}$ (Jankowski et al. 2018) but the IISM introduces significant pulse broadening (see Section 1.4.2) at lower frequencies. However, building telescopes operating at higher frequencies is expensive as they require smooth and very accurately shaped reflecting surfaces. To attain a reasonable balance between pulsar brightness and the strength of propogation effects, pulsar observations are typically conducted in the frequency range of $\sim$ 300 MHz to $\sim$ 4 GHz (Verbiest et al. 2016).

The frequency dispersed and scattered pulses once received by the telescope's focus are in the form of a time series of voltages. This time series is first digitized and time-tagged by a local station clock, which provides the reference time for all the electronics. A hydrogen MASER or a Rubidium clock is typically used and synchronized to the Global Positioning System (GPS) time standard. The digitized time series is then de-dispersed to account for the frequency-dependent delay due to the propagation of the pulsar signal through the IISM. This de-dispersed pulse train is then 'folded' (data samples with the same phase are averaged) at the known pulse period using a 'timing model' (pulsar rotational ephemeris). This results in a high S/N pulse profile, which is typically stable with time. The process of digitizing, de-dispersing and folding is performed by the 'backend' which usually provides folded archives that follow PSRFITS standard, readable by PSRCHIVE[6] (Hotan et al. 2004b; van Straten et al. 2010). These archives are typically a cube of time-tagged coherently de-dispersed time-frequency-polarization data. The archives are usually flux and polarization calibrated. Flux calibration solutions are obtained from observations of a quasar or a radio galaxy, while polarization calibration is simply the inversion of the instrumental polarimetric response. This response can be determined by modelling the variations of the Stokes parameters as a function of parallactic angle (van Straten 2004, 2013). The estimation of the ToAs can be performed from either the total intensity (Stokes I) data or from the full polarization data (van Straten 2006). In this thesis, we use the

[6] http://psrchive.sourceforge.net/

total intensity profiles for estimating ToAs.

The timestamps of the folded observations at this stage are an accurate record of the time of arrival of the signal at the telescope. These times are not necessarily the times at which the chosen fiducial phase of the pulsar's periodic signal arrived at the telescope. This "time of arrival of the fiducial phase" is obtained by convolving and matched-filtering the time series with a 'template' profile (called template-matching). In principle, a template can be any non-constant function, but in practice they resemble the average pulse profile as closely as possible. Templates can be created by integrating a long observation, resulting in a high S/N ratio profile of a pulsar or by using an analytical noise-free template (produced by a Gaussian decomposition of the data). The cross-correlation of the template (S) with the observed data ($O(t)$) is performed by assuming that the pulse profile is well described as a scaled (by a factor A), shifted (by some phase ϕ) version of the template with a constant offset (B) and additive radiometer noise (N). This process is called template matching and is defined by the following equation (Downs & Reichley 1983),

$$O(t) = AS(t - \phi) + B + N(t). \tag{1.13}$$

Various fitting procedures have been implemented to perform template matching, such as a Fourier Phase Gradient (PGS) method (Taylor 1992), a Gaussian Interpolation Shift (GIS) method (Hotan et al. 2005) and a Fourier domain Monte-Carlo method. The time shift $t_{\rm topo}$ is the topocentric ToA or the site arrival time (SAT). It must be noted that these times (i.e, SATs) depend on the pulse phase of the template profile. They are transferred to an inertial reference frame, like the solar system barycenter (the center of mass of the solar system). This transformation takes the topocentric arrival time ($t_{\rm topo}$) and applies corrections for light travel time, frequency-dispersion and relativistic effects to obtain the barycentric-arrival-times ($t_{\rm SSB}$). This time transformation is defined as (Hobbs et al. 2006),

$$t_{\rm SSB} = t_{\rm topo} + \Delta t_{\rm clk} - \Delta t_{\rm DM} + \Delta t_{\rm R\odot} + \Delta t_{\rm S\odot} + \Delta t_{\rm E\odot}, \tag{1.14}$$

where,

- $\Delta t_{\rm clk}$ includes the clock corrections to the observatory and the co-ordinate transformations to convert the locally measured topocentric time to the stationary reference frame of the solar system barycentre. The SATs are converted into GPS-measured Universal Coordinated Time (UTC(GPS); UT1), as measured by the National Institute of Standards and Technology (NIST). They are then converted to UTC. This

UTC time-stamp is converted to the Terrestrial Time (TT(TAI)) standard, which is maintained as an ensemble of atomic clocks around the world. Corrections for TAI are provided by the Bureau International des Poids et Mesures (BIPM). This time at the observatory is then transformed to the SSB via a number of coordinate transformations to account for the Earth's rotation, its revolution around the Sun, and the motion of the Sun to obtain the Barycentric Dynamic Time (TDB) or Barycentric Coordinate Time (TCB), which are generally termed as the barycentric arrival times (BATs),

- $\Delta t_{\rm DM}$ is the total delay due to the propagation through the IISM, solar wind and the ionosphere,

- $\Delta t_{\rm R\odot}$ is the Römer delay or the classical light travel time from the observatory to the Solar System Barycentre(SSB),

- $\Delta t_{\rm S\odot}$ is the Shapiro delay (Shapiro 1964), which is the relativistic correction to the light-travel time caused by the curvature of spacetime by massive bodies in the Solar System,

- and finally, $\Delta t_{\rm E\odot}$ is the Einstein delay that includes relativistic corrections for time dilation and gravitational redshift.

The Barycentric ToAs are then subtracted from the arrival times as predicted by a timing model of the pulsar. The differences between the predictions and the observations, called the 'timing residuals' are the fundamental tools of pulsar timing. All unmodelled physics is contained in them and it is the analysis of these timing residuals that will allow measurements of new parameters and extend our understanding of the pulsar system. It is with the precise modelling of these timing residuals that we can find evidence for the low-frequency stochastic gravitational wave background signal (Hellings & Downs 1983). The various parameters that form the timing model are discussed in the following sub-sections.

1.5.2 The Pulsar Ephemeris

A pulsar ephemeris encapsulates the timing model of a pulsar which describes its spin, astrometry and orbital dynamics. It contains parameters that describe the effect of the IISM along the line-of-sight as well as the motion of the pulsar relative to the SSB.

Spin and Astrometric parameters

Every timing model contains a set of fundamental parameters that are measured upon the discovery of the pulsar. These include the pulsar's spin frequency (ν), its position in right ascension (α) and declination (δ) and its DM. Pulsar timing observations spanning over a year provide an estimate of the spin frequency derivative ($\dot{\nu}$). These five parameters constitute a simple timing model. An erroneous measurement of ν causes the predicted arrival times to become incrementally wrong with time resulting in a linear trend in the timing residuals. An error in the measurement of $\dot{\nu}$ causes a quadratic trend in the timing residuals. An incorrect position introduces a sine wave with a period of a year and similarly the pulsar's proper motion (μ_α and μ_δ) signature (usually expressed in units of mas/yr) also manifests as a sine wave, but with an amplitude that increases linearly with time. Proper motion measurements can be useful for understanding pulsar 'kick velocities' at birth (Hobbs et al. 2005).

Another astrometric parameter that can be measured, especially in near by and precisely timed pulsars, is the parallax. Generally, in astronomy, parallax refers to the apparent movement of a nearby star with respect to a background source, which is caused due to the orbit of the Earth around the Sun. In pulsar timing, since the only object that is measured (timed) is the pulsar, its relative position with respect to the background is not measurable. Hence, parallax in pulsar timing refers to the measurement of the curvature of the emitted wavefront from the pulsar. The closer the pulsar is, the stronger is the curvature of the wavefront which introduces a delay which is maximal if the pulsar is at right angles to the Earth-Sun line as depicted in Figure 1.5. Measurements of pulsar parallaxes are important and useful because they provide a direct measurement of the distance to the pulsar, which is useful for various applications including the study of the electron density models of the Galaxy (Cordes & Lazio 2002; Yao et al. 2017).

Binary pulsar timing

Some pulsars, and most MSPs, are in binary systems which necessitates that the pulsar ephemeris accounts for the effects of the companion star on the pulse arrival times from the pulsar. In order to properly model the arrival times from a binary system, the timing model as described in Equation 1.14 needs to incorporate the additional motion of the pulsar as it orbits the common centre of mass. The extension to the timing model contains four additional terms, as described below (Damour & Taylor 1992),

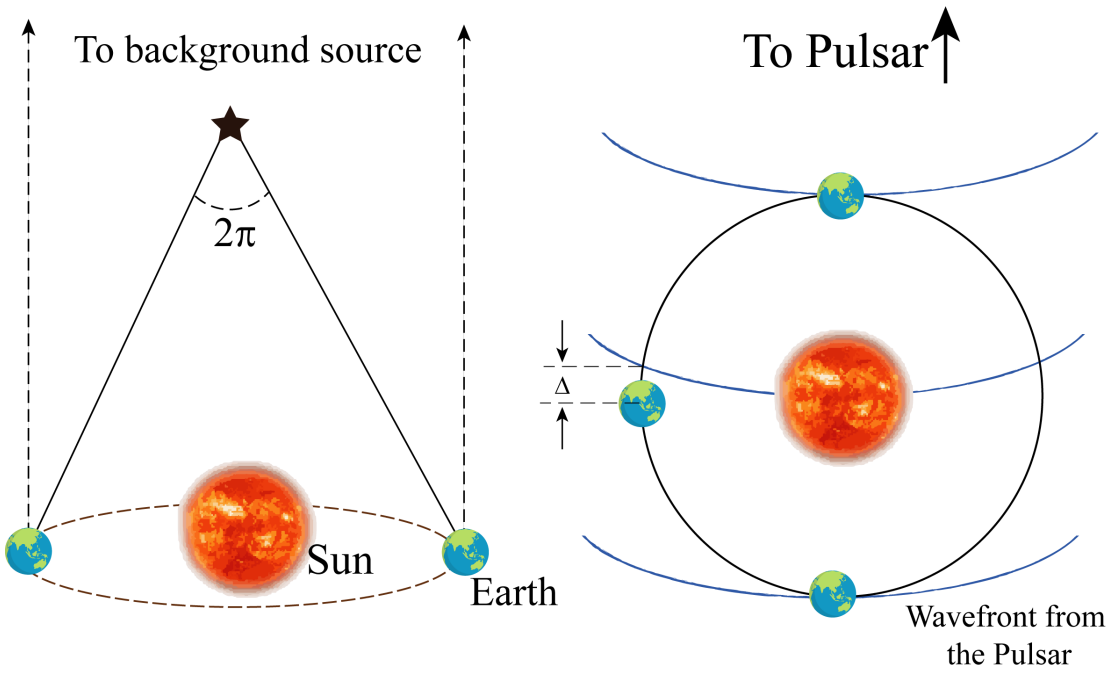

Figure 1.5 Distances in astronomy are typically computed based on the yearly change in position of a nearby source with respect to a background source. However, in pulsar timing, because the background source is not observed, the distance to the pulsar can be measured from observing the curvature of the wavefront originating at the pulsar. This curvature is inversely proportional to the distance to the pulsar and can be measured by means of the half-yearly delay as indicated in the figure. Figure adapted from Verbiest (2009).

$$t_{\rm SSB} = t_{\rm topo} + \Delta t_{\rm clk} - \Delta t_{\rm DM} + \Delta t_{\rm R\odot} + \Delta t_{\rm S\odot} + \Delta t_{\rm E\odot} + \Delta t_{\rm RB} + \Delta t_{\rm SB} + \Delta t_{\rm EB} + \Delta t_{\rm AB}, \quad (1.15)$$

where,

- $\Delta t_{\rm RB}$ is the binary Römer delay that accounts for the light travel time across the orbit,
- $\Delta t_{\rm SB}$ is the binary Shapiro delay that accounts for the additional light travel time due to the curved spacetime around the companion star,
- $\Delta t_{\rm EB}$ is the binary Einstein delay that models the gravitational time-dilation and second-order Doppler corrections to the binary orbit, and
- $\Delta t_{\rm AB}$ is the special relativistic aberration delay due to variations in the aberration of the pulse as a function of binary phase.

Following Damour & Taylor (1992), the above delays can be related to both the Keplerian and relativistic parameters. The Keplerian parameters are:

- the orbital period ($P_{\rm b}$),
- the orbital eccentricity (e),
- the longitude of ascending node ($\Omega_{\rm asc}$),
- the longitude of periastron (ω_0),
- the time of periastron passage (T_0),
- and the projected semi-major axis, $x = a\sin(i)/c$, where i is the inclination angle, a is the semi-major axis and c is the speed of light.

The above parameters are usually sufficient to describe the orbit of non-relativistic binary systems. For a number of binary systems, this description is not sufficient and relativistic corrections must be applied. These corrections are known as the Post-Keplerian (PK) parameters. Under the assumptions that the two orbiting stellar bodies are point masses with negligible spin contributions, the PK parameters should be functions of the a priori unknown pulsar and companion mass (m_p and m_c) and the Keplerian parameters. Measurements of more than two PK parameters then provides unique determination of the mass of the pulsar and the orbiting stars with additional constraints placed by other

PK parameters. Such constraints enable studies of the equation of state of matter at extreme densities and tests of gravity in the strong-field regime. For more detailed review on the relativistic corrections to the timing model, see Damour & Taylor (1992); Lorimer & Kramer (2004).

1.6 Applications of Pulsar Timing

In the short span of five decades, pulsar astronomy has produced a remarkable number of scientific breakthroughs. Pulsars are excellent laboratories for studying gravity in the strong-field regime (Taylor & Weisberg 1982c) and the physics of super-dense matter (Demorest et al. 2010).

Testing theories of Gravity

Undoubtedly, one of the biggest breakthroughs in the field came from the discovery of the first-ever binary pulsar, B1913+16, also known as the Hulse-Taylor binary (Hulse & Taylor 1975). Precise timing analysis of this pulsar provided the first evidence of the existence of gravitational wave (GW) emission which causes the orbital decay of the in-spiraling neutron stars (Taylor & Weisberg 1989). This confirmation and precise characterization of the radiative properties of gravity is not only critical from the point of view of our understanding of fundamental physics, but it has also opened, via ground-based gravitational wave detectors (LIGO), a whole new window on the Universe. Tests of general relativity (GR) using binary pulsars are often presented through a 'mass-mass' diagram, which represents the observed PK parameters as a function of the mass of the pulsar (M_p) and its companion (M_c) for a particular theory of gravity. If all the curves corresponding to every measured PK parameter intersect at the same region, it signifies that the prediction of the component masses by that theory is self-consistent. If the curves do not intersect, the theory can be ruled out to some level of significance. The double pulsar system, PSR J0737–3039A/B (Burgay et al. 2003) is the only system in which both neutron stars have been observed as radio pulsars. It has provided some of the best tests of GR in the strong field regime (Kramer et al. 2006). Gravitationally asymmetric systems, however, such as pulsar-white dwarf (WD) systems are more sensitive in differentiating GR from alternative theories of gravity, like the scalar-tensor theories of gravity. The discovery of more relativistic and asymmetric pulsar systems in the future, possibly including pulsar-black hole binaries can be used to test the "cosmic censorship conjecture" and the "no-hair theorem". Improved timing precision will also allow us to conduct tests of strong equivalence

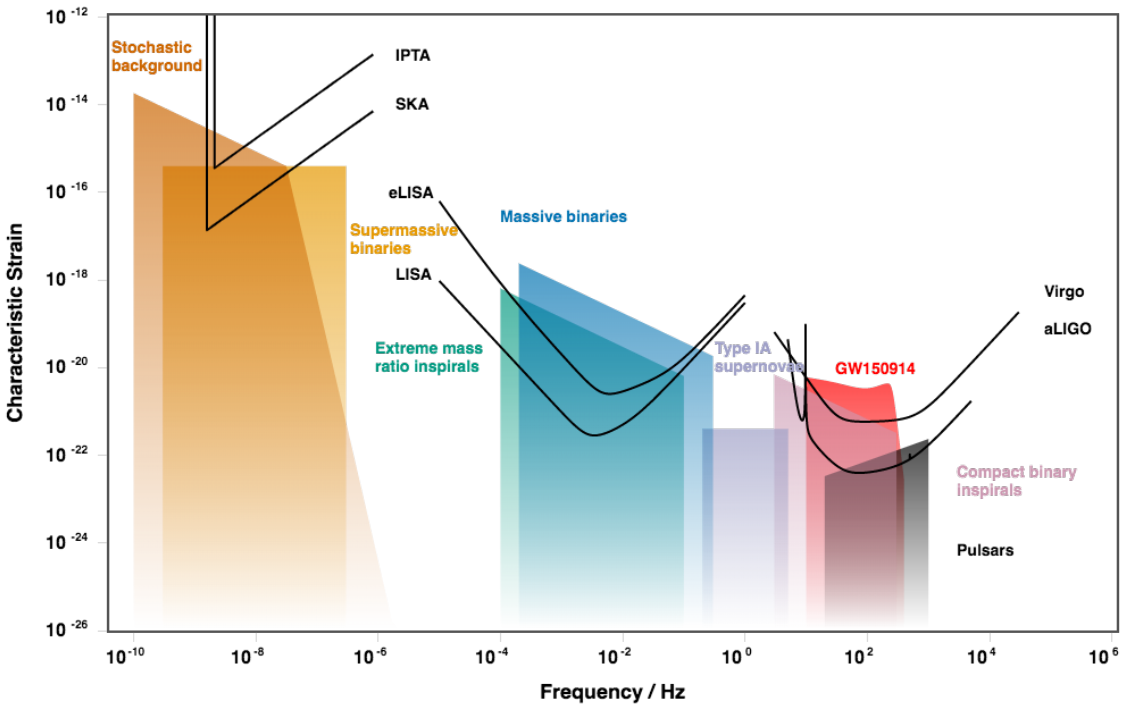

Figure 1.6 A plot of characteristic strain against the GWB frequency for a variety of detectors and sources. Credit: www.gwplotter.com

principles, gravitational dipole radiation, gravitomagnetism and space-time symmetries (Shao et al. 2015).

Low-frequency Gravitational waves

The detection of low-frequency GWs, primarily at nHz frequencies via pulsar timing is one of the main goals of modern pulsar astronomy (Sazhin 1978; Detweiler 1979; Hellings & Downs 1983; Manchester 2017). These will be complementary to the detections by ground-based detectors, like LIGO which are sensitive to gravitational waves in the frequency range of 10 Hz to 10 kHz as shown in Figure 1.6.

Although MSPs have very stable rotational parameters, variations in the timing parameters for a given pulsar have been observed. Therefore, in order to search for an isotropic stochastic background of low-frequency gravitational waves, it is necessary to observe an ensemble of MSPs widely distributed in the sky and search for correlated timing variations among the sample. Gravitational waves passing the Earth will lead to timing residuals whose functional form will depend upon the pulsar-Earth-GW angle. A sample of spatially distributed MSPs that are frequently timed with high precision over a long data span is

known as a pulsar timing array (PTA) (Hellings & Downs 1983; Romani 1989; Foster & Backer 1990). A pulsar timing array acts a multi-arm Galactic-scale detector, which measures the pulsar ToA delays induced by spacetime distortions caused by propagating gravitational waves.

There are numerous GW sources that could lead to detectable signatures in the pulsar data sets, some of which may include the superposition of a large number of GWs from supermassive black hole binaries (SMBHBs) (Rajagopal & Romani 1995; Jaffe & Backer 2003), cosmic strings (Damour & Vilenkin 2000; Sanidas et al. 2013) or inflation (Grishchuk & Sidorov 1989; Grishchuk 2005). Pulsar timing can also be used to search for individual sources of GWs, i.e, individual SMBHBs that produce a continuous wave (Sazhin 1978; Jenet et al. 2004). Currently, searches for GWs with pulsar timing arrays are setting ever more stringent upper limits on the amplitude of the stochastic gravitational wave background (Shannon et al. 2015; Lentati et al. 2015b; Arzoumanian et al. 2015; Lasky et al. 2016; Arzoumanian et al. 2018a). The detection of low-frequency gravitational waves using PTAs will allow astronomers to gain an improved understanding of galaxy evolution and black hole growth (e.g. Taylor et al. 2017,Simon & Burke-Spolaor 2016) and help in investigating the polarization states and constraining the mass of the graviton (Lee et al. 2008; Chamberlin & Siemens 2012; Gair et al. 2015; Cornish et al. 2018; O'Beirne et al. 2019). This will also help to understand the intrinsic symmetry of the gravitational interaction and may provide inputs for quantizing gravity in the strong field regime. The first detection of GWs in the nano-Hertz regime using PTA observations are thus a tantalizing proposition.

Understanding the neutron star population

The transformation of the observed ToAs to the Solar system barycentre using a planetary ephemeris is extremely sensitive to small changes in the assumed position of the pulsar and allows the determination of the astrometric parameters to phenomenal precision. Understanding the spin period, spin-down rate and magnetic field strengths in context with the pulsar positions and velocities enable us to address broader questions about the neutron star population and evolution (Kaspi 2010). Some of the important topics that can be better investigated with improved timing precision are:

- Proper motions of pulsars, which directly help us probe supernova kick physics (Lyne & Lorimer 1994).
- The mass distribution of neutron stars (Freire 2008; Kiziltan et al. 2013).

- The fastest possible spin period for an MSP, thereby helping constrain magnetosphere-accretion disc interactions and the equation of state (Bonanno & Urpin 2015).
- Evolutionary tracks for recently discovered triple systems (Ransom et al. 2014; Luan & Goldreich 2014).
- Formation scenarios for isolated MSPs.

The regular timing of pulsars with high magnetic fields is likely to reveal many glitches (Gavriil et al. 2008; Weltevrede et al. 2011). Glitches are generally accompanied by flux enhancements and profile shape changes and timely detection of glitches could help in the measurement of braking indices (Espinoza et al. 2011b; Dib & Kaspi 2014)

Currently, with proper motions measured for hundreds of pulsars (Hobbs et al. 2005), it is clear that they receive a large kick (≈ 400 km s^{-1}) during their formation. However, the exact physical mechanism responsible for imparting this kick still remains unclear (Lai 2001; Janka 2012). Advances in precision pulsar timing can help in obtaining a better model for the Galactic electron density distribution and model-independent distance with proper motion measurements that can help in improving the reliability and sample size of the pulsar velocity distribution.

Other applications of precision pulsar timing

- Observations of rotational instabilities in pulsars, known as glitches via pulsar timing and the subsequent relaxation processes enable us to probe the neutron star composition in a unique way (Glampedakis & Andersson 2009).
- Since most of the known pulsars are within our Galaxy, the nature of the interaction of their polarized emission with the magnetised IISM makes them excellent probes to study the properties of the Milky Way (Lyne & Smith 1968). The measurement of DMs along many different lines-of-sight helps in modelling the Galactic distribution of free electrons (Cordes & Lazio 2002; Schnitzeler 2012). The combined information from DM and RM measurements have been used to constrain the strength of the Galactic magnetic field (Mitra et al. 2003; Noutsos et al. 2008). Such measurements have also been used to demonstrate the existence of a strong magnetic field in the Galactic centre near the vicinity of the Supermassive Black Hole (SMBH) Sag A^* (Eatough et al. 2013).
- As mentioned earlier, pulsar timing incorporates a model for the pulsar, to predict pulse arrival times. This makes it very sensitive to any process affecting the ToAs

that is not included in the timing model, which led to the first-ever detection of exoplanets around the pulsar B1257+12 (Wolszczan & Frail 1992). Subsequently, a couple of more planets were discovered around pulsars (e.g, Bailes et al. 2011). Pulsar timing is currently far more accurate than optical searches for the detection of planets around main-sequence stars, but far fewer detections have been made.

1.7 Pulsar Noise On Various Timescales

When the pulsar ephemeris takes into account all the parameters described above, ideally one would expect the post-fit timing residuals, i.e, the difference between the observed ToAs and the predicted ToAs after fitting for the model parameters, to be 'white'. However, it is often seen that there are a number of processes that lead to excess noise in the timing residuals. These include pulsar spin rate variations (Shannon & Cordes 2010), changes in the pulsar's magnetosphere (Lyne et al. 2010) time-variable effects of the IISM (Armstrong 1984), astrometric errors and instrumental artefacts (van Straten 2013). For an excellent overview of the pulsar noise budget, refer to Cordes & Shannon (2010).

The most fundamental noise process in the timing residuals is that of the radiometer noise, i.e, noise that originates from the sky background and electronics of the observing system itself. The formal uncertainty on the measurement of a ToA is based on the estimated radiometer noise, which is proportional to the system temperature ($T_{\rm sys}$). This noise is 'white', i.e, the power is the same across all frequencies.

As seen in Section 1.5.1, the timing model is highly dependent on the accuracy of the local time standard maintained by the atomic clocks. While the atomic clocks are stable on short timescales, they tend to drift stochastically on longer ones, manifesting as a 'red' noise process (such a process has more power at lower frequencies). However, since this red noise is intrinsic to atomic clocks, the effect it has on timing residuals is fully correlated for all the pulsars observed. By combining the timing residuals of many precisely-timed pulsars, one can measure this fully correlated red-noise process and thus produce a new, pulsar-based realization of terrestrial time (Hobbs et al. 2012, 2020).

One of the fundamental aspects of pulsar timing is to transfer the ToAs to an inertial reference frame, like the solar system barycenter (SSB), which requires accurate tracking of the motion of the Earth and knowing the masses and orbital parameters of the various celestial bodies in the Solar System. Uncertainties in the masses of major bodies in the Solar System (like Jupiter) can induce long-timescale errors in the position of the SSB, thus leading to a red-noise process in the timing residuals. This noise process, although frequency-independent is correlated among pulsars and thus characterizing it can lead to

better determination of the masses of the planets in the Solar System (Champion et al. 2010; Arzoumanian et al. 2018b; Caballero et al. 2018; Guo et al. 2018; Vallisneri et al. 2020).

Stochastic fluctuations in the column density of free electrons along the line-of-sight to the pulsar cause dispersion variations, significant frequency-dependent red-noise processes in the timing residuals. Since this noise is frequency dependent, it can be modelled and mitigated by using near-simultaneous observations of the same pulsar at different observing frequencies. More recent work on characterizing dispersion variations and their effect on pulsar timing precision is discussed in Jones et al. (2017) .

This thesis focuses on two other noise processes, which are not mentioned above, that are intrinsic to the pulsar and manifest in the pulsar timing residuals on both short and long timescales. These are introduced below and novel techniques to characterize and understand these processes in young and recycled pulsars are studied in Chapters 3, 4 and 5.

1.7.1 Timing noise

The spin-down of pulsars is a deterministic process as described by Equation 1.4. However, superimposed on this deterministic spin-down is a stochastic wandering of the pulse phase, which manifests itself as low-frequency structure in the timing residuals on timescales greater than about a year. This process has a red spectrum and is termed 'timing noise'.

Observations

Figure 1.7 shows the timing residuals for a sample of young radio pulsars observed over a time span of $\sim$ 10 years, showing clear signatures of low-frequency red noise processes. It is evident that improper modelling of timing noise will lead to biased measurements of deterministic parameters. Over the years, there have been many attempts to characterize timing noise across the pulsar population (Cordes & Helfand 1980; Arzoumanian et al. 1994; Shannon & Cordes 2010). Typically it is characterized with a measurement of the second derivative of the spin frequency ($\ddot{\nu}$), which for a large fraction of pulsars is dominated by noise processes. However, modelling timing noise as $\ddot{\nu}$ biases an actual measurement of $\ddot{\nu}$. Several methods have been proposed in the literature to measure the strength of timing noise in pulsars. A detailed discussion of this topic is presented in Chapter 3. However, a few key points are listed here to summarize the conclusions reported in the literature,

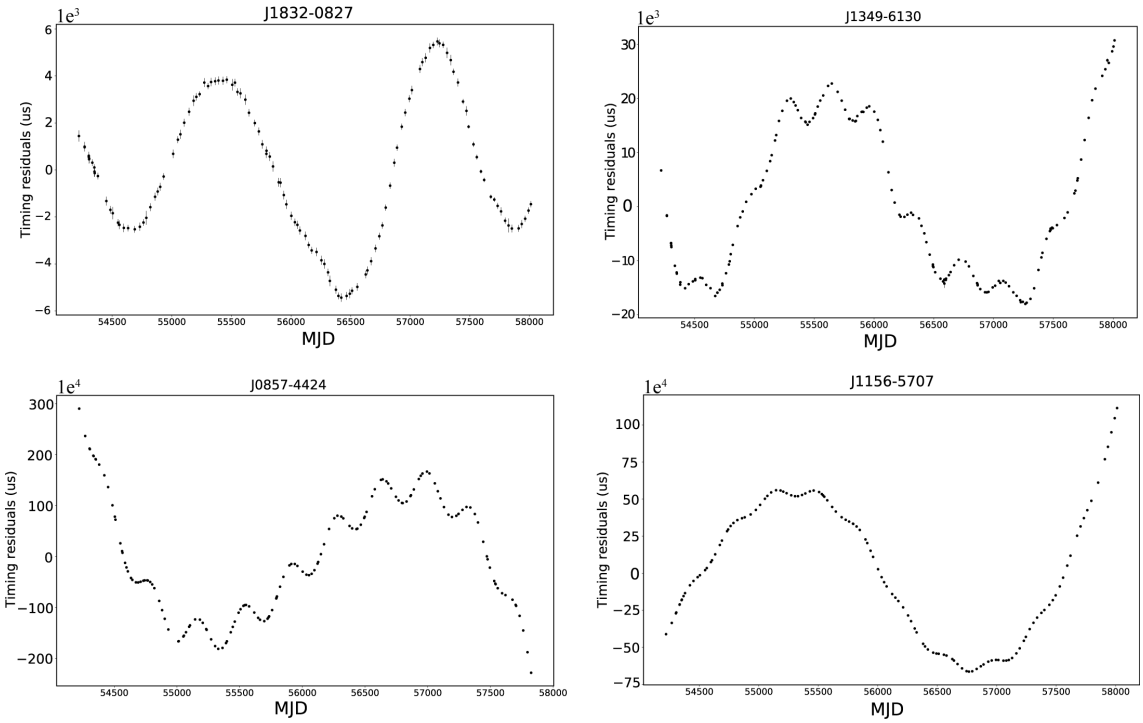

Figure 1.7 Plots of four different pulsars with timing baselines of $\sim$ 10 years showing various levels of timing noise, as indicated by the magnitude of the timing residuals.

- Timing noise is commonly seen from pulsars
- The amplitude of timing noise is stronger in young pulsars as opposed to recycled, millisecond pulsars owing to the significantly larger spin angular momentum and reduced magnetic fields of MSPs.

Measuring and understanding timing noise is not only essential for other applications of pulsar timing, but is also a way to study the neutron star magnetosphere and interior structure.

Interpretations

Timing noise, although observed throughout the pulsar population still has not been fully understood since it was first discussed by Boynton et al. (1969). The wide variety of ways in which timing noise manifests itself in the timing residuals have made it difficult to make conclusive statements about the underlying models. A complicating factor is that the timescales over which timing noise manifests are comparable to the duration over which we have been observing pulsars. As noted by Hobbs (2009), the observations that support random walk models on year-long timescales can turn out to be periodic or

something unanticipated over decadal timescales. In this section, we will briefly discuss a few interpretations of timing noise.

Boynton et al. (1969) studied the timing residuals of the Crab pulsar and interpreted the observed timing noise as a random walk model in either the phase, frequency or spin-down of the pulsar. They theorized that apart from following the regular deterministic spin-down power law as stated in Equation 1.4, the pulsar might undergo sudden step changes at random times in either its pulse phase, frequency or spin-down, which was referred to as phase noise (PN), frequency noise (FN) and spin noise (SN). They defined the strength of these different types of timing noise as,

$$S_{\mathrm{PN}} = \lambda \left\langle \delta\varphi^2 \right\rangle , \tag{1.16}$$

$$S_{\mathrm{FN}} = \lambda \left\langle \delta\nu^2 \right\rangle , \tag{1.17}$$

$$S_{\mathrm{SN}} = \lambda \left\langle \delta\dot{\nu}^2 \right\rangle , \tag{1.18}$$

where $\left\langle \delta\varphi^2 \right\rangle$, $\left\langle \delta\nu^2 \right\rangle$ and $\left\langle \delta\dot{\nu}^2 \right\rangle$ are the mean square values of the steps in phase, frequency and spin-down variations, which were determined over a typical observation time T_{obs}, by splitting them into blocks of duration T. Using this approach they concluded that the timing noise in the Crab pulsar was a random walk in frequency. The Crab pulsar was subsequently studied by Groth (1975), Cordes (1980) and an extended analysis was published by Cordes & Helfand (1980). An important physical consequence of a random walk model is that it must be able to produce both increases and decreases in the relevant parameter. Therefore, it is unlikely that the underlying mechanism responsible for random walk timing noise in frequency is also causing glitches in pulsars (which are only sporadic spin-ups to the neutron star's rotation).

Many physical mechanisms have been proposed to explain timing noise, most of them understood as the response of the neutron star to a varying stochastic torque (Cordes & Greenstein 1981). Models include the accretion of small lumps of matter onto the neutron star causing it to spin-up or down, random pinning or unpinning of vortex lines in the neutron star superfluid, the response of the neutron star to heat pulses, fluctuations in the outer gaps of the magnetosphere (Cheng 1987a), existence of dwarf planets around the neutron star (Cordes & Shannon 2008) and accumulation of many micro-glitches. Contamination from glitches could occur either from small unresolved glitches in the data or glitches occurring prior to the start of the observations, where glitch recovery could affect the measured spin and spin-down parameters. Hobbs (2009) studied the timing noise in a sample of 366 radio pulsars and concluded that the timing noise cannot be explained by a

random walk model and rather, when observed on sufficiently long timescales timing noise exhibits quasi-periodic features. It is currently difficult to argue for or against this claim as the timescales for the quasi-periodic variations are longer than the datasets available for most pulsars.

Long-term observations of PSR B1931+24 by Kramer et al. (2006a), revealed that the radio pulsations from the source turned 'on' for a period of 5-10 days and 'off' for a period of 25-30 days. Interestingly, the spin frequency derivative of the pulsar was 1.5 times greater in the 'on' state as compared to the 'off' state implying that the spin-down torque acting on the pulsar is correlated with the radio emission mechanism. A study of 17 more pulsars by Lyne et al. (2010), revealed the correlations of $\dot{\nu}$ with pulse profile variations.

Characterizing timing noise across the pulsar population is important in understanding the effects of glitches, the dynamics of the pulsar magnetosphere and in obtaining unbiased estimates of pulsar spin-down parameters. **Chapter 3** and **Chapter 4** discuss the properties of timing noise, techniques to characterise them and pulsar spin-down models in greater detail.

1.7.2 Jitter noise

Aside from the excess red noise discussed above, on time scales of minutes to hours, the timing residuals of bright pulsars are typically dominated by an uncorrelated white noise component. This excess white noise can arise from several sources, most significant of which arises due to the differences between an integrated pulse profile (averaged phase-resolved light curve of the pulsar) and a template profile (average of a finite number of pulses). It is generally assumed that the integration of many hundreds of pulses leads to a stable pulse profile which is characteristic of the pulsar (Helfand et al. 1975), however stochastic variations in single pulse morphology seen across the pulsar population introduces detectable fluctuations in the integrated pulse profile thereby leading to the observed excess white noise. Since the formal ToA uncertainty in standard pulsar timing packages is reflective only of the radiometer noise, in an ideal case with no excess noise, the root mean square (rms) timing residual should be equal to the uncertainty of a ToA measurement. However, the excess white noise worsens the rms of the timing residuals and sets a fundamental limit on the attainable timing precision. The variations in pulse profile morphologies was first studied by numerous authors (Cordes & Downs 1985; D'Alessandro et al. 1993a; Kaspi et al. 1994b) but few have focused on MSPs (Sandhu et al. 1997; Kramer et al. 1999; Jenet et al. 2001a) and limitations in the attainable timing precision (Hotan et al. 2006b; Verbiest et al. 2008; Osłowski et al. 2011). In Chapter 5,

we provide a more detailed introduction to this excess white noise component and study pulse-shape variations in a sample of 26 MSPs using high S/N observations obtained with the MeerKAT radio telescope and their effect on the attainable timing precision.

1.8 Thesis Outline

This thesis is broadly split into two topics:

- Long-term timing noise and braking indices for a sample of 85 young, energetic pulsars observed with the CSIRO 64-m Parkes radio telescope,
- Short-term jitter noise on a large sample of MSPs observed using the MeerKAT radio telescope.

A brief description of each of the chapters is given below:

Chapter 2 describes the technical details of the two telescopes used for this thesis: The 64-m Parkes radio telescope and the MeerKAT radio telescope, including a description of the MeerKAT pulsar timing backend.

Chapter 3 describes the application of an improved Bayesian methodology to simultaneously model the stochastic and deterministic timing parameters in a large number of young radio pulsars. Characterization of timing noise, new proper motion measurements and new braking index measurements are reported in this chapter.

Chapter 4 extends the analysis of Chapter 3 and focuses on the measured braking index values for a subset of pulsars and discusses glitch recovery models and the long-term evolution of pulsars.

Chapter 5 analyses the precision timing of MSPs observed with the MeerKAT radio telescope. This chapter specifically focuses on the measurements of 'jitter' noise, its dependence across the observing frequency, single pulse phenomena and optimal observing strategies for a pulsar timing array program with MeerKAT.

Chapter 6 revisits the major results of this thesis and discusses potential future directions.

2

Instrumentation and Data Processing for Pulsar Astronomy

This chapter presents an overview of the observational techniques and processing involved in analyzing radio pulsar data. It provides an overview of the various stages in a generic radio receiver and then focuses on the two telescopes used in this thesis: the CSIRO 64-m Parkes radio telescope in Australia and the SKA-mid pre-cursor, MeerKAT radio telescope in South Africa. The data sets used in Chapters 3 and 4 are part of the young pulsar timing program with Parkes (e.g., P574) and that used in Chapter 5 is part of the MeerTime project with MeerKAT. Both of these projects are briefly described in this chapter.

Please note that most of the sections in this chapter and statements therein are based on standard textbooks, Rohlfs & Wilson (2000) and Lorimer & Kramer (2004), and hence unless required, references are not listed individually.

2.1 Signal Path for a Generic Radio Receiver

Radio pulsars have phase-averaged flux densities between approximately 0.1 mJy and 5000 mJy at 400 MHz (Xie et al. 2019), and benefit from large telescopes, wide observing bandwidths and long integration times. To tackle the deleterious effects of dispersion, we require high-frequency bandwidth. Also, to achieve high precision in pulsar timing experiments and to resolve nanoscale structures in individual pulses, high-time-resolution data products are needed. Thus a good instrument for pulsar observing is one which strikes an optimal balance between high frequency and time resolution.

In this section, an overview of a generic radio receiver is presented, starting from the reception of the electromagnetic radiation at the radio telescope to the creation of

coherently dedispersed voltage-filterbank files that are then processed through pulsar-timing or pulsar-search pipelines.

2.1.1 The Signal-to-Noise Ratio

The sensitivity of a radio telescope depends upon several parameters, some of which are related to the antenna design, while others are related to the electronic systems used in the reception of the radio signal. Almost every electronic receiver is contaminated by some amount of intrinsic noise, either due to white noise in the electronics (caused by the random motion of charged particles), background astronomical sources or terrestrial interference (both natural and artificial). One of the most fundamental parameters to diagnose an observation of a radio signal is the measured signal-to-noise ratio (S/N). This is the relative amplitude of the observed signal compared to the background noise in the observing system. The 'radiometer equation' (introduced in Chapter 1 in equation 1.12)), states that in order to increase the S/N of an observation a telescope needs a large collecting area, a cooled receiver and a wide observing bandwidth, assuming that dispersion delay can be properly removed.

2.1.2 The Front-End

Figure 2.1 shows a schematic of the signal path in a generic radio receiver of a single-dish telescope. The sub-system that couples the incident electromagnetic radiation to the transmission line is called the 'front-end'. This coupling is generally achieved by focusing the incoming electromagnetic signal from a small region of the sky by a primary reflector to the feed horn mounted at its prime focus. The Parkes radio telescope uses a parabolic primary reflector to focus the incoming pulsar signal to the prime focus. One disadvantage in placing the receiver at the focus of the primary reflector is that some fraction of the antenna's surface is blocked by the feed housing. To avoid this, some telescopes have a secondary reflector at the focus, reflecting the signal to the centre of the primary reflector, where the receiver is mounted. Other telescope designs are also used depending upon the required specifications, like the MeerKAT radio telescope which uses an offset-Gregorian feed (this is further discussed below in Section 2.3). The increase in signal strength that the focusing provides as compared to an antenna equally sensitive to radiation in all directions (isotropic) is known as telescope 'gain'. It must be noted that at the wavelengths most commonly used in radio pulsar astronomy, the resolution of a single-dish telescope is limited by diffraction surrounding the reflecting surface and not by atmospheric turbulence.

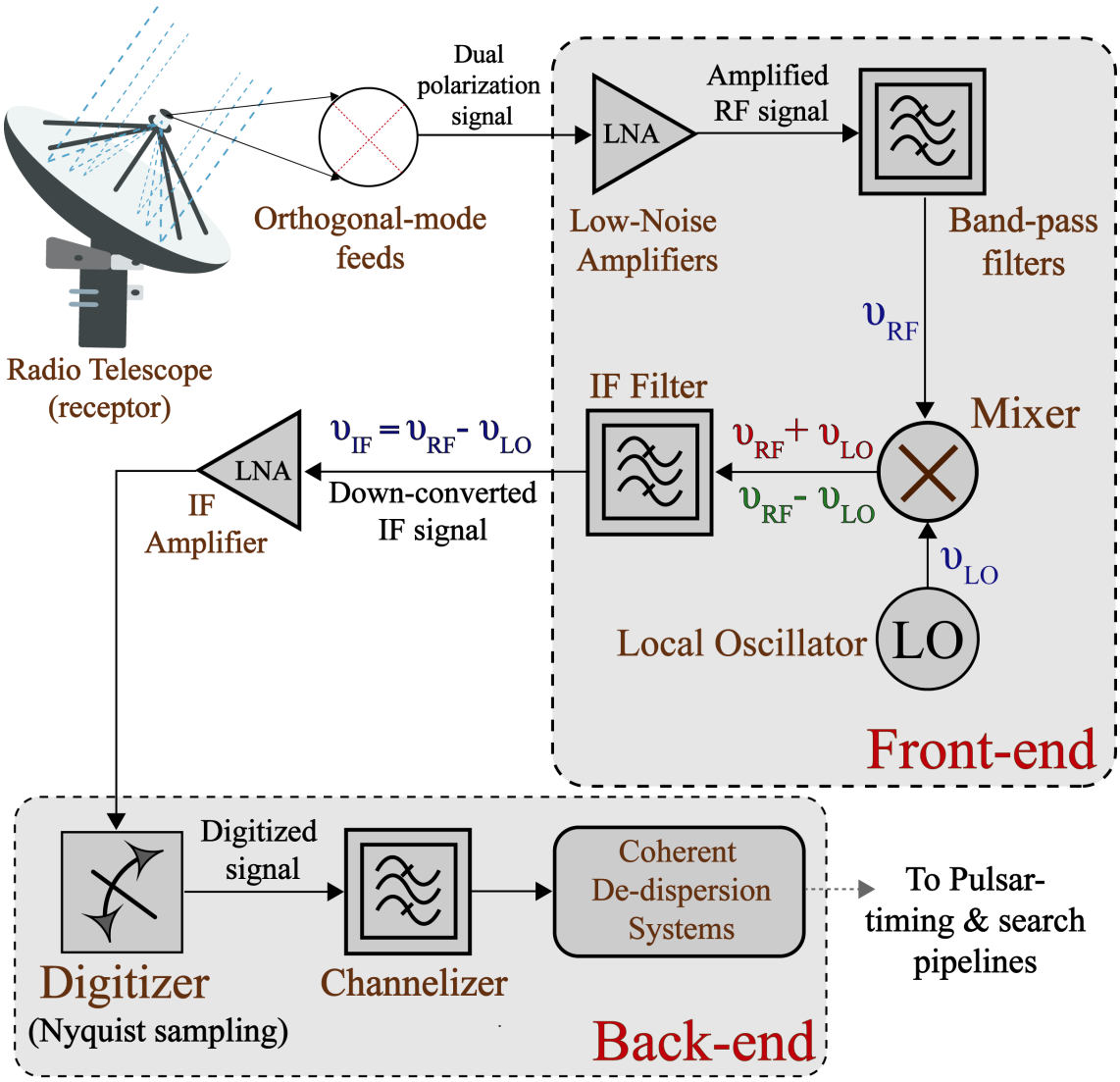

Figure 2.1 A schematic diagram representing a generic radio receiver. The front-end and back-end stages are clearly identified. It must be noted that although a single arrow is output from the orthogonal-mode feeds of the receptor, the various stages listed in the diagram individually apply to both orthogonally-polarized signals.

The functional dependence of the telescope gain on the orientation and distance of the astronomical source with respect to the central axis of the reflector is known as the 'beam shape'. Because of the reflection geometry of a parabolic reflector, the gain drops sharply with distance from the central axis and thus the telescope is more sensitive if the source is in the direct line of sight. The size of the radio telescope beam can be visualized as the angular width at which the gain drops by a factor of 2, also known as the full width half maximum (FWHM). This far-field radiation pattern of the telescope can be approximated as a 2-dimensional Bessel function (Rohlfs & Wilson 2000; Balanis 2005), whose half-power point or the FWHM is given by,

$$\mathrm{FWHM} \sim 1.22\frac{\lambda}{D}\mathrm{rad}, \tag{2.1}$$

where λ is the observing frequency and D is the diameter of the telescope, assuming a paraboloid. It must be noted that this FWHM is defined for the central lobe of the Bessel function, termed as the 'primary beam'. All the other lobes of a radio telescope are termed as its sidelobes.

The receiver usually consists of an orthogonal-mode transducer, which contain two orthogonally-aligned antennas that are sensitive to either circular or linear polarizations. These are positioned at the end of the waveguide which is located at the focus of the reflector. The Parkes multi-beam receiver used a feed horn as the waveguide, whereas recently more novel feed designs have been engineered for the Parkes ultra wideband receiver (Dunning et al. 2015) and the CSIRO phased array feeds (Hampson et al. 2012). The receiver also often contains low-noise amplifiers (LNAs) and cryogenic refrigeration systems that aid in reducing the system temperature. The signal is then typically passed through a bandpass filter, which passes the required bandwidth to the down-conversion unit.

2.1.3 Down-conversion

The pre-amplified radio signal then undergoes a number of amplification and conversion stages. This process is known as superheterodyne mixing. A lot of gain improvement is required through the various amplification stages and since it is often difficult to amplify a signal in a single stage, several stages of amplification are applied. Also, in order to simplify the process of designing electronic components further down the signal path, and to avoid transmission losses (the efficiency of most transmission lines decreases with increasing frequency of the transmitted signal), the observed radio signal, with a frequency ν_{RF} is combined with a synchronized local oscillator signal (ν_{LO}) to produce the required

signal at an intermediate frequency ($\nu_{\rm IF}$). This process is called 'mixing'. An ideal 'mixer' as shown in figure 2.1 is a device that multiplies one input frequency (tone) and a band-limited signal to produce a combined signal at the sum and difference frequencies of the input as described in equation 2.2,

$$\sin(At)\sin(Bt) = \frac{[\cos((A-B)t) - \cos((A+B)t)]}{2}. \tag{2.2}$$

Usually the $\nu_{\rm IF}$ is much less than $\nu_{\rm RF}$, i.e, the difference signal produced by the mixer is chosen for further processing. This process is also called 'down-conversion'. It must be noted here that during down-conversion, the entire band is shifted in frequency, but the width of the band is maintained. If the reference tone of the mixer ($\nu_{\rm LO}$) is placed below the observing band, the top of the band will be converted to a higher frequency than the bottom, assuming the difference signal is passed through the mixer. If the reference tone is chosen to be above the band, the differences will be negative and hence the order of the band is not preserved. These two cases are referred to as *upper-* and *lower-* sidebands respectively. A 'baseband' signal is where the lowest edge of the band is at zero frequency and the highest edge is at a frequency equal to the bandwidth of the observing system. Down-conversion of a signal is typically done in one of two ways: single- and dual-band (quadrature) down-conversion. In single-band down-conversion, the RF signal is band-limited and mixed with a LO signal, while in dual-band down-conversion the RF signal is split into two separate paths, both of which are band-limited and mixed with a LO signal. However, the phase of one of the LO signals is offset by 90° as compared to the other. Recombining the two signals after digitization produces a complex-valued representation of the real-valued signal. This process is also known as 'complex' sampling.

2.1.4 Digitization

The Nyquist sampling theorem states that a continuous time series can be digitized and reproduced if all the spectral content is preserved. It establishes a sufficient condition for a sample rate that permits a continuous-time signal of finite bandwidth to be represented as a discrete sequence of samples while preserving all the information. Following this, it can be established that for real-sampling of the voltage produced by a receiver, the Nyquist sampling rate is twice the highest frequency component or twice the bandwidth itself. Following down-conversion, the IF signal ($\nu_{\rm RF} - \nu_{\rm LO}$) is passed to the digitizer, where it is 'real-sampled' at the Nyquist frequency ($\nu_{\rm Nyquist} = 2\nu_{\rm IF}$) or 'complex-sampled' at half of $\nu_{\rm Nyquist}$ using two digitizers.

2.1.5 The Back-End

The components down the signal-path following down-conversion are collectively termed the 'backend'. Backends used for pulsar observations differ from others in radio astronomy predominantly because pulsar signals change rapidly with time, although in a quasi-periodic manner. It is thus not a surprise that pulsars were first discovered when a high-time resolution receiver was built to study short time-intensity variations (in quasars). The minimum detectable flux density ($S_{\rm min}$) can be computed by re-arranging Equation 1.12 as,

$$S_{\rm min} = \frac{S/N_{\rm min} T_{\rm sys}}{G\sqrt{N_p B t}} \sqrt{\frac{W}{P-W}}, \tag{2.3}$$

where $S/N_{\rm min}$ is the minimum required S/N. To successfully detect radio pulsars, averaging of the time series is performed by summing the phase-resolved signal over an arbitrarily large number of pulse periods (i.e, the spin period of the pulsar). Stacking n observed pulses increases the S/N by $\sqrt{n}$.. This procedure of averaging and stacking the pulses is known as 'folding'. The other predominant goal of the backend is to mitigate the effects of the propagation of the radio signal through the IISM. The following subsections briefly describe the various types of approaches implemented in the backend.

Analogue filterbank spectrometers

One of the straightforward ways to compensate for the effects of frequency-dependent pulse dispersion is to split the observing band into a large number of independent frequency channels and apply an appropriate time delay to each channel. This process is known as 'incoherent de-dispersion'. Equation 1.10 describes the time delay in the arrival time between two pulses at different frequencies. The applied delay causes the pulse to be output at the same time from each frequency channel. This appropriately delayed output from each channel is then added together to produce a de-dispersed time series. It is evident however that a small amount of dispersion is unmodelled within the bandwidth of individual frequency channels. Therefore, in this process, it is important to choose the channel bandwidths such that the dispersive time-delay does not become a significant fraction of the pulse period.

In an analogue filterbank (AFB), the incoming IF signal is split by multiple frequency filters, each signal undergoing independent digitization and detection. One of the simplest methods to digitize a signal is the 1-bit digitization scheme. The output of a 1-bit digitizer is either 0 or 1 depending on whether the running mean of the intensity is above or below a

threshold. 1-bit digitization ensures small data rate and effectively acts as a low-pass filter preventing aliasing effects. However, low bit digitization also has adverse effects on the data (Jenet & Anderson 1998) and it must be noted that the number of channels produced by an AFB is hardware dependent (i.e, fixed) and cannot be altered. Although low-bit sampling appears to be quite crude it has been shown that the loss of sensitivity is a good compromise over storing large quantities of data (a consequence of high bit sampling), especially for large pulsar search surveys and is also robust to RFI (Lorimer & Kramer 2004).

Autocorrelation spectrometers

In an autocorrelation spectrometer, the input IF signal is split into two copies. One copy of the signal is delayed by some amount t and is then multiplied with the original signal (not delayed) to produce a 'lagged' product. The delayed signal is then further delayed and multiplied with the original undelayed signal producing a second lagged product. This process is repeated for an arbitrary number of iterations. The resulting set of lagged products in the time domain can then be used to calculate the power in the frequency domain following the Weiner-Khinchin (WK) theorem.

The WK theorem states that, for a voltage $v(t)$ and its complex conjugate $v^*(t)$ as a function of time t, the auto-correlation function $R(\tau)$ is the Fourier transform of the power spectrum $P(f)$, also expressed as,

$$P(f) = \frac{1}{2\pi} \int_{-\infty}^{+\infty} R(\tau) e^{-2\pi i f \tau} \mathrm{d}\tau, \tag{2.4}$$

where $R(\tau)$ is,

$$R(\tau) = \lim_{T \to \infty} \frac{1}{T} \int_{0}^{T} v(t) v^*(t+\tau) \mathrm{d}t. \tag{2.5}$$

Autocorrelation spectrometers that were used for pulsar studies include the Caltech Fast Pulsar Timing Machine (Navarro et al. 1992) and the Wideband Arecibo Pulsar Processor (Dowd et al. 2000).

Coherent dedispersion systems

All of the backends described above are based on 'incoherent de-dispersion' systems, which do not account for the dispersive delay of the signal within each frequency channel (in the finite bandwidth of each channel). Hankins & Rickett (1975) pioneered a technique in which the phase information of the incoming signal can be used to completely remove the effects of the IISM. This process is known as 'coherent de-dispersion'. They demonstrated

that the effects of the IISM on the propagating electromagnetic radiation can be described as a transfer function H in the frequency domain (as a function of ν), given as,

$$H\left(\nu+\nu_0\right)=\exp\left(i\frac{2\pi D\nu^2}{\nu_0^2\left(\nu+\nu_0\right)}\right), \tag{2.6}$$

where ν_0 is the centre frequency of the observation, and the dispersion, D is related to the dispersion measure DM by,

$$\mathrm{DM}(\mathrm{pc\,cm^{-3}})=2.410331(2)\times10^{-4}\mathrm{D}\left(\mathrm{s\,MHz^2}\right). \tag{2.7}$$

By multiplying the Fourier transform of the observed signal by the inverse of the transfer function (H), the original signal is recovered with an arbitrary phase shift. Coherent de-dispersion results in sharper features in the observed pulse profiles thus leading to higher precision in pulsar timing experiments, which depend on the width of the profile. The development and usage of coherent dedispersion systems was heavily dependent on the progress of electronics and available processing capabilites. With the usage of commercial scale graphics processing units (GPUs), many real-time coherent dedispersion units were developed. Hotan et al. (2006a) used such a backend called the Caltech Parkes Swinburne Recorder II (CPSR2) for high-precision timing of 15 MSPs. Currently, almost every radio telescope uses real-time wideband coherent dedispersion systems, like the Parkes MEDUSA backend, the MeerKAT PT-USE backend (further described below) and many more globally.

2.2 The Parkes Radio Telescope: A single dish

The Parkes radio telescope is a 64-m single-dish telescope located outside the town of Parkes, New South Wales, Australia. Parkes is at a latitude of $-33.13°$ with the Galactic Centre passing within a few degrees of the zenith. With an effective northern declination limit of $+25°$ (Manchester et al. 2013), it can see more than two-thirds of the celestial sphere. The telescope is a national facility operated by the Commonwealth Scientific and Industrial Research Organisation (CSIRO). It has a number of receiver systems that can be switched into the focus beam for different science observations. For most of the pulsar studies, observations are made in three different radio-frequency bands: 10 cm, 20 cm and 50 cm. Observations at 20 cm have been made using the primary beam of the Parkes multi-beam receiver (Staveley-Smith et al. 1996), while the '10cm/50cm' receiver (Granet et al. 2005) was used for observations at 10 cm and 50 cm. The signals are down-converted to IF in the focus cabin and are band-limited and amplified at the receiver control room

to be sent to the backend digitizer systems. A number of backend systems have been developed over the years for pulsar observations; these include, the Wideband Correlator (WBC), the Wide Bandwidth Digital Recording (WBDR) system (Jenet et al. 1997), the two versions of CPSR (1 and 2) (van Straten et al. 2000; van Straten & Bailes 2003; Bailes 2003; Hotan et al. 2007), the ATNF Parkes Swinburne Recorder (APSR) (van Straten & Bailes 2011) and a series of Parkes Digital FilterBank Systems (PDFB1, PDFB2, PDFB3 and PDFB4) (Manchester et al. 2013).

Recently, a new receiver and backend system have been installed at Parkes; the ultra-wide-bandwidth, low-frequency receiver (UWL) operating over a continuous frequency range from 704 to 4032 MHz. It is the first in a line of new receivers planned for the Parkes radio telescope that will eventually provide a continuous frequency coverage from $\sim$ 700 MHz to $\sim$ 24 GHz. The UWL receiver includes a cryogenically cooled feed, LNAs, RF amplifiers and for the first time at Parkes, digitizers that sample the entire RF band directly in the focus cabin and stream the digitized data to the telescope tower. The digitized data are further processed in the tower (e.g, folding, polarization products) by the GPU-based MEDUSA backend. The output from the processor is sent to a data-staging server called EURYALE for data archiving.

The dataset used in Chapters 3 and 4 of this thesis is from the 10 cm, 20 cm and 40 cm observations of the Parkes multibeam and 10cm/50cm receivers and digitized using the PDFB backends. It is part of the Young Pulsar Timing program at Parkes which observes around 260 pulsars in support of the *Fermi* mission (Smith et al. 2008; Weltevrede et al. 2010).

2.2.1 The Young Pulsar Timing program

The regular monitoring of a large number of young pulsars is key to improving our understanding of neutron stars and pulsars, especially magnetospheric dynamics and neutron star interiors (Kramer et al. 2006a; Kerr et al. 2016; Hobbs et al. 2004; Shannon & Cordes 2010; Johnston & Karastergiou 2017; Espinoza et al. 2011b). The young pulsar timing program at Parkes has been monitoring a sample of $\sim$ 260 pulsars over the last $\sim$ 10 years at approximately a monthly cadence. Such a long timing baseline of young and energetic pulsars provides an opportunity to study phenomena on year-long timescales, including structures in the IISM over many lines of sight.

One of the key goals of this timing program is to characterize the spectrum of timing noise (described in Section 1.7.1). Long time spans are key in disentangling timing noise from other secular processes, including the study of glitches and correlated pulse profile

changes. In Chapters 3 and 4 of this thesis, an improved Bayesian inference based timing method is developed and applied on a sample of 85 young radio pulsars. In Chapter 3, we have characterized the spectrum of timing noise for these pulsars and report the measurements of new proper motions and braking indices for a subset of them. In Chapter 4, we further investigate the measurements of new braking indices and test the effects of long-term glitch recovery on the measured braking indices of pulsars.

2.3 The MeerKAT Radio Telescope: An Interferometer

The MeerKAT radio telescope is a precursor for the mid-frequency Square Kilometre Array (SKA). It is located on the SKA site in the Karoo, Northern Cape in South Africa. It consists of 64 antennas, each 13.9 m in diameter, equipped with cryogenically cooled receivers currently operating from 900 MHz to 1670 MHz (L-band). Two other receivers are being commissioned; the Ultra High Frequency (UHF) receiver, operating from 580 MHz to 1015 MHz and the S-band receiver developed by the Max Planck Institute for Radio Astronomy, operating from 1750 MHz to 3500 MHz (Kramer et al. 2016). The array configuration has 61% of the antennas within a 1 km diameter circle and the remaining are distributed out to a radius of 4 km. Figure 2.2 provides a schematic overview of the MeerKAT signal path, mainly focused on pulsar timing processing.

Each of the MeerKAT antennas has a 13.9 metre projected diameter, 'feed-down' offset Gregorian optical configuration (Jonas & MeerKAT Team 2016). The key advantage of this over other antenna designs is the unblocked aperture which results in a higher aperture efficiency, low sidelobes (thereby less susceptible to terrestrial RFI) and the elimination of reflected ground radiation (thus reducing the system temperature). One of the limitations, however, of the feed-down configuration is that the elevation limit is constrained to 15° due to the geometry of the telescope.

The receiver outputs are digitized immediately at the antenna and these digital streams are transported to the Karoo Array Processor Building (KAPB) via optical fibres. The direct digitization (without heterodyne mixing) is implemented to avoid spurious 'mixer' products and hence the digitizers are placed directly behind the receiver packages. Each receiver has an independent 10-bit digitizer (one for each polarization) that minimizes the strength of spurious signals in the ADC's digital output relative to the strength of a narrow-band input RF signal. These signals are then processed by the Correlator/Beamformer (CBF) digital signal processor.

The MeerKAT CBF implements a FX/B type real-time signal processor, i.e, the digitized voltage data streams from each receptor are split into the required number of inde-

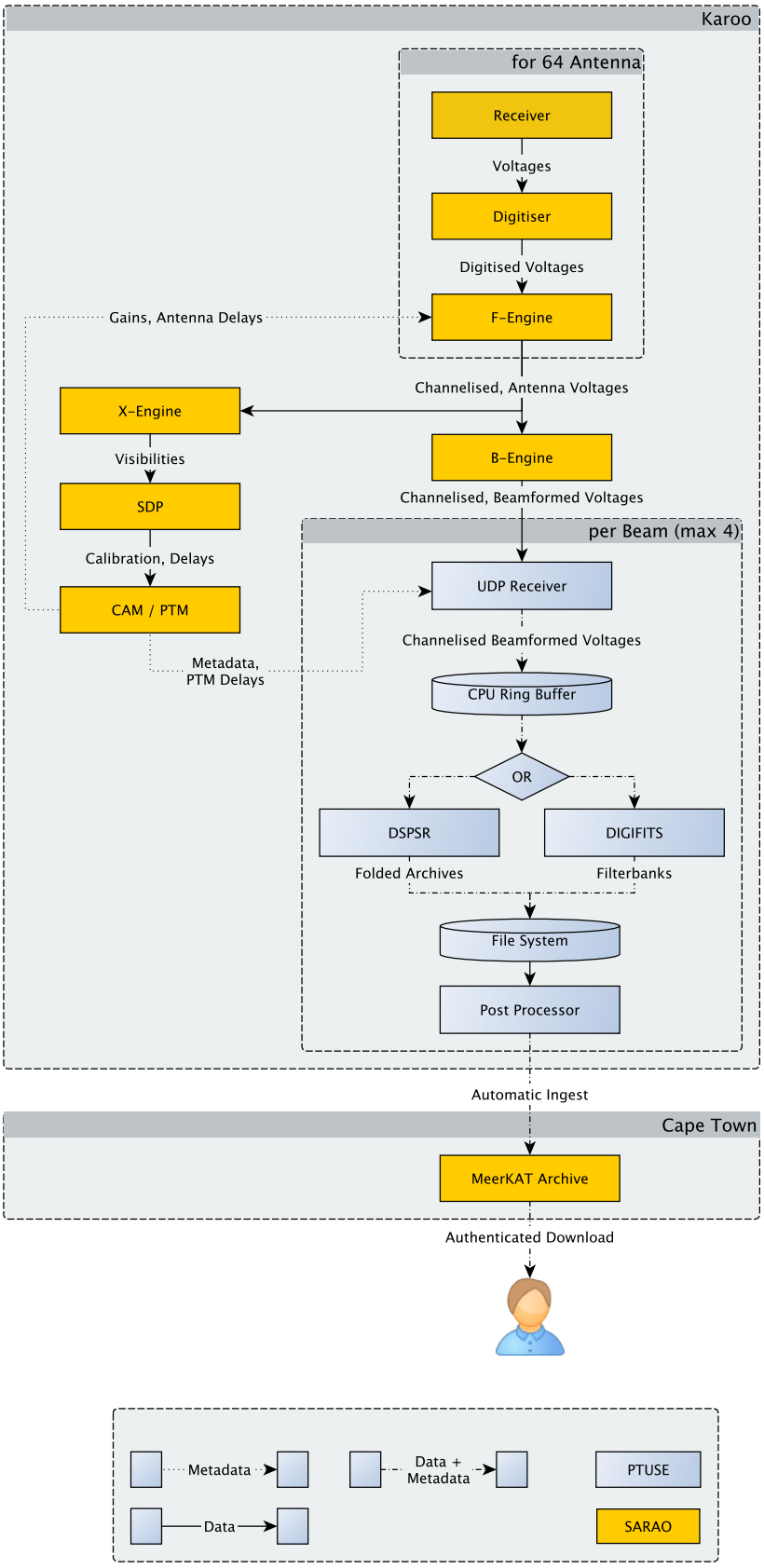

Figure 2.2 A schematic representation of the MeerKAT data flow and the Pulsar Timing User Supplied Equipment (PT-USE). (Credit: Andrew Jameson)

pendent frequency channels prior to correlation (X) and/or beamforming (B) by 'Fourier-engines' (F-engines). This channelization is done by a digital polyphase filter-bank (DFB) which is designed to minimize inter-channel spectral leakage and maintain uniformity of the frequency response across individual channels. It must be noted that the correlation and beamforming (performed by X- and B-engines) is implemented on full polarization data. The output CBF data product used for pulsar timing observations consists of data with 1024 frequency channels, 4 Stokes parameters and full digitized bandwidth with capabilities of recording pulsar single-pulse data down to a resolution of 9 μs. Data from the CBF is then passed on to the Science Data Processing (SDP) unit for data ingestion, data quality checks, calibration and archiving. The SDP processing nodes are a mixture of CPU and GPU clusters and use HDF5 format for storing data on disks.

To ensure coordinated operation of all telescope components, a Control and Monitoring (CAM) subsystem is used. CAM monitors the status of all telescope components, establishes interfaces to operators, developers and observers, aids in telescope configuration (e.g, sub-array building) and in scheduling. Since MeerKAT antenna data is also interfaced with a number of user-supplied digital backends (like the Pulsar Timing User Supplied Equipment; PT-USE) a common communications protocol called KATCP is implemented on all MeerKAT sub-systems to maintain consistency. Some of the other user-supplied backends include a pulsar and fast radio burst seach engine and a SETI signal processor (by the Breakthrough Listen project).

The MeerKAT science project consists of a diverse list of large survey projects (LSPs) which is estimated to occupy $\sim$ 75% of the first five years of MeerKAT operations. A large survey project is defined as one requiring more than 1000 hours of observing time. A total of 10 LSPs were approved by the time allocation committee, among which the pulsar timing LSP, called 'MeerTime' was allocated over $\sim$ 5000 hours of observing time for the five years of MeerKAT operation. An overview of the PT-USE is presented first followed by a brief description of the project and its major science themes in the following subsection.

2.3.1 MeerTime: The Pulsar Timing Key Science Project with MeerKAT.

The MeerTime project (see Bailes et al. 2018) is a large survey project using the MeerKAT radio telescope that will regularly monitor over 1000 radio pulsars to address a wide variety of astrophysical topics (see Section 1.6 for details), including strong-field tests of gravity using relativistic binary pulsars, the detection of the isotropic stochastic nHz gravitational wave background using precision timing of a large sample of millisecond pulsars,

understanding neutron star interiors through regular glitch monitoring of young pulsars, monitoring pulsars in globular clusters and understanding pulsar emission mechanisms by studying radio magnetars. The large collecting area and aperture efficiency, ability to slew the antennas at $\sim 2^{\circ}$/second, wideband receivers, access to the southern skies and the ability to sub-array the 64 dishes make MeerKAT the best pulsar timing instrument in the southern hemisphere.

MeerTime has four major science themes as listed below:

- **Millisecond Pulsar Timing and Gravitational Wave Detection:** The MSP timing project with MeerKAT has been allocated $\sim$ 2100 hours (over five years) and aims to create the best precision timing pulsar dataset. One of the primary science cases related to precision timing of an array of MSPs has been to detect the nanoHertz-frequency isotropic stochastic background of gravitational waves caused due to the merger of supermassive black hole binaries and/or cosmic strings in the early Universe. However, a number of studies have shown (Cordes & Downs 1985; D'Alessandro et al. 1993b; Jenet et al. 2001b; Osłowski et al. 2011; Shannon et al. 2014b) that increase in sensitivity does not always lead to improved precision as the attainable timing precision is fundamentally limited by the intrinsic phase and shape variations of the pulsar on short timescales (see section 1.7.2), known as 'jitter noise'. Chapter 5 of this thesis reports the first precision timing results of a large number of MSPs observed with the MeerKAT radio telescope and reports the measurements of jitter noise and the attainable timing precision. MeerKAT's wideband receivers enable studies of profile evolution and DM variations which will ultimately result in improving our timing precision (Pennucci 2019). The MSP timing program with MeerKAT will also result in a comprehensive MSP census that characterizes the polarization, RM and DM properties of MSPs observable with MeerKAT.

- **The Thousand Pulsar Array**: The regular monitoring of a thousand pulsars with a highly sensitive radio telescope like MeerKAT is in itself a scientific objective that will result in an exceptional legacy dataset exploring the breadth of pulsar phenomenology (Karastergiou et al. 2015). A number of questions regarding neutron star interiors, pulsar environments, the IISM and pulsar magnetospheric dynamics can be addressed with such a dataset. The connection between pulsar radio emission and timing properties have been observed in a few cases, although the connection is not fully understood (Kramer et al. 2006a; Lyne et al. 2010). The high S/N observations combined with high cadence of $\sim$ 1000 pulsars, provides a great opportunity

to study pulsar glitches in unprecedented detail. The sub-arraying capabilities of MeerKAT will enable a more optimized observing strategy to balance long observations of weak pulsars using more receptors ($\gtrsim 16$) and short observations of bright pulsars with one sub-array (~ 16 receptors).

- **Relativistic and Binary Pulsars** will use the improved sensitivity of MeerKAT compared to most other radio telescopes to enable greater precision in measuring pulsar binary parameters which will not only improve our existing measurements but also probe new physics (Kramer 2007).

- **Globular Cluster Pulsar Timing** will be able to observe all of the known globular cluster (GC) pulsars which will result in the most sensitive and comprehensive GC pulsar timing campaign undertaken so far (Hessels et al. 2015). Combining archival data from various radio telescopes with new MeerKAT timing data will provide insights into the proper motions and orbital motions of these pulsars in unprecedented detail.

2.4 Bayesian Inference in Radio Pulsar Timing - An Overview

A large part of the pulsar timing science described in chapter 1 and in this chapter is enabled by a process called model fitting. The model that is fitted to the pulsar ToAs is a complex, multi-parameter mathematical description that encompasses the pulsar's astrometry, spin evolution, radio pulse propagation through the IISM and effects of the solar system (as described in Section 1.5). This *timing model* not only accounts for the geometry of the pulsar, but also must contain the effects of gravity, relativity and binary companions. The parameter estimation is then typically performed by solving for the maximum-likelihood timing model using linear least-squares with standard pulsar timing packages like TEMPO and TEMPO2 (Hobbs et al. 2006).

We advocate as many others before, that a full Bayesian inference based timing-model analysis should be used to overcome many of the limitations posed by the standard least-squares paradigm (see Messenger et al. 2011; Lentati et al. 2014, 2017a; Vigeland & Vallisneri 2014 for a good overview).

Constructing a posterior distribution for a set of model parameters (θ), given data (d), is the primary aim of Bayesian inference. The posterior distribution is given as,

$$p(\theta|d). \tag{2.8}$$

From Bayes theorem, the posterior distribution can be expressed as,

$$p(\theta|d) = \frac{\mathcal{L}(d|\theta)\pi(\theta)}{\mathcal{Z}}, \tag{2.9}$$

where $\mathcal{L}(d|\theta)$ is the likelihood function of the data given the set of model parameters, $\pi(\theta)$ is the prior distributions on θ and $\mathcal{Z}$ is the normalization factor also known as the 'evidence'.

From a pulsar timing perspective, θ typically will represent the set of timing model parameters while d are the times-of-arrival (ToAs). The ToAs can be represented as a sum of both a deterministic and a stochastic component, expressed as,

$$d = d_{\rm det} + d_{\rm sto}. \tag{2.10}$$

Assuming that the stochastic contributions can be modelled as a random Gaussian process, the likelihood ($\mathcal{L}(d|\theta)$) is given as,

$$\mathcal{L}(\mathbf{d}|\theta) \propto \left(\prod_{i=1}^{n}\sigma_i^2\right)^{-\frac{1}{2}} \exp\left(-\frac{1}{2}\sum_{i=1}^{n}\frac{(d_i - \tau(\theta)_i)^2}{\sigma_i^2}\right), \tag{2.11}$$

where $\tau(\theta)$ is the timing model and the uncertainty in the ToA measurement is σ_i. This likelihood assumes that the ToAs are described solely by the timing model parameters (θ). Contributions from additional parameters like white noise, red noise, dispersion measure (DM) variations and the gravitational wave background signal can be added onto this likelihood to describe a more realistic model. See van Haasteren & Levin (2013); Shannon et al. (2015); Lentati et al. (2014, 2015a) for a more in-depth description of the various likelihood formalisms used in pulsar timing.

Just like the likelihood, the priors $\pi(\theta)$ are also described a priori as it incorporates our belief about θ. The choice of priors is highly dependent on the nature of the problem that is being solved. In Chapter 3 we provide a description of the types and ranges of priors used in the timing analysis of young radio pulsars.

One of the major strengths of the Bayesian approach in pulsar timing is that it provides the ability to perform a joint analysis of the timing model parameters including the various stochastic noise contributions, which accounts for the covariances between the timing model and the stochastic processes. However, it also provides the ability to marginalise over some of the timing model parameters (also referred to as 'nuisance parameters') analytically to reduce the dimensionality of the problem, which results in a marginalized posterior distribution,

$$p\left(\theta_i|d\right) = \int \left(\prod_k d\theta_k\right) p(\theta|d), \tag{2.12}$$

and a marginalized likelihood,

$$\mathcal{L}\left(d|\theta_i\right) = \int \left(\prod_{k\neq i} d\theta_k\right) \pi\left(\theta_k\right) \mathcal{L}(d|\theta). \tag{2.13}$$

Bayesian inference allows us to compare and select between alternative models with different parameter ranges by evaluating the model 'evidence'. In Equation 2.9, the Bayesian evidence was introduced, which can be expressed as,

$$\mathcal{Z} \equiv \int d\theta \mathcal{L}(d|\theta)\pi(\theta). \tag{2.14}$$

The evidence that results from a typical Bayesian analysis is a single number, which by itself does not signify anything. However taken in combination with other evidences, it allows us to compare and choose which model explains the data better and by how much. In pulsar timing analyses, evidence comparison allows us to choose between different noise models (white noise over white+red noise), different binary orbit parameters, a GWB detection versus non-detection models, and much more. In Chapters 3 and 4, model selection is used heavily to choose between different model and noise parameters and also to distinguish pulsar spin-down from glitch recovery signals. The ratio of the evidences from two different models is known as the Bayes factor,

$$\mathrm{BF}^{model1}_{model2} \equiv \frac{\mathcal{Z}_{model1}}{\mathcal{Z}_{model2}} \tag{2.15}$$

also expressed as the log Bayes factor,

$$\log \mathrm{BF}^{model1}_{model2} \equiv \log\left(\mathcal{Z}_{model1}\right) - \log\left(\mathcal{Z}_{model2}\right). \tag{2.16}$$

The Bayes factor threshold used to choose one model over the other is often dependent on the nature of the problem. When trying to choose between detection and non-detection models, a higher Bayes factor, typically $|\log \mathrm{BF}| = 8$ is preferred while in pulsar timing analysis, often the model comparisons are between different noise models or timing model parameters which can afford to have lower Bayes factor thresholds, typically $|\log \mathrm{BF}| > 5$. It must be noted here that formally, the comparison of two models is done by multiplying the Bayes factor with the ratio of the prior odds (known as the odds ratio) which denotes our prior belief on the relative likelihood of the the two models. However, in pulsar timing

analysis, the prior odds are often set to unity and hence the odds ratio is the Bayes factor. Model selection in the Bayesian inference paradigm is effective because the Bayes factor penalizes a more complicated model (i.e., having a larger prior volume) over a simpler model even if the likelihood for the latter is smaller. Other alternatives to model selection are also being currently investigated (Wang et al. 2019).

In summary, the Bayesian inference model provides a number of benefits over the standard linear least-squares approach, some of which are outlined below:

- It offers reliable estimates of parameter uncertainties and correlations amongst parameters taking into account the non-linear functional dependence of the timing model parameters.
- It allows to solve for the timing model and stochastic noise parameters simultaneously providing joint probability distributions for both.
- It allows to provide physically informed priors on various timing model parameters while also allowing the marginalization of nuisance parameters.
- It allows us to obtain a quantifiable way of choosing amongst various models using the Bayes factor.

In Chapters 3 and 4, the Bayesian pulsar timing package TEMPONEST (Lentati et al. 2014) is used and further developed upon for a detailed timing analysis of young radio pulsars.

3

Timing of young radio pulsars I: Timing noise, periodic modulation and proper motion

The smooth spin-down of young pulsars is perturbed by two non-deterministic phenomena, glitches and timing noise. Although the timing noise provides insights into nuclear and plasma physics at extreme densities, it acts as a barrier to high-precision pulsar timing experiments. An improved methodology based on Bayesian inference is developed to simultaneously model the stochastic and deterministic parameters for a sample of 85 high-$\dot{E}$ radio pulsars observed for ~ 10 years with the 64-m Parkes radio telescope. Timing noise is known to be a red process and we develop a parameterization based on the red-noise amplitude ($A_{\rm red}$) and spectral index (β). We measure the median $A_{\rm red}$ to be $-10.4^{+1.8}_{-1.7}$ yr$^{3/2}$ and β to be $-5.2^{+3.0}_{-3.8}$ and show that the strength of timing noise scales proportionally to $\nu^1|\dot{\nu}|^{-0.6\pm0.1}$, where ν is the spin frequency of the pulsar and $\dot{\nu}$ its spin-down rate. Finally, we measure significant braking indices for 19 pulsars, proper motions for two pulsars and discuss the presence of periodic modulation in the arrival times of five pulsars.

This chapter has been published in MNRAS (Parthasarathy et al. 2019).

3.1 Introduction

Young neutron stars provide unique insights into astrophysics that are not available from the bulk of the pulsar population. They frequently exhibit two types of deviations from a steady spin-down behaviour, 'glitches' and 'timing noise'. Glitches are sudden jumps in the pulsar's spin frequency acting as probes of neutron star interiors. Timing noise is a type of rotational irregularity which causes the pulse arrival times to stochastically wander about a steady spin-down state. Our sample is representative of pulsars that are spinning down rapidly and present the most promising avenue for detailed studies of timing noise,

glitches and their spin-down behaviour.

The technique of pulsar timing enables the precise measurement of their spin periods (P) and their spin-down rates ($\dot{P}$), allowing us to study their evolution in the $P - \dot{P}$ diagram (Johnston & Karastergiou 2017), see Figure 1. Although young pulsar timing offers several opportunities to explore a plethora of astrophysical phenomena, it is a challenging prospect as most of these astrophysical signals are dominated or biased by timing noise and glitches. A careful methodology is thus needed in the analysis of young pulsar timing data to disentangle the deterministic processes from the stochastic components. For example, young pulsars are thought to be associated with supernova remnants, and measuring their proper motions (Hobbs et al. 2005) allows us to probe the connections between the neutron star and its progenitor, which has implications for birthrate statistics (Manchester 2004). Unbiased measurements of proper motion through pulsar timing can be obtained only if the timing noise in the pulse arrival times is modelled accurately. While understanding the origin of the stochastic signals present in the ToAs is important, it is also essential to characterize and mitigate the effects of these signals as part of the general timing model because it reduces the bias in the estimation of other deterministic pulsar parameters.

3.1.1 Timing noise

Timing noise manifests itself as a red-noise process in the ToAs, implying an autocorrelated process on a time-scale of months to years and is generally described by a wide-sense stationary stochastic signal (Groth 1975). Boynton et al. (1972) attempted to describe the timing noise in the Crab pulsar as random walks in either the phase, frequency or the spin-down parameter of the pulsar. They showed that the power spectra expected from such random walks will be proportional to -2, -4 and -6 for phase, frequency and spin-down respectively. Following this, many attempts have been made to study the timing noise in pulsars over increasing data spans and for a larger sample of pulsars. Cordes & Helfand (1980) studied the timing behaviour of 50 pulsars and found that the timing activity was correlated with $\dot{P}$ but weakly correlated with P and concluded that timing activity is consistent with a random walk origin. As more pulsars with longer data sets were studied, it became apparent that timing noise might be explained by a combination of different random walks in pulsar spin-frequency (ν) and spin-frequency derivative ($\dot{\nu}$) and by discrete jumps in phase and spin-parameters. Timing noise is thought to arise due to changes in the coupling between the neutron star crust and its super-fluid core (Jones 1990) or magnetospheric torque fluctuations (Cheng 1987a, Lyne et al. 2010). It has also

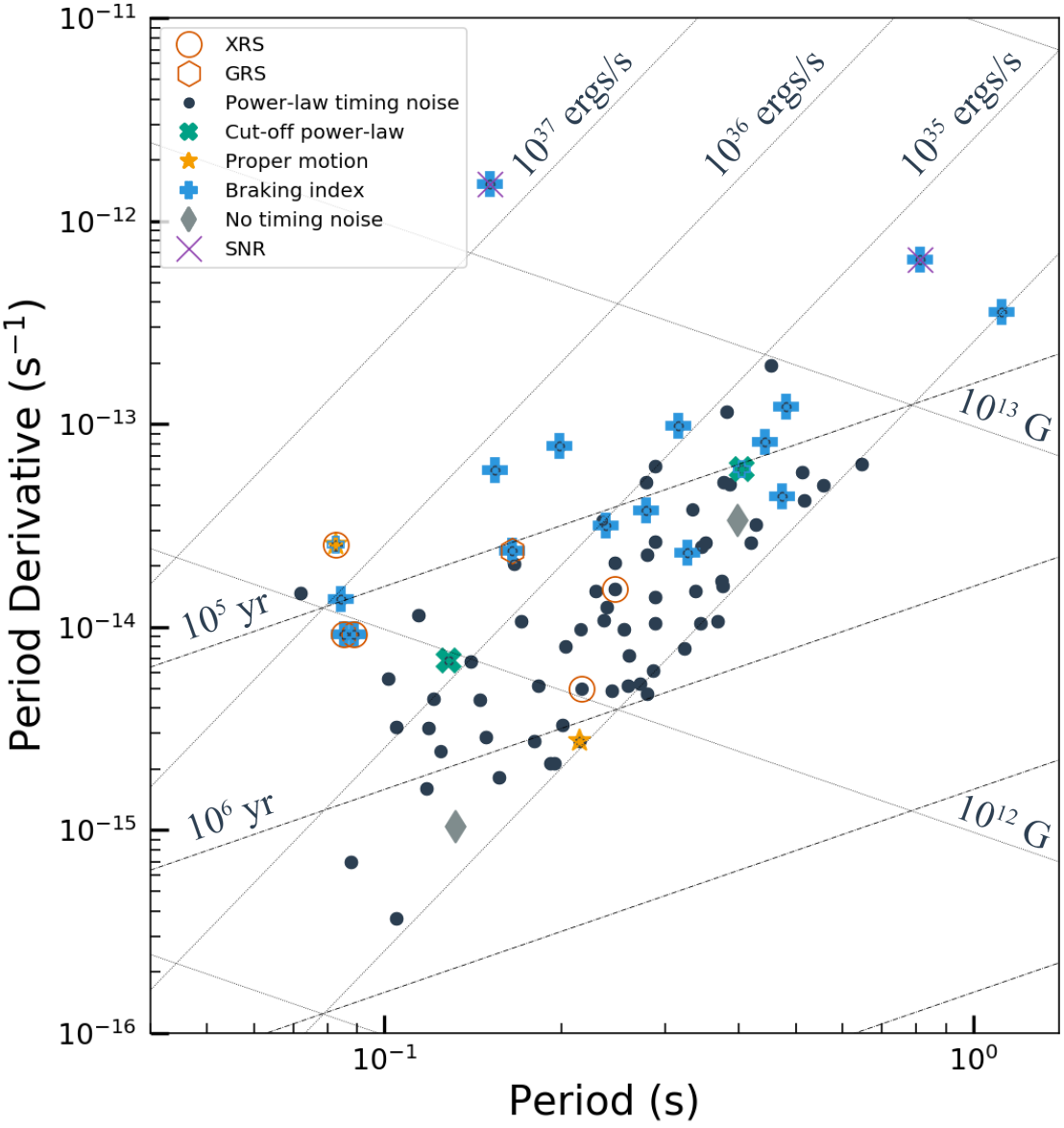

Figure 3.1 $P - \dot{P}$ diagram showing our sample of 85 young pulsars coloured according to their preferred timing model. The different timing models are outlined in Section 3.3. A few pulsars are also highlighted to be X-ray (XRS) or gamma-ray sources (GRS) and/or to have known supernova associations (SNR). Our sample of pulsars mostly have $\dot{E} > 10^{34}$ ergs/s, surface magnetic fields ranging from $10^{12}G$ to $10^{13}G$ with characteristic ages of 10^5 to 10^6 years.

been attributed to microjumps, which are similar to small glitches (Melatos et al. 2008) and fluctuations in the spin-down torque (Cheng 1987b). It has often been suggested that the superfluid interior of a neutron star can have macroscopic Kolmogorov-like turbulence which can contribute to stochasticity in the spin-down processes observed in radio pulsars (Greenstein 1970, Link 2012, Melatos & Link 2014b).

The observations of quasi-periodic state switching of pulsars (Kramer et al. 2006a, Lyne et al. 2010), each state with a distinct spin-down rate, led to alternative descriptions of timing noise being periodic or quasi-periodic processes. Unmodelled planetary companions (Kerr et al. 2015), pulse-shape changes (Brook et al. 2016), accretion from the ISM (Cordes & Greenstein 1981) or free precession (Stairs et al. 2000, Kerr et al. 2016) have also been attributed as explanations for the observed low-frequency structures in the ToAs. Hobbs et al. (2005), studied a large sample of pulsars observed over $\sim$ 10 years and concluded that timing noise is widespread in pulsars, and that it cannot be explained as a simple random walk in pulse phase, frequency or spin-down rate. The timing noise in millisecond pulsars (MSPs) has been mainly studied to understand their sensitivity to nHz-frequency gravitational waves (Lam et al. 2017, Caballero et al. 2016, Lentati et al. 2016a). However, unlike millisecond pulsars, the timing noise in young pulsars is very strong, often contributing many cycles of pulse phase on week to month timescales. Shannon & Cordes (2010) pointed out that the observed strength of timing noise varies by more than eight orders of magnitude over magnetars, young and millisecond pulsars.

3.1.2 Pulsar spin-down and braking index

The long-term spin-down of a pulsar can be approximated as

$$\dot{\nu} = -K\nu^{\mathrm{n}}, \tag{3.1}$$

where K is a constant and n is the braking index. The braking index describes the relationship between the braking torque acting on a pulsar and its spin-frequency parameters, and provides a probe into the physics dictating pulsar temporal evolution. We solve for n by taking the derivative of equation 3.1,

$$n = \frac{\nu\ddot{\nu}}{\dot{\nu}^2}, \tag{3.2}$$

where $\ddot{\nu}$ is the second derivative of the spin frequency. For standard magnetic-dipole braking, the magnetic field strength and the magnetic-dipole inclination angle are assumed to be constant in time, with $n = 3$ (Espinoza et al. 2017). While measuring ν and $\dot{\nu}$ is

trivial using standard timing methods, measuring the long-term $\ddot{\nu}$ is challenging, mainly because of the fact that it is a very small quantity. In 'old' pulsars, with $\nu \sim 1$ Hz and $\dot{\nu} \sim 10^{-15}\,\mathrm{Hz\,s^{-1}}$, the estimated $\ddot{\nu}$ from equation 3.2 is $\sim 10^{-30}\,\mathrm{Hz\,s^{-2}}$. However for the youngest pulsars we estimate $\ddot{\nu}$ to be $< 10^{-20}\,\mathrm{Hz\,s^{-2}}$, which makes these pulsars suitable for studying pulsar braking mechanisms (Johnston & Galloway 1999). If both K and n are constant in time, a pulsar will follow a track in the $P - \dot{P}$ diagram with a slope of $2 - n$. The $P - \dot{P}$ diagram can then be used as an evolutionary tool in which pulsars are born in the upper-left region and as they age and spin-down, they drift towards the cluster of "normal" pulsars, with periods of ~ 0.5 s (Johnston & Karastergiou 2017).

Both timing noise and glitches introduce variations in $\dot{\nu}$ which becomes problematical in the long-term measurement of $\ddot{\nu}$. Glitches are often modelled as permanent changes in spin-frequency (ν) and spin-frequency derivative ($\dot{\nu}$) or as exponential decays in ν over τ days and are typically attributed to either the transfer of angular momentum between the super-fluid interior and the solid crust of the neutron star (Anderson & Itoh 1975, Alpar et al. 1985) or as star quakes in the crystalline outer crust of the neutron star (Ruderman 1969).

3.1.3 Quasi-Periodic modulations

The reflex motion resulting from the orbital motion of a companion to a pulsar, introduces modulations in the ToAs, which led to e.g. the discovery of the double neutron star system B1913+16 (Hulse & Taylor 1975) and the first exoplanets (Wolszczan & Frail 1992).

Precession induces a periodic change in the spin-down torque which causes ToA modulation and since our line of sight cuts across different parts of the neutron star polar cap, there can also be an observed change in the shape of the pulse profile (Link & Epstein 2001). Such events of ToA modulations were reported by Lyne et al. (2010) in 17 pulsars, of which 6 showed correlations with pulse profile variations. Recently, Stairs et al. (2019) reported correlated shape and spin-down changes in PSR J1830–1059, which they attributed to large-scale magnetospheric switching.

Brook et al. (2016) analysed 168 pulsars and searched for correlations between profile shape changes and $\dot{\nu}$ and found that although this correlation is clear in some pulsars, the intrinsic relationship between change in $\dot{\nu}$ and profile variability may be much more complex than previously postulated (see also Kerr et al. 2016).

3.1.4 Proper motions

Pulsars are created in supernovae, and the birth process is expected to impart a high 'kick velocity'. Various mechanisms have been proposed for these kicks, including an asymmetric neutrino emission in the presence of super-strong magnetic fields (Lai & Qian, 1998), a postnatal electromagnetic rocket mechanism (Harrison & Tademaru, 1975), asymmetric explosion of γ-ray bursts (Cui et al., 2007) and hydrodynamical instabilities in the collapsed supernova core (Lai & Goldreich, 2000). While the evidence for such kicks is unequivocal (Johnston et al. 2005), their physical origin remains unclear. A pulsar's proper motion causes sinusoidal variations in ToAs with a periodicity of one year and an amplitude which increases with time.

3.1.5 The Bayesian pulsar timing framework

Lentati et al. (2013) pointed out that in order to obtain an unbiased estimation of the pulsar parameters (proper motions, spin parameters, braking index etc.) it is important to simultaneously model the stochastic (timing noise) and the deterministic (pulsar) parameters. Most of the frequentist approaches (Hobbs et al. 2004, Coles et al. 2011) do not consider the covariances between the timing model and the stochastic processes, and the uncertainties in the parameter estimates, motivating the development of TEMPONEST (Lentati et al. 2014), which performs a simultaneous analysis of the timing model and additional stochastic parameters using the Bayesian inference tool, MULTINEST (Feroz et al. 2009, Feroz et al. 2011). It also allows for robust model selection between different sets of timing parameters based on the Bayesian evidences. We use TEMPONEST to simultaneously model the pulsar parameters and the noise parameters

and use the Bayesian evidence to select the optimal model for each pulsar. Such an analysis allows us to discuss the statistical properties of timing noise and also compare the results with those obtained from other Bayesian tools.

In Section 3.2, we describe the observing program and the data processing pipeline. In Section 3.3, we describe the Bayesian timing analysis in detail and present the mathematical formulation of the timing model. In Section 3.4, we present the basic observational characteristics, the timing solutions, the timing noise models for our sample of pulsars along with the new proper motions. Finally in Section 3.5, we delve into the implications of our results.

3.2 Observations

In this paper, we study 85 pulsars observed at a monthly cadence using the 64-m CSIRO Parkes radio telescope in support of the *Fermi* mission that commenced in February 2007 (Smith et al. 2008, Weltevrede et al. 2010). We selected pulsars for which there were no identified glitches [1]. These pulsars have $\dot{E} > 10^{34}$ ergs/s, surface magnetic fields typically ranging from 10^{12}G to 10^{13}G with characteristic ages of 10^5 to 10^6 years as shown in Figure 3.1. Two pulsars, PSR J1513–5908 and J1632–4818 have known associations with supernova remnants, five other pulsars, PSR J0543+2329, J1224–6407, J1509–5850, J1809–1917, J1833–0827 are known X-ray sources and 3 others, J1509–5850, J1513–5908, J1648–4611 are known gamma-ray sources (Abdo et al. 2013).

Most of these observations were carried out using the 20-cm multi-beam receiver (Staveley-Smith et al. 1996), with 256 MHz of bandwidth divided into 1024 frequency channels and folded in real-time into 1024 phase bins. Some of these pulsars were also observed at radio wavelengths of 10-cm and 40-cm. Each pulsar is observed for a few minutes depending upon its flux density. The observations were excised of radio frequency interference (RFI) and calibrated using standard PSRCHIVE (Hotan et al. 2004b) tools and averaged in frequency, time and polarization. The ToAs of the pulses were computed by correlating a high signal-to-noise ratio, smoothed template with the averaged observations. For this analysis, we use only the 20-cm observations as the 10-cm data are sparsely spaced in time and the 50-cm data are highly corrupted by RFI.

3.3 Timing analysis

Establishing a phase coherent solution to the ToAs is an important step in the process of pulsar timing. We know that most of the young pulsars have a strong presence of timing noise and frequent glitches which makes it difficult to produce and maintain phase-connected timing solutions. We use the pulsar-timing code, TEMPO2 (Hobbs et al. 2006) to attribute relative pulse numbers to the ToAs and obtain phase connection in the timing residuals.

We split the timing analysis into 2 steps. The first step involves phase connecting the timing residuals. The second step involves using the phase connected timing solution in the Bayesian timing package, TEMPONEST, to construct a complete timing model with stochastic and additional deterministic parameters. TEMPONEST allows us to simultaneously model stochastic and deterministic parameters of interest and marginalize over

[1] In subsequent analysis described below, two relatively small glitches were detected and parametrized.

Table 3.1 Observational characteristics of the 85 pulsars described in this paper. The position and spin-down parameters are reported at the mentioned period epoch (PEPOCH) along with the timespan and the MJD range. The 95% confidence limits for the position and spin-parameters reported here are derived from the preferred model for each pulsar. The confidence regions are individually stated, if the upper and lower confidence limits are asymmetric.

PSR	RAJ	DECJ	PEPOCH	ν	$\dot{\nu}$	N_{ToA}	Timespan	MJD Range
	(h:m:s)	(d:m:s)		(s^{-1})	($10^{-14}s^{-2}$)		(yr)	
J0543+2329	$05{:}43{:}11.26^{0.05}_{0.62}$	$23{:}16{:}39.66^{0.91}_{0.03}$	55580	4.06531029396(8)	-25.48351(13)	111	9.6	54505-58011
J0745–5353	07:45:04.48(4)	-53:53:09.56(3)	55129	4.65465907222(10)	-4.73802(14)	173	10.5	53973-57824
J0820–3826	08:20:59.929(9)	-38:26:42.9(13)	55583	8.01046656802(3)	-15.6734(5)	115	9.0	54548-57824
J0834–4159	08:34:17.807(2)	-41:59:35.99(2)	55308	8.25642751376(12)	-29.18213(2)	134	9.9	54220-57824
J0857–4424	08:57:55.832(2)	-44:24:10.65(2)	55335	3.0601045423(4)	-19.6145(10)	170	9.9	54220-57824
J0905–5127	09:05:51.96(2)	-51:27:54.05(2)	55341	2.88766003664(2)	-20.7322(6)	136	10.5	53971-57824
J0954–5430	09:54:06.046(5)	-54:30:52.82(4)	55323	2.11483307064(18)	-19.6358(5)	125	9.9	54220-57824
J1016–5819	10:16:12.071(2)	-58:19:01.07(16)	55333	11.38507898552(7)	-9.05763(13)	128	9.9	54220-57824
J1020–6026	10:20:11.41(19)	-60:26:06.3(12)	55494	7.11838566803(5)	-34.1421(5)	81	6.4	54365-56708
J1043–6116	10:43:55.261(2)	-61:16:50.76(2)	55358	3.46493998447(4)	-12.49169(7)	131	9.9	54220-57824
J1115–6052	11:15:53.722(4)	-60:52:18.61(3)	55366	3.84942036520(10)	-10.70996(13)	130	10.4	54220-58011
J1123–6259	11:23:55.53(12)	-62:59:10.94(8)	55393	3.68410549479(18)	-7.13560(2)	131	10.4	54220-58011
J1156–5707	11:56:07.45(7)	-57:07:02.1(6)	55354	3.4672047206(6)	-31.9149(9)	134	10.4	54220-58011
J1216–6223	12:16:41.96(13)	-62:23:57.00(9)	55391	2.673417841032(14)	-12.02408(14)	90	6.8	54220-56708
J1224–6407	12:24:22.254(6)	-64:07:53.87(4)	55191	4.61936868862(6)	-10.56960(8)	274	10.4	54204-58011
J1305–6203	13:05:21.14(10)	-62:03:21.07(8)	55390	2.33768482203(6)	-17.57335(10)	127	10.4	54220-58011
J1349–6130	13:49:36.62(18)	-61:30:17.12(15)	55429	3.85557384197(19)	-7.60678(3)	171	10.4	54220-58012
J1412–6145	14:12:07.63(10)	-61:45:28.48(8)	55363	3.1720007909(13)	-99.643(4)	162	10.4	54220-58012
J1452–5851	14:52:52.60(10)	-58:51:13.2(11)	55367	2.586365680859(2)	-33.91606(17)	75	6.8	54220-56708
J1453–6413	14:53:32.665(6)	-64:13:16.00(5)	55433	5.57144021375(9)	-8.51812(15)	184	10.4	54220-58012
J1509–5850	15:09:27.156(7)	-58:50:56.01(8)	55378	11.2454488757(7)	-115.9175(16)	129	10.4	54220-58012
J1512–5759	15:12:43.04(10)	-57:59:59.8(11)	55383	7.77009392040(18)	-41.37272(2)	131	10.4	54220-58012
J1513–5908	$15{:}13{:}55.81^{0.11}_{0.1}$	$-59{:}08{:}09.64^{0.04}_{0.11}$	55336	6.59709182778(19)	-6653.10558(27)	151	11.6	54220-58469
J1514–5925	15:14:59.10(3)	-59:25:43.5(3)	55415	6.72054447215(8)	-13.0014(17)	85	6.8	54220-56708
J1515–5720	15:15:09.23(14)	-57:20:50.15(17)	55380	3.48859614104(17)	-7.41624(2)	130	10.4	54220-58012
J1524–5706	15:24:21.42(12)	-57:06:34.64(15)	55383	0.89591729463(9)	-28.60366(2)	128	10.4	54220-58012
J1530–5327	15:30:26.892(2)	-53:27:56.02(4)	55431	3.58476370133(5)	-6.01385(9)	158	10.4	54220-58012
J1531–5610	15:31:27.901(11)	-56:10:55.33(13)	55304	11.8756292823(4)	-194.5360(14)	140	10.4	54220-58012
J1538–5551	15:38:45.016(5)	-55:51:36.95(8)	55421	9.55329718930(4)	-29.2693(6)	85	6.8	54220-56708
J1539–5626	15:39:14.06(18)	-56:26:26.3(2)	55408	4.10854528747(18)	-8.18323(2)	128	10.4	54220-58012
J1543–5459	15:43:56.43(6)	-54:59:15.0(8)	55408	2.6515508603(4)	-36.6285(7)	128	10.4	54220-58012
J1548–5607	15:48:44.015(8)	-56:07:34.3(10)	55408	5.85007580447(19)	-36.73172(3)	128	10.4	54220-58012
J1549–4848	15:49:21.08(17)	-48:48:35.5(3)	55407	3.46794867500(2)	-16.96693(3)	130	10.4	54220-58012
J1551–5310	15:51:41.0(10)	-53:11:00.5(4)	55383	2.20532573802(11)	-94.7569(18)	84	6.8	54220-56708
J1600–5751	16:00:19.90(11)	-57:51:15.3(13)	55377	5.14255433375(2)	-5.63069(3)	129	10.4	54220-58012
J1601–5335	16:01:54.81(2)	-53:35:44.1(4)	55391	3.46645281446(7)	-74.9184(10)	86	6.8	54220-56708
J1611–5209	$16{:}11{:}03.37(01)$	$-52{:}09{:}22.13^{0.1}_{0.11}$	55390	5.47960812333(12)	-15.52478(19)	128	10.4	54220-58012
J1632–4757	16:32:16.66(13)	-47:57:34.5(3)	55419	4.37505274487(4)	-28.8454(7)	83	6.8	54220-56708
J1632–4818	16:32:39.70(3)	-48:18:53.8(8)	55426	1.2289964712(14)	-98.0730(3)	113	10.4	54220-58012
J1637–4553	16:37:58.692(4)	-45:53:26.82(9)	55443	8.41939738252(19)	-22.6194(4)	159	11.1	53971-58012
J1637–4642	16:37:13.75(17)	-46:42:14.2(4)	55398	6.491542203(4)	-249.892(10)	128	10.4	54220-58012

Table 3.1 Observational characteristics of the 85 pulsars described in this paper. The position and spin-down parameters are reported at the mentioned period epoch (PEPOCH) along with the timespan and the MJD range. The 95% confidence limits for the position and spin-parameters reported here are derived from the preferred model for each pulsar. The confidence regions are individually stated, if the upper and lower confidence limits are asymmetric (continued).

JName	RAJ (h:m:s)	DECJ (d:m:s)	PEPOCH	ν (s^{-1})	$\dot{\nu}$ ($10^{-14}s^{-2}$)	N_{ToA}	Timespan (yr)	MJD Range
J1638–4417	16:38:46.226(8)	-44:17:03.2(2)	55410	8.4888197965(4)	-11.5716(7)	128	10.4	54220-58012
J1638–4608	16:38:23.26(9)	-46:08:13.4(3)	55408	3.5951208300(10)	-66.5397(16)	129	10.4	54220-58012
J1640–4715	16:40:13.09(3)	-47:15:38.1(8)	55392	1.9326284729(4)	-15.7266(6)	128	10.4	54220-58012
J1643–4505	16:43:36.91(3)	-45:05:45.8(7)	55580	4.212470392(4)	-56.473(10)	116	9.6	54505-58012
J1648–4611	16:48:22.043(7)	$-46{:}11{:}15.75^{0.19}_{0.2}$	55395	6.0621606076(2)	-87.220(5)	125	10.4	54220-58012
J1649–4653	16:49:24.61(11)	-46:53:09.3(2)	55360	1.79521547256(18)	-15.98143(2)	125	10.4	54220-58012
J1650–4921	16:50:35.109(17)	-49:21:03.76(3)	55599	6.393872581394(2)	-7.43411(5)	112	9.5	54548-58012
J1702–4306	17:02:27.36(2)	-43:06:45.1(4)	55560	4.64018878013(2)	-21.05720(2)	102	9.6	54505-58012
J1715–3903	17:15:14.08(4)	$-39{:}02{:}57.13^{0.06}_{0.12}$	55370	3.5907423095(9)	-48.2784(13)	128	10.4	54220-58012
J1722–3712	17:22:59.21(4)	$-37{:}12{:}04.51^{0.06}_{0.09}$	55362	4.2340633683(7)	-19.4742(11)	131	10.4	54220-58012
J1723–3659	17:23:07.58(17)	-36:59:14.2(8)	55384	4.93279317887(3)	-19.5353(5)	128	10.4	54220-58012
J1733–3716	17:33:26.760(2)	-37:16:55.19(10)	55359	2.96213003717(4)	-13.19989(9)	129	11.1	53971-58012
J1735–3258	$17{:}35{:}56.66^{0.61}_{0.09}$	$-32{:}58{:}21.78^{0.46}_{0.38}$	55355	2.84923231813(2)	-21.1107(3)	89	6.7	54220-56672
J1738–2955	17:38:52.12(2)	$-29{:}55{:}57.39^{0.22}_{0.15}$	55377	2.2551713364(2)	-41.7146(12)	89	6.8	54220-56709
J1739–2903	17:39:34.292(2)	-29:03:02.2(2)	55385	3.09706373618(5)	-7.55345(7)	135	10.4	54220-58012
J1739–3023	17:39:39.79(4)	$-30{:}23{:}12.87^{0.18}_{0.08}$	55351	8.7434194934(13)	-87.1129(2)	133	10.4	54220-58012
J1745–3040	17:45:56.316(12)	-30:40:22.9(11)	55276	2.721579246363(8)	-7.90460(4)	219	13.6	53035-58012
J1801–2154	$18{:}01{:}08.38^{0.63}_{0.05}$	$-21{:}54{:}07.51^{0.09}_{0.81}$	55385	2.66452256901(11)	-11.3721(15)	84	6.8	54220-56708
J1806–2125	$18{:}06{:}19.59^{0.48}_{0.06}$	$-21{:}27{:}55.33^{0.98}_{0.48}$	55349	2.075444041(15)	-50.821(2)	123	11.0	53968-57992
J1809–1917	18:09:43.136(2)	-19:17:38.1(5)	55366	12.0838226201(8)	-372.7882(19)	130	10.4	54220-58012
J1815–1738	18:15:14.67(19)	$-17{:}38{:}06.95^{0.32}_{0.57}$	55364	5.03887545888(10)	-197.4552(11)	86	6.8	54220-56708
J1820–1529	$18{:}20{:}41.11^{0.47}_{0.07}$	$-15{:}29{:}42.37^{0.08}_{0.29}$	55373	3.000716562(16)	-34.130(4)	81	7.4	53968-56671
J1824–1945	18:24:00.56(18)	$-19{:}46{:}03.47^{0.21}_{0.43}$	55291	5.281575552287(3)	-14.6048(5)	149	10.4	54220-58012
J1825–1446	18:25:02.96(17)	$-14{:}46{:}53.75^{0.72}_{0.68}$	55314	3.5816835827(4)	-29.0816(6)	132	10.4	54220-58012
J1828–1057	18:28:33.24(10)	-10:57:26.9(7)	55334	4.05954117419(6)	-34.1114(4)	89	6.8	54220-56708
J1828–1101	18:28:18.8(13)	$-11{:}01{:}51.28^{0.02}_{0.93}$	55356	13.877993641(13)	-284.992(2)	131	11.1	53951-58012
J1830–1059	$18{:}30{:}47.51^{0.11}_{0.1}$	$-10{:}59{:}26.45^{0.88}_{0.74}$	55372	2.4686900068(5)	-36.5201(10)	154	10.4	54220-58012
J1832–0827	18:32:37.013(2)	-08:27:03.7(12)	55397	1.544817633127(2)	-15.24858(4)	124	10.4	54220-58012
J1833–0827	18:33:40.268(3)	-08:27:31.6(18)	55402	11.7249580817(4)	-126.1600(8)	124	10.2	54268-58012
J1834–0731	18:34:15.97(2)	-07:31:05.93(7)	55376	1.94933571114(6)	-22.1210(7)	85	6.7	54268-56708
J1835–0944	18:35:46.653(6)	-09:44:27.2(4)	55130	6.88006896072(4)	-20.7560(11)	41	3.7	54478-55822
J1835–1106	18:35:18.41(5)	-11:06:16.1(9)	55429	6.0270868794(10)	-74.7918(16)	125	10.2	54268-58012
J1837–0559	18:37:23.652(6)	-05:59:28.6(2)	55470	4.97354763055(2)	-8.1858(4)	115	10.2	54303-58012
J1838–0453	18:38:11.4(12)	$-04{:}53{:}25.57^{0.32}_{0.83}$	55339	2.6255980205(5)	-80.1949(3)	91	6.6	54306-56708
J1838–0549	18:38:38.065(6)	-05:49:12.1(3)	55473	4.249688210732(2)	-60.3601(5)	81	6.6	54306-56708
J1839–0321	18:39:37.520(8)	-03:21:10.8(3)	55522	4.187917144798(2)	-21.9566(7)	70	6.6	54306-56708
J1839–0905	18:39:53.46(3)	-9:05:14.1(8)	54979	2.38677780294(7)	-14.8244(10)	55	4.3	54268-55822
J1842–0905	18:42:22.15(2)	-09:05:30.0(3)	55392	2.90152784474(2)	-8.8183(4)	126	10.2	54268-58012
J1843–0355	18:43:06.663(8)	-03:55:56.6(3)	55402	7.557780825655(2)	-5.94013(9)	84	7.5	53968-56708
J1843–0702	18:43:22.439(2)	-07:02:54.6(14)	55380	5.21880961058(15)	-5.81812(2)	128	10.2	54268-58012

Table 3.1 Observational characteristics of the 85 pulsars described in this paper. The position and spin-down parameters are reported at the mentioned period epoch (PEPOCH) along with the timespan and the MJD range. The 95% confidence limits for the position and spin-parameters reported here are derived from the preferred model for each pulsar. The confidence regions are individually stated, if the upper and lower confidence limits are asymmetric (continued).

JName	RAJ (h:m:s)	DECJ (d:m:s)	PEPOCH	ν (s^{-1})	$\dot{\nu}$ ($10^{-14}s^{-2}$)	N_{ToA}	Timespan (yr)	MJD Range
J1844–0538	18:44:05.12(2)	-05:38:34.1(14)	55410	3.91076899155(11)	-14.84390(17)	122	10.2	54268-58012
J1845–0743	18:45:57.1833(4)	-07:43:38.57(2)	55336	9.551586249996(12)	-3.345425(2)	130	10.3	54267-58012
J1853–0004	18:53:23.027(8)	-00:04:33.4(3)	55446	9.85832573140(2)	-54.1604(5)	118	10.1	54306-58012
J1853+0011	18:53:29.980(8)	00:11:30.6(3)	55163	2.513260850307(15)	-21.17846(12)	37	3.4	54597-55822

nuisance parameters that are of no interest to this analysis. For example, in one of the timing models, we fitted the timing noise parameters (white noise and red noise) while simultaneously searching over a wide range of position and spin parameters, while keeping the dispersion measure (DM) fixed. We compute a Bayesian log-evidence value associated with the models for each pulsar to determine which timing model is preferred.

The ToAs for each pulsar are considered to be a sum of both deterministic and stochastic components:

$$t_{\rm tot} = t_{\rm det} + t_{\rm sto}, \tag{3.3}$$

The deterministic components in our timing models include various permutations of the pulsar position, spin, proper motion and the spin-down parameters while the stochastic contribution is computed by introducing additional parameters that describe the white and red noise processes. The white noise is modelled by adjusting the uncertainty on individual ToAs to be,

$$\sigma^2 = F{\sigma_{\rm r}}^2 + {\sigma_{\rm Q}}^2, \tag{3.4}$$

where F, referred to as EFAC, is introduced as a free parameter to account for instrumental distortions and ${\sigma_{\rm r}}^2$ is the formal uncertainty obtained from ToA fitting. In our analysis we use a global EFAC flag for our 20-cm observations. An additional white noise component (${\sigma_{\rm Q}}^2$), commonly referred to as EQUAD, is used to model an additional source of time independent noise measured for each observing system.

In young pulsars, radio-frequency independent timing noise is the dominant contributing factor towards the red-noise in the ToAs. Many approaches have been taken to improve the parameter estimates by removing some portion of this low-frequency timing noise. Hobbs et al. (2004) developed a technique to 'whiten' the timing residuals using

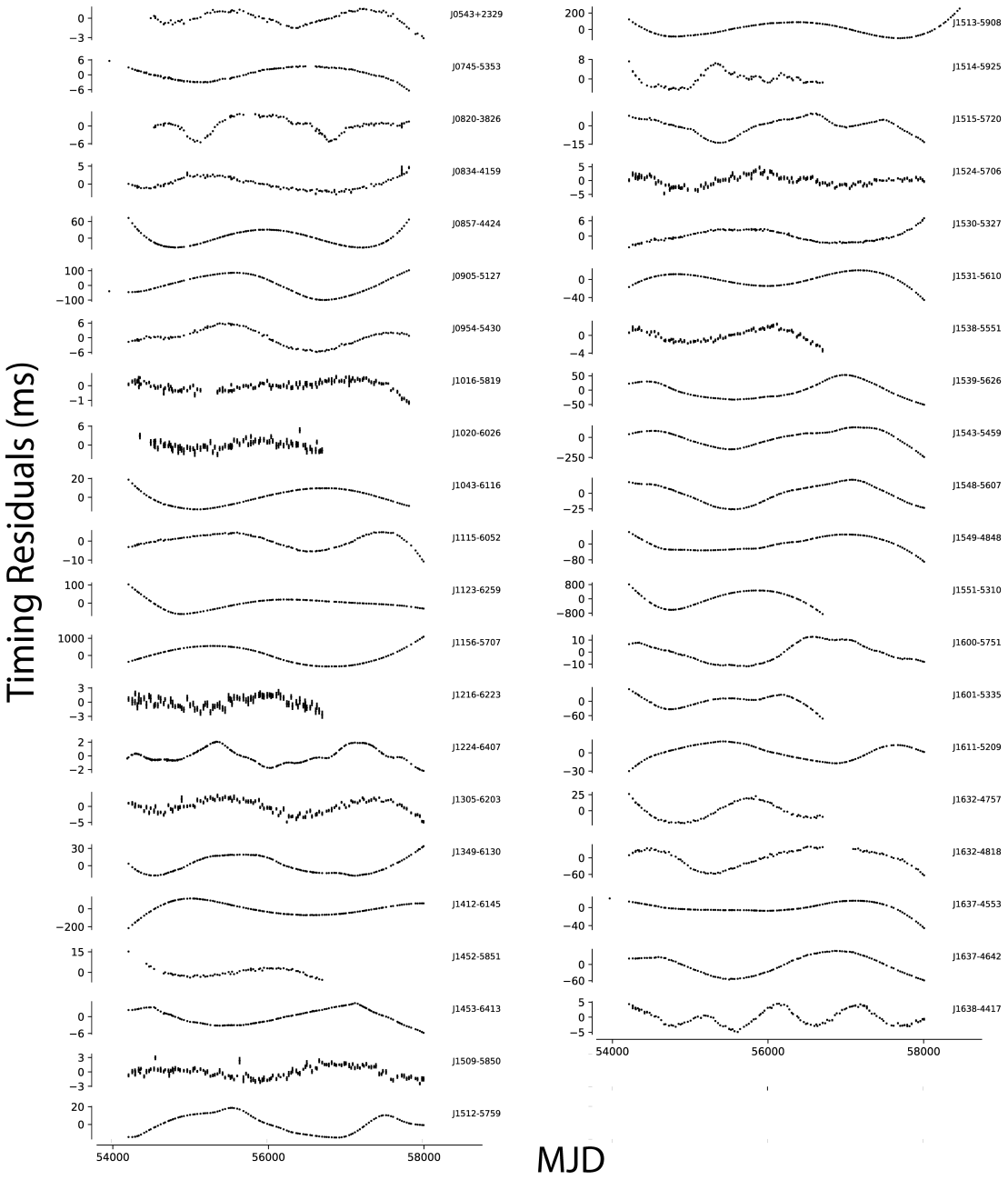

Figure 3.2 Phase-connected timing residuals depicting different levels of timing noise. The timing residuals from the preferred model are shown here, but without removing the contribution of the timing noise.

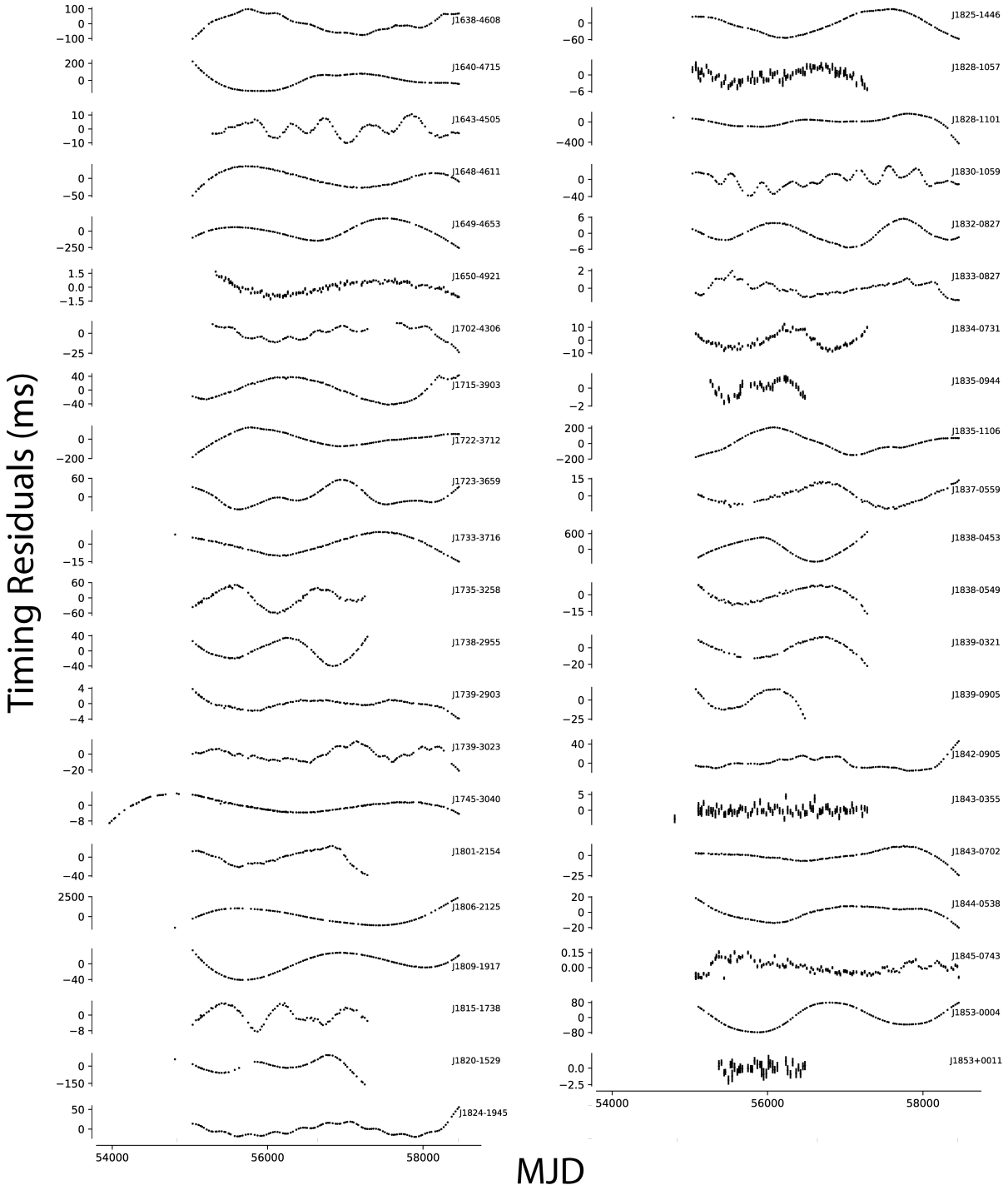

Figure 3.2 Phase-connected timing residuals depicting different levels of timing noise. The timing residuals from the preferred model are shown here, but without removing the contribution of the timing noise (continued).

harmonically related sinusoids, that allowed the measurements of proper motions for a large sample of young pulsars using standard timing methods. Coles et al. (2011) argued that the previously developed "pre-whitening" methods assumed that the measurements were uncorrelated which resulted in a bias in the parameter estimates. They proposed a new method of improving the timing model fit by using the Cholesky decomposition of the covariance matrix, which described the stochastic processes in the ToAs. They argued that the optimal approach to characterise timing noise, especially those dominated by the presence of strong red noise is to analyze the power spectral density of the pulsar timing residuals. They modelled the timing noise in pulsars using a power-law model to fit for an amplitude (A) and a spectral index estimate (β). This technique has been used to determine the timing noise parameters and proper motions of millisecond pulsars (Reardon et al. 2016).

van Haasteren & Levin (2013) later developed a joint analysis of the deterministic timing model and the stochastic parameters using a Markov Chain approach and argued that the stationarity of the time-correlated residuals breaks down in the fitting process and that failure to account for the covariances between the deterministic and stochastic parameters leads to incorrect estimation of the uncertainties in the spectral estimates, especially for quadratic spin-down parameters. However, Lentati et al. (2013) pointed out that because the parameter space changes with the linearisation of the timing model, it becomes difficult to perform model selection with the approach in van Haasteren & Levin (2013).

In our analysis we do not search for DM variations and fix the value for the DM in all the models. This is justified as Petroff et al. (2013) found only upper limits to DM variations in the pulsars under consideration here. We model the timing noise as a power-law power spectrum characterised with a red-noise amplitude ($A_{\rm red}$) and a spectral index (β):

$$P_{\rm r}(f) = \frac{A_{\rm red}^2}{12\pi^2}\left(\frac{f}{f_{\rm yr}}\right)^{-\beta}, \tag{3.5}$$

where f_{yr} is a reference frequency of 1 cycle per year and $A_{\rm red}$ is in units of yr$^{3/2}$.

Motivated by the observations of quasiperiodic timing noise observed in many pulsars, we also model the timing noise as a cut-off power law as described by:

$$P_{\rm r,CF}(f) = \frac{A(f_{\rm c}/f_{\rm yr})^{-\beta}}{[1+(f/f_{\rm c})^{-\beta/2}]^2}, \tag{3.6}$$

where $f_{\rm c}$ is the corner frequency and A is $(A_{\rm red}^2/12\pi^2)$. We also consider the fact that in

young pulsars, the measured timing noise spectral index tends to be steeper as compared to the rest of the pulsar population, with measured values of $\beta \sim 9$ (Shannon et al. 2014a) and so we include low-frequency components with frequencies $f < 1/\mathrm{T_{span}}$ to model the lowest frequency timing noise.

A systematic search for periodic modulations in the ToAs is also conducted. We search for harmonic modulations by fitting for a sinusoid with an arbitrary phase, frequency and amplitude and compare the Bayes factor of this model with the others. We also simultaneously model the stochastic parameters with the proper motion parameters to obtain a more robust estimation of the transverse velocity of the pulsar.

Finally, we search for a braking index, which is caused due to the deceleration of the spin-down rate due to the associated decrease in the magnetic torque. For young pulsars, this braking introduces a measurable second derivative of the spin frequency,

$$\ddot{\nu}_b = n\frac{\dot{\nu}^2}{\nu}, \tag{3.7}$$

and potentially even a third frequency derivative,

$$\dddot{\nu}_b = n(2n-1)\frac{\dot{\nu}^3}{\nu^2}. \tag{3.8}$$

Analysing the braking indices from a large sample of young pulsars offers a window into the various processes that govern the pulsar spin down. Pulsar braking is a deterministic process and is manifested as low-frequency structures in the ToAs.

3.3.1 The Bayesian Inference Method

At the heart of all Bayesian analysis is the Bayes' theorem, which for a given set of parameters Θ in a model H, given data D, can be written as:

$$\Pr(\Theta \mid D, H) = \frac{\Pr(D \mid \Theta, H)\Pr(\Theta \mid H)}{\Pr(D \mid H)}, \tag{3.9}$$

where

- $\Pr(\Theta \mid D, H) \equiv \Pr(\Theta)$ is the posterior probability distribution of the parameters,
- $\Pr(D \mid \Theta, H) \equiv L(\Theta)$ is the likelihood of a particular model,
- $\Pr(\Theta \mid H) \equiv \pi(\Theta)$ is the prior probability distribution of the parameters,
- and $\Pr(D \mid H) \equiv Z$ is the Bayesian evidence.

Table 3.2 Prior ranges for the various stochastic and deterministic parameters used in the timing models. $\Delta_{\rm param}$ is the uncertainty on a *parameter* from the initial TEMPO2 fitting.

Parameter	Prior range	Type
Red noise amplitude ($A_{\rm red}$)	$(-20,-5)$	Log-uniform
Red noise slope (β)	(0,20)	Log-uniform
EFAC	$(-1,1.2)$	Log-uniform
EQUAD	$(-10,-3)$	Log-uniform
Corner frequency ($f_{\rm c}$)	$(0.01/T_{\rm span},10/T_{\rm span})$	Log-uniform
Low frequency cut-off (LFC)	$(-1,0)$	Log-uniform
Sinusoid amplitude	$(-10,0)$	Log-uniform
Sinusoid phase	$(0,2\pi)$	Uniform
Log-sinusoid frequency	$(1/T_{\rm span},100/T_{\rm span})$	Log-uniform
Proper motion	$\pm$ 1000 mas/yr	Uniform
RAJ, DECJ, ν, $\dot{\nu}$, $\ddot{\nu}$	$\pm$ 10000 $\times\Delta_{\rm param}$	Uniform

The way we discriminate one model over the other is by considering the evidence (Z) which is the factor required to normalize the posterior over Θ,

$$Z = \int L(\Theta)\pi(\Theta)\mathrm{d}^n\Theta, \tag{3.10}$$

where n is the dimensionality of the parameter space and the "odds ratio", R,

$$R = \frac{Z_1}{Z_2}\frac{Pr(H_1)}{Pr(H_0)}, \tag{3.11}$$

where $\frac{Pr(H_1)}{Pr(H_0)}$ is the *a priori* probability ratio for the two models.

Assuming the prior probability of the two models is unity, the odds ratio R reduces to the Bayes factor which is then the probability of one model compared to the other. Since in our analysis we compute the log-evidence, the log Bayes factor is then simply the difference of the log-evidences for the two models. A model is preferred if the log Bayes factor is greater than 5. This states that with equal prior odds, we can expect there to be a $1e^{-5}$ chance, (i.e, 1 in 150) that one hypothesis is true over the other. This is similar to Lentati & Shannon (2015), who state that a Bayes factor of > 3 is strong and > 5 is very strong. If multiple models have a Bayes factor greater than 5, we select model A, with a Bayes factor of X, if A is the simpler model and other models have Bayes factors not greater than X+n,

where $n = 5$ is the threshold. All of these models are computed using the 'Bayesian young pulsar timing' pipeline that is cluster-aware and simultaneously processes multiple models for each pulsar. We use ~ 25 different timing models for each pulsar, leading to a total of 2125 models, which were processed in less than 15 hours. The pipeline and the relevant instructions can be found in https://bitbucket.org/aparthas/youngpulsartiming.

The Bayesian pulsar timing approach is powerful because it allows for the simultaneous modelling of stochastic and deterministic parameters while also allowing for robust model selection based on the principles of Bayesian inference. The unique timing models that we use for each pulsar are:

- No stochastic parameters (NoSP),
- Stochastic parameters using a power-law model (PL),
- Stochastic parameters using a cutoff power-law model (CPL),
- Proper motion and stochastic parameters (PL+PM),
- $\ddot{\nu}$ and stochastic parameters (PL+F2),
- Model with low-frequency components and stochastic parameters (PL+LFC),
- Model with a single sinusoidal fit and stochastic parameters (PL+SIN).

Table 3.2 provides a list of unique parameters used in our different timing models along with their prior ranges. We choose wide prior ranges for the red noise amplitude and spectral index because timing noise in young pulsars is strong and can have a relatively steep spectral index. To perform an unbiased search for the proper motion, our prior distributions range from -1000 mas/yr to +1000 mas/yr. Similarly, to ensure unbiased priors for position, spin and spin-down parameters, the uncertainties of the initial least-squares fit values for each of these parameters are multiplied by 10^4.

Using various reasonable permutations of these models, we build more sophisticated timing models leading to a total of 25 different models per pulsar. It must be noted that in all of the above models, including the NoSP model, the position (RAJ and DECJ) and the spin parameters (ν and $\dot{\nu}$) are fitted simultaneously with the other relevant model parameters.

3.4 Results

In Table 3.1 we present the position and spin parameters for the pulsars in our sample with their 95% credible regions as calculated from the posterior distributions along with their

observation timespan. Figure 3.2 shows the timing residuals from the preferred model, without subtracting the modelled timing noise.

This is the first time that the timing noise has been consistently modelled using Bayesian inference for a large sample of young pulsars. In Table 3.3 we present the preferred timing model, the Bayes factor of that model relative to the base model, which in this case is the model in which the position, spin frequency, spin frequency derivative and a power-law timing noise are fitted for. The Bayes factor is zero if the preferred model is the base model (*PL*). For the first 19 pulsars listed, we report significant detections of $\ddot{\nu}$ and the derived braking index values (n) from the preferred model, while for the rest, we report their upper and lower limits as derived from the *PL+F2* model. The braking index is estimated by using equation 3.2 on the entire posterior distribution of ν, $\dot{\nu}$ and $\ddot{\nu}$. The values for $A_{\rm red}$ and β are derived from the preferred model as stated in the second column.

We find that for two pulsars, PSR J1843–0355 and PSR J1853+0011, a model without the timing noise is preferred, while for 58 other pulsars, a model with only the power-law timing noise is strongly preferred. There is marginal to strong evidence for the presence of low-frequency components which are much longer than the data set for five pulsars. We find marginal evidence supporting a cut-off frequency in the power-law timing noise model for PSR J1512–5759.

A model with a $\ddot{\nu}$ is preferred for 19 pulsars, out of which for three pulsars, the model with low-frequency components is preferred, and for one other pulsar a model with a proper motion is preferred. The braking indices for these pulsars, along with the implications on glitch recovery models and pulsar spin-down are discussed in a second paper (Parthasarathy et al 2019b, submitted; Chapter 4). A model with only the proper motion is preferred for PSR J0745–5353. Table 3.4 lists the values for the proper motion in right ascension and declination in mas yr^{-1}, i.e., $\mu_\alpha = \dot{\alpha}\cos\delta$ and $\mu_\delta = \dot{\delta}$ and contains the computed transverse velocity using the distance derived from the DM using the electron-density model of Yao et al. (2017). PSR J1702–4306 shows indication for periodic modulation in its ToAs, which is discussed further in Section 3.5.3. It was noted that for PSR J1830–1059, an unpublished glitch was reported[2], on July 29, 2009 (MJD 55041). For this pulsar a model with a glitch, a $\ddot{\nu}$, and a cut-off power law fit is preferred. It is interesting to note here that we find an evidence for a cut-off frequency for only 2 pulsars out of the 85 in our sample.

Figure 3.3 shows the distribution of $A_{\rm red}$ and β extracted from the preferred model

[2]http://www.jb.man.ac.uk/ pulsar/glitches/gTable.html

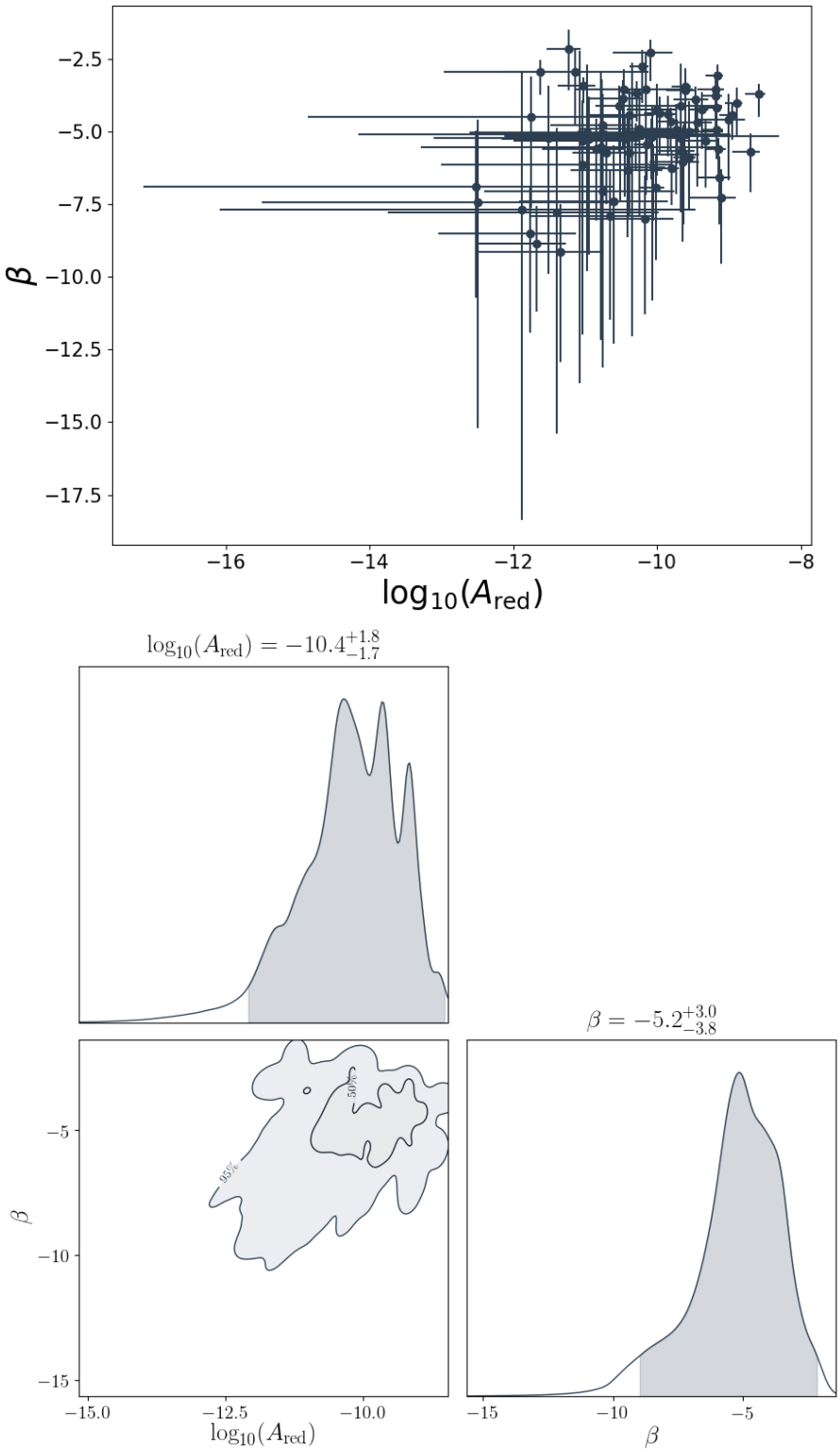

Figure 3.3 **Top:** The distribution of red noise amplitude against spectral indices for our sample of pulsars for which a power-law timing model is preferred. The error bars are 95% confidence limits obtained from the preferred model. **Bottom:** Posterior distribution of the red noise amplitude and spectral indices from the preferred model for each pulsar are normalized and added together to form an integrated posterior distribution as shown here.

for each pulsar in our sample except for the two pulsars for which the cut-off power law model is preferred. The errors shown in the plot are the 2.5% and 97.5% confidence limits on both the parameters. The median value for $\log_{10}(A_{\rm red})$ is $-10.4^{+1.8}_{-1.7}$ yr$^{3/2}$ and for β is $-5.2^{+3.0}_{-3.8}$. Figure 3.3 also shows the integrated posterior distribution for the timing noise parameters. Contours are plotted for the 50% and 95% confidence intervals with the accompanying histograms.

We test the robustness of the timing noise model by comparing them to an independent Bayesian analysis tool, ENTERPRISE[3] (Enhanced Numerical Toolbox Enabling a Robust Pulsar Inference Suite), which is developed for timing noise and gravitational wave analysis in pulsar timing data. With ENTERPRISE, we use a Parallel-Tempering Ensemble Markov Chain Monte Carlo (PTMCMC) sampler. The prior ranges for the noise models are identical and in both the cases the red noise is modelled as a power law. Since ENTERPRISE does not allow for full non-linear sampling of the timing model and only does implicit marginalization over the parameters in the linear perturbation regime, we compare the noise models for the pulsars that prefer the power-law model only. The distributions are similar to that shown in Figure 3.3 with median values of the $\log_{10}(A_{\rm red})$ and β being, $-10.4^{+1.8}_{-1.7}$, $-10.3^{+1.6}_{-1.8}$ and $-5.2^{+3.0}_{-3.8}$, -5.2 ± 3.3 using TEMPONEST and ENTERPRISE respectively.

3.5 Discussion

3.5.1 Timing noise

Various attempts have been made to quantify timing noise in pulsars. Cordes & Helfand (1980) proposed an 'activity parameter' (A) that measured the timing noise relative to the Crab pulsar,

$$A = \log_{10}\left[\frac{\sigma_{\rm TN,2}(T)}{\sigma_{\rm TN,2}(T)_{\rm Crab}}\right], \tag{3.12}$$

where $\sigma_{\rm TN,2}(T)$ is the RMS residual phase from a second order least squares polynomial fit. They found that this parameter is strongly correlated with the characterstic age of the pulsars. Arzoumanian et al. (1994) measured the strength of the timing noise (Δ_8) after a cubic polynomial fit to the ToAs over a time period (T_8), of 10^8 s and found a strong correlation with the pulsar period derivative,

$$\Delta_8 = \log_{10}\left(\frac{|\ddot{\nu}|}{6\nu}T_8^3\right). \tag{3.13}$$

[3]https://github.com/nanograv/enterprise

Table 3.3 A summary of the preferred timing model, its Bayes factor compared to the base model, and 95% confidence limits on the timing noise parameters ($A_{\rm red}$ and β) for each pulsar are reported. The first 19 pulsars listed have a significant detection of $\ddot{\nu}$ and n while for the rest the lower 2.5% and upper 97.5% confidence limits are reported from the *PL+F2* model.

PSR	Best Model	Bayes factor	$\log_{10}(A_{\rm red})$ ($\rm yr^{3/2}$)	β	$\ddot{\nu}$ ($10^{-23}s^{-3}$)	n
J0857–4424	PL+F2	171.61	$-11.3^{+1.2}_{-0.6}$	$-9.1^{+3.8}_{-1.6}$	3.63(16)	2890(30)
J0954–5430	PL+F2	5.96	$-10.4^{+0.6}_{-0.3}$	$-4.4^{+2.1}_{-0.8}$	0.032(8)	18(9)
J1412–6145	PL+F2	29.99	$-10.7^{+1.1}_{-0.6}$	$-7.9^{+3.6}_{-1.6}$	0.62(4)	20(3)
J1509–5850	PL+F2	6.54	$-11.1^{+3.1}_{-2.1}$	$-5.1^{+8.6}_{-2.9}$	0.12(16)	11(3)
J1513–5908	PL+F2	44.08	$-9.7^{+0.4}_{-0.2}$	$-5.7^{+1.3}_{-0.6}$	189.6(2)	2.82(6)
J1524–5706	PL+F2	13.99	$-10.2^{+1.0}_{-0.7}$	$-3.6^{+3.6}_{-1.3}$	0.038(2)	4.2(7)
J1531–5610	PL+F2	100.57	$-11.8^{+1.3}_{-0.6}$	$-8.5^{+3.4}_{-1.6}$	1.37(2)	43(1)
J1632–4818	PL+F2	18.69	$-9.6^{+0.8}_{-0.5}$	$-5.0^{+2.7}_{-1.1}$	0.48(4)	6(1)
J1637–4642	PL+F2	54.34	$-9.7^{+0.6}_{-0.3}$	$-4.9^{+2.2}_{-0.9}$	3.2(15)	34(3)
J1643–4505	PL+F2+LFC	3.24	$-10.1^{+0.5}_{-0.3}$	$-2.3^{+1.0}_{-0.4}$	0.11(2)	15(6)
J1648–4611	PL+F2	13.13	$-10.4^{+0.8}_{-0.5}$	$-6.3^{+2.3}_{-0.9}$	0.44(8)	40(10)
J1715–3903	PL+F2	4.19	$-9.2^{+0.2}_{-0.1}$	$-3.8^{+1.3}_{-0.6}$	0.4(11)	70(40)
J1738–2955	PL+F2	5.37	$-9.6^{+0.5}_{-0.2}$	$-5.8^{+2.4}_{-1.0}$	-0.5(16)	-70(40)
J1806–2125	PL+F2	5.56	$-9.1^{+0.3}_{-0.1}$	$-6.6^{+1.6}_{-0.7}$	1.1(4)	90(60)
J1809–1917	PL+PM+F2	94.14	$-11.7^{+1.1}_{-0.6}$	$-9.0^{+3.5}_{-1.4}$	2.70(3)	23.5(6)
J1815–1738	PL+F2+LFC	3.18	$-11.8^{+3.1}_{-1.5}$	$-4.5^{+3.1}_{-1.4}$	0.73(8)	9(3)
J1824–1945	PL+F2+LFC	32.02	$-10.9^{+0.3}_{-0.1}$	$-3.4^{+0.6}_{-0.3}$	0.05(2)	120(20)
J1830–1059	CPL+F2	19.55	$-8.5^{+0.3}_{-0.1}$	$-13.6^{+6.2}_{-2.8}$	0.16(19)	31(7)
J1833–0827	PL+F2	15.98	$-10.2^{+0.2}_{-0.1}$	$-2.8^{+1.2}_{-0.6}$	-0.19(13)	-15(2)
J0543+2329	PL	--	$-10.5^{+0.4}_{-0.2}$	$-3.6^{+1.8}_{-0.7}$	(-0.07,0.01)	(-2,10)
J0745–5353	PL+PM	20.13	$-10.5^{+0.5}_{-0.3}$	$-3.9^{+1.7}_{-0.6}$	(-0.01,0.02)	(-140,680)
J0820–3826	PL+LFC	6.15	$-11.1^{+1.8}_{-1.0}$	$-3.0^{+1.9}_{-0.8}$	(-0.15,0.06)	(-480,600)
J0834–4159	PL	--	$-10.9^{+1.2}_{-0.8}$	$-5.3^{+4.0}_{-1.5}$	(-0.02,0.02)	(-20,40)
J0905–5127	PL	--	$-9.6^{+0.2}_{-0.1}$	$-5.0^{+0.8}_{-0.4}$	(-0.06,0.14)	(-40,160)
J1016–5819	PL	--	$-11.5^{+1.6}_{-1.0}$	$-5.2^{+4.7}_{-1.8}$	(-0.04,0.01)	(-70,260)
J1020–6026	PL	--	$-11.9^{+4.2}_{-2.4}$	$-7.7^{+10.7}_{-4.7}$	(0.01,0.04)	(10,30)
J1043–6116	PL	--	$-10.7^{+0.5}_{-0.3}$	$-5.7^{+1.8}_{-0.7}$	(0.01,0.03)	(10,90)
J1115–6052	PL	--	$-10.5^{+0.7}_{-0.4}$	$-5.2^{+2.3}_{-0.9}$	(0.02,0.03)	(10,170)

Table 3.3 A summary of the preferred timing model, its Bayes factor compared to the base model, and 95% confidence limits on the timing noise parameters ($A_{\rm red}$ and β) for each pulsar are reported. The first 19 pulsars listed have a significant detection of $\ddot{\nu}$ and n while for the rest the lower 2.5% and upper 97.5% confidence limits are reported from the *PL+F2* model (continued).

PSR	Best Model	Bayes factor	$\log_{10}(A_{\rm red})$ ($\rm yr^{3/2}$)	β	$\ddot{\nu}$ ($10^{-23}s^{-3}$)	n
J1123–6259	PL	--	$-10.1^{+0.3}_{-0.2}$	$-6.3^{+1.8}_{-0.8}$	(-0.05,0.1)	(-340,1300)
J1156–5707	PL	--	$-9.1^{+0.2}_{-0.1}$	$-5.6^{+0.9}_{-0.4}$	(-0.73,-0.04)	(-250,100)
J1216–6223	PL	--	$-11.0^{+1.6}_{-0.9}$	$-5.0^{+4.8}_{-2.3}$	(-0.01,0.01)	(-30,40)
J1224–6407	PL+LFC	11.09	$-11.6^{+0.5}_{-0.3}$	$-2.9^{+0.8}_{-0.4}$	(-0.05,-0.02)	(-200,100)
J1305–6203	PL	--	$-11.0^{+2.0}_{-1.3}$	$-6.1^{+5.9}_{-2.2}$	(0.01,0.02)	(1,20)
J1349–6130	PL	--	$-9.8^{+0.2}_{-0.1}$	$-4.7^{+1.0}_{-0.5}$	(-0.03,0.09)	(-200,1000)
J1452–5851	PL	--	$-11.4^{+2.4}_{-1.4}$	$-7.8^{+7.6}_{-2.9}$	(0.02,0.03)	(5,10)
J1453–6413	PL	--	$-10.3^{+0.2}_{-0.1}$	$-3.7^{+1.0}_{-0.4}$	(-0.01,0.02)	(-70,250)
J1512–5759	CPL	2.99	$-10.0^{+0.2}_{-0.1}$	$-7.0^{+2.5}_{-1.1}$	(-0.03,0.18)	(-10,130)
J1514–5925	PL	--	$-9.6^{+0.3}_{-0.1}$	$-3.6^{+1.6}_{-0.8}$	(-0.07,0.26)	(-300,1600)
J1515–5720	PL	--	$-9.8^{+0.2}_{-0.1}$	$-4.4^{+1.5}_{-0.6}$	(-0.02,0.08)	(-140,760)
J1530–5327	PL	--	$-10.8^{+0.7}_{-0.4}$	$-4.8^{+2.7}_{-1.1}$	(-0.02,-0.01)	(-200,70)
J1538–5551	PL	--	$-10.8^{+1.5}_{-1.0}$	$-5.1^{+4.8}_{-1.9}$	(-0.12,0.02)	(-140,100)
J1539–5626	PL	--	$-9.7^{+0.2}_{-0.1}$	$-5.1^{+1.0}_{-0.5}$	(-0.09,0.1)	(-570,1140)
J1543–5459	PL	--	$-9.2^{+0.2}_{-0.1}$	$-4.9^{+1.0}_{-0.5}$	(-0.2,0.21)	(-40,80)
J1548–5607	PL	--	$-10.1^{+0.3}_{-0.1}$	$-5.2^{+1.5}_{-0.6}$	(-0.06,0.08)	(-30,60)
J1549–4848	PL	--	$-9.7^{+0.2}_{-0.1}$	$-5.2^{+1.3}_{-0.6}$	(0.02,0.19)	(30,330)
J1551–5310	PL	--	$-9.1^{+0.4}_{-0.2}$	$-7.3^{+2.3}_{-1.0}$	(0.42,1.43)	(10,50)
J1600–5751	PL	--	$-10.0^{+0.2}_{-0.1}$	$-4.4^{+1.4}_{-0.6}$	(-0.06,0.04)	(-1000,1600)
J1601–5335	PL	--	$-9.6^{+0.5}_{-0.2}$	$-6.0^{+2.8}_{-1.2}$	(-0.21,0.32)	(-10,40)
J1611–5209	PL	--	$-10.1^{+0.2}_{-0.1}$	$-5.5^{+1.2}_{-0.5}$	(-0.09,0.03)	(-200,200)
J1632–4757	PL	--	$-10.6^{+1.3}_{-0.8}$	$-7.4^{+4.9}_{-1.9}$	(-0.04,0.17)	(-20,150)
J1637–4553	PL	--	$-10.3^{+0.3}_{-0.1}$	$-5.2^{+1.1}_{-0.5}$	(0.03,0.13)	(40,300)
J1638–4417	PL	--	$-10.0^{+0.4}_{-0.3}$	$-4.3^{+2.3}_{-0.9}$	(-0.07,0.08)	(-430,1000)
J1638–4608	PL	--	$-8.9^{+0.2}_{-0.1}$	$-4.0^{+1.2}_{-0.5}$	(-0.36,0.23)	(-30,40)
J1640–4715	PL	--	$-9.3^{+0.3}_{-0.1}$	$-5.3^{+1.6}_{-0.7}$	(0.06,0.31)	(45,330)
J1649–4653	PL	--	$-10.2^{+0.8}_{-0.4}$	$-8.0^{+3.3}_{-1.5}$	(-0.1,0.02)	(-75,60)
J1650–4921	PL	--	$-12.5^{+3.0}_{-1.8}$	$-7.4^{+7.8}_{-2.9}$	(0.01,0.02)	(25,100)

Table 3.3 A summary of the preferred timing model, its Bayes factor compared to the base model, and 95% confidence limits on the timing noise parameters ($A_{\rm red}$ and β) for each pulsar are reported. The first 19 pulsars listed have a significant detection of $\ddot{\nu}$ and n while for the rest the lower 2.5% and upper 97.5% confidence limits are reported from the *PL+F2* model (continued).

PSR	Best Model	Bayes factor	$\log_{10}(A_{\rm red})$ ($\rm yr^{3/2}$)	β	$\ddot{\nu}$ ($10^{-23}s^{-3}$)	n
J1702–4306	PL+SIN	7.1	$-9.6^{+0.2}_{-0.1}$	$-3.5^{+0.8}_{-0.3}$	(-0.05,0.24)	(-50,360)
J1722–3712	PL	--	$-9.2^{+0.2}_{-0.1}$	$-4.2^{+0.8}_{-0.4}$	(-0.28,0.07)	(-320,270)
J1723–3659	PL	--	$-9.6^{+0.2}_{-0.1}$	$-5.9^{+1.4}_{-0.6}$	(-0.27,0.13)	(-340,420)
J1733–3716	PL	--	$-10.8^{+0.8}_{-0.4}$	$-5.6^{+2.5}_{-1.0}$	(-0.01,0.01)	(-20,35)
J1735–3258	PL	--	$-9.0^{+0.4}_{-0.2}$	$-4.6^{+2.1}_{-0.9}$	(-0.85,0.22)	(-540,510)
J1739–2903	PL	--	$-10.5^{+0.3}_{-0.2}$	$-4.1^{+1.6}_{-0.7}$	(0.01,0.02)	(3,85)
J1739–3023	PL	--	$-9.2^{+0.2}_{-0.1}$	$-3.1^{+0.8}_{-0.4}$	(-0.13,0.18)	(-15,40)
J1745–3040	PL	--	$-11.0^{+1.0}_{-0.6}$	$-5.3^{+2.3}_{-0.9}$	(-0.01,0.02)	(-20,30)
J1801–2154	PL	--	$-9.2^{+0.3}_{-0.1}$	$-3.6^{+1.4}_{-0.6}$	(-0.15,0.16)	(-305,720)
J1820–1529	PL+LFC	3.18	$-12.5^{+4.6}_{-1.9}$	$-6.9^{+3.8}_{-1.9}$	(-1.26,0.32)	(-320,290)
J1825–1446	PL	--	$-9.5^{+0.3}_{-0.2}$	$-3.9^{+1.2}_{-0.4}$	(-0.09,0.07)	(-40,70)
J1828–1057	PL	--	$-10.8^{+2.5}_{-1.6}$	$-5.6^{+6.6}_{-2.6}$	(0.01,0.03)	(4,15)
J1828–1101	PL	--	$-8.6^{+0.2}_{-0.1}$	$-3.7^{+0.8}_{-0.4}$	(-0.02,2.52)	(-1,60)
J1832–0827	PL	--	$-10.4^{+0.3}_{-0.1}$	$-5.1^{+1.4}_{-0.6}$	(-0.01,0.01)	(-10,10)
J1834–0731	PL	--	$-9.7^{+0.9}_{-0.6}$	$-4.1^{+3.7}_{-1.4}$	(-0.07,0.05)	(-30,50)
J1835–0944	PL	--	$-10.3^{+1.0}_{-0.6}$	$-5.2^{+6.9}_{-2.5}$	(-0.1,0.22)	(-150,640)
J1835–1106	PL	--	$-9.0^{+0.2}_{-0.1}$	$-4.4^{+0.9}_{-0.4}$	(-0.48,0.6)	(-50,120)
J1837–0559	PL	--	$-10.2^{+0.8}_{-0.5}$	$-4.9^{+3.0}_{-1.1}$	(-0.04,0.04)	(-300,620)
J1838–0453	PL	--	$-8.7^{+0.3}_{-0.1}$	$-5.7^{+1.4}_{-0.6}$	(-2.57,-0.37)	(-100,30)
J1838–0549	PL	--	$-10.8^{+1.6}_{-1.0}$	$-7.1^{+6.1}_{-2.2}$	(0.08,0.11)	(10,15)
J1839–0321	PL	--	$-10.1^{+2.1}_{-1.8}$	$-5.2^{+5.7}_{-1.1}$	(0.02,0.17)	(20,200)
J1839–0905	PL	--	$-9.4^{+0.4}_{-0.2}$	$-4.7^{+2.2}_{-0.9}$	(0.19,0.37)	(210,510)
J1842–0905	PL	--	$-9.4^{+0.2}_{-0.1}$	$-4.3^{+1.4}_{-0.6}$	(-0.1,0.09)	(-400,670)
J1843–0355	NoSP	2.64	NA	NA	NA	NA
J1843–0702	PL	--	$-10.4^{+0.5}_{-0.3}$	$-5.3^{+2.0}_{-0.8}$	(0.02,0.06)	(40,1350)
J1844–0538	PL	--	$-10.4^{+0.5}_{-0.2}$	$-5.7^{+2.2}_{-1.0}$	(-0.01,0.05)	(-6,150)
J1845–0743	PL	--	$-11.2^{+0.3}_{-0.2}$	$-2.2^{+1.4}_{-0.7}$	(-0.01,0.03)	(-60,85)
J1853–0004	PL	--	$-9.8^{+0.2}_{-0.1}$	$-6.3^{+1.3}_{-0.6}$	(-0.04,0.43)	(-10,230)

Shannon & Cordes (2010) argued that statistics based on a cubic fit ($\ddot{\nu}$) underestimates the strength of the timing noise and proposed that the RMS timing noise after a second order fit is a more accurate diagnostic (i.e. they simply use $\sigma_{\rm TN,2}\,(T)$ without the Crab as reference). They also developed a metric ($\sigma_{\rm P}$),

$$\sigma_{\rm P} = C_2 \nu^{\alpha} |\dot{\nu}|^{\beta} T^{\gamma}, \tag{3.14}$$

which linked the timing noise with the measured pulsar parameters. Using a maximum likelihood approach they determined the coefficients α, β, γ and the scaling factor ($C2$) given the pulsar parameters and the time span (T).

We characterise the strength of the timing noise in our pulsars using the equation,

$$\log_{10}({\sigma_{\rm TN}}^2) = 2\log_{10}(A_{\rm red}) + \log_{10}\left(\frac{T}{1{\rm yr}}\right)(\beta - 1)\,, \tag{3.15}$$

where T signifies the time span over which $\ddot{\nu}$ is measured. Previous metrics for timing noise relied upon modelling it as either a second-order or a cubic polynomial which directly affected the measurements of higher order spin-down parameters. Since we characterize the timing noise as a power-law using the amplitude and spectral index, it allows us to measure an unbiased value for the pulsar spin-down parameters.

To determine the correlation between different pulsar parameters and the strength of the timing noise ($\sigma_{\rm TN}$), we perform a linear least-squares regression analysis between $\sigma_{\rm TN}$ (with $T = 10$ y) and $\sigma_{\rm P}$,

$$\sigma_{\rm P} = \nu^{a}\,|\dot{\nu}|^{b}. \tag{3.16}$$

The correlation coefficient (r), is computed in a linear regression analysis. We search over the parameter space spanned by arbitrary scaling coefficients, a and b to find the maximally correlated scaling relationship.

The various pulsar parameters can then be expressed in terms of ν and $\dot{\nu}$ as:

- Spin-period derivative: $\nu^{-2}|\dot{\nu}|^{1}$
- Spin-down age: $\nu^{1}|\dot{\nu}|^{-1}$
- Surface magnetic field strength: $\nu^{-3/2}|\dot{\nu}|^{1/2}$
- Magnetic field at the light cylinder: $\nu^{3/2}|\dot{\nu}|^{1/2}$
- Rate of loss of rotational kinetic energy: $\nu^{1}|\dot{\nu}|^{1}$

and are represented in Figure 3.4.

Since the correlation coefficients maintain rotational symmetry in the (a, b) plane and following the discussion in Jankowski et al. (2018), any combination of (a, b) that has the same ratio will have the same correlation coefficient. For example, the spin-down derivative can be expressed as $\nu^1|\dot{\nu}|^{-1/2}$ or $\nu^{-2}|\dot{\nu}|^1$. In our analysis, we set the $a = 1$, which results in the various pulsar parameters being expressed as a function of b as shown in Figure 3.4. We then find that the maximum absolute correlation coefficient for $\sigma_{\rm TN}$ occurs at $b = -0.9 \pm 0.2$ for our sample of young pulsars.

This suggests that the timing noise is more closely correlated with spin-period derivative and spin-down age of the pulsar as compared to $\dot{E}$. Analysing the relationship of the timing noise with observing time span, we find no evidence for band-limited timing noise, which would be expected to flatten over longer timing baselines. We compare our results with those of Shannon & Cordes (2010), who reported a scaling relation of $\nu^{-0.9\pm0.2}|\dot{\nu}|^{1.0\pm0.05}$, which can also be expressed as $\nu^1|\dot{\nu}|^{-1.1\pm0.2}$. We find that our scaling relationships are consistent with those reported by Shannon & Cordes (2010).

To test the robustness of this correlation, we also include the timing noise parameters of 8 MSPs from a sample of 49 pulsars from the International Pulsar Timing Array Data release 1 (Verbiest et al. 2016) for which the preferred stochastic model is the spin-noise process [4] (Lentati et al. 2016a). The MSPs have a typical observing span of ∼10 years and the timing noise is modelled as a power-law process using TEMPONEST. We find that on adding the MSPs to our sample, we obtain a stronger correlation and the maximum absolute correlation occurs for $b = -0.6 \pm 0.1$, (Figure 3.4). van Haasteren & Levin (2013) derive an expression (equation 22 in their paper) for relating the power spectral density to the average RMS in the post-fit timing residuals, which can be used to relate T^γ in equation 3.14 to β in equation 3.15 as $\gamma = \frac{\beta-1}{2}$. From such a relation, we obtain a value of γ to be 2 ± 0.1, consistent with Shannon & Cordes (2010). The correlation coefficients obtained for pulsar age, $\dot{E}$ and magnetic field strength are also shown in Figure 3.4.

Figure 3.5 shows the correlation between $\sigma_{\rm TN}$ and the timing noise metric ($\sigma_{\rm P}$) for $a = 1$ and $b = -0.6 \pm 0.1$. For the young pulsar sample, the error bars are 95% confidence limits computed from the measured posterior distributions, while for the MSPs, they are adopted from the 1σ confidence limits from Lentati et al. (2016a). It is evident that the timing noise is stronger in young pulsars as compared to older pulsars (MSPs) in which case, we measure smaller values for the red-noise amplitude and shallower spectral indices. Our parametrization of timing noise from measured values of $A_{\rm red}$ and β can be

[4] Uncertainties in the Solar System Barycenter (SSB) have been identified to introduce rednoise signatures in the ToAs of the highest precision MSPs, however, those effects are sub-dominant in the MSP datasets studied here (**?**)

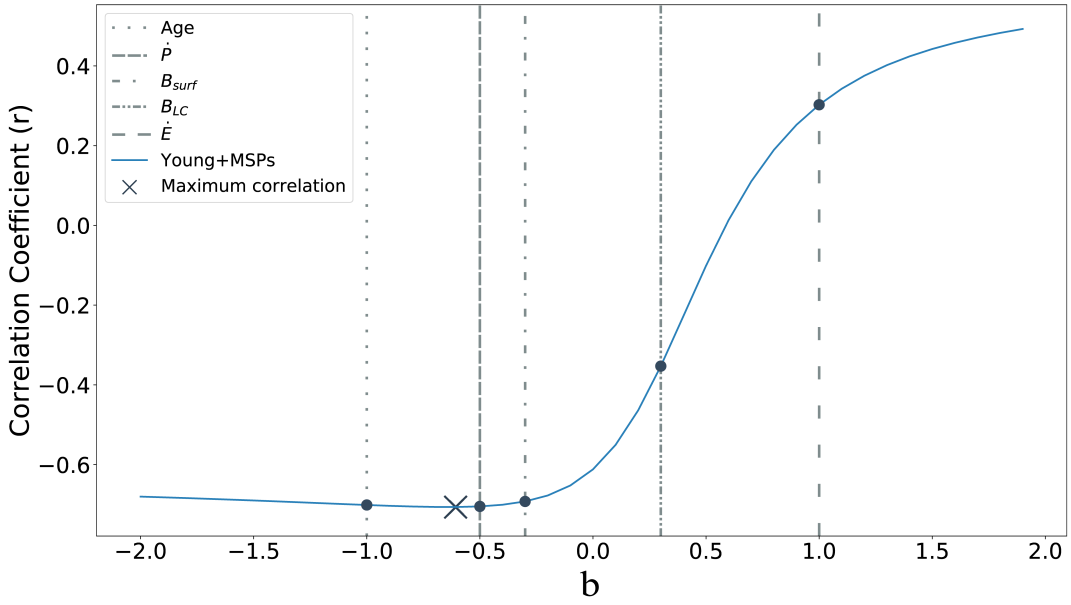

Figure 3.4 The relationship between the correlation coefficient (r), which measures the strength of the timing noise for various values of $\sigma_{\rm P}$ and b, for a fixed value of a=1.

used to predict the relative strength of timing noise in new pulsars given their spin-down parameters.

We find marginal evidence for the presence of a corner frequency ($f_{\rm c}$) in PSR J1512–5759. The posterior distribution of the corner frequency and the timing noise parameters for this pulsar are shown in Figure 3.6. We find that for five pulsars, a model with a low-frequency component (LFC) is preferred. This model implements extra sinusoidal fits at frequencies much longer than the dataset. It is worth noting here that the measurement of low-frequency components is strongly correlated with the amplitude of the red noise (see Figure 3.7) in the timing residuals. The prospects of detecting signatures at low-frequencies is greater when the red-noise amplitude is larger. This is clearly reflected in the Bayes factors obtained for both PSR J0820–3826 (BF of 6.15) and PSR J1820–1529 (BF of 3.18), which have measured red-noise amplitudes of $-11.1^{1.8}_{1.0}$ yr$^{3/2}$ and $-12.5^{4.6}_{1.9}$ yr$^{3/2}$ respectively. For PSR J1643–4505, although the Bayes factor is just 3.24, the measured red-noise amplitude is relatively larger ($-10.1^{0.5}_{0.3}$ yr$^{3/2}$), thus leading to a relatively well constrained posterior for the LFC parameter as shown in Figure 3.7. The low Bayes factor can perhaps be attributed to the additional detection of $\ddot{\nu}$.

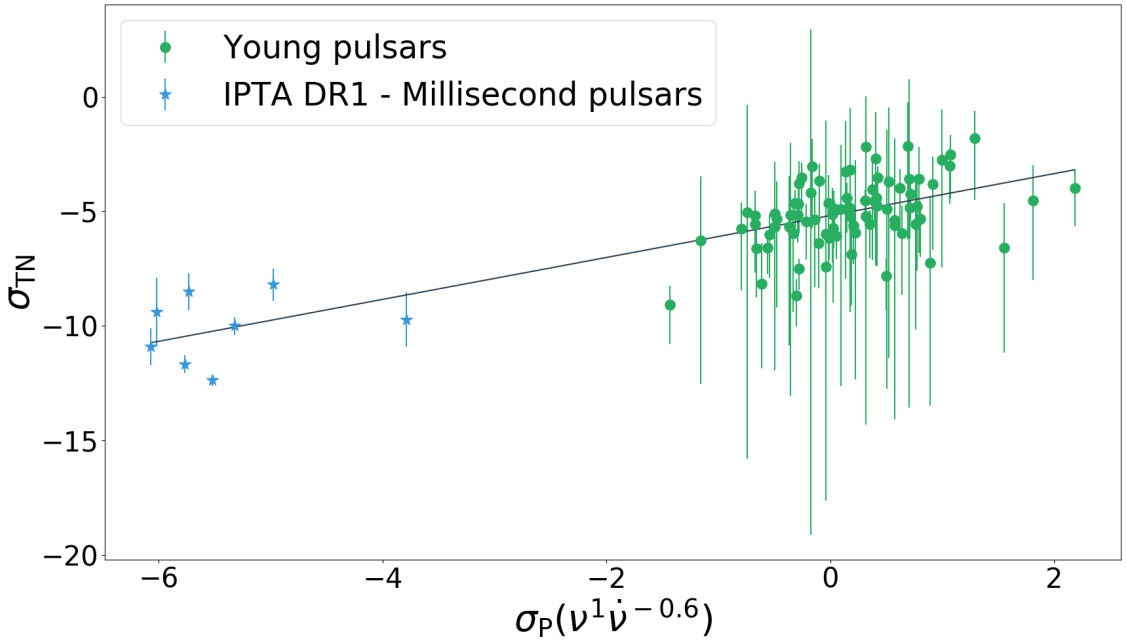

Figure 3.5 Relationship between the timing noise strength and the timing noise metric at the maximally correlated values of a and b for our sample of young pulsars and millisecond pulsars from the International Pulsar Timing Array data release 1 (IPTA DR1) sample.

3.5.2 Proper motions and pulsar velocities

For the 2 pulsars listed in Table 3.4, the posterior distributions of the proper motions are shown in Figure 3.8.

PSR J0745–5353 shows a clear detection of a proper motion signature. Assuming a distance of 0.57 kpc, the derived transverse velocity of 220 ± 30 km/s is typical of the population of pulsars as a whole. For PSR J1809–1917, we measure a significant proper motion in right ascension, while the proper motion in declination is consistent with zero. The transverse velocity computed from μ_α is $\sim$ 300 kms^{-1}, which is reasonable in terms of the transverse velocities for the general pulsar population.

PSR J1745–3040 has a previously reported proper motion from both the frequentist method (Zou et al. 2005), with μ_α of 6 ± 3 mas/yr, μ_δ of 4 ± 26 mas/yr and the Bayesian method (Li et al. 2016), with μ_α of 11.9 ± 16 mas/yr, μ_δ of 50 ± 12 mas/yr. In our analysis the proper motion model is marginally better than the power-law model (PL) with a Bayes factor of 2. From this model, we obtain a μ_α of 9.9 ± 3.5 mas/yr and a μ_δ of 10.5 ± 27.6, which are consistent with the previous measurements. PSR J1833–0827 has a previously reported timing proper motion (Hobbs et al. 2005), but the preferred model in our analysis shows a strong detection of $\ddot{\nu}$.

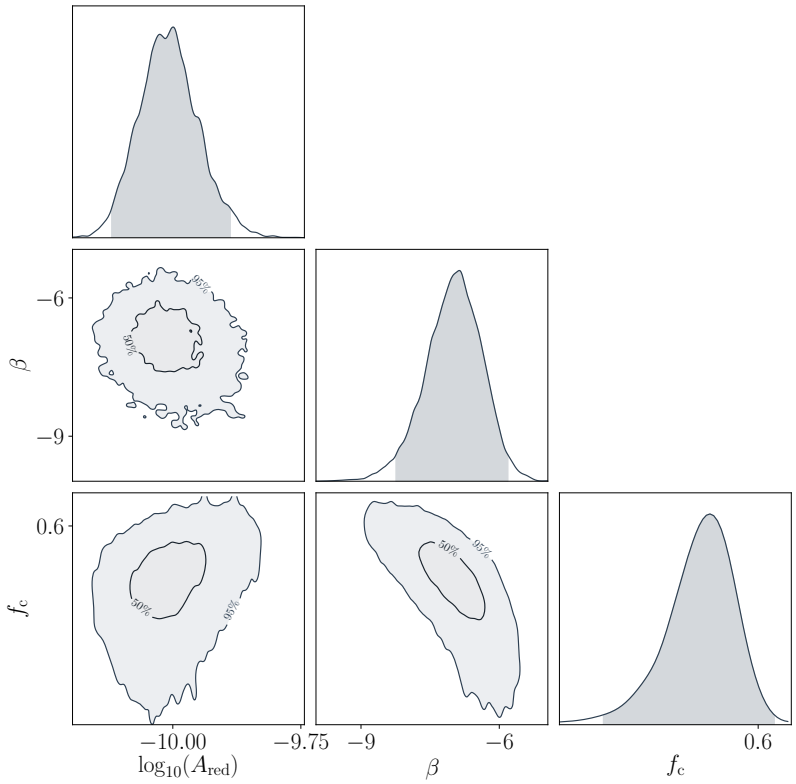

Figure 3.6 Posterior distribution of the corner frequency parameter along with the timing noise parameters for PSR J1512–5759. This model is positively preferred with a Bayes factor of 3.23.

Table 3.4 Proper motions for 2 pulsars reported with their pulsar distance (as estimated from the DM in Yao et al. (2017) and the computed transverse velocities using the proper motion in right ascension ($V_{\alpha \rm T}$) and total ($V_{\rm T}$). The error bars reported are 95% confidence limits. The epoch for the position is the same as the epoch of the period reported in Table 3.1.

PSR	μ_α	μ_δ	$\mu_{\rm tot}$	Distance	$V_{\alpha \rm T}$	$V_{\rm T}$
	(mas/yr)	(mas/yr)	(mas/yr)	(kpc)	(km/s)	(km/s)
J0745–5353	−60(10)	50(10)	80(10)	0.57	-	220(30)
J1809–1917	−19(6)	50(90)	60(90)	3.27	−300(100)	900(1300)

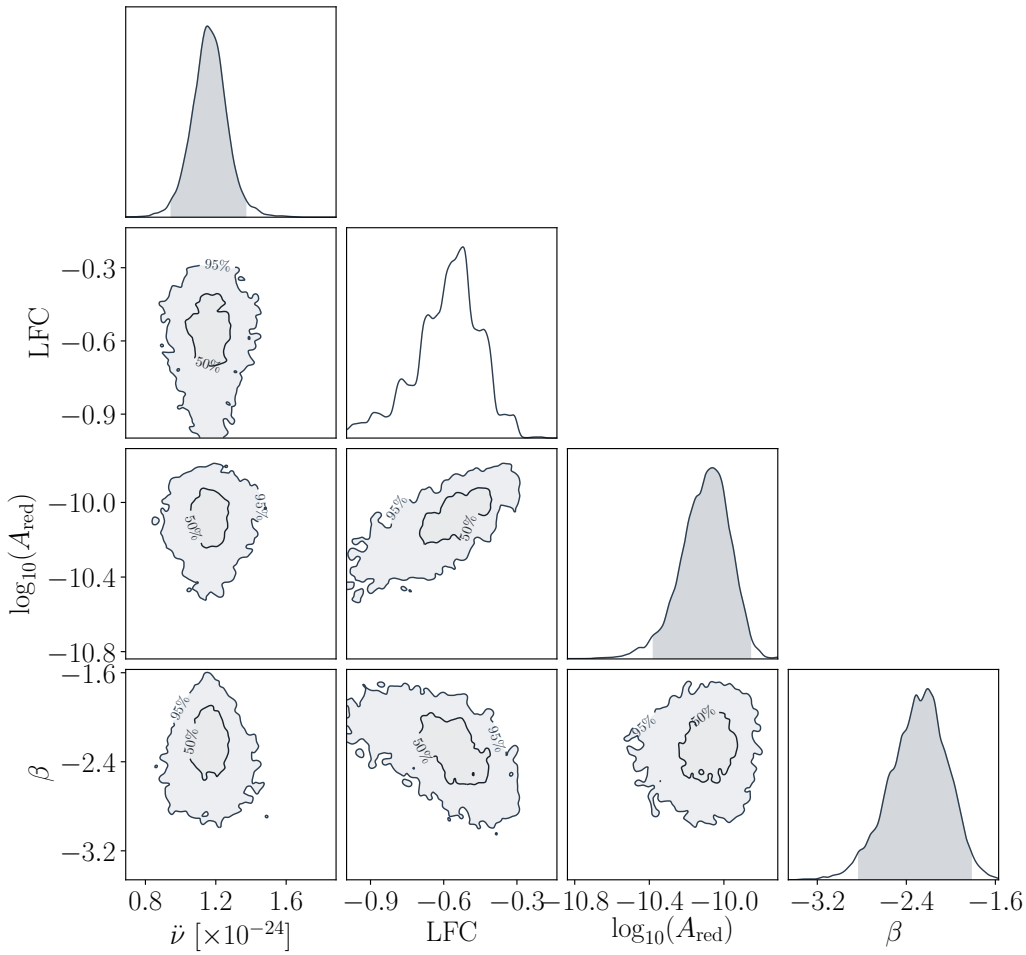

Figure 3.7 Posterior distribution of the low-frequency component, a $\ddot{\nu}$ along with the timing noise parameters for PSR J1643–4505.

There are 2 other pulsars, PSR J1453–6413 (Bailes et al. 1990) and J1825–1446 (Dexter et al. 2017) that have a previously reported interferometric proper motions with greater than 3σ significance. In our analysis, the uncertainties associated with the proper motion measurements are quite large for these pulsars with the preferred models being a power-law model for PSR J1453–6413 and a sinusoidal fitting model for PSR J1825–1446.

Unbiased measurements of proper motion and other such deterministic parameters in pulsars that are strongly contaminated with timing noise strongly underscores the evidence-based model selection that we have employed here. Increasing the timing baselines will help to discover further significant proper motion measurements.

3.5.3 Pulsars with planetary companions?

To search for periodic modulations in our pulsars, we fit for a sinusoid with varied amplitudes, phases and frequencies and compare the evidences to choose the preferred model. Here we comment on five pulsars present in our sample that have been previously studied in the context of periodic signals in their timing residuals.

PSR J1637–4642 was reported to show marginal evidence for a single sinusoid in Kerr et al. (2016). We find that the preferred model for this pulsar is *PL+F2*. In order to further test this, we fitted for a sinusoid simultaneously with $\ddot{\nu}$ but find that this model (PL+F2+SIN) only has a Bayes Factor of 2.9, which does not pass a Bayes factor threshold of 5 over the much simpler model.

PSR J1825–1446 showed strong evidence for a single sinusoid according to Kerr et al. (2016). We however find that, the *PL+SIN* model does not meet the threshold to be preferred over the *PL* model. The model with a sinusoidal fitting has a Bayes factor of only 1.7.

For PSR J1830–1059, we find evidence for a glitch with parameters similar to those in the catalogue and find that the best model is one which includes the glitch, $\ddot{\nu}$ and a cut-off power law model. This pulsar is notable for correlated profile and $\dot{\nu}$ changes (Brook et al. 2016, Kerr et al. 2016). Stairs et al. (2019) performed an exhaustive analysis on multi-hour long observations of this pulsar and reported that the pulsar undergoes mode-changing between two stable, extreme profile states. They stated that the observed mode transition rate can perhaps be explained by the chaotic behaviour model as previously suggested by Seymour & Lorimer (2013). The detection of a glitch in 2009, further complicates the theoretical models invoking explanations based on pinned vortices inside neutron stars. We conclude that the deviation from a simple power-law, the presence of a glitch and the identified mode changing make this pulsar more complex and demands

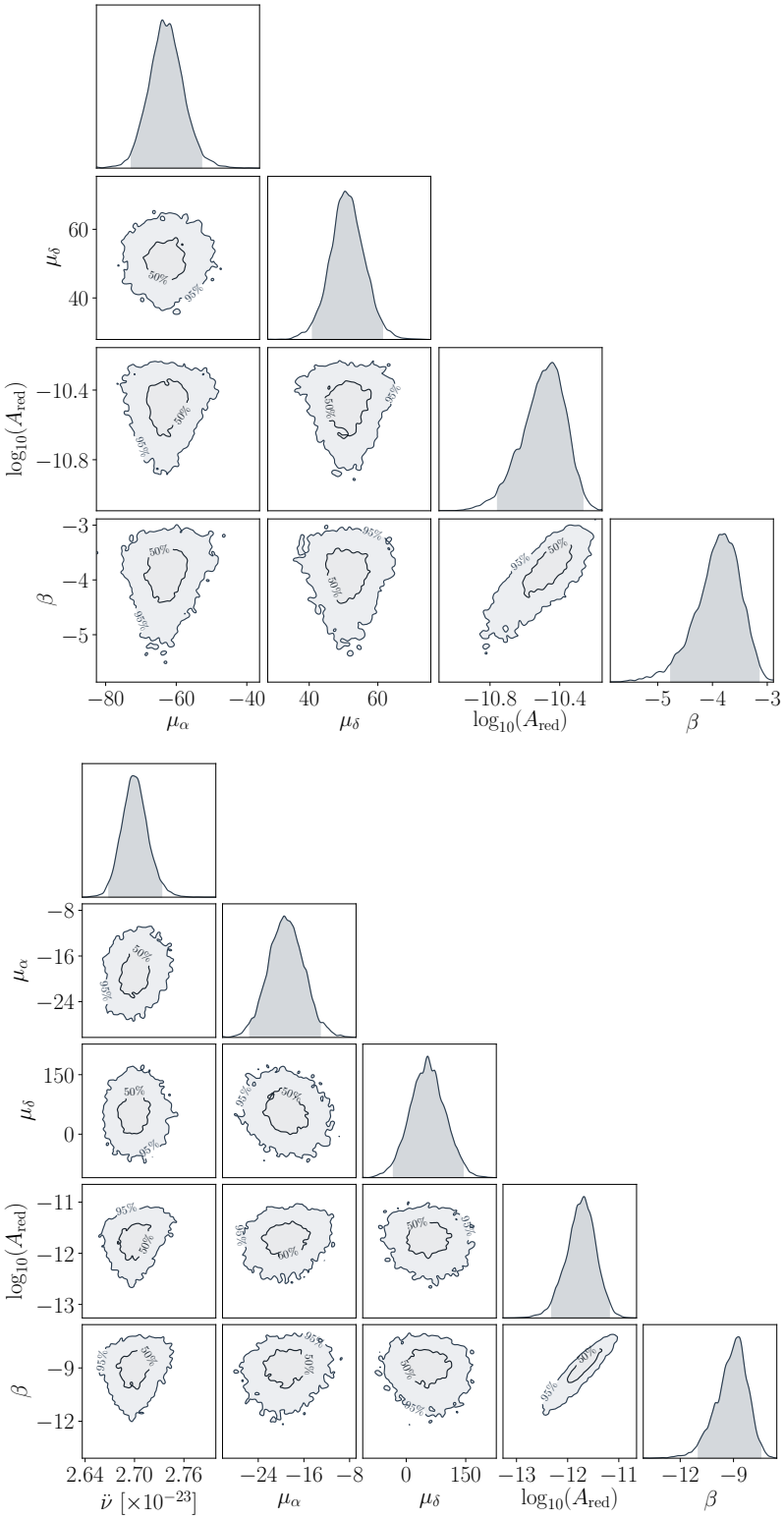

Figure 3.8 **Top:** Posterior distribution of the proper motion and the timing noise parameters for PSR J0745–5353. **Bottom:** Posterior distribution of the proper motion, $\ddot{\nu}$ and the timing noise parameters for PSR J1809–1917.

further investigation.

PSR J1638–4608 was reported to show a strong evidence for a single sinusoid fitting in Kerr et al. (2016). Close examination however revealed the presence of 2 new glitches. The amplitudes of these glitches are very small, on the order of 10^{-8} Hz and 10^{-9} Hz. We find that, after taking the glitches into account, the glitch inclusive model (*GL+SIN*) has a Bayes factor of ∼60 as compared to the model with only the stochastic parameters (PL).

It is useful to note here that although the pulsars presented in this analysis were manually selected to not have any identified glitches in the data set, we subsequently found that the two pulsars discussed above had detected glitches. This was missed in the initial manual search owing to the small glitch amplitudes. We decided to retain them in the paper, because for one of the sources, the glitches were unpublished, while for the other, it significantly changed the favoured model.

For PSR J1702–4306, Kerr et al. (2016) saw strong evidence for a single sinusoid with a projected semi-major axis ($a_{\rm n}$) of 2.9 ± 0.7 ms and an orbital period ($P_{\rm b}$) of 391 ± 10 days. In our data, we find that the sinusoidal model is strongly preferred over the *PL* model by a Bayes factor of 7.1. We measure $a_{\rm n}$ to be 2.6 ± 0.2 ms and $P_{\rm b}$ to be 316 days. It is unclear if these effects are caused due to neutron star precession or due to the presence of a planetary companion, as discussed in Kerr et al. (2016).

3.6 Conclusions

We have applied an improved methodology based on Bayesian inference on a large sample of high $\dot{E}$, young pulsars to measure different stochastic and deterministic parameters of interest. We have shown that evidence-based model selection is a powerful technique to disentangle stochastic processes from deterministic ones and to obtain unbiased measurements of pulsar parameters. For each pulsar in our sample, a total of 25 different models were compared and the best model was selected based on a Bayes factor threshold of 5. The power-law model was preferred for 58 pulsars, while we found no evidence of timing noise in two pulsars. The low-frequency component (*PL+LFC*) model was preferred for five pulsars and in two other pulsars we measure a proper motion signature. Marginal evidence for the presence of a corner frequency in the power-law was detected in two pulsars. We report two new glitches in PSR J1638–4608 and find evidence for periodic modulation in the ToAs of both PSR J1638–4608 and PSR J1702–4306. We have also compared our timing noise models with an independent Bayesian package, ENTERPRISE and obtained consistent results.

We characterize the timing noise as a power-law based on the red-noise amplitude ($A_{\rm red}$) and spectral index (β) and report that there is a strong correlation between the spin-period derivative of the pulsar and the strength of the timing noise. We develop a metric that can be used to determine the relative strength of the timing noise in any pulsar given its spin-down parameters. On adding MSPs to our sample, we notice that the correlation gets stronger, which is consistent with what is expected.

Finally, we measure significant $\ddot{\nu}$ measurements for 19 pulsars and also report their braking indices. We discuss the significance of the braking index measurements, their robustness and the effects of glitch recovery models in the next chapter.

4

Timing of young radio pulsars II. Braking indices and their interpretation

In the previous chapter, we detected a significant value of the braking index (n) for 19 young, high-$\dot{E}$ radio pulsars using ~ 10 years of timing observations from the 64-m Parkes radio telescope. Here we investigate this result in more detail using a Bayesian pulsar timing framework to model timing noise and to perform selection to distinguish between models containing exponential glitch recovery and braking index signatures. We show that consistent values of n are maintained with the addition of substantial archival data, even in the presence of glitches. We provide strong arguments that our measurements are unlikely due to exponential recovery signals from unseen glitches even though glitches play a key role in the evolution of a pulsar's spin frequency. We conclude that, at least over decadal time scales, the value of n can be significantly larger than the canonical 3 and discuss the implications for the evolution of pulsars.

This chapter has been published in MNRAS (Parthasarathy et al. (2020))

4.1 Introduction

The spin-down of pulsars is one of the most prominent features of their rotation (Davies et al. 1969, Cole 1969). Considering the magnetic field of a neutron star in a vacuum to have dipolar configuration and assuming that the magnetic axis is misaligned with the rotation axis, it must radiate and lose energy, which contributes to the observed slow down (Gunn & Ostriker 1969). Under the simplest assumption that magnetic dipole radiation is the only braking mechanism, we expect the spin-frequency (ν) and the spin-frequency derivative ($\dot{\nu}$) to follow, $\dot{\nu} \propto -\nu^3$. However, pulsars reside in dense plasma environments in which particles are accelerated up to very high energies. Such plasma

outflows can result in radial deformation of pulsar's magnetic field lines, which could result in a large fraction of the angular momentum and energy loss in the form of particles (Manchester et al. 1985, Harding et al. 1999), and additionally contribute to the underlying magnetic braking (Spitkovsky 2006). The observations of quasi-periodic magnetospheric processes correlated with spin-down measurements (Kramer et al. 2006a, Lyne et al. 2010), strengthens the argument that a pulsar wind plays a substantial role in the pulsar braking mechanism. Observations of glitches, sudden spin-up events, alter the normal spin-down of pulsars (Espinoza et al. 2011b). Glitches are thought to arise from the transfer of angular momentum from a more rapidly spinning neutron star superfluid component to the crust (Baym et al. 1969, Anderson & Itoh 1975, Melatos & Warszawski 2009). Coupling and decoupling between the crust and the superfluid core can decrease the moment of inertia with time, leading to further departures from the conventional spin-down due to magnetic dipole braking (Ho & Andersson 2012). Pulsar braking is also thought to be dependent on the temporal evolution of the magnetic field strength (B) and the inclination angle between the magnetic and the rotational axis (α) (Tauris & Konar 2001, Young et al. 2010, Lyne et al. 2013, Johnston & Karastergiou 2017). Finally, gravitational wave emission can also contribute to the energy losses in a pulsar. Thus, the supposition that a neutron star is a magnetic dipole rotating in a vacuum must be treated with caution.

The braking index (n) is used to parameterize the spin evolution of pulsars and is defined by relating the spin-frequency and its derivative through a power law:

$$\dot{\nu} = -K\nu^{\mathrm{n}}. \tag{4.1}$$

K depends on the moment of inertia of the neutron star and its magnetic moment. Although K is often assumed to be constant in time, deviations from a constant magnetic moment can occur due to decay (or growth) of the magnetic field (Blandford et al. 1983) or changes in the dipole alignment (Candy & Blair 1986) which makes K time-dependent (Blandford & Romani 1988, McKinney 2006). Neglecting these effects allows us to write the braking index as,

$$n = \frac{\nu\ddot{\nu}}{\dot{\nu}^2}, \tag{4.2}$$

where $\ddot{\nu}$ is the second derivative of the spin-frequency.

The characteristic age of the pulsar is usually written as $\tau_c = -\nu/2\dot{\nu}$ with the implicit assumption that $n = 3$ and that the initial period of the pulsar is much less than its current period. However, given the variety of phenomena discussed above that can potentially contribute to pulsar braking, the characteristic age must be taken with caution (when

interpreting it as a bona-fide age estimate of the pulsar).

There are challenges associated with measuring the long-term $\ddot{\nu}$. In most cases, the value arising from pure spin-down is dominated by other phenomena like timing noise or glitches. Timing noise is caused by stochastic rotational irregularities of the neutron star about a steady state (Groth 1975) and is seen in all classes of pulsars (Hobbs et al. 2004, Shannon & Cordes 2010, Namkham et al. 2019, Parthasarathy et al. 2019). The cause of timing noise has been attributed to both neutron star interiors, arising from the cross-coupling between the neutron star crust and its superfluid core (Jones 1990), or from magnetospheric torque fluctuations (Cheng 1987a). Failure to model timing noise leads to biased estimates of pulsar parameters (Coles et al. 2011). Developing upon previous Bayesian pulsar timing frameworks (van Haasteren & Levin 2013, Lentati et al. 2014), Parthasarathy et al. (2019) (hereafter PSJ19) characterise the timing noise as a power-law process (see Equation 4.4) in a sample of 85 high $\dot{E}$, young radio pulsars and report the median red-noise amplitude, $\log_{10}\left(\frac{A_{\rm red}}{yr^{3/2}}\right)$ to be $-10.4^{+1.8}_{-1.7}$ and the spectral index (β) to be $-5.2^{+3.0}_{-3.8}$ and show that the strength of timing noise scales proportionally to $\nu^1|\dot{\nu}|^{-0.6\pm0.1}$. The modelling of timing noise simultaneously with the timing model will allow for unbiased measurements of pulsar parameters.

The presence of glitches, and in particular the glitch recovery, further complicates the measurement of $\ddot{\nu}$ and hence the braking index. Following a glitch event, a pulsar enters a recovery stage during which an increase in the spin-down rate and a relaxation towards the pre-glitch rotational state is observed over a timescale of days to years (Yu et al. 2013, Fuentes et al. 2017). Both the spin-up event and the subsequent recovery stage are interpreted as the presence of a superfluid component in the inner crust and core of the star (Haskell & Melatos 2015). Johnston & Galloway (1999) and Alpar & Baykal (2006) point out that a post-glitch relaxation process can dominate the spin-down evolution of a pulsar resulting in large ($n > 3$) values of braking indices.

Because of the difficulties outlined above, it has been common in the literature to only report values of n when they are close to the canonical value of 3. Lyne et al. (2015a) reported a braking index of 2.35(1) for the Crab pulsar (PSR J0534+2200) from 45 years of timing data. They note that the braking index value is close to 2.5 in the intervals between glitches. Similarly, the braking index and spin-down properties of the Vela pulsar are also well studied. While Shannon et al. (2016b) determined the long-term value of n to be < 8, Espinoza et al. (2017) reported $n = 1.7(2)$ using different techniques. Using inter-glitch models to obtain spin-down rates, Akbal et al. (2017) measured $n = 2.8(1)$. It is important to note the reported long-term values of n are smaller than the values

reported for the linear regimes between glitches (where $n \sim 30$).

Braking index values ranging from ~ 0.03 for PSR B0540–69 (Marshall et al. 2016) to ~ 3.15 for PSR J1640–4631 (Archibald et al. 2016 have been reported. In PSR J1513–5908, the braking index was measured in a series of papers (Kaspi et al. 1994a, Livingstone et al. 2005, Livingstone & Kaspi 2011) with the updated value being 2.832 ± 0.003 . This pulsar has never been observed to glitch in $\sim$ 25 years of observations. In contrast, PSR J0537–6910 has the highest glitch rate of any pulsar (Middleditch et al. 2006) with $\sim$45 observed glitches in $\sim$ 14 years of observations. Antonopoulou et al. (2018) reported that the spin-evolution of this pulsar is characterised by a well-defined negative braking index of $-1.22(4)$. Using the same dataset, Ferdman et al. (2018) and Andersson et al. (2018) reported that the trend in the interglitch behaviour leads to a larger value of $n \sim 7$.

In this paper, we measure n for a sample of young pulsars using Bayesian inference. In Section 4.2, we report the measured values of n for the 19 pulsars in our sample. In Section 4.3, we use simulated and historical data sets to test the robustness of the measured values. In Section 4.4 we introduce a glitch recovery model to test if unseen glitches before our data set affect the measurement of n. In Section 4.5, using Monte Carlo simulations we investigate the presence of exponential glitch recoveries on long timescales. In Section 4.6, we develop a parameterization for the detectability of braking index and discuss the implications of high values of n and the evolution of pulsars with time.

4.2 Measured Braking Indices

In PSJ19, we described the observations and the methodology involved in obtaining timing solutions for 85 young radio pulsars observed with the CSIRO 64-m Parkes radio telescope. A total of 19 pulsars had a preferred model which included $\ddot{\nu}$ as shown in Table 3 of PSJ19. Here we reproduce the values of $\log_{10}(A_{\rm red})$, β, ν, $\dot{\nu}$, $\ddot{\nu}$, n and the preferred model for these 19 pulsars in Table 4.1. In addition we place upper limits on the remaining pulsars in the sample. For clarity, we redefine the various models listed in Table 4.1 below. In each timing model, we fitted for the pulsar position, spin (ν) and spin-down parameter ($\dot{\nu}$) in addition to

- a power-law timing noise and $\ddot{\nu}$ (PL+F2),
- a power-law, $\ddot{\nu}$ and low-frequency components longer than the data set (PL+F2+LFC),
- a power-law, $\ddot{\nu}$ and proper motion (PL+F2+PM),
- a cut-off power law and a $\ddot{\nu}$ (CPL+F2).

Figure 4.1 shows the derived values of n (Equation 4.2) and the 97.5% upper limits.

Of the 19 braking index measurements, four of them have $n < 10$, eleven have $10 < n < 100$, two of them are > 100 and two of them are negative. Only for PSR J1513–5908 is the value close to $n = 3$ as expected from a simple model of a magnetic dipole in vacuum. Two questions thus arise. The first is whether the measured values of n are robust to the passage of time and the second is whether or not unseen glitches affect the measured values of n? We answer these questions in the next three sections.

4.3 Robustness of the braking index measurements

4.3.1 Comparisons with simulated data sets.

We first test the efficacy of TEMPONEST (Lentati et al. 2014) in this context, by simulating timing residuals for the 19 pulsars discussed in this paper with various induced signatures as per the preferred model and check the consistency with which we recover the input parameters. The simulated timing residuals are generated using LIBSTEMPO[1] with data spans similar to the actual observations. The times of arrival (ToAs) are considered to be a combination of deterministic and stochastic components. White noise components are modelled by adjusting the uncertainty on a ToA to be,

$$\sigma^2 = F{\sigma_{\rm r}}^2 + {\sigma_{\rm Q}}^2, \tag{4.3}$$

where the parameter F, referred to as the EFAC, accounts for instrumental distortions and ${\sigma_{\rm r}}^2$ is the formal uncertainty obtained from ToA fitting. An EQUAD ($\sigma_{\rm Q}^2$) is introduced to model time independent noise per observing system. The timing noise is modelled to be a power-law described by a red-noise amplitude ($A_{\rm red}$) and spectral index (β),

$$P_{\rm r}(f) = \frac{A_{\rm red}^2}{12\pi^2}\left(\frac{f}{f_{\rm yr}}\right)^{-\beta}, \tag{4.4}$$

where f_{yr} is a reference frequency of 1 cycle per year and $A_{\rm red}$ is in units of yr$^{3/2}$. A model with a cut-off power law was favoured for PSR J1830–1059 which was simulated following the power spectrum,

$$P_{\rm r,CF}(f) = \frac{A(f_{\rm c}/f_{\rm yr})^{-\beta}}{[1 + (f/f_{\rm c})^{-\beta/2}]^2}, \tag{4.5}$$

where $f_{\rm c}$ is the corner frequency and A is $(A_{\rm red}^2/12\pi^2)$.

[1] https://github.com/vallis/libstempo

Table 4.1 The timing noise parameters $A_{\rm red}$, β (as defined in equation 4.4), the measured spin parameters (ν, $\dot{\nu}$, $\ddot{\nu}$) along with the braking index (n) values and the preferred model (as described in Section 4.2) for 19 pulsars.

PSR	$\log_{10}(A_{\rm red})$ ($\rm yr^{3/2}$)	β	ν (s^{-1})	$\dot{\nu}$ ($10^{-14}s^{-2}$)	$\ddot{\nu}$ ($10^{-23}s^{-3}$)	n	Preferred Model
J0857–4424	$-11.3^{+1.2}_{-0.6}$	$-9.1^{+3.8}_{-1.6}$	3.0601045423(4)	–19.6145(10)	3.63(16)	2890(30)	PL+F2
J0954–5430	$-10.4^{+0.6}_{-0.3}$	$-4.4^{+2.1}_{-0.8}$	2.11483307064(18)	–19.6358(5)	0.032(8)	18(9)	PL+F2
J1412–6145	$-10.7^{+1.1}_{-0.6}$	$-7.9^{+3.6}_{-1.6}$	3.1720007909(13)	-99.643(4)	0.62(4)	20(3)	PL+F2
J1509–5850	$-11.1^{+3.1}_{-2.1}$	$-5.1^{+8.6}_{-2.9}$	11.2454488757(7)	–115.9175(16)	0.12(16)	11(3)	PL+F2
J1513–5908	$-9.7^{+0.4}_{-0.2}$	$-5.7^{+1.3}_{-0.6}$	6.59709182778(19)	–6653.10558(27)	189.6(2)	2.82(6)	PL+F2
J1524–5706	$-10.2^{+1.0}_{-0.7}$	$-3.6^{+3.6}_{-1.3}$	0.89591729463(9)	–28.60366(2)	0.038(2)	4.2(7)	PL+F2
J1531–5610	$-11.8^{+1.3}_{-0.6}$	$-8.5^{+3.4}_{-1.6}$	11.8756292823(4)	–194.5360(14)	1.37(2)	43(1)	PL+F2
J1632–4818	$-9.6^{+0.8}_{-0.5}$	$-5.0^{+2.7}_{-1.1}$	1.2289964712(14)	–98.0730(3)	0.48(4)	6(1)	PL+F2
J1637–4642	$-9.7^{+0.6}_{-0.3}$	$-4.9^{+2.2}_{-0.9}$	6.491542203(4)	–249.892(10)	3.2(15)	34(3)	PL+F2
J1643–4505	$-10.1^{+0.5}_{-0.3}$	$-2.3^{+1.0}_{-0.4}$	4.212470392(4)	–56.473(10)	0.11(2)	15(6)	PL+F2+LFC
J1648–4611	$-10.4^{+0.8}_{-0.5}$	$-6.3^{+2.3}_{-0.9}$	6.0621606076(2)	–87.220(5)	0.44(8)	40(10)	PL+F2
J1715–3903	$-9.2^{+0.2}_{-0.1}$	$-3.8^{+1.3}_{-0.6}$	3.5907423095(9)	–48.2784(13)	0.4(11)	70(40)	PL+F2
J1738–2955	$-9.6^{+0.5}_{-0.2}$	$-5.8^{+2.4}_{-1.0}$	2.2551713364(2)	–41.7146(12)	–0.51(16)	–70(40)	PL+F2
J1806–2125	$-9.1^{+0.3}_{-0.1}$	$-6.6^{+1.6}_{-0.7}$	2.075444041(15)	–50.821(2)	1.1(4)	90(60)	PL+F2
J1809–1917	$-11.7^{+1.1}_{-0.6}$	$-9.0^{+3.5}_{-1.4}$	12.0838226201(8)	–372.7882(19)	2.70(3)	23.5(6)	PL+PM+F2
J1815–1738	$-11.8^{+3.1}_{-1.5}$	$-4.5^{+3.1}_{-1.4}$	5.03887545888(10)	–197.4552(11)	0.73(8)	9(3)	PL+F2+LFC
J1824–1945	$-10.9^{+0.3}_{-0.1}$	$-3.4^{+0.6}_{-0.3}$	5.281575552287(3)	–14.6048(5)	0.05(2)	120(20)	PL+F2+LFC
J1830–1059	$-8.5^{+0.3}_{-0.1}$	$-13.6^{+6.2}_{-2.8}$	2.4686900068(5)	–36.5201(10)	0.167(19)	31(7)	CPL+F2
J1833–0827	$-10.2^{+0.2}_{-0.1}$	$-2.8^{+1.2}_{-0.6}$	11.7249580817(4)	–126.1600(8)	–0.198(13)	–15(2)	PL+F2

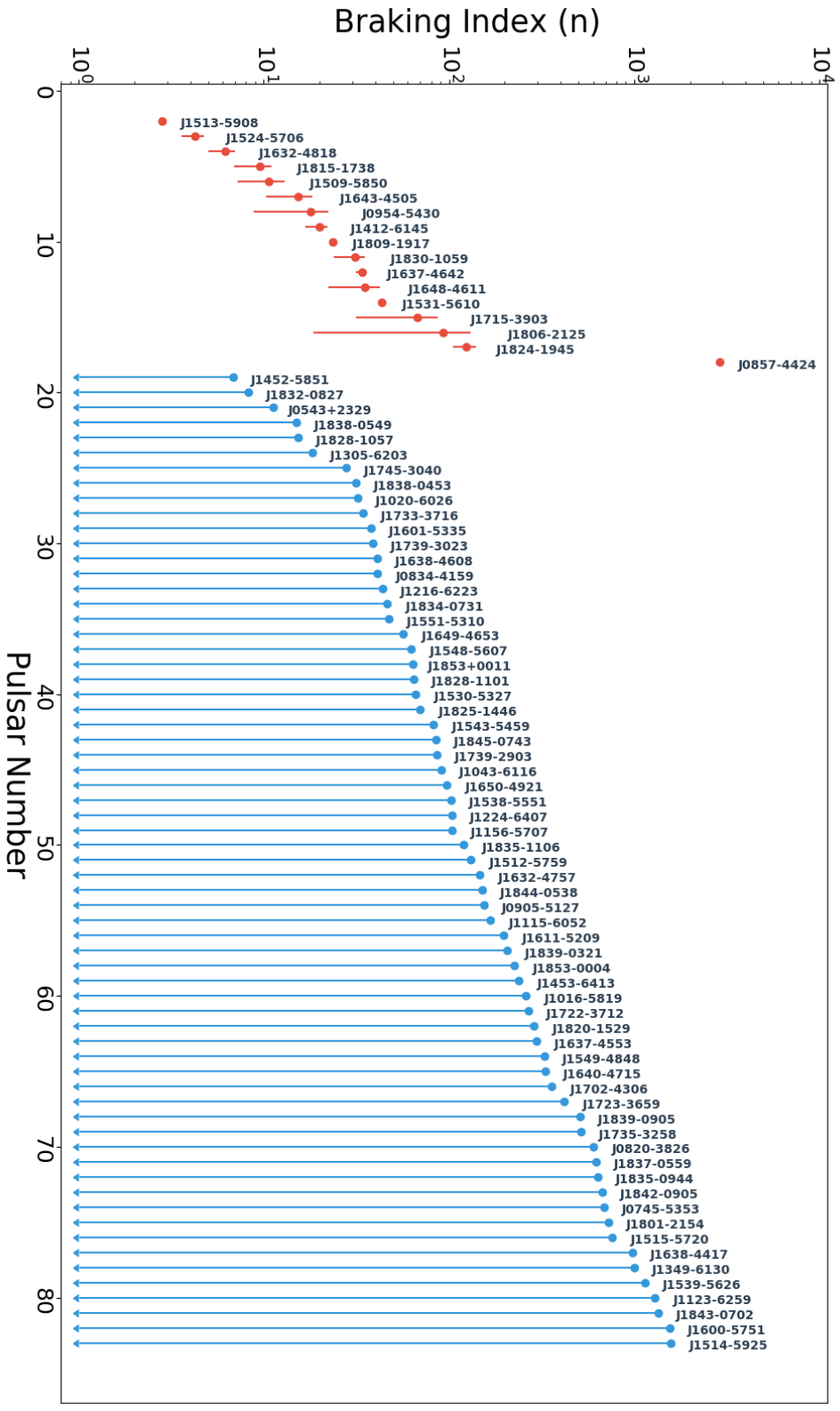

Figure 4.1 Braking index detections (red points) and upper limits (blue points) on our sample of 85 pulsars, excluding the 2 pulsars with negative braking indices. The error bars are 97.5% and 2.5% limits on the detections and 97.5% upper limits on the non-detections.

Table 4.2 Prior ranges for the various stochastic and deterministic parameters used in the timing models. $\Delta_{\rm param}$ is the uncertainty on the marginalized timing model parameters from the initial TEMPO2 fitting.

Parameter	Prior range	Type
Red noise amplitude ($A_{\rm red}$)	$(-20,-5)$	Log-uniform
Red noise slope (β)	(0,20)	Log-uniform
EFAC	$(-1,1.2)$	Log-uniform
EQUAD	$(-10,-3)$	Log-uniform
Corner frequency ($f_{\rm c}$)	$(0.01/T_{\rm span},10/T_{\rm span})$	Log-uniform
Low frequency cut-off (LFC)	$(-1,0)$	Log-uniform
$\ddot{\nu}$	$\pm$ 10000 $\times\Delta_{\rm param}$	Uniform
Proper motion	$\pm$ 1000 mas/yr	Uniform

To maintain consistency in the simulations, a model with low-frequency components (LFC) with timescales longer than the data set, were simulated for PSRs J1643–4505, J1815–1738 and J1824–1945 and a model with a proper motion signature was simulated for PSR J1809–1917. Finally, the simulated timing residuals were modified to include a braking index signature.

We use the Bayesian pulsar timing package, TEMPONEST to search for the stochastic parameters and the braking index value in the simulated data sets. The prior ranges on the stochastic parameters, corner frequency, low-frequency components, $\ddot{\nu}$ and the proper motion are reported in Table 4.2. Our measurements of the stochastic, braking index and other induced parameters (proper motion, corner frequency and LFC) are consistent between the observed and simulated data sets for all 19 pulsars. Figures 4.2 and 4.3 show the consistency in the measured values of red noise amplitudes, spectral indices, and the derived braking index values from the real and simulated data sets for a sample of six pulsars. The shaded regions in the plots represent 50% and 95% confidence intervals.

4.3.2 Using legacy data sets.

We obtained historical data for 9 of the 19 pulsars and prepended these data to those used in PSJ19. The historical data is also at 20-cm wavelengths observed with the 64-m CSIRO Parkes radio telescope. The data set used in PSJ19 is hereafter called the PSJ19-data set and the data set that includes the historical data is called the legacy data set. Figure 4.4 shows the timing residuals for these nine pulsars with the added data.

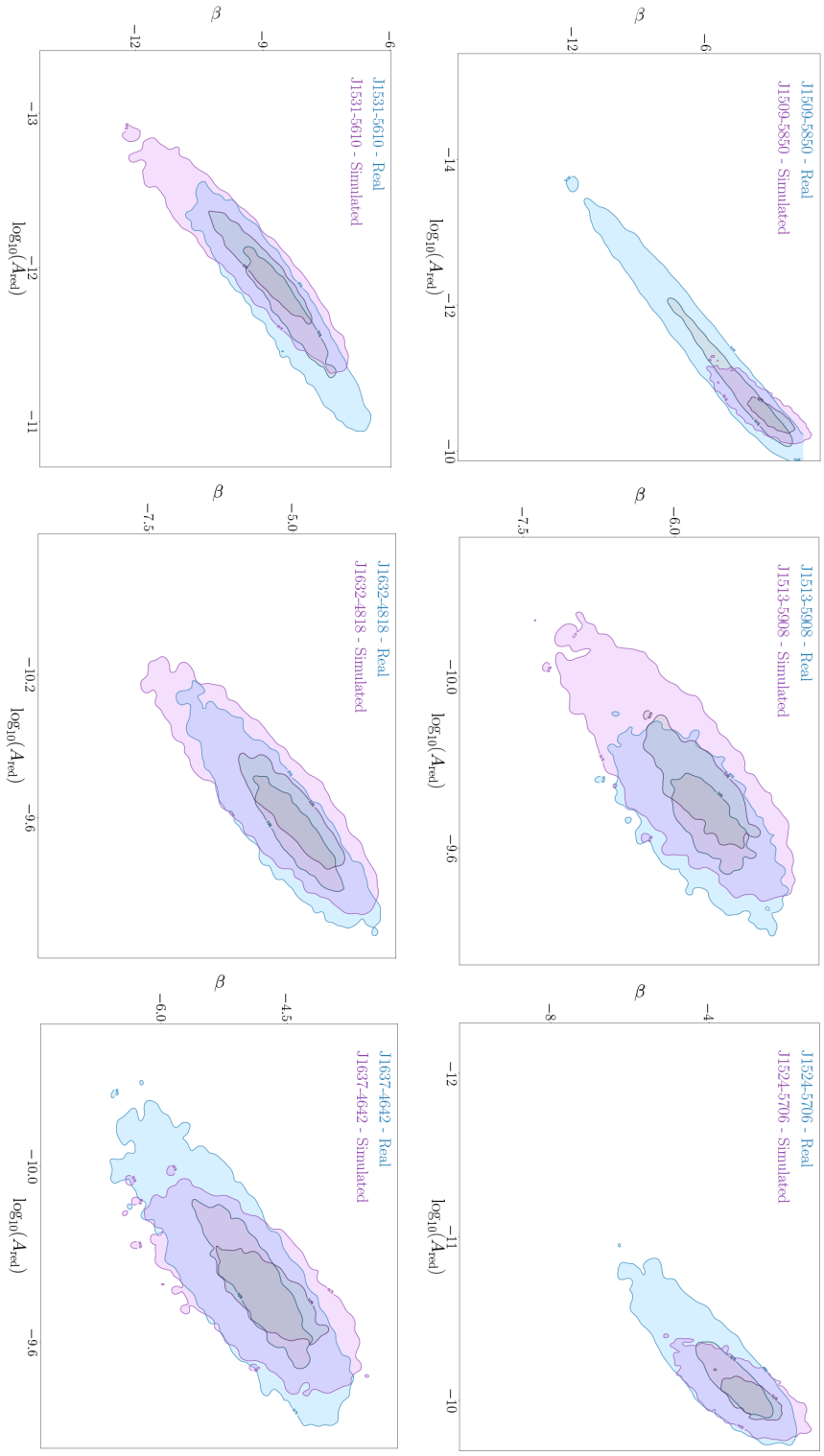

Figure 4.2 Posterior distributions of the red noise amplitudes and spectral indices for a sample of six pulsars. The blue posteriors represent real data, while the purple posteriors represent simulated data.

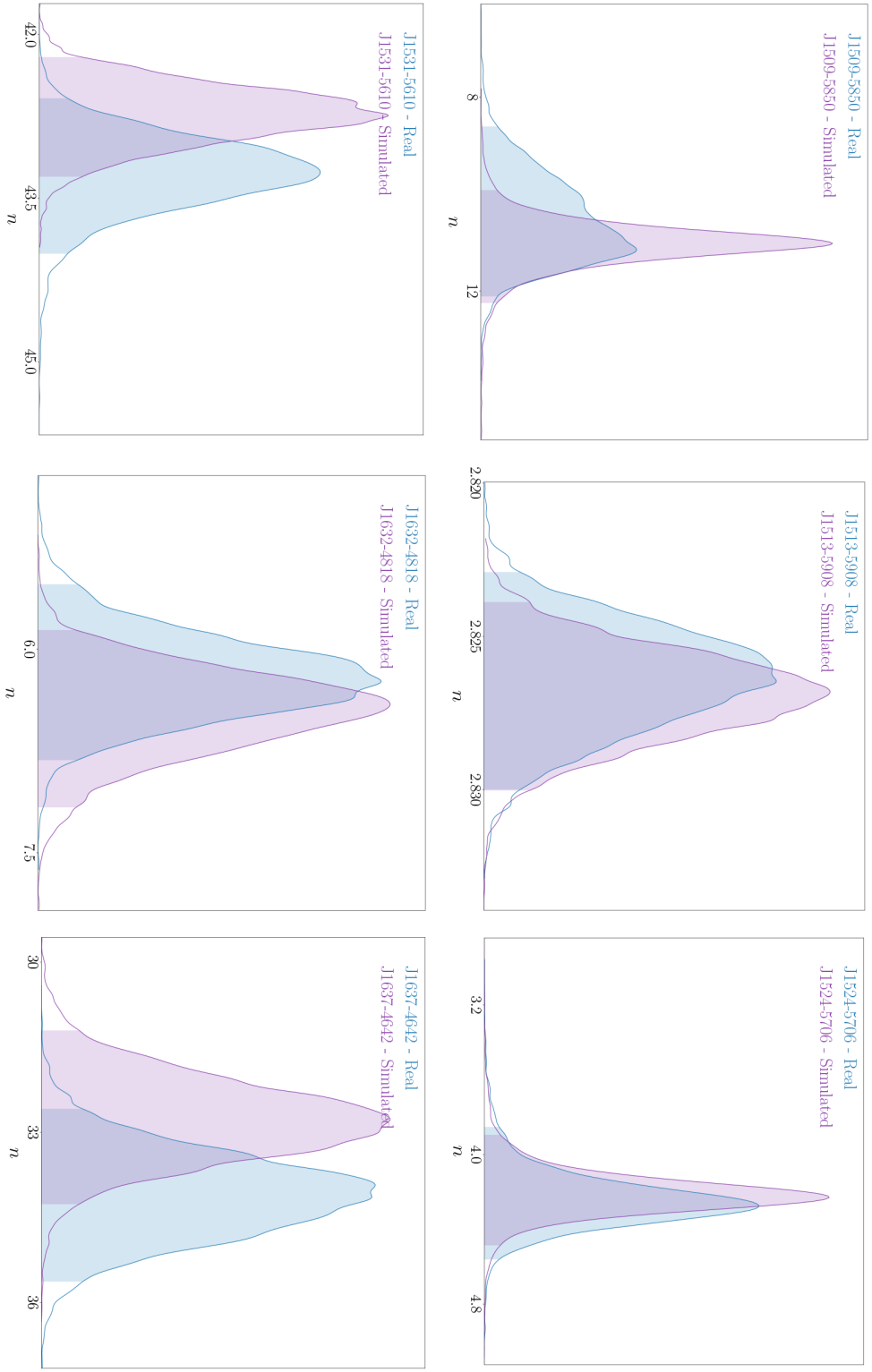

Figure 4.3 Posterior distributions of the braking index measurements for a sample of six pulsars. The blue posteriors represent real data, while the purple posteriors represent simulated data.

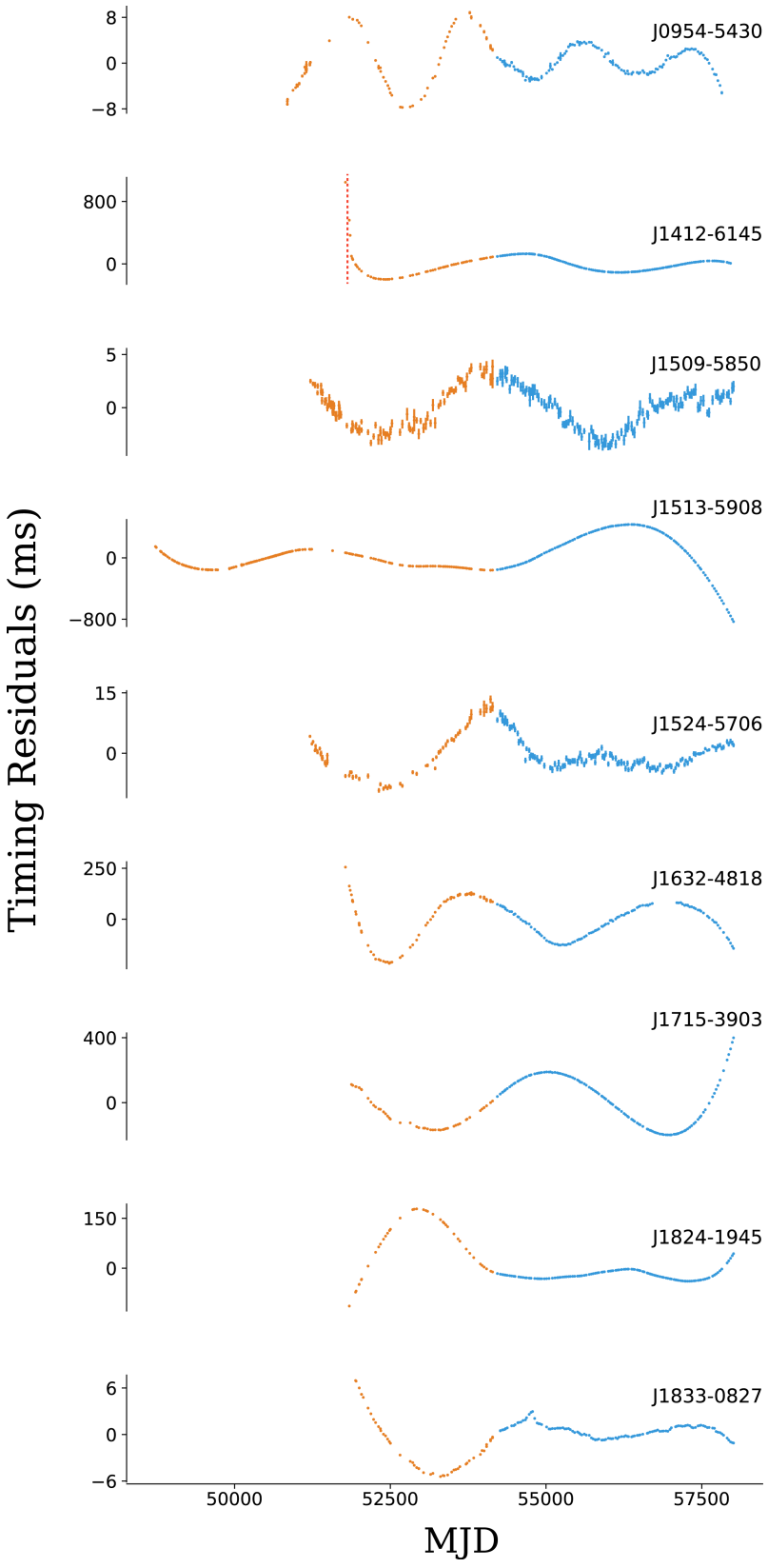

Figure 4.4 Phase connected timing residuals for nine pulsars with added archival data sets (orange) are shown here before subtracting the timing noise model. The vertical dashed line in PSR J1412–6145 shows the epoch of the glitch reported in Yu et al. (2013). For PSRs J1632–4818 and J1715–3903, the new glitches described in Section 4.3.2 are modelled in these timing residual plots.

Figure 4.5 shows the posterior distributions for six pulsars that have consistent values (overlapping confidence intervals) of $\ddot{\nu}$, braking index and the timing noise parameters using the legacy data set. A model with power-law timing noise and $\ddot{\nu}$ (PL+F2) was still favoured for three pulsars and PL+F2+LFC for PSR J1824–1945. For PSR J1412−6145, we fitted for the glitch parameters as reported in Yu et al. (2013) while simultaneously modelling the stochastic and braking index parameters. The preferred model in this case is one with the glitch parameters (PL+F2+GL). For PSR J1833–0827, we measure a proper motion signal with the legacy data set, with the proper motion in right ascension (μ_α) being -37 ± 7 mas yr^{-1}, in declination (μ_δ) being 3 ± 26 mas yr^{-1} and the total proper motion ($\mu_{\rm tot}$) being 39 ± 10 mas yr^{-1}. At a distance of 4.38 kpc (from DM estimates), this amounts to a high transverse velocity of 800 ± 200 kms^{-1}. The preferred timing model with the legacy data set is PL+F2+PM with a log Bayes factor of 21. It must be noted that the measured braking index remains unchanged within uncertainties.

PSRs J1513–5908, J1632–4818 and J1715–3903 exhibited clear inconsistencies in either the $\ddot{\nu}$ or the timing noise parameters after adding archival data. These are further investigated below on a case-by-case basis.

PSR J1513–5908: This pulsar has not been observed to glitch. With 28.4 years of radio timing data from 1982 June to 2010 November, Livingstone & Kaspi (2011) reported a braking index value of 2.832 ± 0.003. They also reported a detection of the third derivative of the spin-frequency ($\dddot{\nu}$) to be $-0.9139(2) \times 10^{-31}$ s^{-4}.

We notice that a model with a $\dddot{\nu}$ is preferred over the PL+F2 model in the legacy data and including it as part of the timing model results in consistent measurements of $\ddot{\nu}$ and the timing noise parameters. An expression for $\dddot{\nu}$ can be derived by taking two derivatives of equation 4.1 and is written as,

$$\dddot{\nu} = \frac{n(2n-1)\dot{\nu}^3}{\nu^2}. \tag{4.6}$$

The validity of the spin-down law can then be tested by calculating the expected second braking index (m_0), which is written as,

$$m_0 \equiv n(2n-1), \tag{4.7}$$

and if equation 4.1 accurately describes the spin-down of the pulsar, then $m_0 = m$, where m is,

$$m = \frac{\nu^2\dddot{\nu}}{\dot{\nu}^3}. \tag{4.8}$$

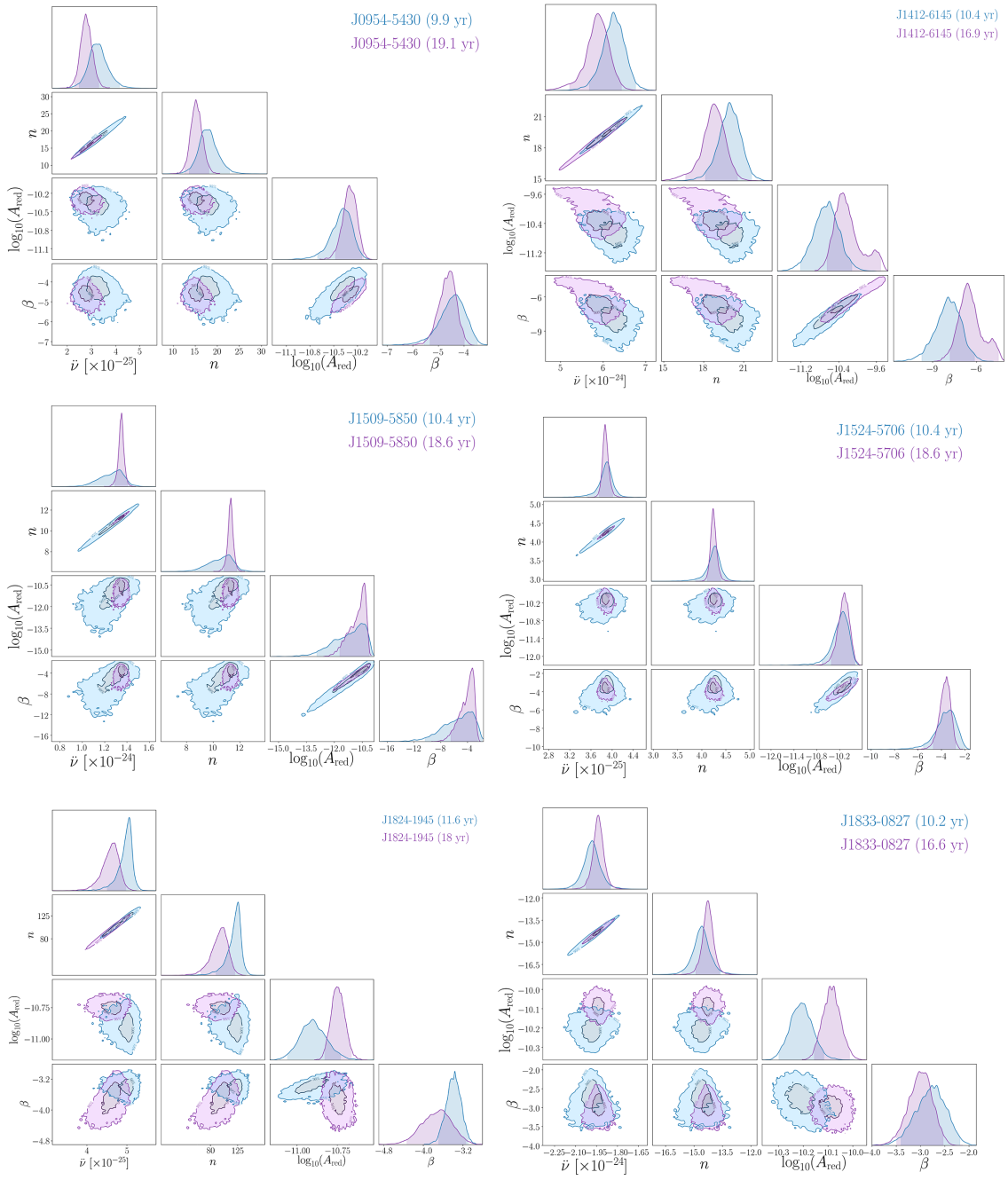

Figure 4.5 Posterior distributions of six pulsars comparing the original (in blue) and the longer (legacy) data sets (in purple). We account for a previously published glitch at MJD $\sim$ 51868 for PSR J1412–6145.

A value of m can be measured from higher order frequency derivatives of a pulsar, which is only possible in the youngest pulsars that have large spin-down and minimal timing noise. We measure the value of m to be 14.4 ± 2.2 and the computed value of m_0 to be 13.23 ± 0.03, which are in agreement with each other within uncertainties. In Figure 4.6 we show our measurements of $\ddot{\nu}$, $\dddot{\nu}$ (F3), n, m_0, m and the timing noise parameters which are consistent with the measurements reported in Livingstone et al. (2005) within 95% confidence limits. Our measurements of timing noise and the absence of glitches in this pulsar are in contrast to the suggestions made by Hobbs et al. (2010b) that timing noise in pulsars with characteristic ages less than 10^5 yr is due to unmodelled glitch recovery.

PSR J1632–4818: Using TEMPONEST, we searched for glitches in the legacy data set and found evidence for the presence of a glitch at MJD 53962±10 and with a glitch amplitude of $(1.1 \pm 0.2) \times 10^{-8}$ Hz. The detection was also supported by the fact that the log Bayes factor for the glitch-search model was 17, which is much higher than our Bayes factor threshold of 5 (used in PSJ19). Figure 4.7 shows the posterior distributions of timing noise, $\ddot{\nu}$ and braking index measurements for the PSJ19 and legacy data sets, before and after accounting for the glitch.

PSR J1715–3903: Similar to PSR J1632–4818, we found evidence for the presence of a glitch at MJD 57724±2 in the PSJ19 data set, with a glitch amplitude of $(1.9 \pm 0.1) \times 10^{-8}$ Hz and the glitch model is strongly preferred over a model without the glitch with a Bayes factor of 35. Figure 4.8 shows the measured posterior distributions of $\ddot{\nu}$, braking index and the timing noise parameters for both the data sets before and after modelling for the glitch. It is evident from Figure 4.8 that the uncertainties on the measurement of the braking index have improved after accounting for the glitch.

4.3.3 Summary

In Table 4.3, we report the time-span of the legacy data sets along with the updated braking index values using the updated timing models for PSR J1412–6145, J1513–5908, J1632–4818 and J1715–3903. There are three important results from this section. First, we showed through simulations that TEMPONEST is capable of recovering braking indices in the presence of strong timing noise. Secondly, we demonstrated that TEMPONEST is capable of detecting glitches within the time span of the datasets. Thirdly, we demonstrated that increasing the overall data span maintains the value of n even in the presence of glitch activity.

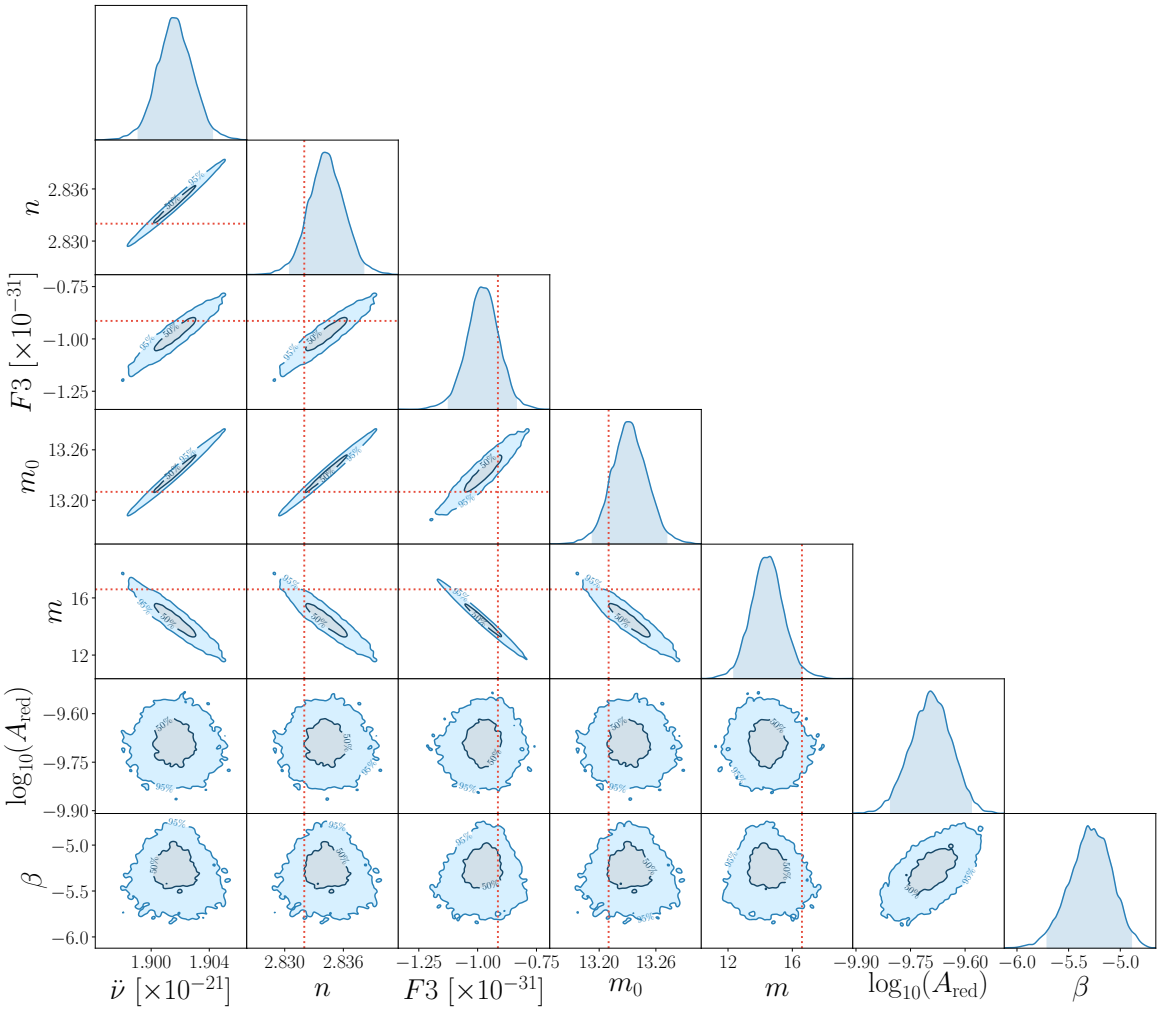

Figure 4.6 Posterior distributions of $\ddot{\nu}$, $\dddot{\nu}$, n, m_0, m and the timing noise parameters for PSR J1513–5908 measured from 25.4 years of radio timing data. The dashed orange lines are measurements from Livingstone & Kaspi (2011).

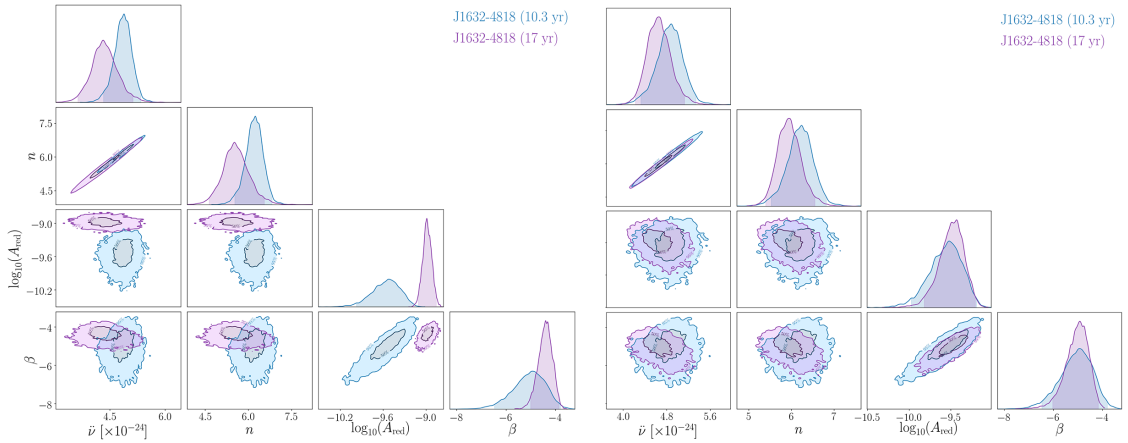

Figure 4.7 Posterior distributions for PSR J1632–4818, for the PSJ19 (in blue) and legacy data sets (in purple) before (left) and after (right) modelling the glitch.

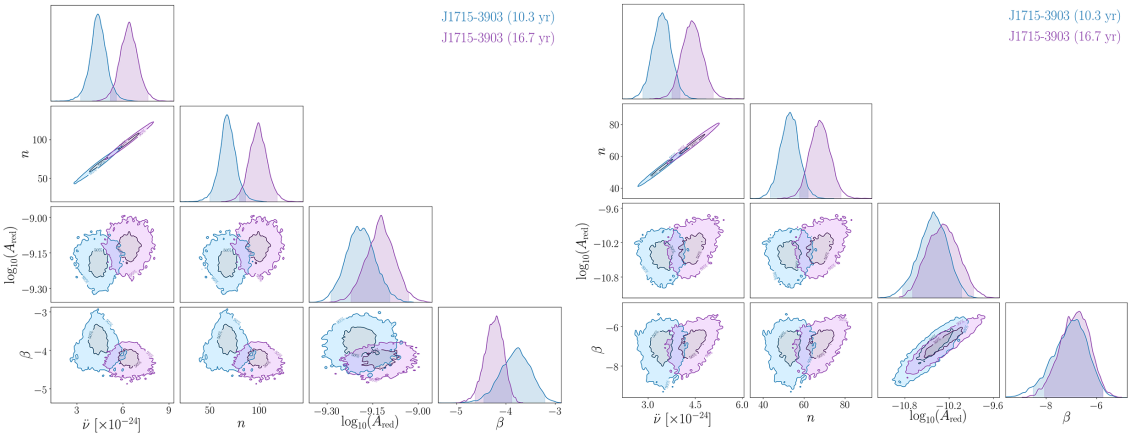

Figure 4.8 Posterior distributions for PSR J1715–3903, for the PSJ19 (in blue) and legacy (in purple) data sets before (left) and after (right) modelling the glitch.

Table 4.3 Braking index measurements for nine pulsars before and after increasing the time span of the data as measured from the preferred timing models.

PSR	Old timespan (yr)	New MJD Range	New timespan (yr)	Old braking index	New braking index	Old timing model	New timing model
J0954–5430	10	50849–57824	19	18(9)	15(3)	PL+F2	PL+F2
J1412–6145	10	51782–58012	16.9	20(3)	19(2)	PL+F2	PL+F2+GL
J1509–5850	10	51221–58012	18.5	11(3)	11.2(5)	PL+F2	PL+F2
J1513–5908	11.6	48732–58012	25	2.826(3)	2.834(3)	PL+F2	PL+F2+F3
J1524–5706	10	51212–58012	18.6	4.3(7)	4.2(1)	PL+F2	PL+F2
J1632–4818	10	51782–58012	14	6.2(7)	5.9(5)	PL+F2	PL+F2+GL
J1715–3903	10	51878–58012	14	70(40)	68(10)	PL+F2	PL+F2+GL
J1824–1945	11.6	51844–58012	18	120(20)	88(15)	PL+F2+LFC	PL+F2+LFC
J1833–0827	10	51782–58012	16.6	−15(2)	−14.2(6)	PL+F2	PL+F2+PM

4.4 Glitch recovery

Here we investigate whether unseen glitches in the past affect the measured value of n. Of crucial importance is not the glitch size itself but rather the recovery from the glitch. Generally the form of the recovery is taken to be an exponential which asymptotes towards a frequency increment parameter, $\nu_{\rm GLD}$, with a glitch decay time of $\tau_{\rm GLD}$. Typically, glitch recovery is expressed as $Q \equiv \nu_{\rm GLD}/\nu_{\rm g}$, where $\nu_{\rm g}$ is the total increment in the pulsar spin-frequency due to the glitch, expressed as $\nu_{\rm GLD} + \nu_{\rm p}$. Here, $\nu_{\rm p}$ is the permanent increment in the pulse frequency. The exponential form of the recovery implies that the epoch of the glitch is not important and since we are interested in glitches before our data set, the $\nu_{\rm p}$ is set to zero. In what follows therefore, the glitch is assumed to occur one day prior to the start of our data sets. We also keep in mind that the presence of $\ddot{\nu}$ (and hence a braking index) manifests itself as a cubic in the timing residuals.

We can imagine several cases of interest. First, it is clear that very small values of $\nu_{\rm GLD}$ and/or small decay times will have little effect on our ability to measure $\ddot{\nu}$. For large decay times (longer than our dataset) the exponential looks linear and will be absorbed into the fits of ν and $\dot{\nu}$ and will hence not affect $\ddot{\nu}$. However, for decay times comparable to our data span (i.e. from 1000 days to 5000 days) the exponential mimics a (partial) cubic, and can therefore masquerade as a $\ddot{\nu}$ term. This will always serve to **increase** $\ddot{\nu}$ and hence also increase the value of n. Larger values of $\nu_{\rm GLD}$ will lead to larger values of n. In general, the induced value of n is largely independent of the other pulsar parameters; it depends only on $\nu_{\rm GLD}$ and $\tau_{\rm GLD}$. However, the presence of timing noise complicates such

analysis.

We assume the presence of an unseen glitch before the data set for each of our 19 pulsars and search for evidence of glitch recovery signals spanning a $\nu_{\rm GLD}$ range of 10^{-14} to 10^{-3} Hz and a $\tau_{\rm GLD}$ range of 1 to 10,000 days. We use a log-uniform prior for the glitch decay parameters. The prior ranges for the timing noise parameters and $\ddot{\nu}$ are as reported in Table 4.2. We then fitted for three different timing models and compared their log-evidences. These are:

- the timing model as reported in Tables 4.1 and 4.3,
- the timing model with a glitch recovery signal (TimingModel+GLR)
- the timing model, without a cubic polynomial (F2), but including a glitch recovery signal (TimingModel-F2+GLR)

For PSR J0954–5430, the three models that we compare are PL+F2, PL+F2+GLR and PL+GLR, since the timing model as reported in Table 4.1 is PL+F2. However, for PSR J1412–6145, since the updated timing model reported in Table 4.3 is PL+F2+GL, the three models to compare are PL+F2+GL, PL+F2+GL+GLR and PL+GL+GLR (without the F2).

Table 4.4 reports the log-evidences for the three timing models for 19 pulsars in our sample. The preferred model for each pulsar is highlighted. Two things are apparent; first that there is much stronger evidence for a cubic term than for an exponential. Secondly, that although TimingModel+GLR and TimingModel have similar log-evidences, the simpler model would always be preferred. This is following the Occam principle, which states that all other things being equal, a simpler model is more likely than a complicated one. Taken together, this shows that there is little evidence for an exponential signal in the data. It is also important to note that the Bayesian inference framework enables us to identify cases when we cannot distinguish between models. In this case, distinguishing between a braking index and a glitch recovery signal is important while interpreting the measurements.

Finally we note that PSRs J1531–5610, J1806–2125, J1809–1917 and J1833–0827 have glitches detected before our data span. The glitch sizes are a few $\times 10^{-5}$ Hz as reported in Yu et al. (2013) and Espinoza et al. (2011b) and the difference between the MJD of the first ToA in our data set and the glitch epochs are $\sim$ 2500, 2300, 1000 and 4200 days respectively. Yu et al. (2013) also measure glitch recovery times of a few hundred days for 3 of these pulsars. If correct, then no evidence of the glitch would remain in the residuals of our data as is confirmed by Table 4.4.

Table 4.4 Comparison of log-evidence values for models with glitch recovery and braking index for 19 pulsars. The preferred model for each pulsar is highlighted.

PSR	TimingModel+GLR (with F2 & GLR)	TimingModel (with only F2)	TimingModel-F2+GLR (with only GLR)
J0857–4424	1144	**1150**	807
J0954–5430	1357	**1358**	934
J1412–6145	1184	**1197**	1165
J1509–5850	1593	**1594**	1565
J1513–5908	2961	**2962**	2452
J1524–5706	1156	**1157**	721
J1531–5610	1082	**1083**	1056
J1632–4818	717	**725**	460
J1637–4642	727	**728**	684
J1643–4505	705	**706**	698
J1648–4611	739	**746**	707
J1715–3903	893	**901**	725
J1738–2955	510	**511**	481
J1806–2125	572	**572**	528
J1809–1917	943	**946**	774
J1815–1738	517	**518**	510
J1824–1945	1546	**1548**	986
J1830–1059	958	**960**	943
J1833–0827	1345	**1346**	617

4.5 Glitch simulations

We have shown in the above section that there is no (Bayesian) evidence for the presence of an exponential glitch recovery signal in our data, even in those pulsars known to have glitched prior to our data set. However, we also noted that a long decay time (> 1000 days) could induce a positive n in the residuals. In this section, we therefore consider the possibility of long glitch recovering times contaminating our data.

Using the TEMPO2 package, we measure the induced $\ddot{\nu}$ as determined when fitting for F2 for different simulated data sets with a typical data span of 15 yr, and for 1000 days $< \tau_{\rm GLD} <$ 10000 days. Using these measurements, we empirically determine the link between $\nu_{\rm GLD}$, $\tau_{\rm GLD}$ and the induced $\ddot{\nu}$ as

$$\ddot{\nu} = 10^{-14} \ \frac{\nu_{\rm GLD}}{\tau_{\rm GLD}} s^{-3} \tag{4.9}$$

with $\nu_{\rm GLD}$ in Hz and $\tau_{\rm GLD}$ in days. For a given pulsar this translates into an induced n via Equation 4.2. Second, for each pulsar we compute the glitch rate and typical glitch size. For this we use the metric for the glitch rate given by Fuentes et al. (2017) along with the parameterisation of large glitch sizes given in the same paper. As a check on the metric, we use Poisson statistics and determine that we expect ∼3.2 pulsars in our sample to have glitched in the 15 year observing span of the data. We have shown above that indeed 3 pulsars have undergone glitches in this time span, in good agreement with the predictions of Fuentes et al. (2017).

We then perform a Monte Carlo simulation in the following way:

- For each pulsar, we determine the glitch rate, and then using Poisson statistics randomly select a date in the past for the glitch to have occurred.
- Draw a glitch size from the distribution of large glitches given in Fuentes et al. (2017).
- For a given $\tau_{\rm GLD}$, extrapolate forwards in time to the start of our data set and then compute the effective glitch size at that date assuming an exponential recovery.
- Compute the induced $\ddot{\nu}$ and hence n from Equation 4.9 above.
- If the induced n is greater than the upper limit for a given pulsar from Table 4.1 then count this as a detection.

The output of the simulation shows that the most likely 'detections' of n are, unsurprisingly, in pulsars with a high glitch rate and/or for which the upper limit on n is small.

For example, PSR J1809–1917 has the highest detection probability of 0.98 with a median induced n of 21 followed by PSR J1531–5610 with a detection probability of 0.86 and a median induced n of 37.2. Both these pulsars feature in Table 4.1. The question now arises as to how the addition of timing noise affects these results and whether TEMPONEST can detect long timescale glitch recovery signals.

We consider the cases of PSR J1809–1917 and J1531–5610. We simulate a 10 yr data set with an induced $\nu_{\rm GLD}$ of 4×10^{-6} Hz, a $\tau_{\rm GLD}$ of 5000 days and the glitch epoch set one day before the first data set. A power-law timing noise signal is induced with $A_{\rm red}$ and β as in Table 4.1. We set $\ddot{\nu} = 0$. Fitting for the three different models; PL+F2, PL+GLR and PL+F2+GLR using TEMPONEST, we find that in both the cases, the PL+GLR model is preferred over the PL+F2+GLR model (with Bayes factors of 12 and 7 respectively), while the PL+F2 model is strongly disfavoured (with Bayes factors of ~ -200).

These simulations together with the results from Table 4.4 have shown that:

- the braking indices are robust to the addition of legacy data, which is crucial in indicating a lack of exponential signal in the PSJ19 data,
- the model with $\ddot{\nu}$ is preferred over an exponential glitch recovery model for all 19 pulsars,
- given the glitch size and rate distributions as in Fuentes et al. (2017), there are not enough unseen glitches prior to the beginning of our dataset to explain the values of n we obtain even for long recovery times,
- for long exponential glitch recovery times comparable to our data span, TEMPONEST will detect and distinguish the presence of a glitch recovery signal from a cubic term.

In conclusion, there is strong evidence for a cubic term in the residuals of the 19 pulsars rather than an exponential term and the measured values of braking indices are unlikely due to an exponential glitch recovery.

4.6 Implications

In Figure 4.9, we show evolutionary tracks for each of our pulsars given their measured braking index. From equation 4.1, if K and n are assumed to be constant in time, then the pulsars follow a track with slope $2 - n$ in the P-$\dot{P}$ diagram. So, for pure magnetic braking with a constant dipolar magnetic field, we expect neutron stars to follow lines with slope of -1. However, previously measured values of n have been different from the

expected value of 3 and in this paper we have reported $n \gg 3$, implying that neutron stars can exhibit substantial torque decay and that the simple dipolar spin-down model is clearly imperfect.

We find evidence for a mild correlation (r = 0.34±0.01) between the characteristic age and n as shown in Figure 4.10. The correlation coefficient is computed based on the Spearmann correlation test, which is typically robust to outliers. PSR J1513–5908 is the youngest pulsar in our sample with a characteristic age of 1.6 kyr, while PSR J1824–1945 has a characteristic age of 570 kyr. PSR J0857–4424 has the highest measured n which is clearly an outlier for its characteristic age; this is further discussed in Section 4.6.3. In PSJ19, we reported limits on n for pulsars for which the $\ddot{\nu}$ model was not preferred. Adding pulsars from PSJ19 with the most constrained upper limits on n (represented by blue circles) does not affect this correlation. If we consider a line of constant age drawn at $\tau_{\rm c} \sim 120$ kyr in Figure 4.9, we detect n in 12 out of the 19 younger pulsars as opposed to detecting n in only 7 out of 66 pulsars with $\tau_{\rm c} > 120$ kyr. Two questions thus arise, first why do we measure significant braking indices in the younger pulsars and secondly, how can we connect the short-term braking values with the long-term evolutionary tracks in P-$\dot{P}$ space?

4.6.1 The detectability of braking index

To address the first question posed above, we discuss the various factors that play a role in measuring a braking index. The detectability of n for a pulsar depends on, ν, $\dot{\nu}$, $\ddot{\nu}$, $T_{\rm span}$, the mean red-noise amplitude ($A_{\rm red}$(TN)) and the spectral index ($\beta(TN)$) of the timing noise.

Consider the residuals, $R(t)$, induced through a $\ddot{\nu}$:

$$R_{\ddot{\nu}}(t) = \frac{1}{6}\left(\frac{\ddot{\nu}}{\nu}\right) t^3, \tag{4.10}$$

The residuals are sampled at equal intervals over a time span $-T/2 < t < T/2$. The variance of these residuals is then

$$\sigma^2_{\ddot{\nu}}(T) = \frac{1}{16128}\left(\frac{\ddot{\nu}}{\nu}\right)^2 T^6. \tag{4.11}$$

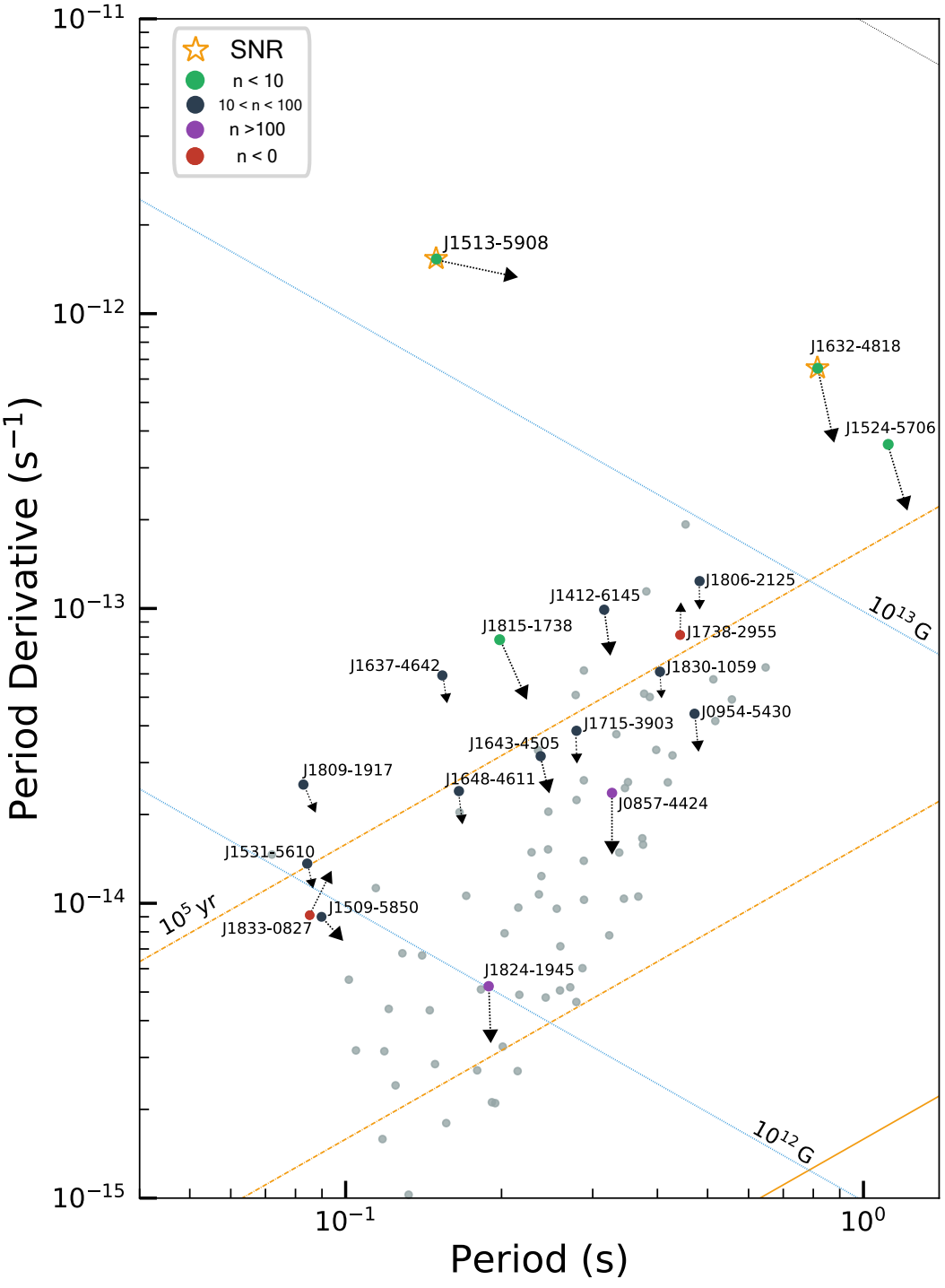

Figure 4.9 The P-$\dot{P}$ diagram of the 19 pulsars discussed in this paper plotted over the rest of the pulsars discussed in PSJ19 (grey circles). Lines of constant age are in orange (dashed line), while lines of constant magnetic fields are in blue. The circles (filled) are colored based on the measured braking index value of the pulsar. The dashed arrows show the time-evolution of the pulsars which follow a slope of $2 - n$. The length of the arrows are arbitrary to preserve clarity.

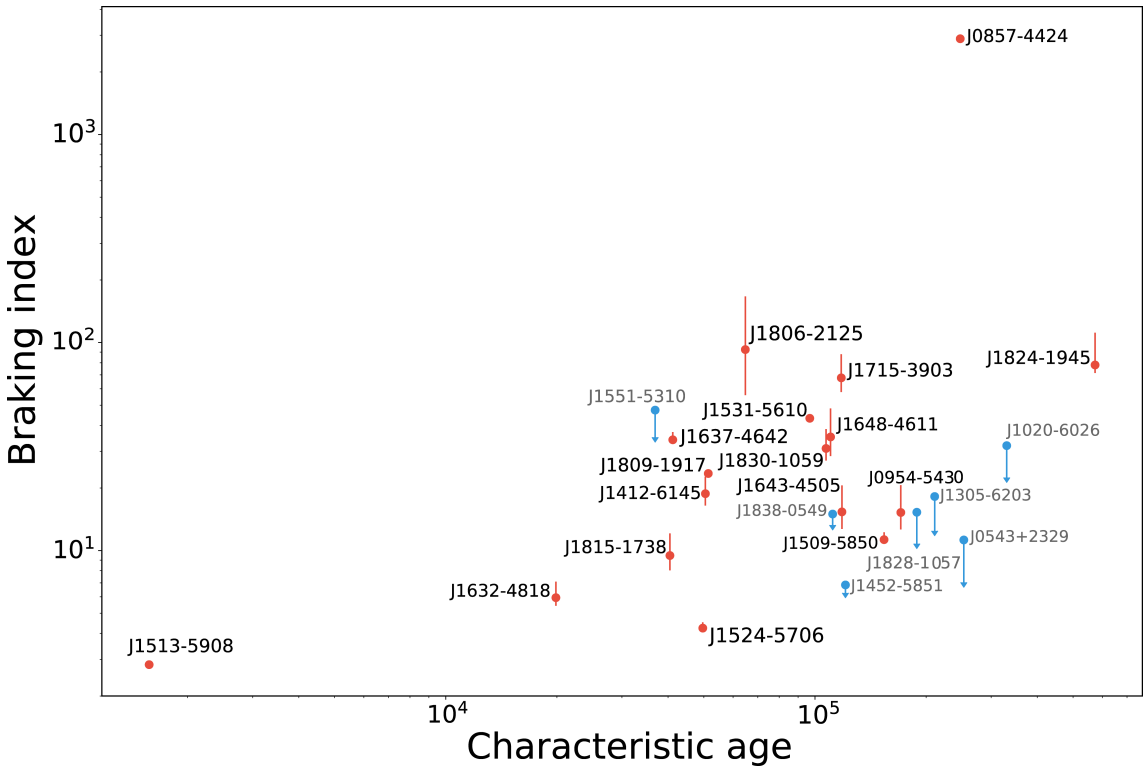

Figure 4.10 Plot showing the relation between the characteristic age (τ_c) and braking index for 17 pulsars discussed in this paper (red circles) along with seven non-detections of n (from PSJ19) with strongly constrained limits (blue circles). The uncertainties on the red circles are 97.5% and 2.5% confidence limits. PSRs J1738–2955 and J1833–0827 are not included in this plot owing to their negative braking indices. These pulsars have characteristic ages of 85 kyr and 147 kyr respectively.

The variance of a power law, expressed as $P(f) = Af^{\beta}$ is

$$\begin{aligned}\sigma^2_{\rm PL} &= \int_{1/T}^{\infty} df A f^{\beta} \\ &= \frac{A}{\beta+1} f^{\beta+1}\Big|_{1/T}^{\infty}, \\ &= -\frac{A}{\beta+1} T^{-\beta-1}\end{aligned} \tag{4.12}$$

where A is the amplitude and β is the spectral index. Relating equations 4.11 and 4.12, and expressing $\ddot{\nu}$ in terms of n (from equation 4.2) we derive an expression for the power spectral density associated with n

$$P_n(f) = \frac{n^2}{2688}\left(\frac{\dot{\nu}}{\nu}\right)^4 f^{-7}. \tag{4.13}$$

This can be used to assess the detectability of a cubic in the presence of other noise sources in the timing residuals. White noise, arising largely due to measurement errors, has a flat spectrum and if the amplitude of the cubic is higher than the white noise level, it will be detectable. Timing noise is a red noise process and is modelled as a power law process with a spectral index β (see equation 4.4). Considering equation 4.13 we can see that:

- the power spectral density of the cubic is larger in pulsars with smaller characteristic ages ,
- in pulsars where the spectral index of the timing noise is $\beta > -7$, the cubic spectral power will dominate over the timing noise for large time intervals,
- in pulsars where $\beta < -7$ (steep timing noise) the timing noise will dominate the cubic even with long observing time spans.

The S/N (S) of a deterministic signal (r) characterized by a noise covariance matrix (C) is expressed as,

$$S = \sqrt{\boldsymbol{r}^{\dagger}\mathbf{C}^{-1}\boldsymbol{r}}. \tag{4.14}$$

The covariance matrix (C) describes the contributions from stochastic red noise and white noise components. A cubic signal is likely to be detected when $S \gg 1$. As the parameters describing the red noise process are measured directly from the data, there is an inherent degeneracy between the noise covariance matrix and the signal, which is not taken into account in this methodology. In the frequency domain, the noise covariance matrix is

diagonal ($C_{ij} = 0$ for $i \neq j$) and is expressed as,

$$C_{ii} = \left(A f_i^{\beta} + \frac{2T\sigma_{WN}^2}{N} \right), \tag{4.15}$$

where σ_{WN} is the variance of the white noise components and is assumed to be equal in all observations.

Using the noise covariance matrix and the signal, a detection statistic can be calculated to determine the S/N of a cubic in the presence of white and red noise components,

$$S^2 = \sum_i r_i^{\dagger} r_i C_{ii}^{-1} = \left(\frac{n^2}{2688} \right) \left(\frac{\dot{\nu}}{\nu} \right)^4 \sum_i \frac{f_i^{-7}}{A f_i^{\beta} + (2T\sigma_{WN}^2/N)}. \tag{4.16}$$

Using the red noise models, the time T and the $\sigma_{\rm WN}$ for each of the pulsars in PSJ19, we can compute a S_3 based on equation 4.16 for $n = 3$. For 15 of the 19 pulsars with measured braking indices, we find that $S_3 \gg 1$, giving a good indication of the usefulness of the metric. The remaining four pulsars have large values of n which when scaled accordingly will boost the value of S_3. Pulsars for which we do not detect a significant value of n but have $S_3 > 1$ seem to favour a model with low-frequency components. The youngest pulsar in our sample without a measured n is PSR J1551–5310. It has $S_3 = 0.9$ due to a combination of dominant timing noise ($\beta = -7.3$) and a relatively short timing baseline of ~ 7 years. The value of S_3 increases with time in those pulsars with shallow timing noise, hence we expect to detect more braking indices as our time span increases.

4.6.2 Pulsar evolution in the P-$\dot{P}$ diagram.

For PSR J1513–5908 we stated that since our measurement of the second braking index (m) is consistent with the expected value from the standard spin-down model, it is reasonable to assume that n has not yet evolved with time. It is thus interesting to speculate on the future evolution of PSR J1513−5908. If its braking index remains constant, the evolutionary track will take it above the bulk of the population in the P-$\dot{P}$ plane. It will cross the radio death-line with a period of ~ 7 s, and perhaps then occupy the part of the P-$\dot{P}$ diagram containing the X-ray dim isolated neutron stars (Turolla 2009; Rigoselli et al. 2019). On the other hand its braking index could increase with time, and bring it close to PSR J1632–4818 in ~ 34 kyr, eventually following evolutionary tracks characterised by larger values of n to become a $\sim$1 s pulsar with ever decreasing $\dot{P}$.

PSRs J1738–2955 and J1833–0827 have a negative braking index implying that they evolve upwards and to the right in P-$\dot{P}$ space. A similar upward evolution is seen for PSR

J1734–3333, which has a measured n of 0.9±0.2 (Espinoza et al. 2011a) and is speculated to attain the rotational properties of a magnetar in $\sim$ 30 kyr as a consequence of surface magnetic field growth. PSR J1833–0827 is at a distance of ∼4.3 kpc, estimated both from DM (Yao et al. 2017) and HI absorption measurements (Weisberg et al. 1995), and has been plausibly associated with the SNR W41 (Gaensler & Johnston 1995). Our transverse velocity measurement of 800±200 km s^{-1}, suggests that the pulsar is indeed moving away from the SNR. We speculate that the magnetic field of the pulsar could still be increasing, thus causing the negative braking index. Another possibility is that the geometry of this pulsar is evolving towards orthogonality as is the case for the Crab pulsar (Lyne et al. (2013)). The dense plasma from the pulsar wind nebula surrounding this pulsar (Esposito et al. 2011) could exert a retardation torque on the neutron star causing a change in α (Beskin & Nokhrina 2007). Constraints on the viewing geometry and its time dependence could prove fruitful.

What then is the link between the high values of n measured here over $\sim$ 15 year time-scales with the evolution over timescales of Myr? We know of pulsars with similar characteristics to the ones discussed here, but with higher glitch rates. The spin-down of these pulsars is dominated by large braking indices ($n > 50$) between the glitches followed by a "reset" of the $\dot{\nu}$ at the glitch itself (Yu et al. 2013, Espinoza et al. 2011b). Espinoza et al. (2011b) therefore argue that the long-term value of n is indeed close to the canonical value of 3. Could it be then, that in our sample of pulsars, we are measuring n in between glitches separated by $>$ 20 yr and that a future glitch will reset the $\dot{\nu}$ back to its expected value from $n = 3$? Based on the theoretical work of Alpar et al. (1993) and Alpar & Baykal (2006) who postulated a weak coupling between the crust of the star and the superfluid interior, Yu et al. (2013) demonstrated an observational relationship describing the inter-glitch value of $\ddot{\nu}_g$:

$$\ddot{\nu}_g = 10^{-2.8\pm1.4}\ \dot{\nu}/T_g \tag{4.17}$$

where T_g is the mean time between glitches. In turn, Fuentes et al. (2017) showed that $T_g \propto \dot{\nu}^{-1}$. Combining this with equation 4.2, yields the remarkable relationship for the braking index between glitches, n_g, which then depends only on ν,

$$n_g = 10^{-0.2\pm1.4}\ \nu. \tag{4.18}$$

We do not find a good correlation between n and ν in our data, a formal fit yields $n_g = 10^{+0.3}\ \nu$ but with a large scatter. We therefore surmise that our values of n contain an "intrinsic" value higher than 3 coupled with an inter-glitch value. We also note that if

the glitch resets the evolutionary track back to a slope described by $n = 3$ for long glitch intervals, then this implies that the change in $\Delta\dot{\nu}/\dot{\nu}$ must be larger than 10^{-2} in this set of pulsars. Therefore, there should be a correlation between $\Delta\dot{\nu}/\dot{\nu}$ and the waiting time between glitches. However, current data is too sparse to determine this. In any case, the evidence remains strong for n to increase in the long-term in order to populate the $P - \dot{P}$ plane with the known pulsar population, either due to the alignment of the magnetic and rotational axes of the pulsar (Johnston & Karastergiou 2017) or magnetic field decay (Viganò et al. 2013).

If the braking index is indeed increasing with age, then it could imply that older pulsars have smaller inclination angles, as proposed by Tauris & Manchester (1998), Weltevrede & Johnston (2008), Johnston & Karastergiou (2019). Measuring the pulsar's geometry would then help to confirm this idea. For the 19 pulsars in this sample, only three pulsars have been subject to geometrical analysis (PSRs J1513–5908, J1531–5610 and J1648–4611), and even these are poorly constrained (Rookyard et al. 2015). Comparisons between n and α for a large sample of young pulsars will be an important test to further constrain theoretical predictions.

4.6.3 A wide-orbit companion for PSR J0857–4424?

A gravitational interaction between a pulsar and a companion in a wide orbit can manifest itself as the second derivative of the pulsar spin period (Matthews et al. 2016; Kaplan et al. 2016; Bassa et al. 2016). This can be expressed as (from Kaplan et al. 2016),

$$\ddot{P} = \frac{G^{1/3} M_{\rm c} P \sin i}{(M_{\rm c} + M_{\rm psr})^{2/3}\, c} \left(\frac{2\pi}{P_{\rm b}}\right)^{7/3} \cos\phi, \tag{4.19}$$

where G is the gravitational constant, c is the speed of light, $M_{\rm psr}$ is the mass of the pulsar, $M_{\rm c}$ is the mass of the orbiting companion, P is the pulsar's spin period, i is the orbital inclination angle, a is the orbital semi-major axis and ϕ is the orbital phase. If we attribute the entirety of the measured $\ddot{P}$ to this effect then the orbital period ($P_{\rm b}$) is given by

$$P_{\rm b} = \left(\frac{M_{\rm c} \cos\phi \sin i G^{1/3} P 2\pi^{7/3}}{(M_{\rm c} + M_{\rm psr})^{2/3} \ddot{P}}\right)^{3/7}, \tag{4.20}$$

For simplicity, if we assume a circular orbit, with $M_{\rm psr}$ of $1.44 M_{\odot}$ and $\sin i = 0.5$, and additionally set $\cos\phi = 1$, we can derive an empirical relation between $M_{\rm c}$ and the maximum $P_{\rm b}$ for a range of companion masses.

We consider the case for PSR J0857–4424, the pulsar with the highest value of n

Table 4.5 Estimated upper limits on the orbital periods and orbital separations for three different companion masses for PSR J0857–4424 computed using equation 4.20.

Companion mass ($M_\odot$)	Orbital period (yr)	Orbital separation (AU)
0.1	60	20
1	130	35
10	230	85

in our sample. We take companion masses of 0.1, 1 and $10M_\odot$ and compute P_b using equation 4.20. Table 4.5 reports the computed orbital periods, and the corresponding orbital separation for various companion masses. The estimated distance to PSR J0857–4424 from the DM measurement is ~ 2.8 kpc. At this distance, a $0.1M_\odot$ main-sequence star will have an apparent magnitude of ~ 29, while $1M_\odot$ and $10M_\odot$ main-sequence stars will have apparent magnitudes of ~ 17 and ~ 11 respectively. We examined the *Gaia* database for stars within a radius of 10 arcsec from the pulsar position and found no objects (Lindegren et al. 2018). Since the limiting magnitude for *Gaia* is 20, we can place an upper limit of $\sim 0.8M_\odot$ on a main sequence companion. However, if the companion is a $1M_\odot$ white dwarf or a neutron star, it would not be detected by *Gaia*.

It is hard to determine the likelihood of such a wide binary system existing. While we know at least one system with an orbital period in excess of 50 yr (Lyne et al. 2015b, Ng et al. 2019), the companion is a 15 $M_\odot$ main sequence star easily seen in the optical. At least one millisecond pulsar (Thorsett et al. 1993) appears to have a low-mass companion in a very long orbit but this system is in a globular cluster which permits such exotic formation scenarios via dynamical interactions. Therefore we entertain a binary orbit as a potential explanation of the high braking index of PSR J0857–4424 albeit an unlikely one.

4.7 Conclusions

There are several strands to the work presented here. First, we restate the important point that implementing a full timing model, which includes timing noise parameterization into a Bayesian framework like TEMPONEST, means that models can be evaluated and compared based on their Bayesian evidence. This is not possible in the generalized least-squares method implemented in TEMPO2. We have shown that the values of n derived in PSJ19

are robust to the addition of historical data, which emphasizes that they are unlikely to be due to unseen exponential glitches in the past. Even in the presence of glitches, successful detection and modelling of the glitch parameters maintains the consistency of n across long timing baselines. Furthermore, we show that we can distinguish between models with and without an exponential glitch recovery signal and that any unseen glitch prior to our data commencing, must have little or no influence on the results presented here either because (a) the glitch size is small and/or (b) that the glitch decay time is less than 1000 days. This is supported by glitch statistics which inform that it is highly unlikely for all the pulsars presented here to have suffered large enough glitches in the immediate past to cause the presence of an exponential signal in the data.

We are therefore left with the conclusion that the large values of n measured here are indeed indicative of the way a pulsar spins down, at least over a timescale of a decade or more. We consider it likely that n gets reset at the time of a glitch and that the inter-glitch value of n can be large. We predict a correlation between the wait time between glitches and the value of the step in $\dot{\nu}$.

Based on these results, we discuss the implications of the evolution of pulsars in the P-$\dot{P}$ diagram and find a moderate correlation of braking index with characteristic age, which can be attributed to either magnetic field decay and/or changes in the pulsar's inclination angle. We discuss an evolutionary path for PSR J1513–5908 depending on the future behaviour of its braking torque and speculate on the effect of a dense PWN surrounding PSR J1833–0827 in imparting it with a negative braking index. We outline a metric to compute the detectability of n in the presence of timing noise. Finally we explore the possibility of a wide-orbit companion inducing a very high braking index in PSR J0857–4424.

5

'Jitter' limits from 25 southern declination millisecond pulsars using the MeerKAT radio telescope

In this chapter, we make the transition from studying long-term timing noise in young pulsars to short-term jitter noise in MSPs. We use the state-of-the-art SKA precursor, the MeerKAT radio telescope, to make very high S/N observations of MSPs observed over a wide frequency bandwidth of ∼856 MHz. This enables us to report jitter measurements from 25 MSPs that are part of the MeerKAT pulsar timing array (MPTA) program. Jitter levels are presented for the first time in 13 of 25 MSPs and we show that in others, the measured levels of jitter are consistent with previously published results. This implies that jitter is a ubiquitous feature of radio pulsar emission, that will become more important with increasingly sensitive radio telescopes. In PSR J2241–5236 we estimate that stochastic profile variations cause an implied jitter of just ~ 4 ns in an hour, which is the lowest level of jitter ever measured in a pulsar. Using the large fractional bandwidth of MeerKAT, we study frequency-dependent profile evolution and measure jitter as a function of observing frequency. We find that, in PSR J0437–4715, jitter decorrelates across the observing band. We also find that along with phase jitter, time-varying frequency dependence of the profile in PSR J0437–4175 places a fundamental limit on our ability to measure its dispersion measure. Using a high-time resolution of $9\mu s$, we present a statistical analysis of the single pulse phenomenology for a subset of bright MSPs and discuss these results in the context of jitter and precision timing. Finally, we discuss optimization strategies for the MeerKAT pulsar timing program and its role in the context of the International Pulsar Timing Array (IPTA). In summary, this chapter reports a preliminary analysis of the various properties of jitter noise and single pulse phenomenology in MSPs observed with the MeerKAT radio

telescope.

5.1 Introduction

The precise monitoring of periodic radio pulses emitted from MSPs has enabled some of the most stringent tests of fundamental physics (Kramer et al. 2004; Cordes et al. 2004). It has been used to test the theory of general relativity (Taylor & Weisberg 1982a; Kramer et al. 2006b), alternative theories of gravity (Zhu et al. 2015), constrain neutron star equations of state (Demorest et al. 2010; Antoniadis et al. 2013), measure irregularities in terrestrial time standards (Petit & Tavella 1996; Hobbs et al. 2010a), detect planetary-mass companions (Wolszczan & Frail 1992) and potentially to detect and characterise nHz-frequency gravitational radiation (Hellings & Downs 1983; Foster & Backer 1990). Precision long-term timing of an ensemble of the most stable MSPs to $<$ 100 ns rms residuals has led to upper limits on the stochastic gravitational wave background (Shannon et al. 2015; Lentati et al. 2016b; Arzoumanian et al. 2018c; Perera et al. 2019), allowing constraints on the formation and evolution scenarios of black holes and their host galaxies.

The pulsar timing residuals, which are the differences between the observed pulse times-of-arrival (ToAs) and those predicted by a timing model, are a fundamental diagnostic tool in accessing the quality of the timing model (Edwards et al. 2006). Numerous studies since the 1970s have shown that the scatter in timing residuals are larger than expected from the formal uncertainties alone (Groth 1975; Cordes & Downs 1985; Osłowski et al. 2011; Shannon et al. 2014b; Lam et al. 2019). This excess noise can be categorised into a time-correlated red-noise component and an uncorrelated white-noise component. One of the main contributing sources to the red noise is caused by rotational irregularities in the pulsar's spin period also known as 'timing noise' (Boynton et al. 1972; Cordes 1980). Timing noise manifests itself as low-frequency noise in the pulsar timing residuals over timescales of months to years. Many studies have attempted to characterize the strength and non-stationarity of timing noise across the pulsar population (Shannon & Cordes 2010; Namkham et al. 2019) finding that although timing noise is widespread across the pulsar population, it is weaker in millisecond pulsars (Lam et al. 2017; Parthasarathy et al. 2019). Additional contributions to the red-noise component can arise from quasi-periodic processes, due to magnetospheric torque variations (Kramer et al. 2006a; Lyne et al. 2010), unmodelled planetary companions (Kerr et al. 2015), unmodelled dispersion measure variations (Keith et al. 2013), turbulence in the interstellar medium (Cordes & Shannon 2010; Lam et al. 2017; Reardon et al. 2019) and uncertainties in the solar system ephemerides (Champion et al. 2010).

On timescales of minutes to hours, the excess noise in the timing residuals is typically dominated by the uncorrelated white-noise component. This excess white noise, in addition to radiometer noise, can arise from several sources, the most significant of which arises from differences between the integrated pulse profile (averaged phase-resolved light curve of the pulsar) and a template profile (average of a finite number of pulses). This difference contributes directly to the excess white noise which results in observed ToA uncertainties being higher than the predicted formal ToA uncertainty. The formal uncertainty in the arrival time is derived from the template-matching algorithm (often implemented in the Fourier domain), which models the integrated pulse profile (P) as a scaled (by a factor A) and offset (by a factor B) version of the template (O) rotated by a phase shift ϕ with additional white noise $N(t)$, expressed as (Taylor 1992),

$$P(t) = AO(t - \phi) + B + N(t). \tag{5.1}$$

Observations of single pulses from pulsars with high S/N exhibit variations in their pulse morphology and have shown correlated variations in their phase and amplitudes (Drake & Craft 1968; Helfand et al. 1975; Jenet et al. 1998). Aside from the fact that pulse profile variability adversely affects the attainable precision in pulsar timing experiments with MSPs, it is important to acknowledge that the general phenomenology in slow pulsars has been extensively studied across the pulsar population on both short (seconds to hours) and long (months to years) timescales. Since the early 1970s, it was known that emission changes can occur in pulsars on short timescales (Backer 1970b,c); where pulse profiles were observed to switch between two or more distinct emission states (known as *mode changing*) or where the profile was either in a weak emission state or completely turned 'off' (known as *nulling*). Pulsars categorized as *intermittent* have been observed to cycle between quasi-periodic phases in which the radio emission is either clearly present or invisible (Kramer et al. 2006a; Camilo et al. 2012; Lyne et al. 2017) and in some cases the observed emission changes have been correlated with the pulsar's rotational behaviour. Changes in pulse morphology have also been attributed to precession of the pulsar's spin axis, which causes different regions of the emission beam to orient along our line-of-sight (Weisberg et al. 1989). In an important study, Cordes & Downs (1985) analysed 24 pulsars and concluded that pulse shape variations or 'jitter' were significant in a large fraction of their sample and proposed that it is likely to occur in all pulsars with varying degrees of importance.

Profile changes in MSPs have been reported in very few cases. Hotan et al. (2004a) & van Straten (2013) showed that previous claims of mode-switching in PSR J1022+1001

(Kramer et al. 1999) are in fact due to instrumental polarimetric calibration errors. However, Shannon et al. (2016a) reported a broad-band profile change in PSR J1643–1224 (also observed by Brook et al. 2016) which may have been due to a disturbance or a state change in the pulsar's magnetosphere. Very recently, the brightest and closest MSP, PSR J0437–4715 exhibited a significant change in its integrated pulse profile (Kerr et al, submitted), indicating that such abrupt profile changes may be common among MSPs as well. Contrasting to observations in young pulsars, the profile changes in both these MSPs were not accompanied with changes in their spin-down rate.

A few studies have recently focused on studying 'jitter' noise in MSPs and its effect on limiting the attainable precision through pulsar timing (Liu et al. 2012; Osłowski et al. 2011; Shannon et al. 2014b; Lam et al. 2019). Jitter noise is a stochastic process common to all pulsars, arising from intrinsic self-noise in the pulsar emission mechanism and is observed as a wide-band phenomenon (Taylor et al. 1975; Rickett 1975). The formal ToA uncertainty computed from standard pulsar timing techniques depends on the signal-to-noise ratio (S/N) and the frequency-dependent effective pulse width ($W_{\rm eff}(\nu)$), expressed as (Downs & Reichley 1983; Cordes & Shannon 2010),

$$\sigma_{\rm S/N}\left(S|W_{\rm eff}(\nu)\right) = \frac{W_{\rm eff}(\nu)}{S\sqrt{N_\phi}}, \tag{5.2}$$

where N_ϕ is the number of bins across the pulse phase ϕ and S is the peak-to-off-pulse S/N. The effective pulse width depends on the pulse spin period (P), the shape of the template (O) and the observing frequency (ν). Since single pulse morphology changes stochastically from pulse to pulse, and can be measurable in high S/N observations, the averaged pulse profile (P) will have a shape that is different from the template, thus causing an excess scatter in the measured ToA uncertainty. This excess scatter can be measured from its contribution to the root mean square (rms) of the ToAs, expressed as $\sigma_{\rm j}(N_{\rm p})$, where $N_{\rm p}$ is the number of averaged pulses or can also characterised with a dimensionless jitter parameter ($f_{\rm j}$), as the ratio of $\sigma_{\rm j}(N_{\rm p})$ to the pulse period (P). Unlike the formal ToA uncertainty ($\sigma_{\rm S/N}$), $\sigma_{\rm j}$ is independent of the S/N. Narrow-band diffractive interstellar scintillation (DISS) along with the frequency dependence of the pulse profile can also lead to additional scatter in the ToAs. However, the contribution of DISS for low DM (the integrated electron density along the line of sight to the pulsar) pulsars is negligible as compared to $\sigma_{\rm j}$, especially in the high S/N regime with short observing spans ($\sim$ few $\times$ 100 s).

Osłowski et al. (2011) analysed 25 hours of high-precision timing data of PSR J0437–4715 using the CSIRO 64-m Parkes radio telescope, at an observing frequency of $\sim$ 1400

MHz reporting that in 1 hour ($N_{\rm p} \sim 12{\times}10^5$ pulses), pulse jitter limits the attainable timing precision to $\sim$ 30 ns. Shannon & Cordes (2012) reported the jitter in PSR J1713+0747 to be $\sim$ 20 ns also in an hour. Jitter measurements for a sample of 22 MSPs as part of the Parkes Pulsar Timing Array (PPTA) (Manchester 2017) program were reported by Shannon et al. (2014b) with PSR J1909–3744 showing the lowest levels of jitter noise of $\sim$ 10 ns in an hour. They modelled the contribution of jitter as a function of observing time (T) as $\approx 0.5 W_{\rm eff}\sqrt{P/T}$. More recently, Lam et al. (2019) detected jitter in 43 MSPs as part of NANOGrav's timing program (McLaughlin 2013) and found significant frequency dependence of jitter in 30 MSPs. These studies clearly show that pulse jitter is a generic property of MSPs, that it dominates the white noise budget when observing with increased S/N and that robust characterisation of jitter noise is vital in the search for the stochastic nHz gravitational wave background using precision pulsar timing.

The MeerKAT radio telescope is several times more sensitive than the Parkes telescope and offers the opportunity to detect and constrain jitter in many more MSPs. In Section 5.2 we describe the MeerTime MSP observing program and the relevant data processing by the observing backend. In Section 5.3, we describe the data reduction pipeline and the various processing steps leading to the production of pulse times-of-arrival (ToAs). We discuss the methodology used to estimate jitter, report jitter measurements for 25 MSPs and discuss its frequency dependence in Section 5.4. In Section 5.5 we discuss fundamental limits imposed on the precision with which the DM can be measured in PSR J0437–4715. Statistical studies of single pulses allow us to link timing variations and shape variations providing further insights into the phenomenon of jitter. In Section 5.6, we present various statistical properties of MSP single pulses and discuss these results in the context of timing variations. Finally, in Section 5.7, we discuss the implications of our results and the role of the MPTA in aiding high precision pulsar timing and PTA experiments.

5.2 Observations

The MeerKAT radio telescope is the South African precursor for the SKA-mid radio telescope located in the Karoo, capable of observing the large population of known pulsars in the Southern hemisphere and in the Large and Small Magellanic Clouds. The MeerTime collaboration (Bailes et al. 2018) is one of the Large Survey Projects with the MeerKAT radio telescope, which was provisionally awarded many months of observing time. The MeerKAT Pulsar Timing Array program (MPTA) is one of the four major science themes as part of MeerTime, which focuses on precision timing of MSPs and is poised to contribute to an internationally coordinated effort to detect the stochastic gravitational wave

background using pulsar timing arrays. A credible detection of this background ($\sim 4\sigma$) is hoped to be achieved by timing $\sim$ 40 pulsars over a time span of $\sim$ 10 years with 100 ns timing precision (Jenet et al. 2005; Siemens et al. 2013). The current observing strategy for the MPTA has been to attain sub-microsecond timing precision on as many pulsars as possible in less than 24 hours. For each pulsar, we set the integration time to match the median expected time either based on previous observations from the MeerKAT MSP census program or previous monitoring. A maximum integration time of 2048 seconds is imposed per epoch and a minimum integration time of 256 seconds is used if sub-microsecond timing precision is achievable in less than that time. The MPTA, since commencing observations from February 2019, attains a timing precision of $< 1\mu s$ on $\sim$ 60 MSPs in a total observing time of just 10 hours. The Parkes Pulsar Timing Array, in comparison, achieves sub-microsecond precision in 22 MSPs in 24 hours and NANOGrav achieves $< 1\mu s$ timing precision on 71 MSPs.

For our jitter analysis, we selected MSPs observed with MeerKAT that exceeded a S/N per pulse of unity following Shannon & Cordes (2012). These included $\sim$ 200 observations of 25 pulsars over a span of about eight months. Approximately 80% of these observations have an integration time of $<$ 15 minutes each. We used the 20-cm (L-band) receiver with a system temperature of $\sim$ 18 K, operating at a frequency range between 856 MHz and 1712 MHz. The dual-polarization and channelized signal from the beamformer are processed in the Pulsar Timing User Supplied Equipment (PT-USE) using the DSPSR software library (van Straten & Bailes 2011). DSPSR provides two signal processing pipelines and produces fold-mode and search-mode data products. Pulsar timing applications use the fold-mode pipeline to produce frequency- and phase-resolved averages of the polarised flux for the target pulsar. The key digital signal processing operations performed are:

- phase coherent dedispersion to the specified DM,
- formation of Stokes parameters from orthogonal-polarisation inputs and
- phase folding based on evaluation of a pulsar phase predictor for each time sample.

Search-mode applications (for single pulses) on the other hand, use DIGIFITS to produce filter-bank data products. The output time-series are decimated to a lower bit rate and may be used for multiple applications such as pulsar searching and single-pulse studies.

The boresight polarimetric response of the MeerKAT tied-array was estimated using the Measurement Equation Modeling (MEM) technique described in van Straten (2004). Following Liao et al. (2016), the MEM implementation was updated to include observations of an artificial noise source that is coupled after the orthomode transducer (OMT) and to

ignore the assumption that the system noise has insignificant circular polarisation. The updated model was fitted to observations of the closest and brightest millisecond pulsar, PSR J0437−4715, made over a wide range of parallactic angles, and both on-source and off-source observations of PKS 1934−63.

The best-fitted model parameters indicated that the degree of mixing between linear and circular polarisation is exceptionally low. Also, the non-orthogonality of the receptors is very low, as characterised by the intrinsic cross-polarisation ratio (IXR) (Carozzi & Woan 2011), which varies between 50 and 80 dB across the band. Since larger values of IXR correspond to lower levels of receptor non-orthogonality, the MeerKAT tied-array beam exceeds the minimum performance ($\mathrm{IXR_{min}} \sim 30\,\mathrm{dB}$) recommended for high-precision pulsar timing (Foster et al. 2015) by 2 to 3 orders of magnitude.

Therefore, for many applications, it is sufficient to calibrate only the differential gain and differential phase of the tied-array response. The differential gain is calibrated to within 1% during the procedure that is used to phase up the tied array, and a technique to determine and calibrate the differential phase during this procedure is currently under development and testing. For the analysis presented in this chapter, we use only the total intensity profiles.

5.3 Data reduction and analysis

The coherently dedispersed folded archives and search-mode data products produced by PT-USE are automatically ingested by the MeerKAT *kat-archive*. They are then transferred to the OzStar HPC facility at Swinburne University of Technology through an authenticated download for post-processing. PT-USE produces folded archives of 8 second integrations with 4 Stokes parameters, 1024 frequency channels across the observing bandwidth and 1024 phase bins. Although the receiver has a bandwidth of 856 MHz, a portion of the bandwidth is ignored due to bandpass filter roll-off, which reduces the usable bandwidth to 775.75 MHz and thus the number of frequency channels to 928. These archives are further processed by the fold-mode processing pipeline MEERPIPE[1], which generates integrated full-frequency and time resolution PSRFITS based archives (van Straten et al. 2010), RFI-excised archives using a modified version of COASTGUARD (Lazarus et al. 2016), decimated archives of various user-specified frequency and time resolution and associated ToA files for each data product.

MEERPIPE is a modular, python-based pipeline that utilizes the capabilities of advanced HPC facilities like OzStar for parallelizing large number of observations to accelerate

[1] https://bitbucket.org/meertime/meerpipe/src/master/

processing times. It utilises the Python bindings of PSRCHIVE (Hotan et al. 2004b) to manipulate the folded archives. Various components of MEERPIPE are sufficiently general to use with files in PSRFITS format. The various processing steps in MEERPIPE are logged for future reference and to aid in reproducibility. A master configuration file can be used to control various components of the pipeline and in choosing the output data products.

The fragmented 8 second folded archives are first grouped together using *psradd*. The data are then aligned using an up-to-date pulsar ephemeris. The ephemerides used for observing and timing are first automatically checked following a series of pre-defined standards[2] which is then followed by a manual vetting process. These are automatically version controlled[3] and used by PT-USE through *git*, ensuring accountability. The noise-free templates used for timing are similarly version-controlled[4] and are generated either manually (using *paas*) or automatically wavelet-smoothed using *psrsmooth*. Frequency-dependent template profiles (or portraits) are generated for pulsars which show significant profile evolution across frequency using PULSEPORTRAITURE[5] (Pennucci 2019).

To resolve single pulses in MSPs, the time series are recorded at a time-resolution of $9\mu s$ across 768 frequency channels and are stored in PSRFITS format. Post-processing of the single pulses is currently done in a somewhat ad-hoc manner, however, a single-pulse pipeline is currently being developed[6] to enable automatic post-processing of search-mode data.

RFI excision was implemented using a modified version of COASTGUARD[7]. The folded data cube with full-frequency and time resolution after integrating the 4-Stokes parameters is used to excise RFI. This version of COASTGUARD uses a template profile to identify the phase-bins containing the pulsar signal and to compute profile residuals by subtracting the observed profile from the template. Using various metrics as described in Lazarus et al. (2016), RFI mitigation is performed on the Fourier transform of the profile residuals. COASTGUARD has also been modified to parallelize the processing using multiple compute cores on OzStar, thus significantly reducing the processing time. For the analysis presented here, only frequency integrated template profiles were used for RFI excision. Furthermore, manual inspection of the output archives were performed to ensure that no residual RFI is present in the data.

The reference signal produced by the incoherent sum of the noise diode signals from

[2] http://wiki.pulsarastronomy.net/meertime/doku.php?id=how_to_update_folding_ephemerides
[3] https://bitbucket.org/meertime/meertime_ephemerides/src/master/
[4] https://bitbucket.org/meertime/meertime_templates/src/master/
[5] https://github.com/pennucci/PulsePortraiture
[6] https://bitbucket.org/meertime/meertimesinglepulse/src/master/
[7] https://github.com/aparthas3112/coast_guard

each antenna in the MeerKAT array, deviates from 100% linear polarization; its polarization state varies linearly from $\sim 20\%$ circular polarisation at 900 MHz to $\sim 60\%$ circular polarisation at 1670 MHz. Therefore, it is not possible to use this signal to calibrate the absolute gain, differential gain and differential phase of the system, based on the *ideal feed assumption*, in which an ideal noise diode signal is assumed to be identically coupled to each receptor. The differential gain is calibrated to within 1% during the procedure that is used to phase up the tied array, leaving only the absolute gain and differential phase to be calibrated. The absolute gain can be calibrated using a separate set of flux calibration observations of a standard candle, such as PKS B1934−638. Fortunately, in a subset of MeerTime observations, the differential phase also happens to be very close to zero. Therefore, for these observations, it is sufficient to perform only the projection, basis and backend corrections. Thus, for the MeerKAT tied-array beam, only the feed hand (basis) and parallactic angle (projection) corrections are required. These corrections are implemented in *pac* (using the -XP option), which is used in MEERPIPE.

The cleaned and vetted archives are then decimated into various data products containing different numbers of frequency channels and sub-integrations as specified by the user in a master configuration file. These data products are further used to produce ToAs. The ToAs are calculated by cross correlating the sub-banded observations with a frequency integrated template profile in the Fourier domain. The formal uncertainties produced by this method assumes that the only source of noise in the measurement is white radiometer noise and thus, underestimates the true ToA uncertainty. We use *pat* to produce sub-banded ToAs following the IPTA convention that describes the meta-data specified for each ToA. Wideband ToAs that account for frequency-dependent profile evolution are also produced. For the results presented here, we used profiles that are frequency-averaged to 32 channels with 8 second sub-integrations.

5.4 Jitter measurements

In this section we first describe the methodology used to estimate jitter measurements using frequency averaged ToAs for the MeerKAT pulsars. We then use wideband templates to examine if there is any frequency dependence of jitter.

5.4.1 Methodology

The sub-banded ToAs produced by MEERPIPE were fitted to curated pulsar ephemerides to obtain sub-banded timing residuals. Since these are typically ~ 5 minute long observations,

only the spin-frequency (ν) and DM parameters are fitted for. Only ToAs derived from profiles with S/N $>$ 10 are retained in the analysis. To compute the root mean square (rms) uncertainty of jitter in $T_{\rm sub}(= 8{\rm s})$, we first frequency average the sub-banded timing residuals and compute the quadrature difference of the rms of the frequency-averaged residuals and the rms expected from ideal simulated data sets as expressed in equation,

$$\sigma_J^2\left(T_{\rm sub}\right) = \sigma_{\rm obs}^2\left(T_{\rm sub}\right) - \sigma_{\rm sim}^2\left(T_{\rm sub}\right). \tag{5.3}$$

The uncertainties from the observed, frequency-averaged ToAs are induced to an idealised ToA data set to generate the simulate data. For the analysis presented here, we simulate $\sim$ 1000 realisations of the data for each pulsar (for every epoch) in order to obtain the variance of $\sigma_{\rm sim}^2\left(T_{\rm sub}\right)$. We assume that all excess noise observed in the arrival time measurements are caused due to jitter since other effects that lead to such short-timescale perturbations vary more strongly with observing frequency and cause perturbations in the ToAs on longer ($\sim$ hours) timescales than what is reported here (Shannon & Cordes 2012). Distortions in the pulse profile caused due to imperfect polarization calibration typically tend to vary with the parallactic angle of the receiver and are caused on much longer timescales than a few minutes. The methodology presented here is similar to that discussed in Shannon et al. (2014b), except that we use simulated ToAs rather than simulated profiles. Since jitter is expected to scale proportionally to $1/\sqrt{N_{\rm p}}$, where $N_{\rm p}$ is the number of pulses, we can estimate the implied jitter in one hour to be,

$$\sigma_J\left(1{\rm hour}\right) = \sigma_J\left(T_{\rm sub}\right)/\sqrt{3600/\left(T_{\rm sub}\right)}. \tag{5.4}$$

We also use the Bayesian pulsar timing package, TEMPONEST (Lentati et al. 2014) as a consistency check for our jitter measurements. To estimate jitter using TEMPONEST, we determine the standard white noise parameter, EQUAD, used commonly in pulsar timing analyses. EQUAD represents a source of time-independent noise which could arise from stochastic shape variations in the integrated pulse profile.

We claim to detect jitter in a pulsar if $\sigma_{\rm obs}^2\left(T_{\rm sub}\right)$ is greater than 95% of the simulated $\sigma_{\rm sim}^2\left(T_{\rm sub}\right)$ values, which suggests that the rms of the frequency-averaged residuals is higher due to excess scatter in the observed ToAs than that caused due to radiometer noise.

5.4.2 Jitter measurements from frequency-averaged ToAs

Table 5.1 reports the jitter measurements for 25 MSPs in our sample using frequency averaged ToAs. We detect jitter in a total of 13 pulsars, five of which are new. In the

remaining 12 pulsars, we placed upper limits on the jitter, out of which eight were new. Pulsars with either new jitter measurements or upper limits are highlighted in the table. PSR J2241–5236 has the lowest level of jitter hitherto reported. Our measurements are consistent within uncertainties with previously published values which are also reported in the table.

In Figure 5.1, we show a representative sample of frequency averaged timing residuals of eight pulsars with different levels of jitter. For ease of comparison, the timing residuals are all on the same y-scale.

5.4.3 Frequency dependence of jitter

Utilizing the wide fractional bandwidth of MeerKAT, we study the frequency dependence of jitter in our sample of MSPs. Based on the S/N of the observation, we frequency-average across the observing bandwidth, and generate ToAs per sub-band to compute σ_J as a function of frequency channel. Except in PSR J0437–4715, we do not detect significant frequency dependence of jitter. Higher S/N observations of these pulsars, especially during scintillation maxima might enable such studies.

In PSR J0437–4715, we find that jitter decreases with increasing observing frequency. At the lower part of the band at $\sim$ 910 MHz, we measure σ_J to be 63$\pm$25 ns, at $\sim$ 1300 MHz, we measure σ_J to be 50$\pm$15 ns, while at $\sim$ 1660 MHz, we measure σ_J to be only 24$\pm$20 ns. This is consistent with Shannon et al. (2014b), who reported jitter to be modestly greater at lower frequencies. However, it is important to note that PSR J0437–4715 shows significant frequency-dependent profile evolution. In our measurements discussed so far, we use a frequency-averaged template which models the data well at $\sim$ 1300 MHz and thus the uncertainties on the jitter measurements at lower and higher bands are biased due to template fitting errors. To account for these limitations, we generated a wideband template that models the frequency evolution of the profile and present the results below.

Using PulsePortraiture and the methodology described in Pennucci (2019), we created a frequency-dependent smoothed template for PSR J0437–4715. Figure 5.2 shows the total intensity profiles of the wideband template at various observing frequencies. Using the wideband template, we computed wideband ToAs with uncertainties that account for the frequency-dependent profile evolution. Figure 5.3 shows the frequency dependence of jitter using frequency-averaged and wideband templates. From the wideband ToAs, at $\sim$ 910 MHz, we measure σ_J to be 64$\pm$20 ns, at $\sim$ 1300 MHz, we measure σ_J to be 50$\pm$13 ns, while at $\sim$ 1660 MHz, we measure σ_J to be 42$\pm$12 ns. The deviations in the

Table 5.1 Jitter measurements and upper limits for 25 MSPs in our sample. For each pulsar, the parameters reported here are corresponding to the brightest observation, i.e, with the highest average S/N per pulse. For reference, the median S/N per pulse computed from all observations per pulsar is also reported. Columns four to six report the integration time, the mean ToA error and the weighted RMS values in 8 s sub-integrations. The last two columns report the implied jitter in one hour and a reference to a previously published jitter measurement where available. S+2014 indicates Shannon et al. (2014b) and L+2019 indicates Lam et al. (2019)

PSR	Max S/N_{pulse}	Median S/N_{pulse}	T_{obs} (s)	σ_{ToA} (μs)	WRMS (μs)	Implied σ_j(hr) (ns)	Previous σ_j(hr) (ns)
J0125–2327	3.6	3.6	256	0.183	1.108	48±13	-
J0437–4715	139	112	180	0.019	0.868	50±10	48.0±0.6 (S+2014)
J07110–6830	1.6	1.6	256	0.619	1.323	<70	< 90 (S+2014)
J0900–3144	2.9	2.5	256	0.554	3.687	<130	-
J1017–7156	2.4	2.2	256	0.149	0.259	<10	< 100 (S+2014)
J1022+1001	23.3	5.6	256	0.167	2.054	130±20	280±140 (S+2014), 79±2 (L+2019)
J1045–4509	2.9	2.0	256	0.555	3.368	130±75	< 900 (S+2014)
J1157–5112	1.7	1.5	3064	3.675	32.848	<690	-
J1600–3053	1.9	1.4	256	0.118	0.711	<30	< 200 (S+2014)
J1603–7202	8.1	3.8	512	0.297	3.947	180±40	300±56 (S+2014)
J1622–6617	1.6	1.5	256	2.158	26.291	<300	-
J1629–6902	1.5	1.4	256	0.331	1.917	<60	-
J1643–1224	2.4	2.0	256	0.303	1.647	<60	< 500 (S+2014), 31±12 (L+2019)
J1730–2304	3	1.7	256	0.451	1.973	80±45	< 400 (S+2014)
J1744–1134	6.6	2.6	512	0.026	0.686	30±6	37.8±0.8 (+2014), 44±1 (L+2019)
J1756–2251	2.1	1.7	1345	0.926	21.176	<500	-
J1757–5322	1.9	1.4	1242	0.704	4.196	130±45	-
J1802–2124	1.3	1.4	256	0.545	8.485	<80	-
J1909–3744	9.6	3.2	256	0.021	0.199	9±3	8.6±0.8 (S+2014), 14±0.5 (L+2019)
J1918–0642	2.1	2.1	512	0.681	1.645	<55	-
J2010–1323	1.5	1.5	256	0.224	1.048	<80	59±3 (L+2019)
J2039–3616	1.1	1.1	512	0.166	0.937	<25	-
J2129–5721	3.3	3.3	360	0.285	0.493	<11	< 400 (S+2014)
J2145–0750	11.1	3.6	256	0.331	3.883	200±20	192±6 (S+2014), 173±4 (L+2019)
J2241–5236	10.3	2.3	512	0.011	0.086	3.8±0.8	< 50 (S+2014)

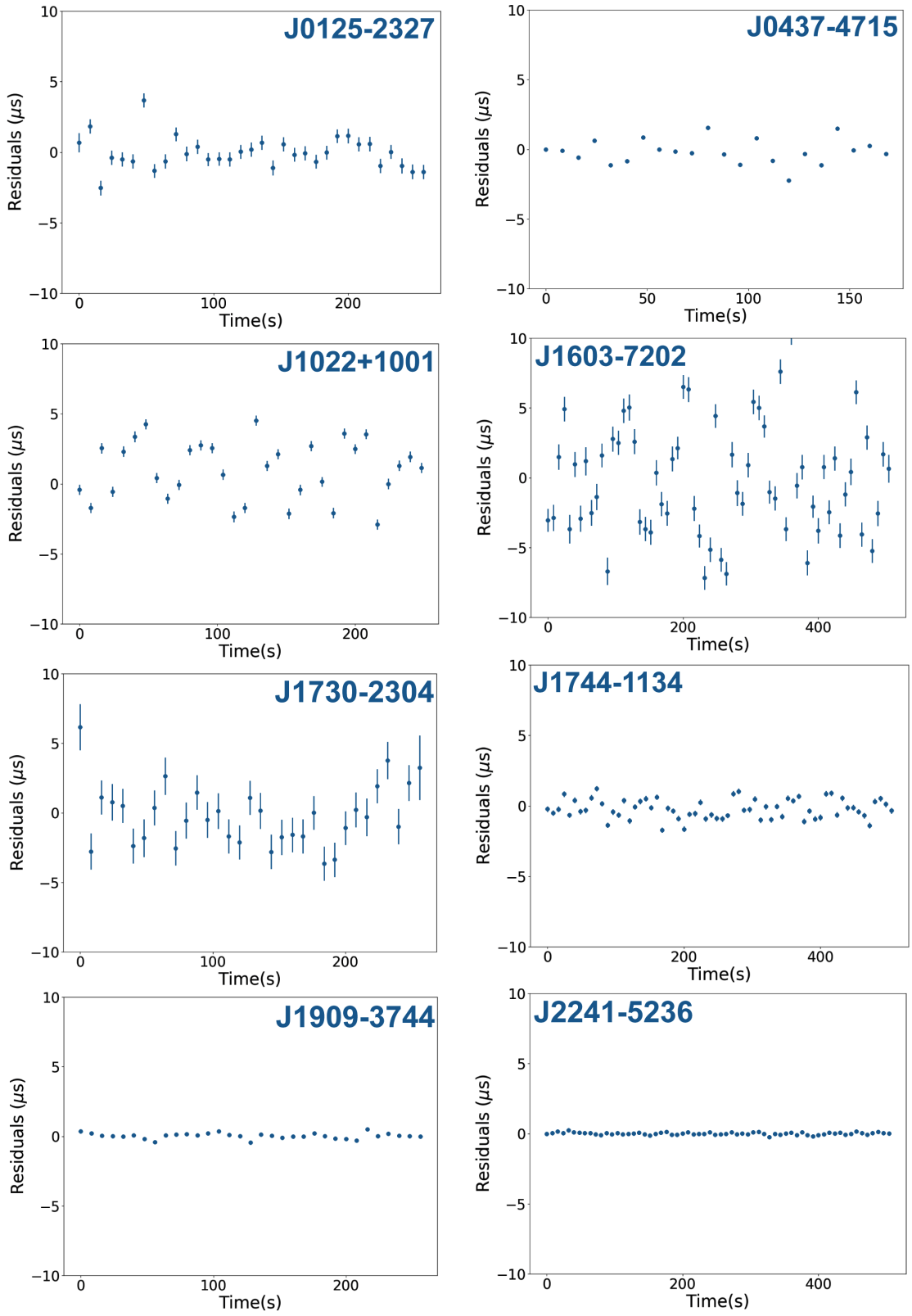

Figure 5.1 Frequency averaged timing residuals for eight pulsars in our sample showing varying levels of jitter. All y-axes are plotted on the same scale for ease of comparison.

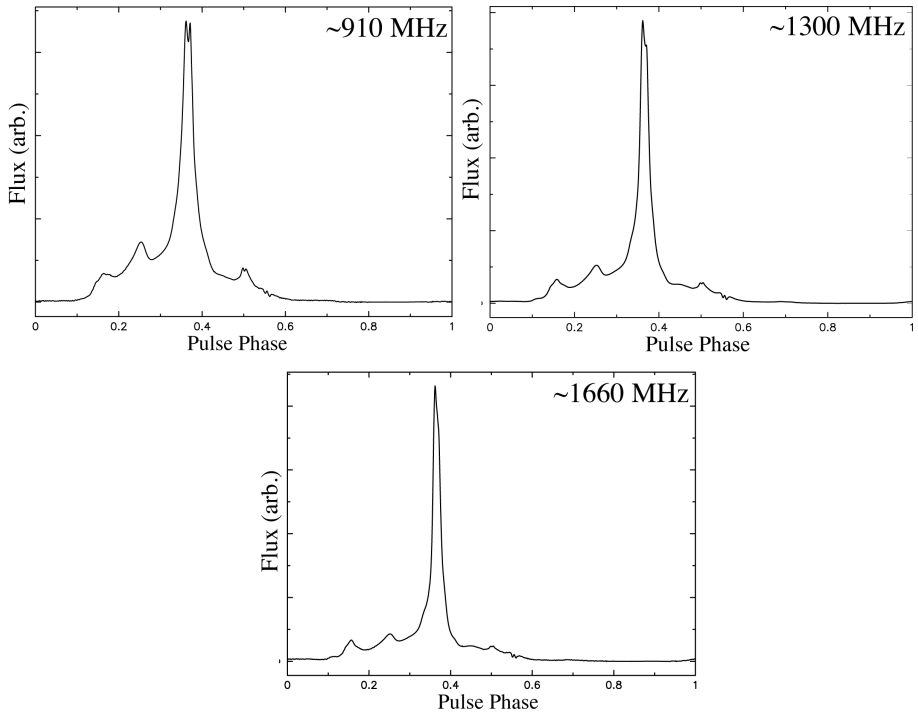

Figure 5.2 Frequency-dependent templates for PSR J0437–4715 plotted at lower, middle and higher observing frequency bands. The peak component of the profile changes across the frequency bands with the emission from the wing components growing weaker with increasing frequency.

measurements of $\sigma_{\rm J}$ using frequency-averaged and wideband ToAs are consistent within uncertainties. The varying levels of jitter in higher and lower frequency bands in PSR J0437–4715 is most likely to be due to the narrowing of the pulse profile at higher frequencies.

Owing to our ability to measure jitter in individual sub-bands and also to the high flux density of the pulsar, we can estimate the degree of correlation of jitter between the bands. In Figure 5.4, we show the correlation of wideband ToAs between different frequency bands. We see a high degree of correlation ($\sim$0.9) between adjacent frequency bands, while the degree of correlation significantly reduces ($\sim$ 0.4) between the lowest and highest frequency bands.

Assuming a reference frequency of $\sim$ 910 MHz, we compute the correlation strength ($r_{\rm j}$) as a function of increasing channel separation as shown in Figure 5.5. It is clear that with increasing channel separation the ToAs begin to decorrelate, implying that jitter is not broadband across the full the observing bandwidth of MeerKAT.

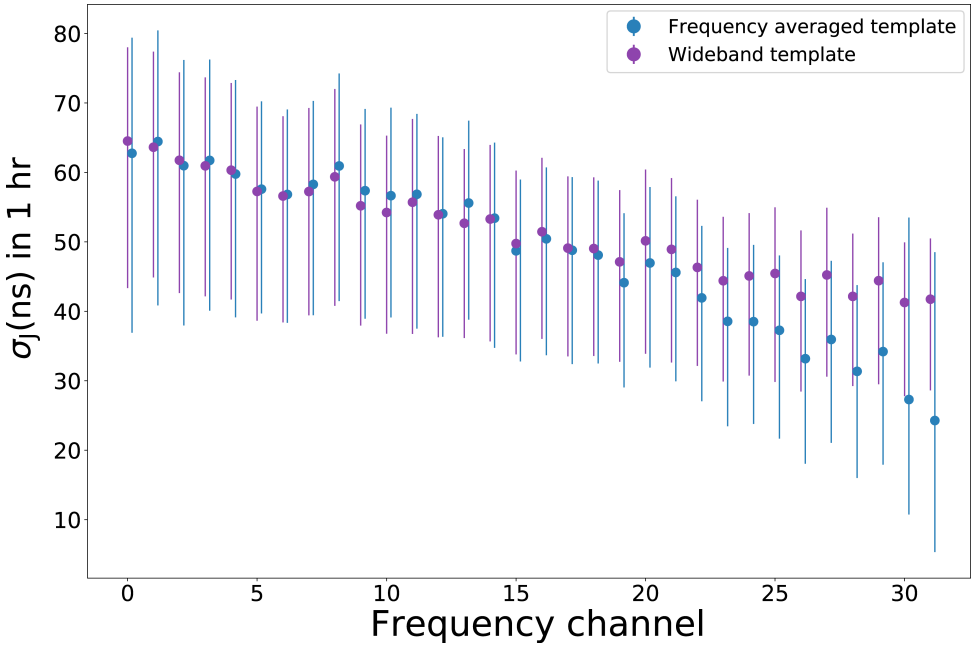

Figure 5.3 Jitter as a function of observing frequency for PSR J0437–4715 using ToAs generated from frequency-averaged (blue) and wideband templates (purple). The frequency-averaged points are offset by 0.25 channels for clarity. The observing bandwidth is averaged to 32 frequency channels. There is a moderate dependence of jitter on observing frequency.

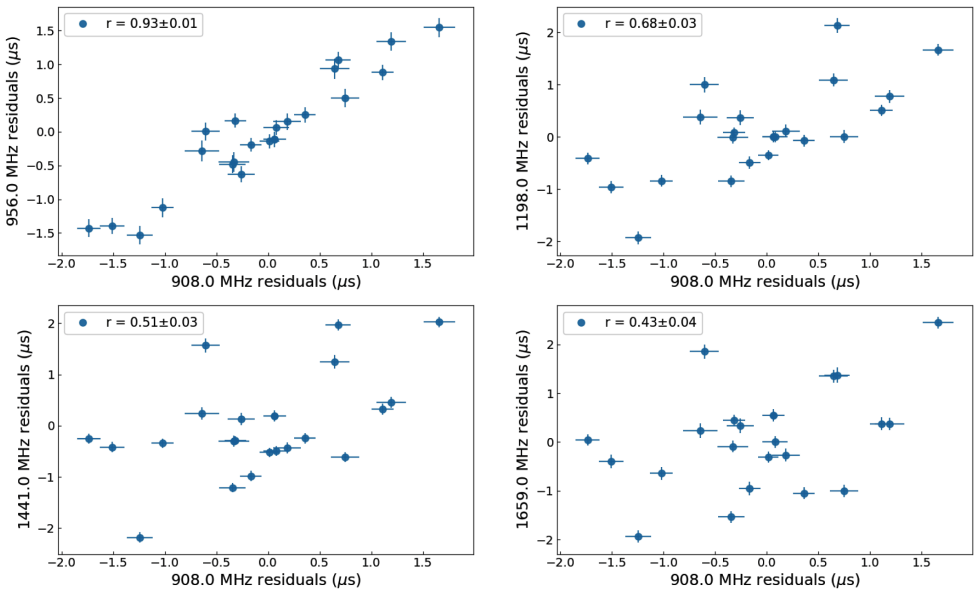

Figure 5.4 The four panels show the correlation of wideband ToAs between different frequency channels for PSR J0437–4715. The first panel (top left) represents this correlation between adjacent frequency bands while the fourth panel (bottom right) represents the same but between the lowest and highest frequency bands of MeerKAT (a bandwidth of 777.75 MHz). Each ToA is computed from an 8 s integrated profile.

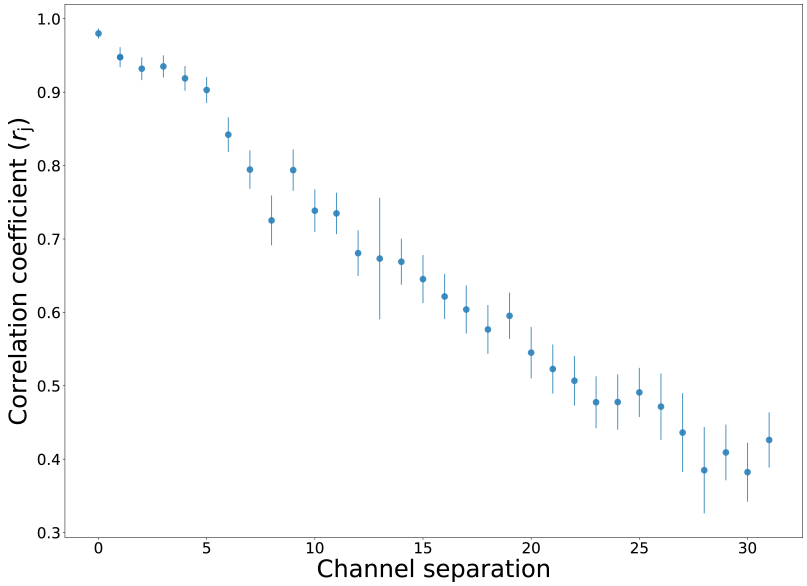

Figure 5.5 ToA correlation as a function of frequency channel separation for PSR J0437–4715 showing the increasing decorrelation of jitter with increasing channel separation. The lowest frequency channel at a frequency of $\sim$ 910 MHz is considered as the reference frequency. The total observing bandwidth of MeerKAT is represented across 32 frequency channels.

5.5 Limits on DM measurements in PSR J0437–4715

The decorrelation of jitter in PSR J0437–4715, implies that at the lower and the higher frequency bands, the emission statistics are increasingly independent of each other. In Figure 5.6, we show the post-fit timing residuals from each frequency channel plotted serially in time across a 256 s observation. Each cluster of ToAs is 8 s long, with the red points representing the lower frequency bands and the blue points representing the higher frequency bands. A striking feature is the varying frequency dependence of the arrival times on a timescale of $\sim$ 8 seconds. This would naively be interpreted as a change in DM.

It must be noted that if wideband templates are not used to compute the ToAs, then a temporally constant frequency-dependent term is dominant in the timing residuals due to profile evolution.

A direct implication of the time-varying frequency dependence is that the measured values of DM on short timescales ($\sim$ 8 s) varies. Considering each 8 s subintegration to be an independent observation and measuring their DMs, we see that the values have a median of 2.6419 pc cm^{-3} with a standard deviation of 2.7×10^{-4} cm^{-3} pc as shown in Figure 5.7.

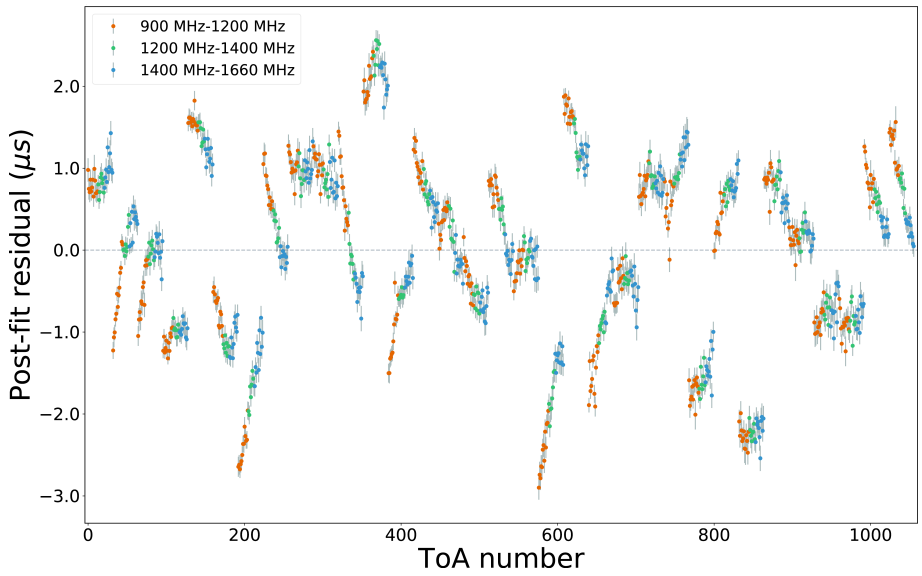

Figure 5.6 Post-fit wideband timing residuals of PSR J0437–4715 estimated using 8 s integrated profiles containing 32 frequency channels over a 256 s observation. Each set of ToAs are colored based on the frequency channel as indicated in the plot. The timing residuals are plotted serially (as ToA numbers) to showcase the varying frequency dependence for each ToA set.

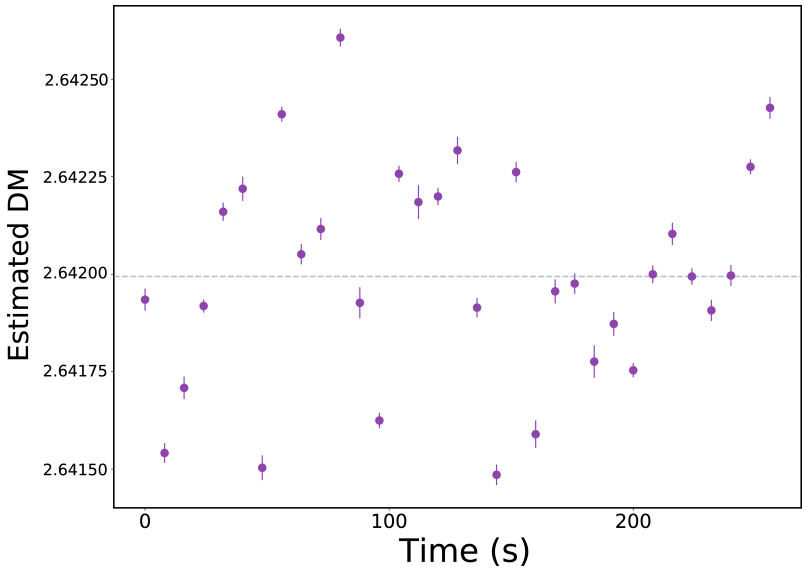

Figure 5.7 Estimated values of DM for every 8 s subintegration of PSR J0437–4715 from fits to the timing residuals shown in Figure 5.6. The horizontal dashed line represents the median estimated DM value of 2.6419 pc cm^{-3}. It is evident that the estimated DM value clearly changes on very short timescales and that the scatter far exceeds the formal errors.

These time-dependent 'dispersion-measures' suggest that the delay as a function of observing frequency deviates from the $1/\nu^2$ relation significantly and so we might expect that the single pulses might deviate even more strongly. We investigate this effect by analysing the single pulses of this pulsar. While a more detailed statistical analysis is presented in Section 5.6, here we present DM measurements for single pulses. For each pulse with full frequency resolution, we compute arrival times and estimate the DM. Figure 5.8 shows the distribution of the estimated DMs measured from single pulses with a median value of 2.643 cm^{-3} and a standard deviation of 8.5×10^{-3} cm^{-3} pc which is larger than that estimated from the folded archives, as expected. The timing residuals are generated by using a smoothed version of the pulse as a template to avoid correlating the noise in the profile. A $1/\nu^2$ relation does not fit the timing residuals well indicating that these frequency-dependent variations are not due to the IISM and are intrinsic to the pulsar emission. These variations introduce a fundamental limit on our ability to measure the DM of the pulsar .

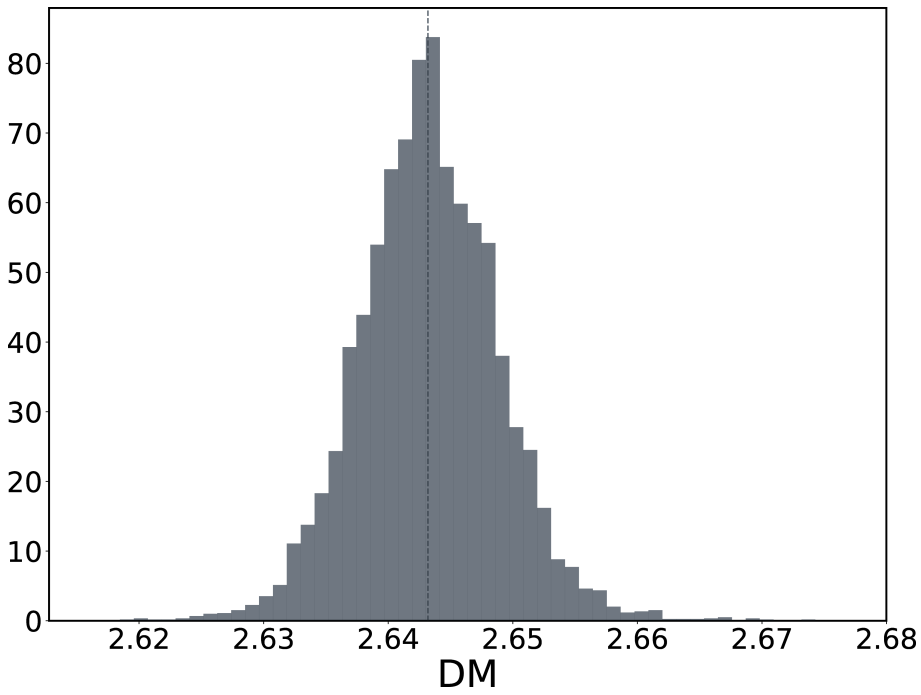

Figure 5.8 Distributions of measured DM values from $\sim$ 47000 single pulses of PSR J0437–4715.

5.6 Single pulse phenomenology

The phenomenon of jitter can be better understood by examining whether timing variations are due to the shape variations of single pulses. Single pulses from MSPs have been studied in relatively few cases compared to more slower, normal pulsars, owing to their low S/N per pulse. In this section, we discuss various statistical properties of single pulses from MSPs in our sample.

Out of the 25 pulsars listed in Table 5.1, we present a statistical analysis of single pulses for eight pulsars with detected jitter measurements. Some pulsars with inferred jitter measurements (from Section 5.4) did not have associated search mode observations to enable single pulse analysis and others with upper limits on jitter had very low S/N single pulses.

For each pulsar, a set of statistical properties were determined to study and compare their emission properties. These are described below:

- **Characterising variations in single pulse morphology:** Examining the brightest pulses and their phase-resolved modulation can provide insights into the state of plasma and generation of radio emission. We examine a number of statistical properties to characterise single pulse amplitude and shape variability. We use principal component analysis (PCA) to study shape variations in the brightest single pulses. PCA provides a rigorous statistical method to analyse temporally correlated variations in total intensity profiles. To implement this we form an $N_{bin} \times N_{bin}$ covariance matrix from the profile residuals of single pulses described as,

$$\mathbf{C} \equiv \langle P \otimes P \rangle - T \otimes T, \tag{5.5}$$

  where P is the total intensity vector of a single pulse profile weighted by its S/N, T is the mean of all single pulses and $\otimes$ denotes the outer product. For the covariance matrix to have full rank, the number of integrated pulses should at least be equal to or higher than the dimensions of the covariance matrix which is given by the number of phase bins (N_{bin}) in the profile. The total number of phase bins for most pulsars is 256 except for PSRs J1603–7202 and J2241–5236, which have 512 and 128 phase bins respectively. To characterise shape variations, we determine the eigenvectors and eigenvalues of the covariance matrix. The principal axes that describe the N_{bin} dimensional vector space are defined by the eigenvectors. The most significant eigenvectors, identified by the highest eigenvalue define the axis along which the profile variations are the largest. Significant eigenvectors deviate

strongly from a Gaussian distribution and hence we use a normality test to identify them. If the number of significant eigenvectors is less than the number of input profiles, it implies that the observed shape variations are caused due to a fewer number of underlying components. Osłowski et al. (2011) and Shannon & Cordes (2012) used a similar technique to identify shape variations in PSR J0437–4715 and J1713+0747 respectively.

We further characterise single pulse variability by computing the phase-resolved modulation index as,

$$m_I(\phi) = \frac{\sqrt{\sigma_I^2(\phi) - \sigma_{\rm off}^2}}{I(\phi)}, \tag{5.6}$$

where $\sigma_I(\phi)$ and $I(\phi)$ are the rms and the mean intensity computed at phase ϕ and $\sigma_{\rm off}$ is the rms intensity computed from an off-pulse window. We investigate temporal correlations in single pulse emission by computing the auto-correlation function (ACF) of the peak intensity of consecutive single pulses. The implications of these measurements for each pulsar are discussed on a pulsar-by-pulsar basis.

- **Single pulse energy distributions** provide a measurement of energy contained in a pulse or sub-component(s) of a pulse and the type of distribution allows us to probe the pulse emission mechanism. We measure the integrated S/N by defining windows around the main component and various sub-components of the main pulse and interpulse depending on the profile morphology. In cases where multiple sub-components were present, the size of the windows were chosen to be similar (wherever reasonable) to enable a more direct statistical comparison. The instantaneous S/N over a selected window is computed as,

$$S/N = \frac{\sum_{i=1}^{N_{\rm window}} (A_i - B)}{\sqrt{N_{\rm window}}\,\sigma_{\rm off}}, \tag{5.7}$$

where A_i is the pulse flux density at the i-th bin, B is the mean off-pulse flux density, $N_{\rm window}$ is the number of phase bins in the selected component window and $\sigma_{\rm off}$ is the off-pulse rms flux density. RFI excision on single pulses is implemented using standard PSRCHIVE tools and COASTGUARD, whenever necessary. Residual RFI was manually inspected and removed from the analysis. A least-squares minimisation of the data fit by a model for the pulse energy distribution was performed using log-normal and Gaussian distributions. The log-normal model was defined as,

$$P(E) = \frac{1}{E\sigma_\ell\sqrt{2\pi}} \exp\left[\frac{-\left(\log_{10}(E) - \mu_\ell\right)}{2\sigma_\ell^2}\right], \tag{5.8}$$

where μ_ℓ and σ_ℓ parameterise the distribution. For the Gaussian model, we fit for the mean (μ_g) and standard deviation (σ_g) of the pulse energy distribution. A χ^2 statistic was used for quantifying the goodness of fit of the preferred distribution.

- **Timing properties of single pulses** are analysed by computing frequency-averaged single pulse ToAs and investigating correlations between single pulse properties and corresponding ToAs. We also measure jitter as a function of the number of pulses integrated (N_p) and show that the arrival time uncertainties obtained from averaged profiles due to template fitting are consistent with the measured pulse-to-pulse variations and that jitter typically scales as $1/\sqrt{N_\mathrm{p}}$.

5.6.1 PSR J0437–4715

We present a statistical analysis of single pulses from PSR J0437–4715 and show that they are consistent with previously published analyses (Jenet et al. 2001a, Osłowski et al. 2014, and Shannon et al. 2014b). The single pulses of PSR J0437–4715 have been studied extensively and owing to its high flux density, pulse shape variations cause excess timing uncertainty, at least four times greater than that predicted from radiometer noise alone (Osłowski et al. 2014). This variability in both phase and total intensity can be clearly seen in the left panel of Figure 5.9, which shows $\sim$ 100 consecutive frequency-averaged single pulses. We confine the pulse phase to show only the selected on-pulse window, which spans more than $\sim$ 85% of the total pulse phase. In the right panel of Figure 5.9, the brightest thirty single pulses normalised to their peak intensities are shown. This provides a representative sample of the varying pulse shape morphology amongst the brightest pulses.

To characterise the brightest single pulses quantitatively, we compute a covariance matrix from the brightest 1000 pulses following equation 5.5. We then solve the eigenproblem of the covariance matrix to determine the significant eigenvectors and eigenvalues. Figure 5.10 shows N_bin eigenvalues and the three most significant eigenvectors corresponding to the highest eigenvalues. We identify significant eigenvectors by testing the null hypothesis that an eigenvector comes from a normal distribution, since the eigenvectors corresponding to low eigenvalues resemble white noise. We detect 47 significant eigenvectors that characterise the brightest pulses of PSR J0437–4715. Although every single pulse appears to have a different pulse shape morphology, they can be characterised effectively by a

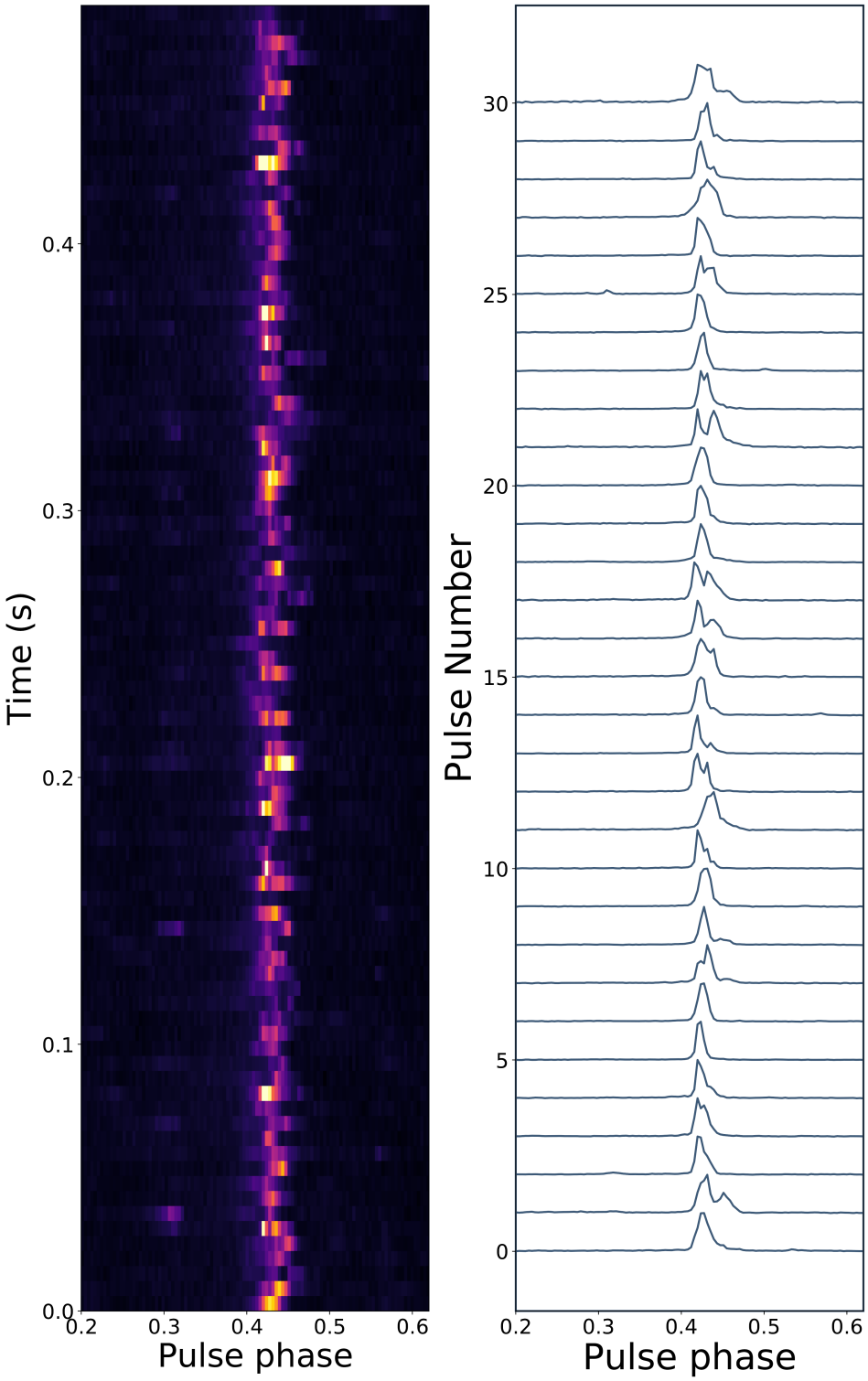

Figure 5.9 Consecutive single pulses of PSR J0437-4715 (left) and the brightest 30 pulses (right) normalised to their peak intensities are shown across the on-pulse region of pulse phase.

linear combination of the significant basis eigenvectors.

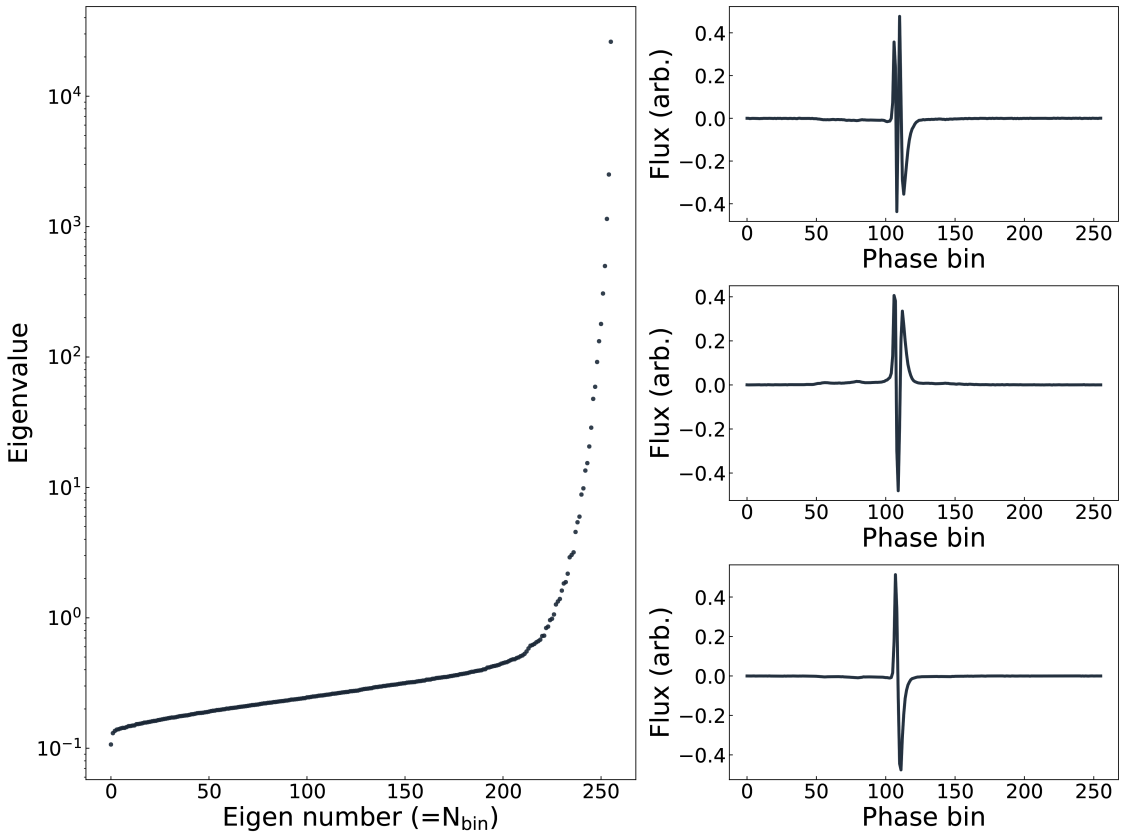

Figure 5.10 Eigenvalues computed from the profile residual covariance matrix for PSR J0437–4715 are shown in the left panel. The number of eigenvalues is the same as the number of phase bins used. The three most significant eigenvectors are plotted in the vertical panels on the right.

We analysed $\sim$ 47000 pulses and detected every single pulse (the lowest S/N was $\sim$ 20), indicating that the pulse emission in this pulsar shows no evidence for nulling. The phase-resolved modulation index across the selected on-pulse window is shown in the top panel of Figure 5.11. In the bottom three panels (from top), we show the integrated pulse profile formed from averaging the single pulses, the integrated profile formed from averaging the brightest 100 pulse profiles and the profile residual after subtracting the profiles in the second and third panels. We computed the auto-correlation function from the peak flux intensities of single pulses and find no evidence of temporal correlations amongst the pulses.

The modulation index is highest towards the leading edge of the main component,

consistent with previous results (Osłowski et al. 2014[8]). The brightest pulses coincide in phase with the leading edge of the integrated profile as indicated by the vertical dotted line across the four panels. The brightest pulses are narrower than the rest and do not exhibit strong emission in the wings of the profile.

The profile of PSR J0437–4715 has multiple components that span the majority of the pulse phase. The S/N distribution was analysed by selecting different windows spanning the pulse profile as shown in Figure 5.12. The profile formed by averaging the brightest 100 pulses is shown in the subplot along with the integrated profile. The S/N histograms for the C1, C2 and the full profile windows show log-normal distributions, consistent with previously published studies (Shannon et al. 2014b).

We estimated the level of jitter noise by integrating increasing number of pulses from 10 to $\sim$ 10000 and find that jitter scales proportionally with $1/\sqrt{N_p}$ as shown in Figure 5.13. This relation is consistent within uncertainties over multiple epochs.

5.6.2 PSR J0125–2327

PSR J0125–2327 is a binary pulsar with a spin-period of $\sim$ 3.6 ms, discovered in the GBNCC survey. With MeerKAT, the observed median S/N per pulse was $\sim$ 4 with estimated σ_J to be 48$\pm$13 ns in an hour. Statistical properties of single pulses from PSR J0125–2327 have not been previously reported. In Figure 5.14, $\sim$ 140 consecutive single pulses are shown with varying phase and amplitudes. A total of $\sim$ 15000 pulses were analysed with a maximum S/N of $\sim$ 15. At 20cm wavelengths, the pulse profile has multiple components with a main strong component towards the leading edge of the profile and multiple weaker components towards the trailing edge.

The phase-resolved modulation index over the on-pulse window is shown in the upper panel of Figure 5.15. In the middle and lower panels, we show the integrated pulse profiles formed from averaging the single pulses and the mean profile formed from integrating the brightest 1000 pulses. The modulation index is strongest towards the leading part of the on-pulse profile. The brightest pulses are narrower and have weaker emission near the second component and align with the centre of the peak component of the integrated profile. This suggests that the brightest pulses will have similar arrival times as the rest of the pulses. In Figure 5.16, single pulse ToAs are plotted against their corresponding S/N and we see no correlation between the two quantities. The ToAs of the brightest pulses (S/N $>$ 8) have a Gaussian distribution and have similar arrival times as the rest

[8]The off-pulse variance was not subtracted to unbias the measured modulation index in Osłowski et al. (2014)

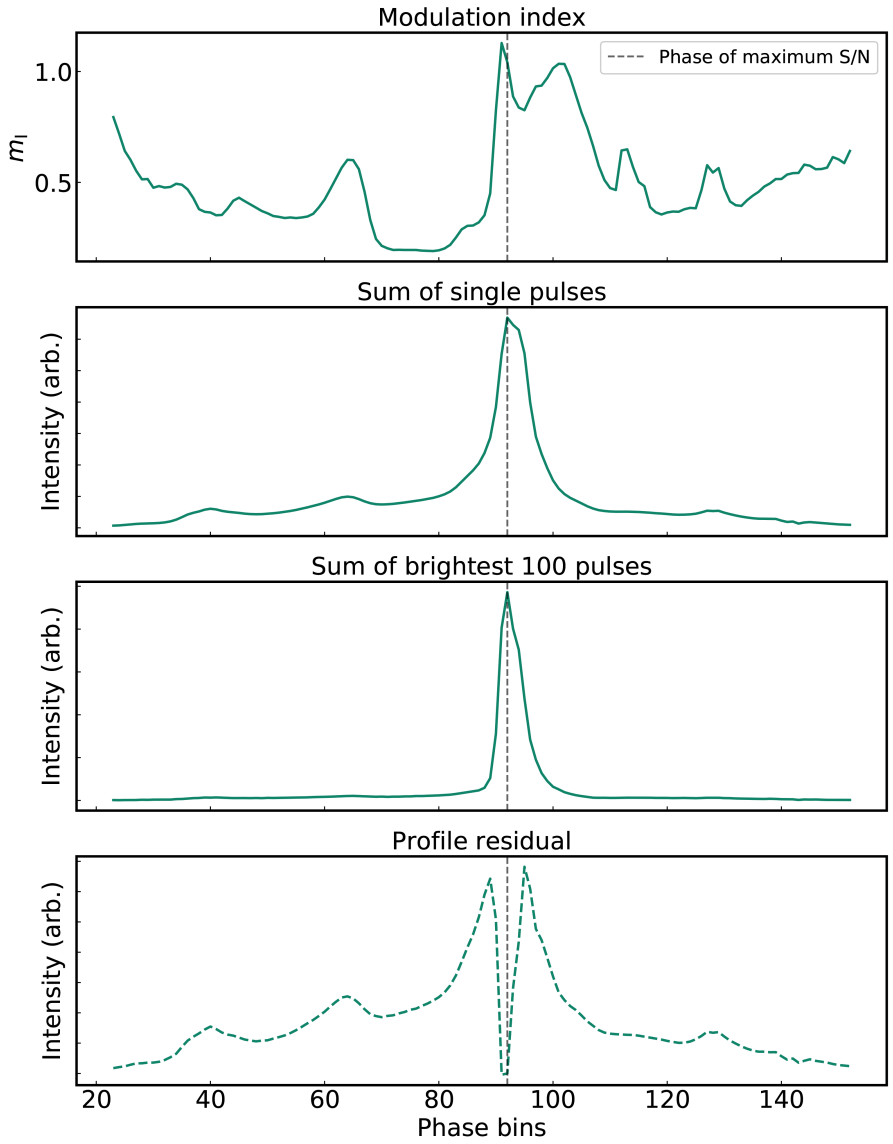

Figure 5.11 Phase-resolved modulation index for PSR J0437–4715 (top panel) shown across the on-pulse region. The second panel shows the integrated profile from $\sim$ 47000 single pulses. The third panel shows the integrated profile from the brightest 100 pulses and the last panel shows the profile residual after subtracting the profiles in the second and third panel. The vertical grey dashed line represents the phase of maximum S/N for the profile shown in the third panel.

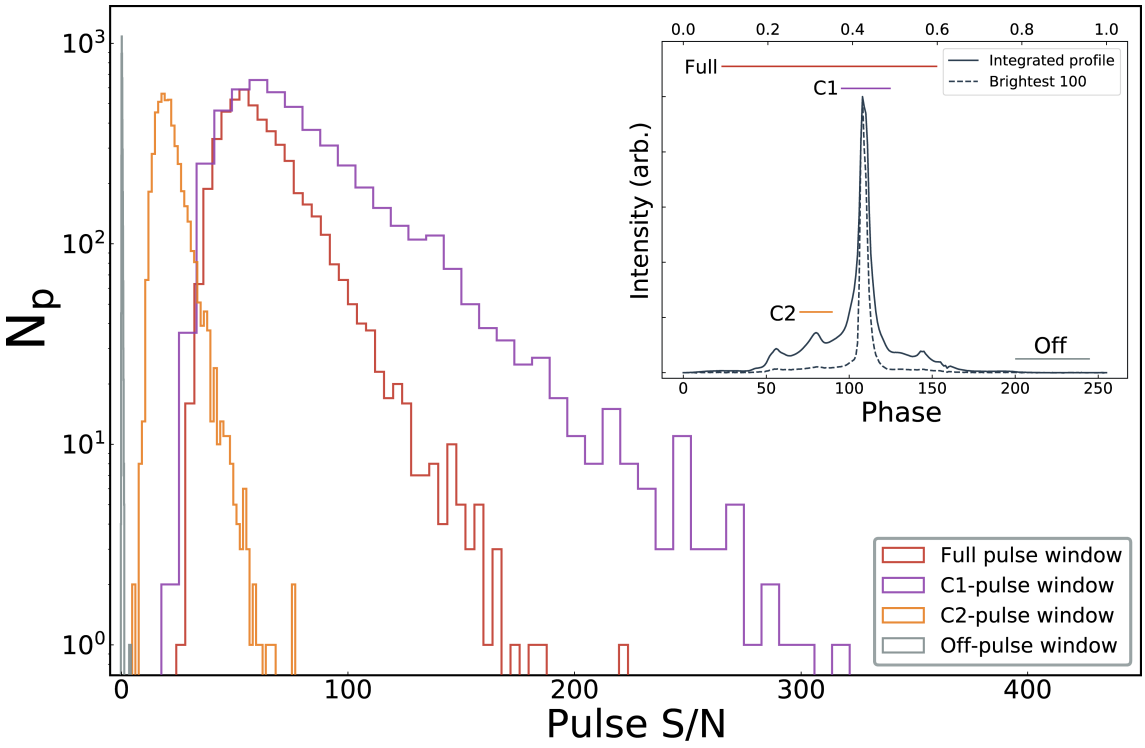

Figure 5.12 Single pulse S/N histograms for PSR J0437–4715. The various histograms shown correspond to selected windows across the pulse profile. The windows used are shown in the sub-plot containing the integrated profile (solid line) and the mean profile derived from averaging the brightest 100 single pulses (dashed line). The sub-plot represents the profiles with the number of phase bins (bottom axis) and the phase in turns (top axis). The S/N per profile across a selected window is computed using Equation 5.7.

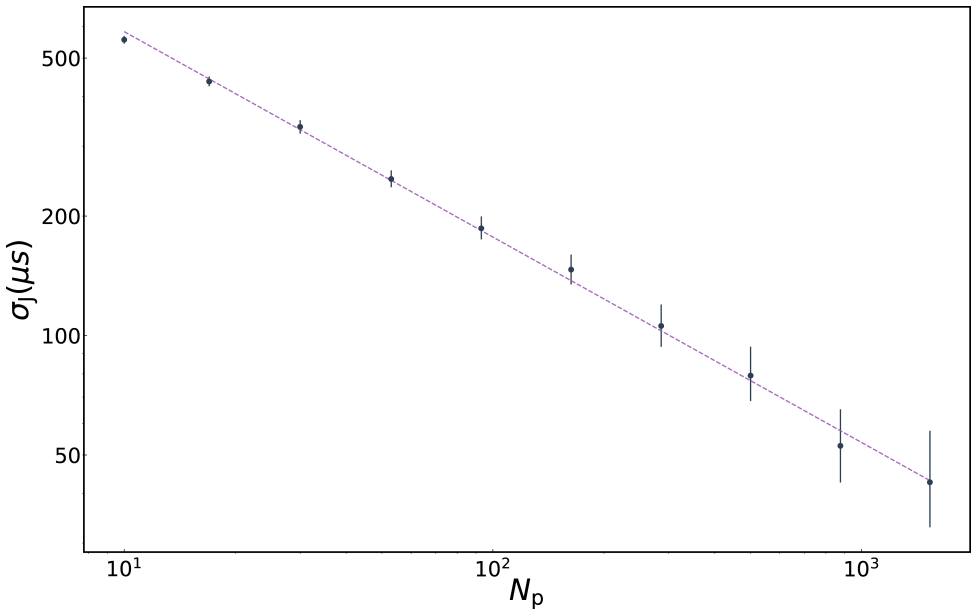

Figure 5.13 Estimated jitter levels ($\sigma_J(N_p)$) for PSR J0437–4715 as a funtion of number of pulses. The dashed line is the best fitting model across the measurements for jitter noise scaling as $1/\sqrt{N_p}$.

of the pulses. We find that the profile variability of the brightest pulses is characterised by only ten significant eigenvectors obtained from an eigen decomposition of the profile residual covariance matrix computed following Equation 5.5. We also find no evidence of temporally-correlated emission, estimated from the auto-correlation function of peak flux intensities.

The distribution of S/N computed from single pulses is shown in Figure 5.17 for two selected windows over the full on-pulse region and the peak component (C1). Both these components follow a log-normal distribution and have similar S/N values. A profile formed from the brightest 1000 pulses is shown in the sub-plot, along with the integrated profile from single pulses. While the bright pulses span the entire on-pulse phase region, the brightest pulses arise from the leading component (C1).

We find that the jitter scales as $1/\sqrt{N_p}$ and the measured values are consistent at different epochs. In Figure 5.18, we show estimated values of jitter with increasing number of integrated pulses ($\sigma_J(N_p)$) with the dashed line being the best-fit model.

5.6.3 PSR J1022+1001

PSR J1022+1001 is a relatively bright MSP with a rotation period of $\sim$ 16 ms. Owing to its rotational stability and low mean arrival time errors, it is a part of the Parkes

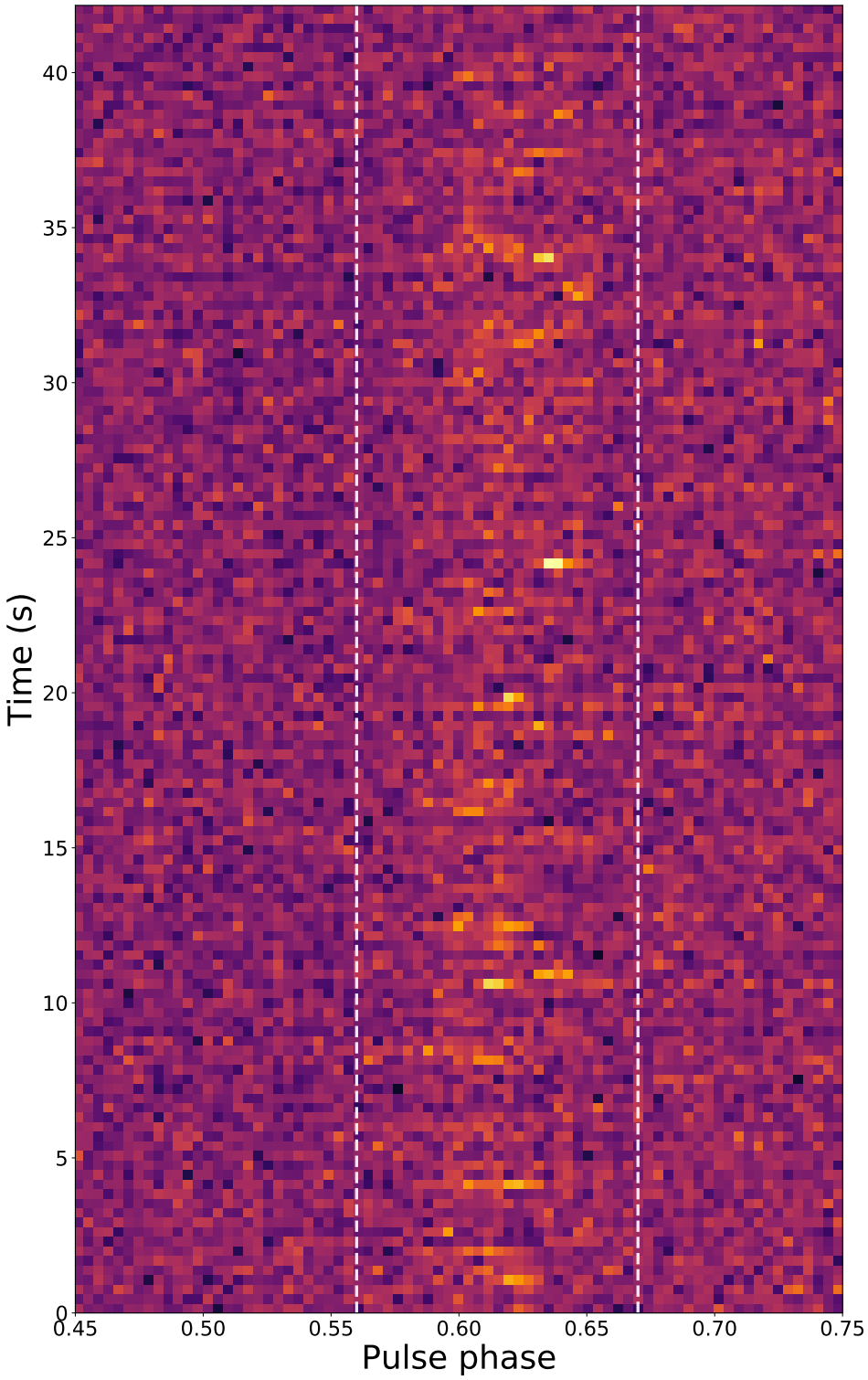

Figure 5.14 Consecutive single pulses of PSR J0125–2327 shown across the on-pulse region of pulse phase. The vertical white dashed lines are plotted around the detected emission region.

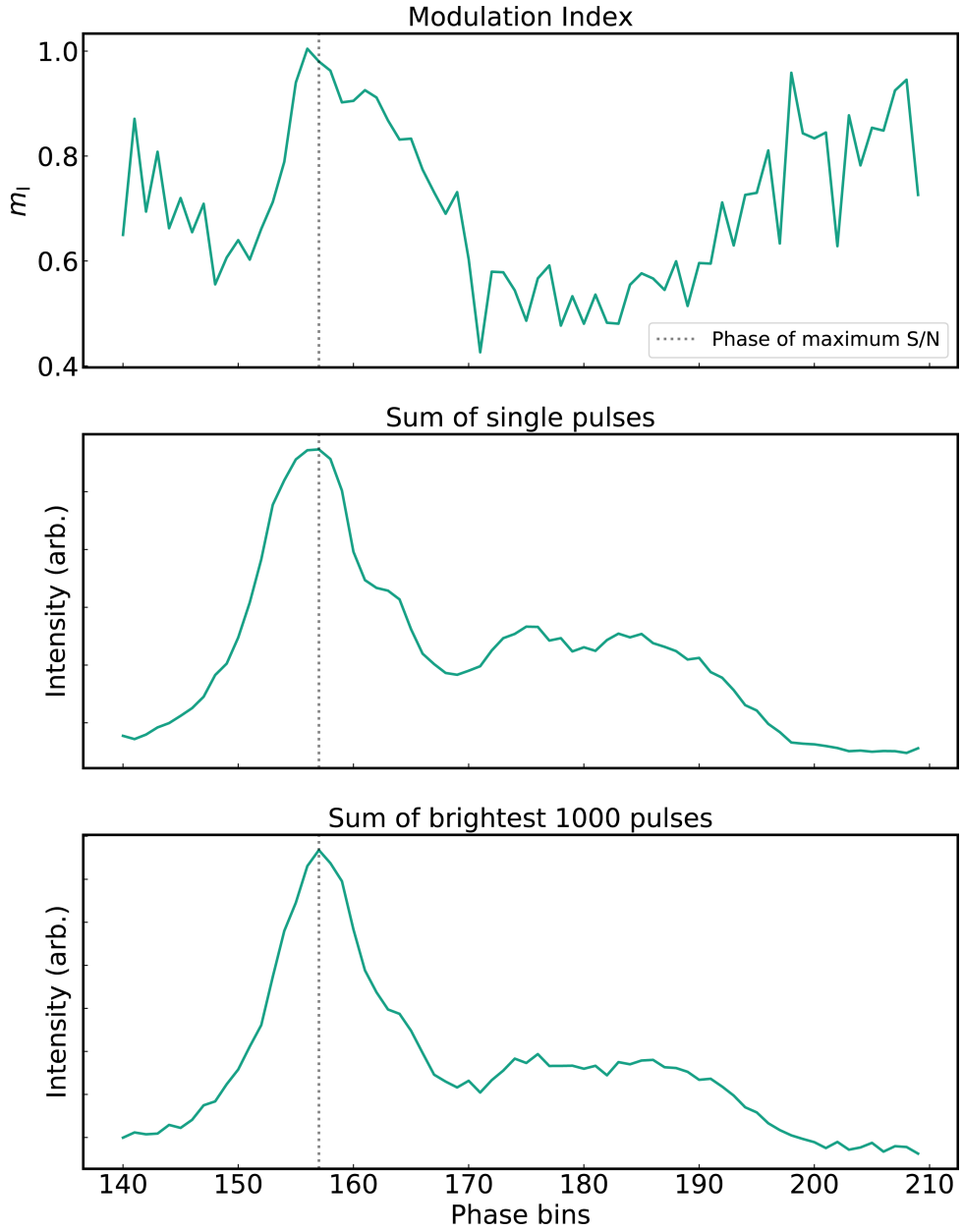

Figure 5.15 Phase-resolved modulation index for PSR J0125–2327 shown across the on-pulse region in the upper panel. The middle panel shows the integrated profile from 15000 single pulses and the lower panel shows the integrated profile from the brightest 1000 pulses. The vertical grey dashed line represents the phase of maximum S/N for the profile shown in the lower panel.

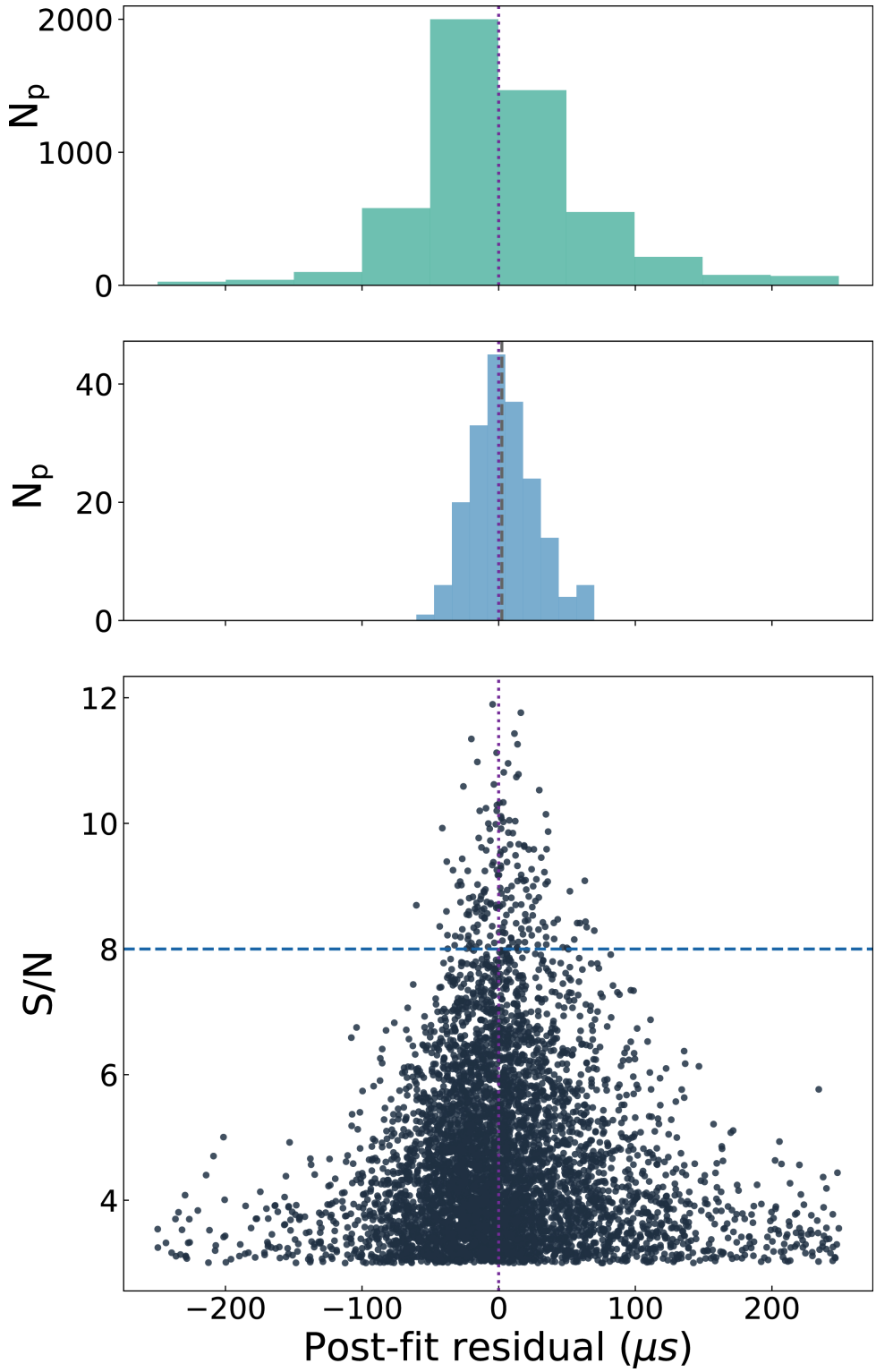

Figure 5.16 ToAs computed from a randomly chosen subset of $\sim$ 10000 single pulses plotted against their corresponding S/N for PSR J0125–2327. The distribution of ToAs for pulses with $3 < \mathrm{S/N} < 8$ are shown in the top panel and for the brightest pulses with $\mathrm{S/N} > 8$ are shown in the middle panel. The ToAs of the brightest pulses do not show a systematic shift in the arrival times as compared to the rest of the pulses.

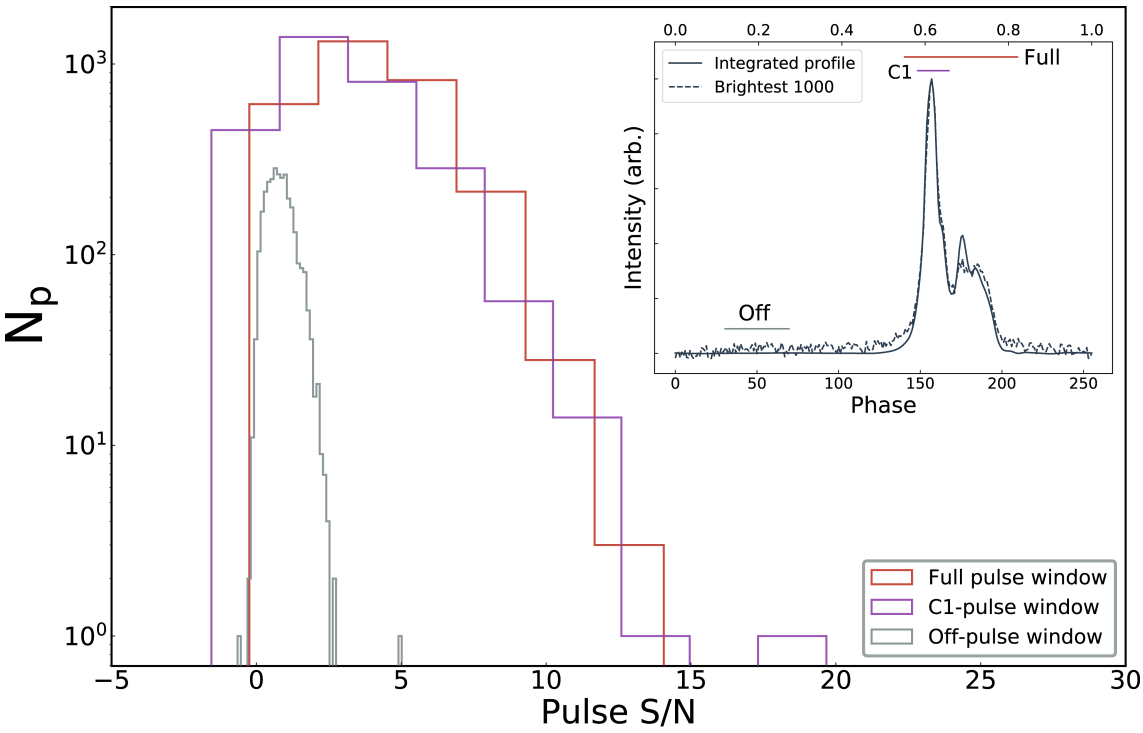

Figure 5.17 Single pulse S/N histograms for PSR J0125–2327. See Figure 5.12 caption for further details.

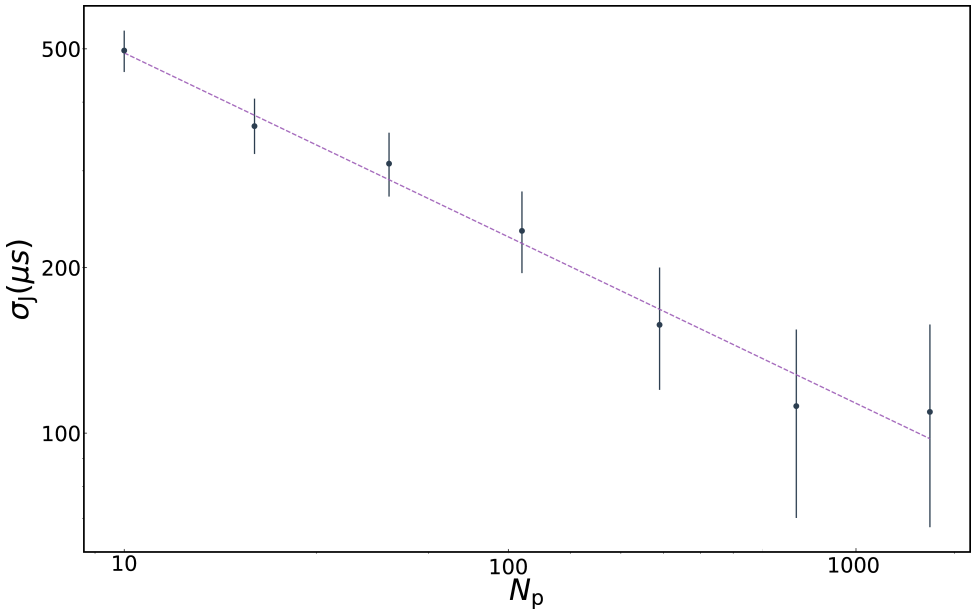

Figure 5.18 Estimated jitter levels ($\sigma_J(N_p)$) for PSR J0125–2327 as a funtion of number of pulses. The dashed line is the best fitting model across the measurements for jitter noise scaling as $1/\sqrt{N_p}$.

Pulsar Timing Array program (PPTA) (Manchester 2017). It has a white dwarf binary companion with an orbital period of 7.8 days and has been used for tests of gravity (Freire et al. 2012). Previous measurements of pulse shape variations have shown that there is excess scatter in the ToAs, larger than that expected from only radiometer noise.

The pulse profile at 20cm wavelengths has a double peaked structure and shows a strong dependence on the observing frequency. In Figure 5.19, we show $\sim$ 50 consecutive pulses (left panel) that exhibit strong variations in phase and amplitude and the 30 brightest pulses from across the entire observation (right panel). We analysed $\sim$ 20000 pulses with a maximum S/N of $\sim$ 30. The profile variations of the brightest pulses are characterised by only ten significant eigenvectors obtained from a PCA analysis of the profile residual covariance matrix.

In the upper panel of Figure 5.20, we show the phase-resolved modulation index computed across the on-pulse region. The middle and lower panels of the same figure show the integrated profile formed from averaging the single pulses and the mean profile from the brightest 100 pulses. The modulation index grows increasingly stronger across the pulse profile and becomes strongest towards the trailing edge of the second peak component. The modulation index of the first component is $\sim$ two times smaller than the second component. The brightest pulses are dominated by emission from the second peak component and coincide in phase with the trailing edge of the second component as shown by the vertical dotted lines.

From the auto-correlation function of pulse peak flux intensities, we find no evidence of temporal correlations amongst pulses. The single pulse S/N distributions of the pulse profile and its peak components are shown in Figure 5.21 and follow a log-normal distribution. While the integrated pulse profile formed from 100 brightest pulses shows evidence of both the components, the second component (C2) is much more prominent than the first (C1). This is also supported by S/N distributions, which shows that the brightest pulses originate from C2.

We estimate $\sigma_{\rm J}$ to be 130$\pm$20 ns in an hour for PSR J1022+1001 and find that our measurements of jitter scale as $1/\sqrt{N_{\rm p}}$. These measurements are consistent over multiple epochs.

5.6.4 PSR J1603–7202

PSR J1603–7202 has a spin period of $\sim$ 15 ms and at 20cm wavelengths, similar to PSR J1022+1001, has two sub-components connected by a more dominant bridge of emission. Figure 5.22, shows $\sim$ 50 consecutive pulses with detectable emission at the two domi-

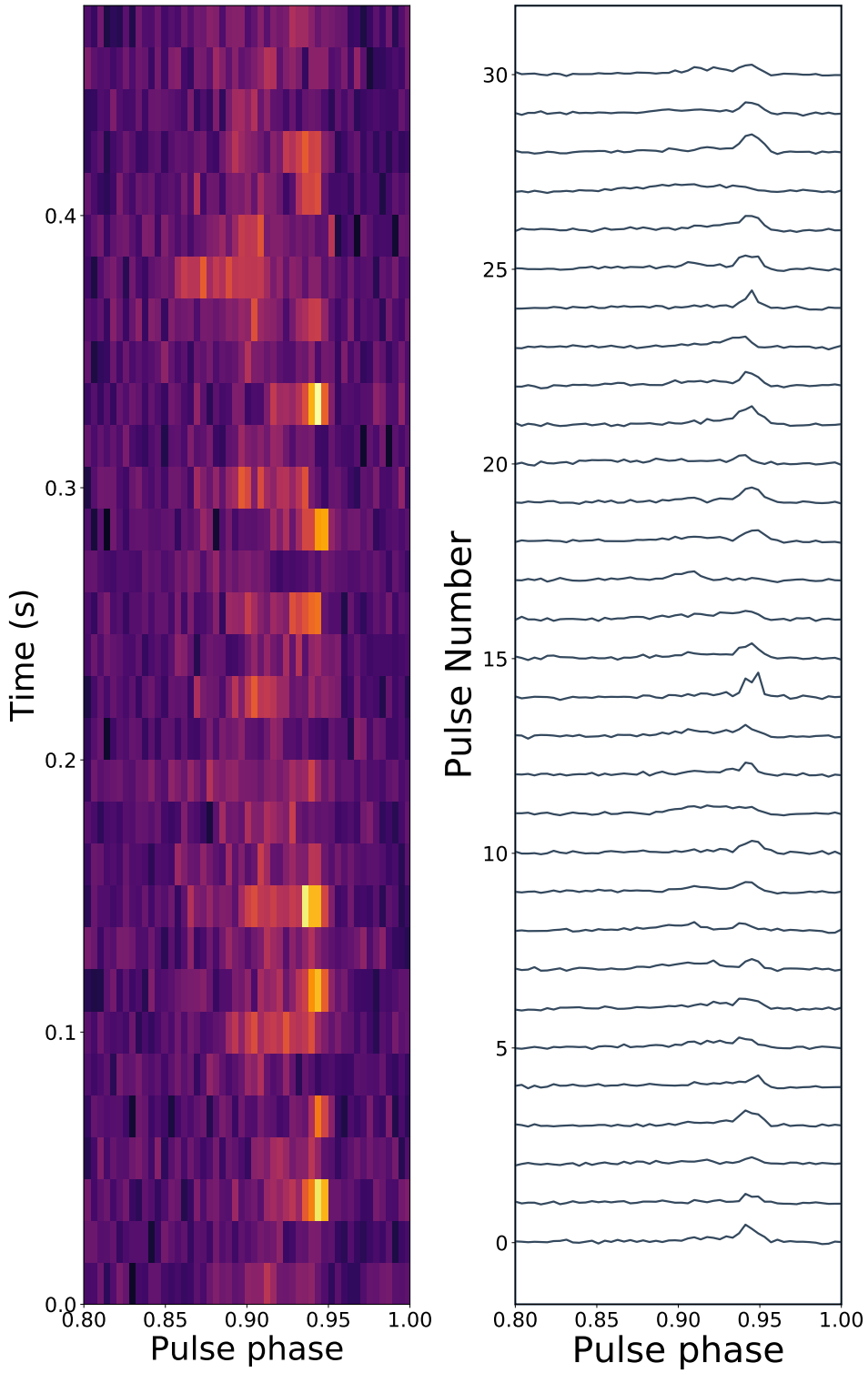

Figure 5.19 Consecutive single pulses of PSR J1022+1001 (left) and the brightest 30 pulses (right) shown across the on-pulse region of pulse phase.

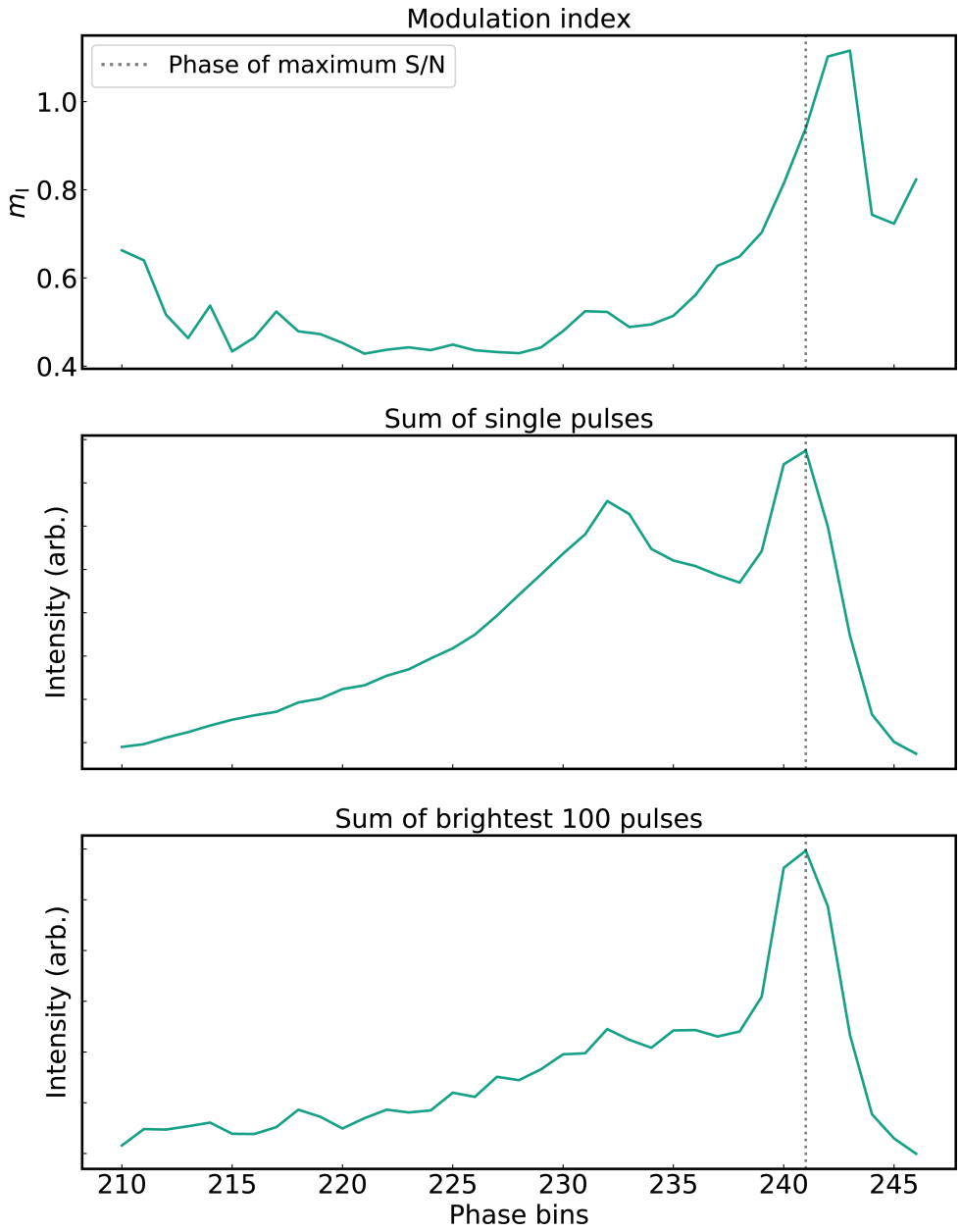

Figure 5.20 Phase-resolved modulation index for PSR J1022+1001 shown across the on-pulse region in the upper panel. The middle panel shows the integrated profile from 15000 single pulses and the lower panel shows the mean profile from averaging the brightest 100 pulses. The vertical grey dashed line represents the phase of maximum S/N for the profile shown in the lower panel.

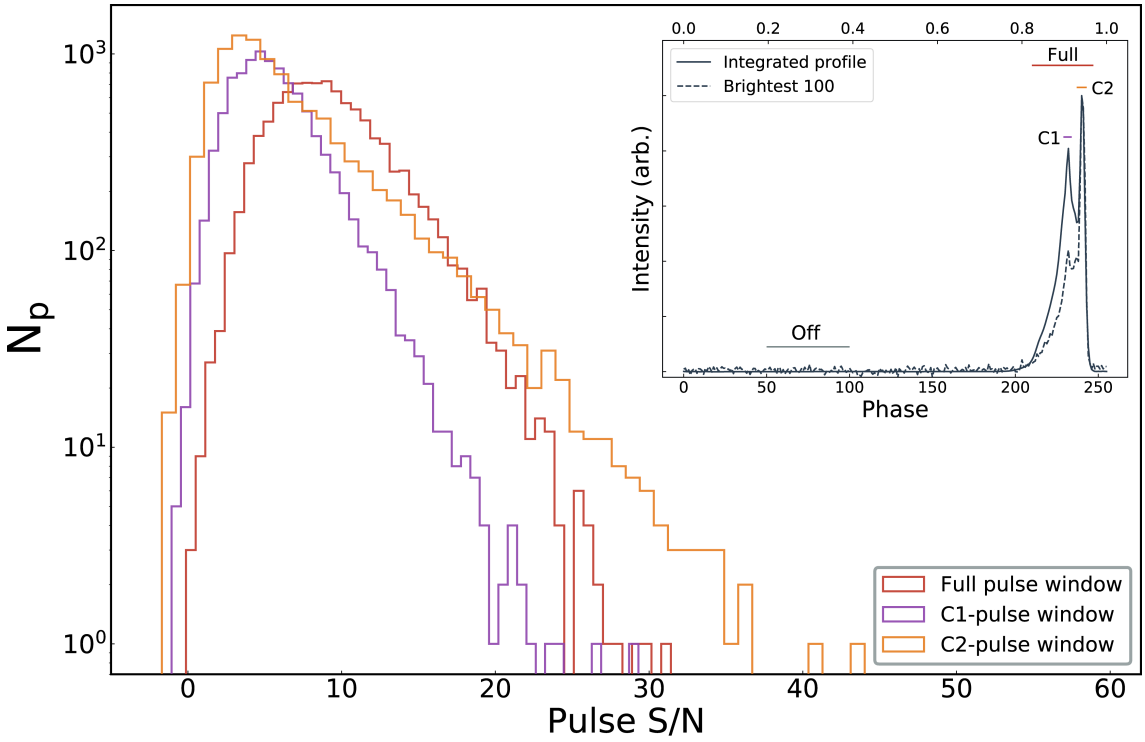

Figure 5.21 Single pulse S/N histograms for PSR J1022+1001. The off-pulse distribution, which is Gaussian and centered at zero is not shown here for clarity. See Figure 5.12 caption for further details.

nant components and across the emission bridge. We analysed $\sim$ 20000 pulses with the maximum S/N per pulse of $\sim$ 17.

In Figure 5.23, starting from the upper panel, we show the phase-resolved modulation index across the on-pulse window, the integrated profile formed from averaging the single pulses and the mean profile from the brightest 100 pulses. The modulation index is strongest towards the leading edge of first component and is much weaker towards the second component. Although the bright pulses are prominent across both the components (C1 and C2), the brightest ones are dominated by the first component (C1). We find no evidence for temporal correlations in the single pulse peak intensities.

We measure the S/N distribution of the single pulses and the two peak components, which follow a log-normal distribution. In Figure 5.24, we show these distributions for windows pertaining to the on-pulse, off-pulse and the two dominant components (C1 and C2). Consistent with Figure 5.23, we see that the brightest pulses originate from the first component.

We estimate $\sigma_{\rm J}$ to be 180$\pm$40 ns in an hour and find that it scales as $1/\sqrt{N_{\rm p}}$ similar to other pulsars discussed above.

5.6.5 PSR J1744–1134

PSR J1744–1134 has a spin period of $\sim$ 4 ms and has a relatively narrow main pulse profile with an interpulse at 20cm wavelengths. We analysed $\sim$ 35000 single pulses with a maximum S/N of $\sim$ 12. Figure 5.25 shows a series of $\sim$ 100 consecutive single pulses. It is interesting to note that the phase and amplitude modulation is low compared to pulsars like J1022+1001 and J1603–7202. We did not detect single pulses from the interpulse.

The phase-resolved modulation index across the on-pulse window is shown in the upper panel of Figure 5.26 along with the integrated pulse profile from averaging the single pulses and the mean profile from the brightest 1000 pulses in the bottom two panels respectively. The modulation index is weaker towards the peak of the pulse profile indicating low levels of amplitude modulation. The brightest pulses coincide with peak of the integrated profile indicating that their corresponding ToAs have arrival times similar to pulses with average S/N. We do not find evidence for temporal correlations in peak flux intensities of single pulses.

We estimated the S/N distributions for both the peak pulse component and the interpulse as shown in Figure 5.27. The distribution of the peak profile component tends towards a Gaussian distribution consistent with low amplitude modulation. We do not detect significant emission from the interpulse (C1). We estimate $\sigma_{\rm J}$ to be 30$\pm$6 ns in an

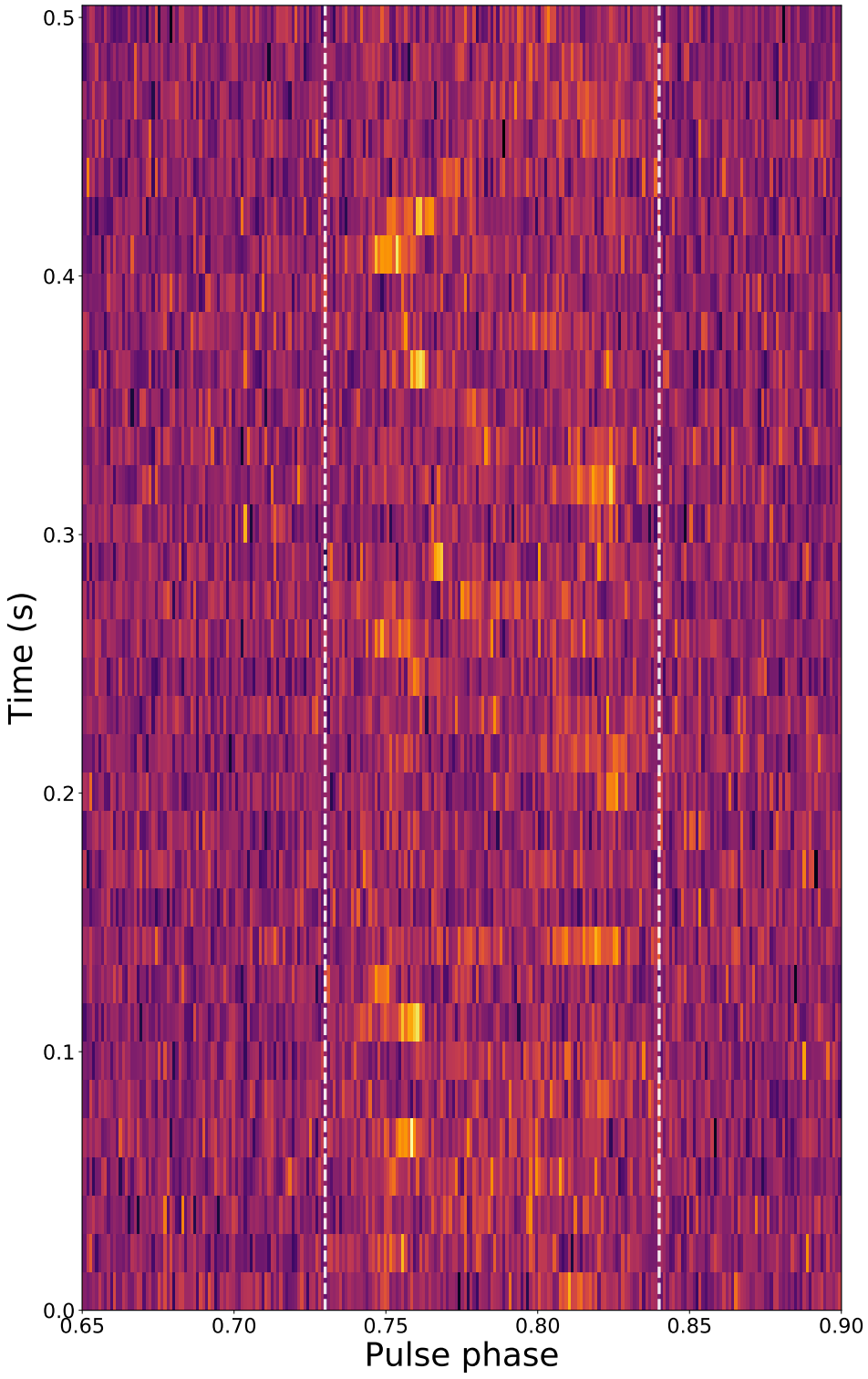

Figure 5.22 Consecutive single pulses of PSR J1603–7202 shown across the on-pulse region of pulse phase. The vertical white dashed lines are plotted around the detected emission region.

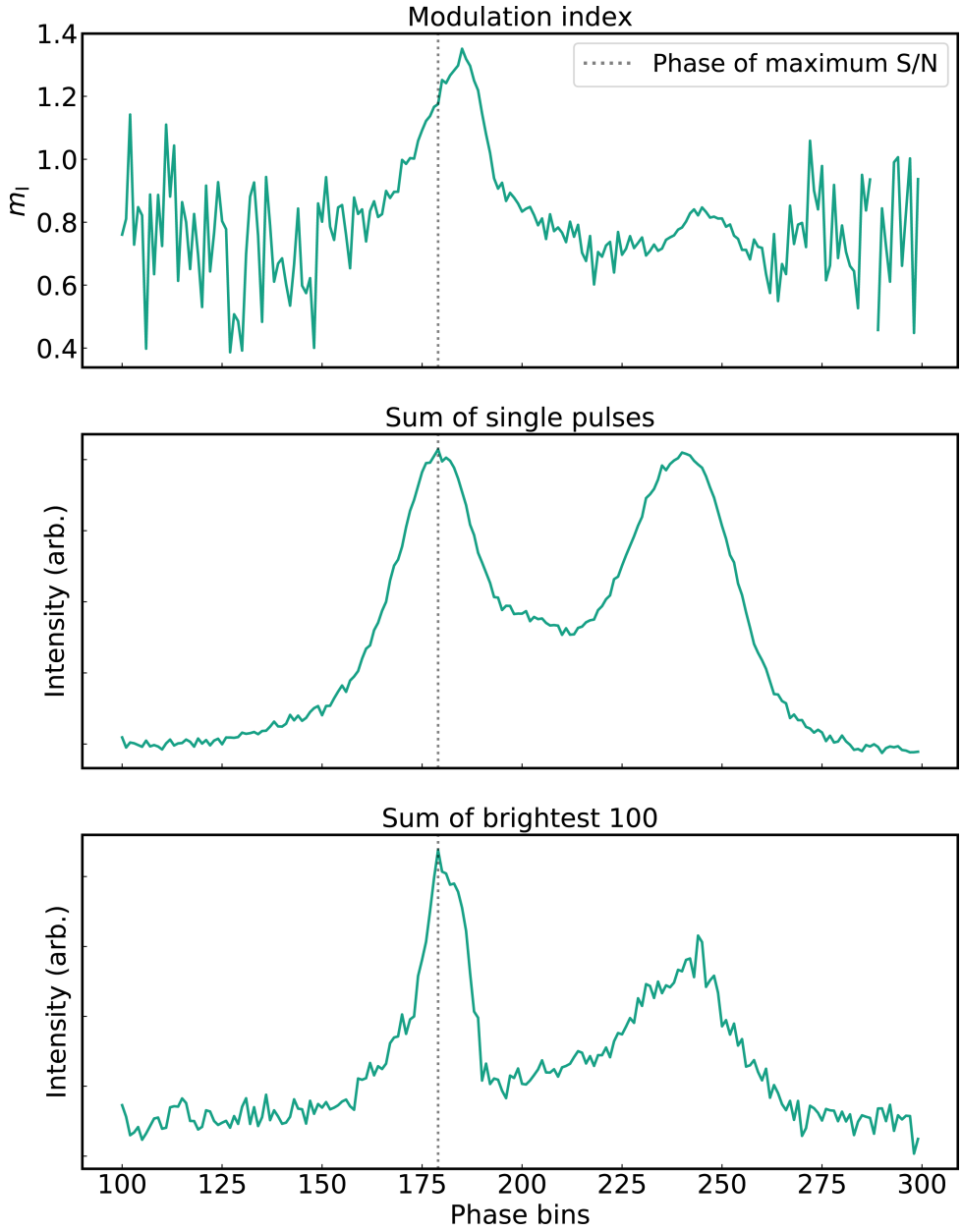

Figure 5.23 Phase-resolved modulation index for PSR J1603–7202 shown across the on-pulse region in the upper panel. The middle panel shows the integrated profile from 20000 single pulses and the lower panel shows the mean profile from the brightest 100 pulses. The vertical grey dashed line represents the phase of maximum S/N for the profile shown in the lower panel.

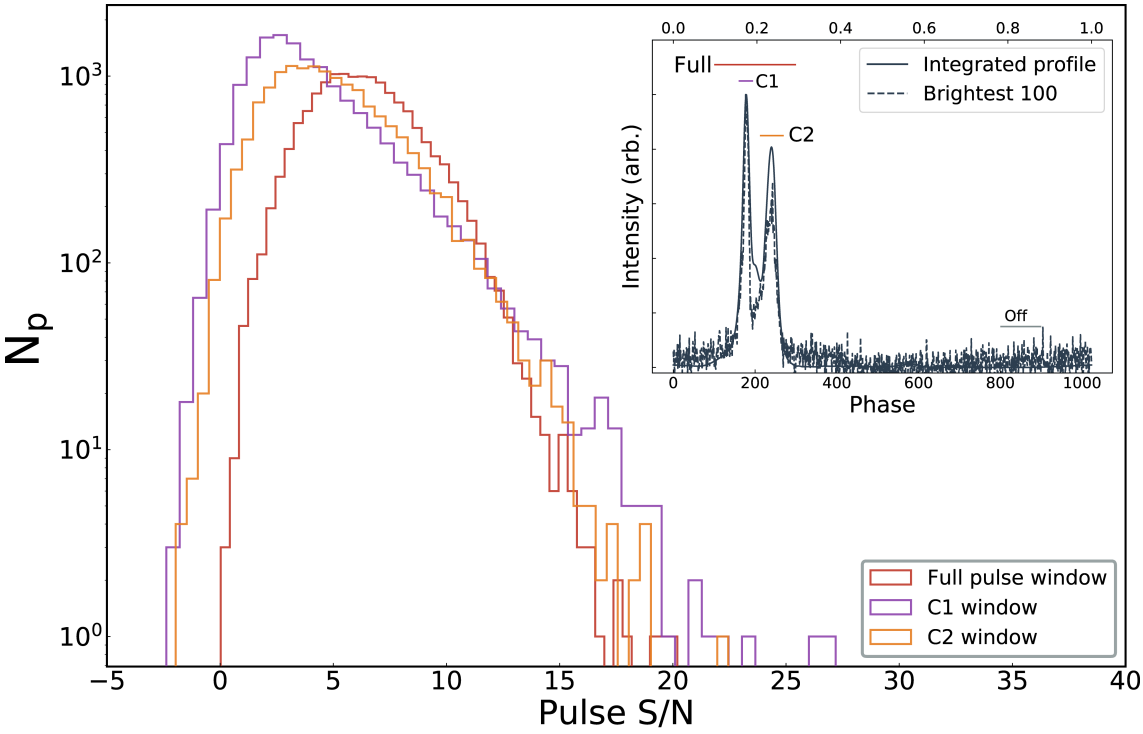

Figure 5.24 Single pulse S/N histograms for PSR J1603–7202. The off-pulse distribution, which is Gaussian and centered at zero is not shown here to preserve clarity. See Figure 5.12 caption for further details.

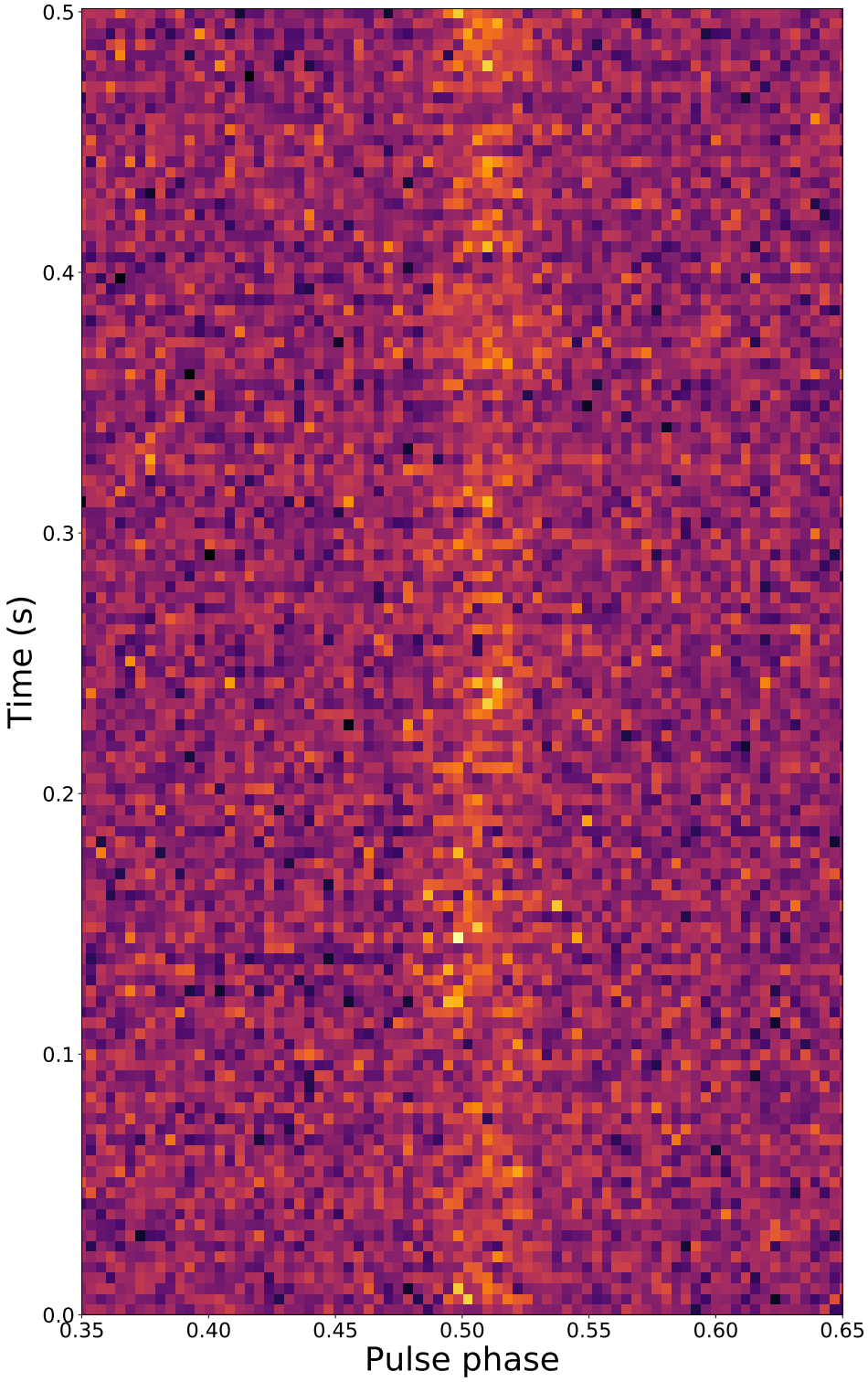

Figure 5.25 Consecutive single pulses of PSR J1744–1134 shown across the on-pulse region of pulse phase. The interpulse region is not shown here due to lack of any single pulse detection.

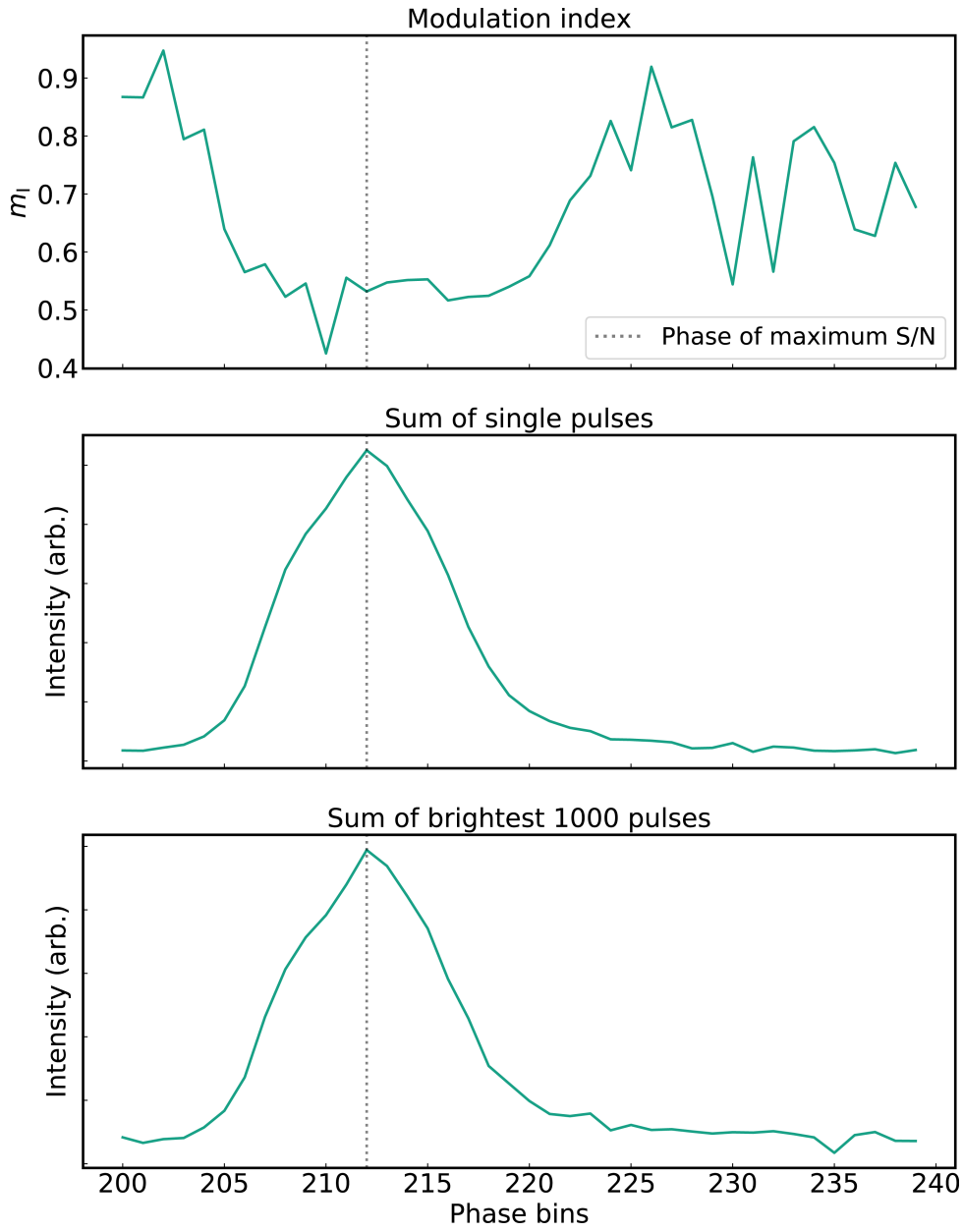

Figure 5.26 Phase-resolved modulation index for PSR J1744–1134 shown across the on-pulse region in the upper panel. The middle panel shows the integrated profile from 35000 single pulses and the lower panel shows the integrated profile from 1000 brightest pulses. The vertical grey dashed line represents the phase of maximum S/N for the profile shown in the lower panel.

hour and similar to other pulsars it scales as $1/\sqrt{N_{\rm p}}$.

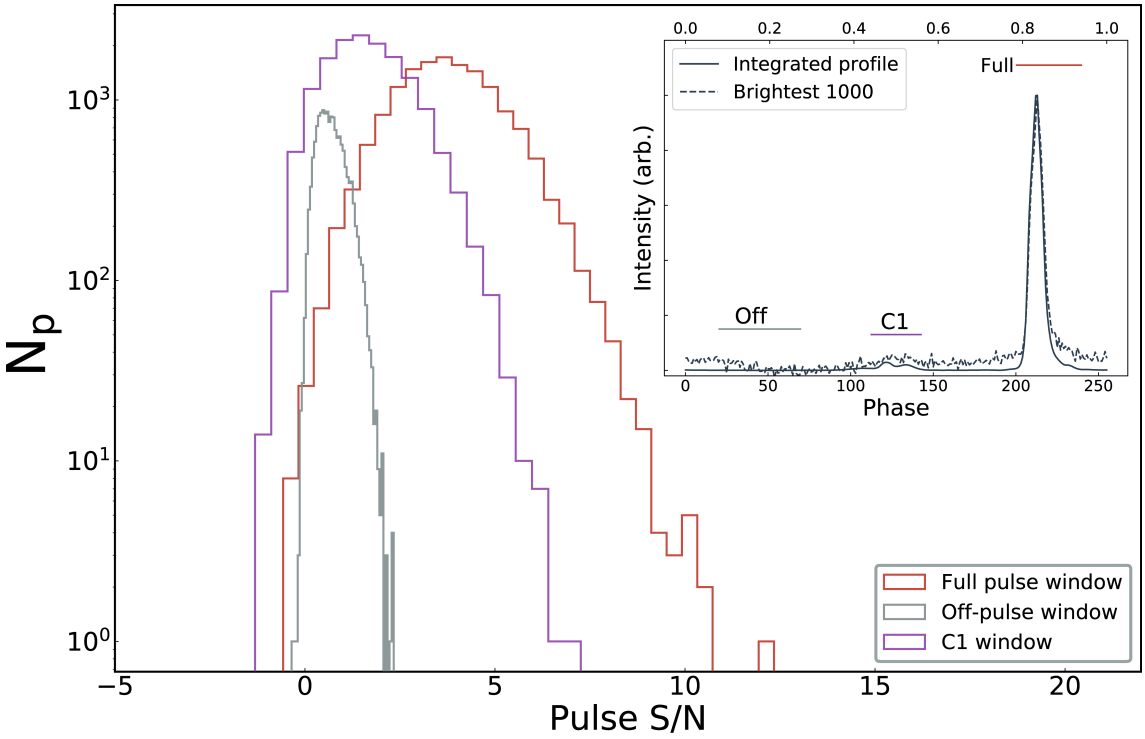

Figure 5.27 Single pulse S/N histograms for PSR J1744–1134. See Figure 5.12 caption for further details.

5.6.6 PSR J1909–3744

PSR J1909–3744 is one of the most precisely timed pulsars owing to its extremely stable rotational behaviour, narrow pulse profile and high flux density. At 20 cm wavelengths, the pulse profile consists of a narrow main component with an interpulse. We analysed $\sim$ 35000 pulses with a maximum S/N of $\sim$ 20. In Figure 5.28, we show $\sim$ 200 consecutive pulses (left panel) and the 30 brightest pulses (right panel) with varying profile morphologies. The profile variability of the brightest pulses are characterised by only 12 significant eigenvectors. A striking observation is that the pulse emission appears to null occasionally with one such region highlighted by two horizontal dashed lines at $\sim$ 0.28 seconds. This is the first reported detection of nulling phenomenon in this pulsar. Integrating the flux densities over the nulling region reveals no detection of emission as shown in Figure 5.29. We do not detect single pulses from the interpulse.

The phase-resolved modulation index across the on-pulse window is shown in the top

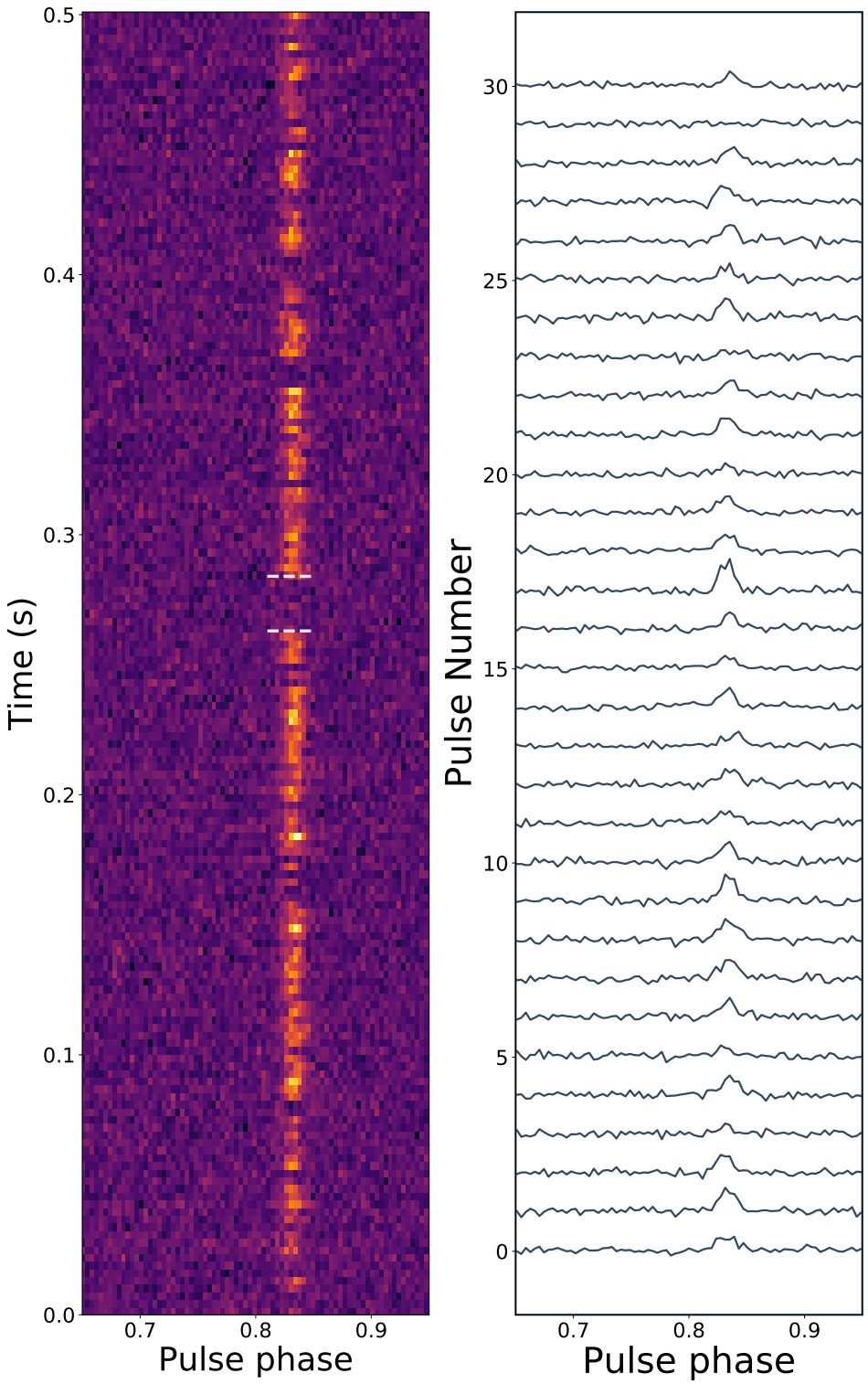

Figure 5.28 Consecutive single pulses of PSR J1909–3744 (left) and the brightest 30 pulses (right) shown across the on-pulse region of pulse phase. The two horizontal dashed lines in the left panel indicate nulling behaviour observed in single pulses.

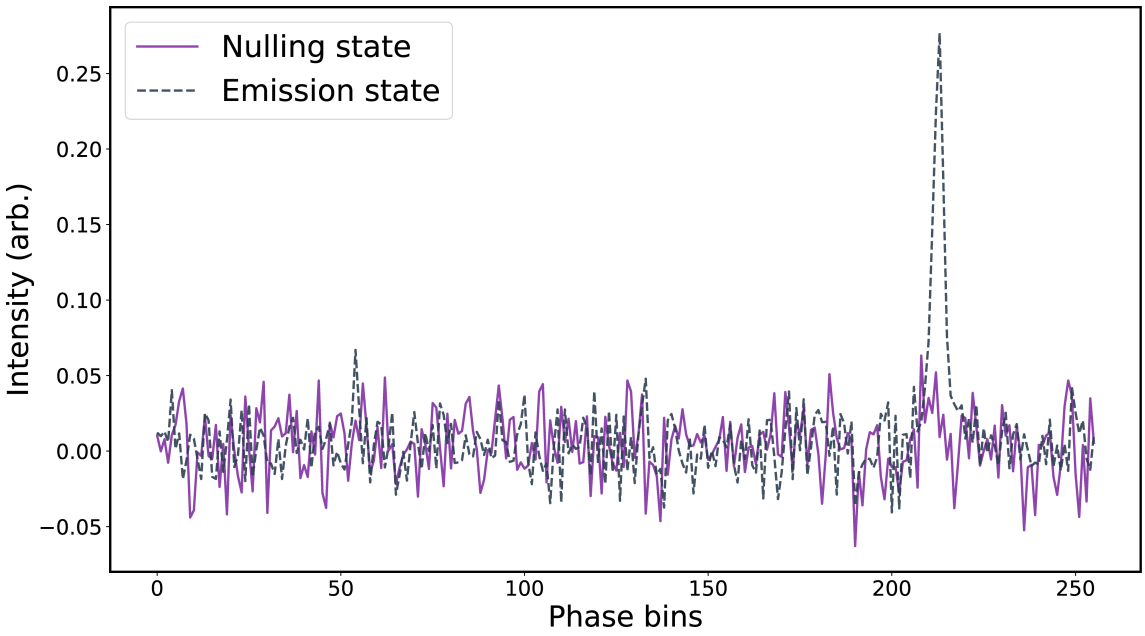

Figure 5.29 Profile formed from integrating the amplitudes of 8 consecutive pulses over the region highlighted in Figure 5.28 is shown in purple. There is no sign of the pulse in the nulling region. An integrated profile formed from adding 8 pulses in the emission region is also shown here (black dashed line) for reference.

panel of Figure 5.30 along with the integrated profile formed from the single pulses and the mean profile formed from the brightest 100 pulses in the bottom two panels. The modulation index across the on-pulse profile is similar to that measured from the off-pulse regions and has low values. The peak of the brightest pulses coincides with the centre of the integrated profile as shown by the vertical dotted line. It is also interesting to note that the mean profile formed from the brightest pulses has relatively more flux density towards its leading edge as compared to the integrated profile. This results in the brightest pulses (S/N $>$ 18) having later times of arrival than pulses with average S/N (5 $<$ S/N $<$ 18) as shown in Figure 5.31. There is also a moderate correlation observed between the S/N of single pulses with their corresponding arrival times.

The S/N distribution of single pulses for J1909–3744 appears to follow a Gaussian distribution as shown in Figure 5.32. The distribution is broader about the mean value indicating that the amplitude modulation is lower, which contributes to the low levels of jitter observed in this pulsar.

We estimate the value of $\sigma_{\rm J}$ to be 9$\pm$3 ns in an hour and find that when integrating from 10 to 10000 pulses, jitter scales as $1/\sqrt{N_{\rm p}}$.

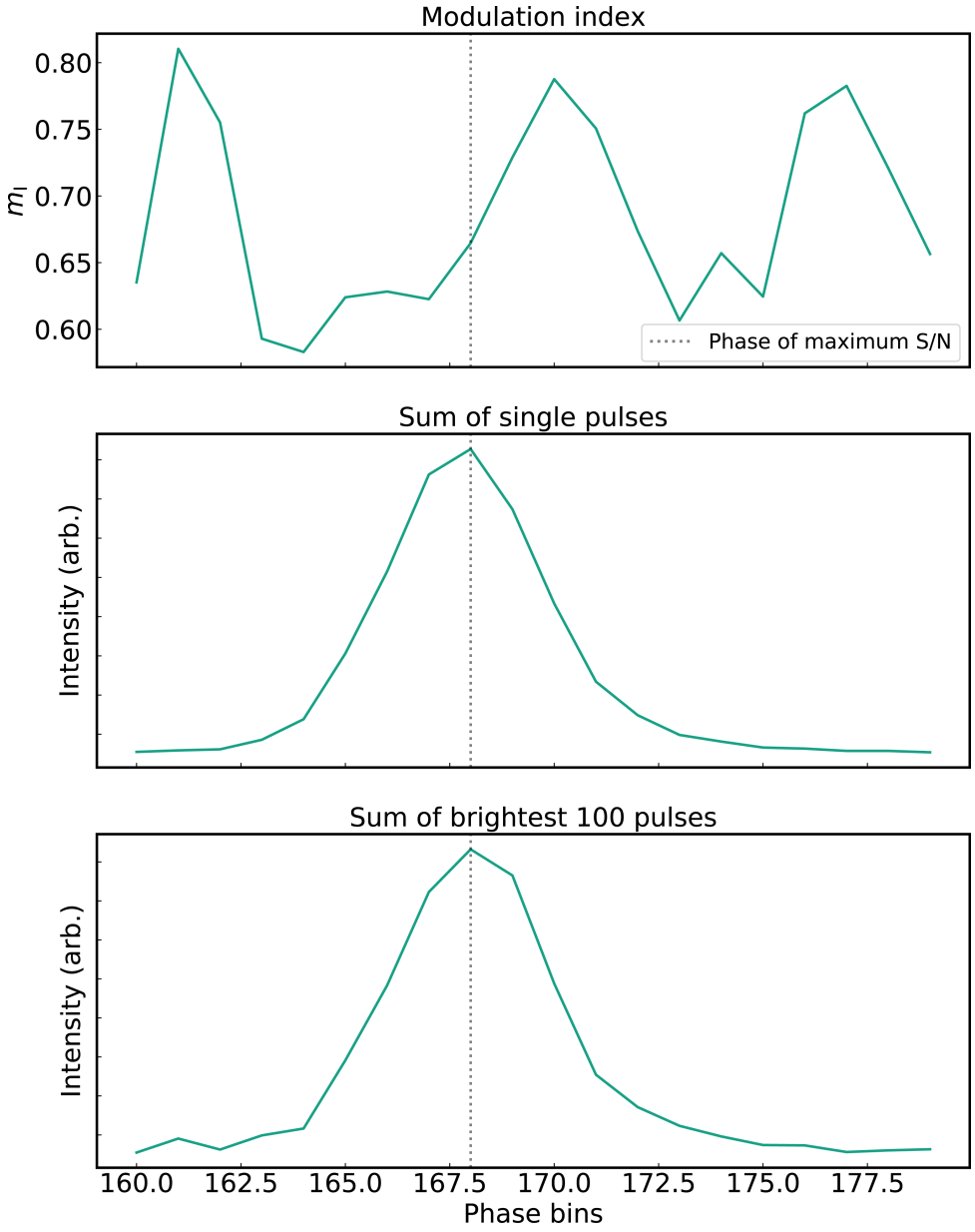

Figure 5.30 Phase-resolved modulation index for PSR J1909–3744 shown across the on-pulse region in the top panel. The middle panel shows the integrated profile from 30000 single pulses and the lower panel shows the integrated profile from 100 brightest pulses. The vertical grey dashed line represents the phase of maximum S/N for the profile shown in the lower panel.

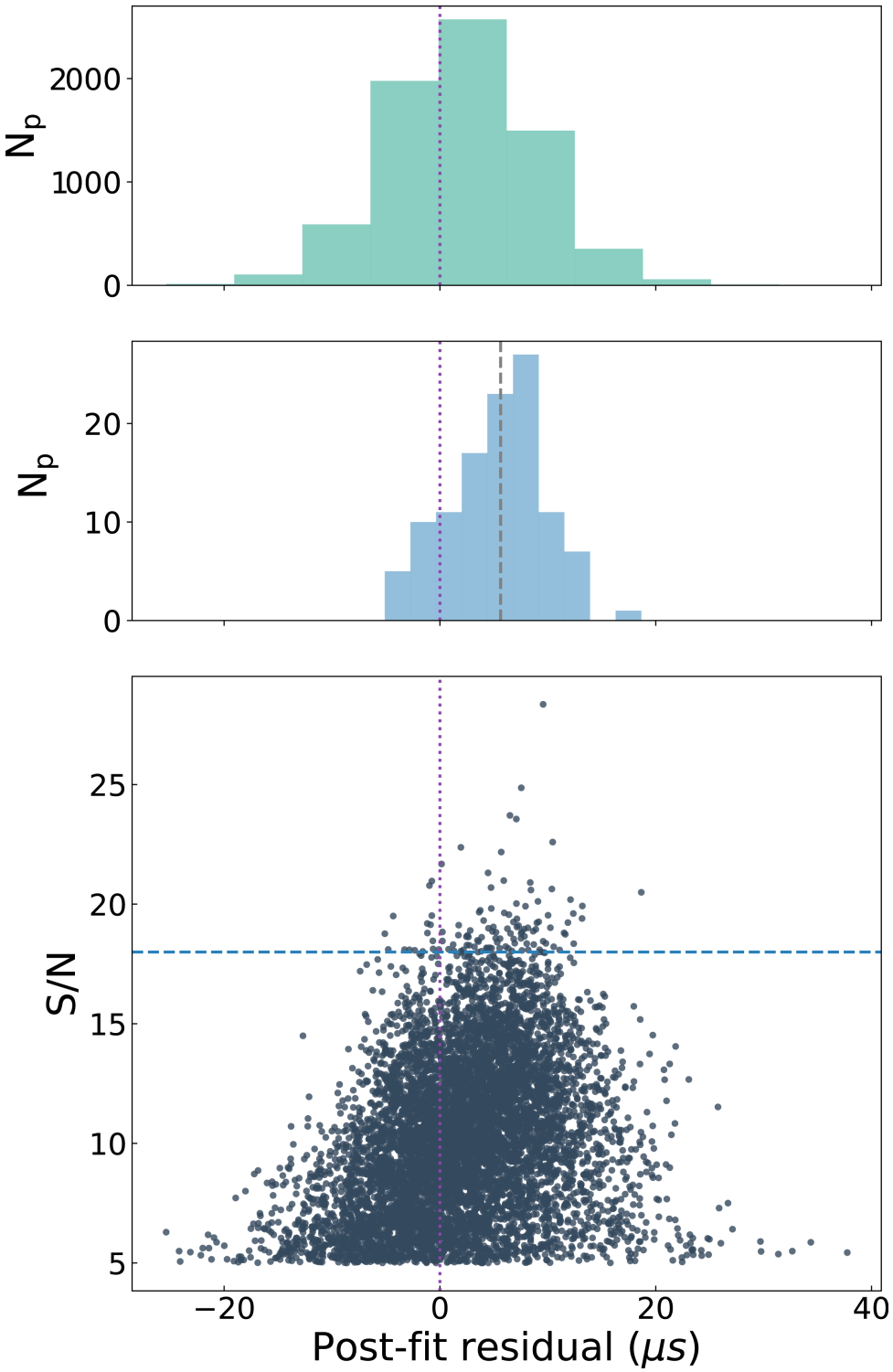

Figure 5.31 ToAs computed from a randomly chosen subset of ∼ 10000 single pulses plotted against their corresponding S/N for PSR J1909–3744. The distribution of ToAs for pulses with 5 < S/N < 18 are shown in the top panel and for the brightest pulses with S/N > 18 are shown in the middle panel. The blue dashed horizontal line represents the S/N threshold for selecting the brightest pulses. The vertical dashed line in the middle panel represents the median of the histogram, while the vertical dotted line across all three panels is at zero μs.

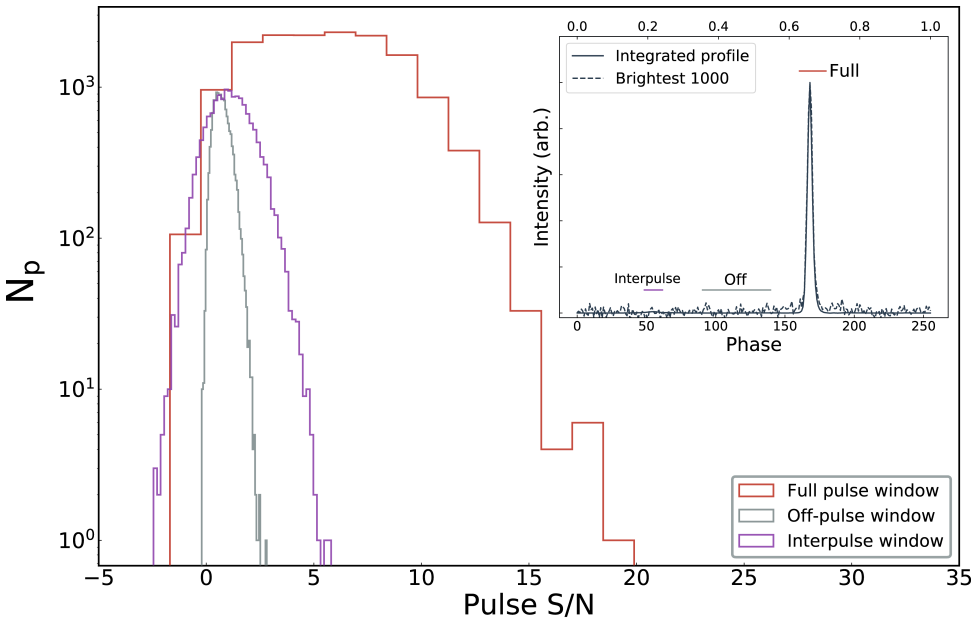

Figure 5.32 Single pulse S/N histograms for PSR J1909–3744. See Figure 5.12 caption for further details.

5.6.7 PSR J2145–0750

PSR J2145–0750 has a spin period of ∼ 15 ms and is a relatively bright pulsar at 20cm wavelengths. Its pulse profile shows complex structures dominated by two main components (C1 and C2) connected by a bridge of emission and a precursor. We detect single pulses from both the main components and none from the precursor. We analysed ∼ 16000 pulses with a maximum S/N of ∼ 50. Figure 5.33 shows consecutive single pulses exhibiting variable emission in phase and amplitude at the two main components and across the emission bridge. It also shows the 30 brightest pulses with varying profile morphology and also highlighting that the first component is more dominant amongst the brightest pulses. The profile variability is characterised by 24 significant eigenvectors, the second largest number of eigenvectors after PSR J0437–4715 in our sample.

The phase-resolved modulation index is shown in the upper panel of Figure 5.34 along with the integrated pulse profile formed from the single pulses and the mean profile formed from the brightest 100 pulses in the bottom two panels. The modulation index exhibits interesting structure, with high levels of modulation towards the leading edge of the first component, and trailing edge of the second component. The bridge of emission also exhibits greater modulation index. The brightest pulses are dominated by emission from the first component.

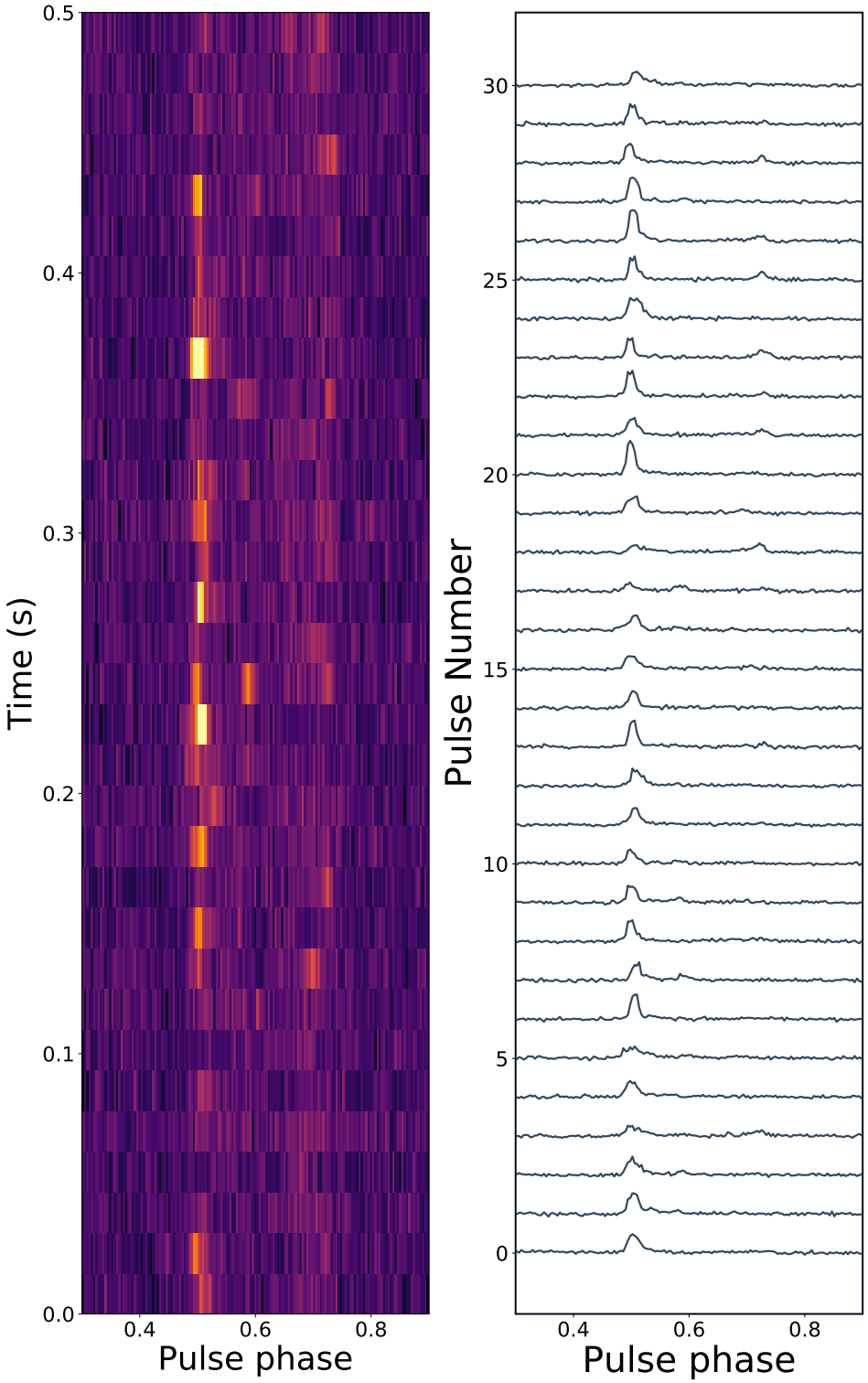

Figure 5.33 Consecutive single pulses of PSR J2145–0750 (left) and the brightest 30 pulses (right) shown across the on-pulse region of pulse phase.

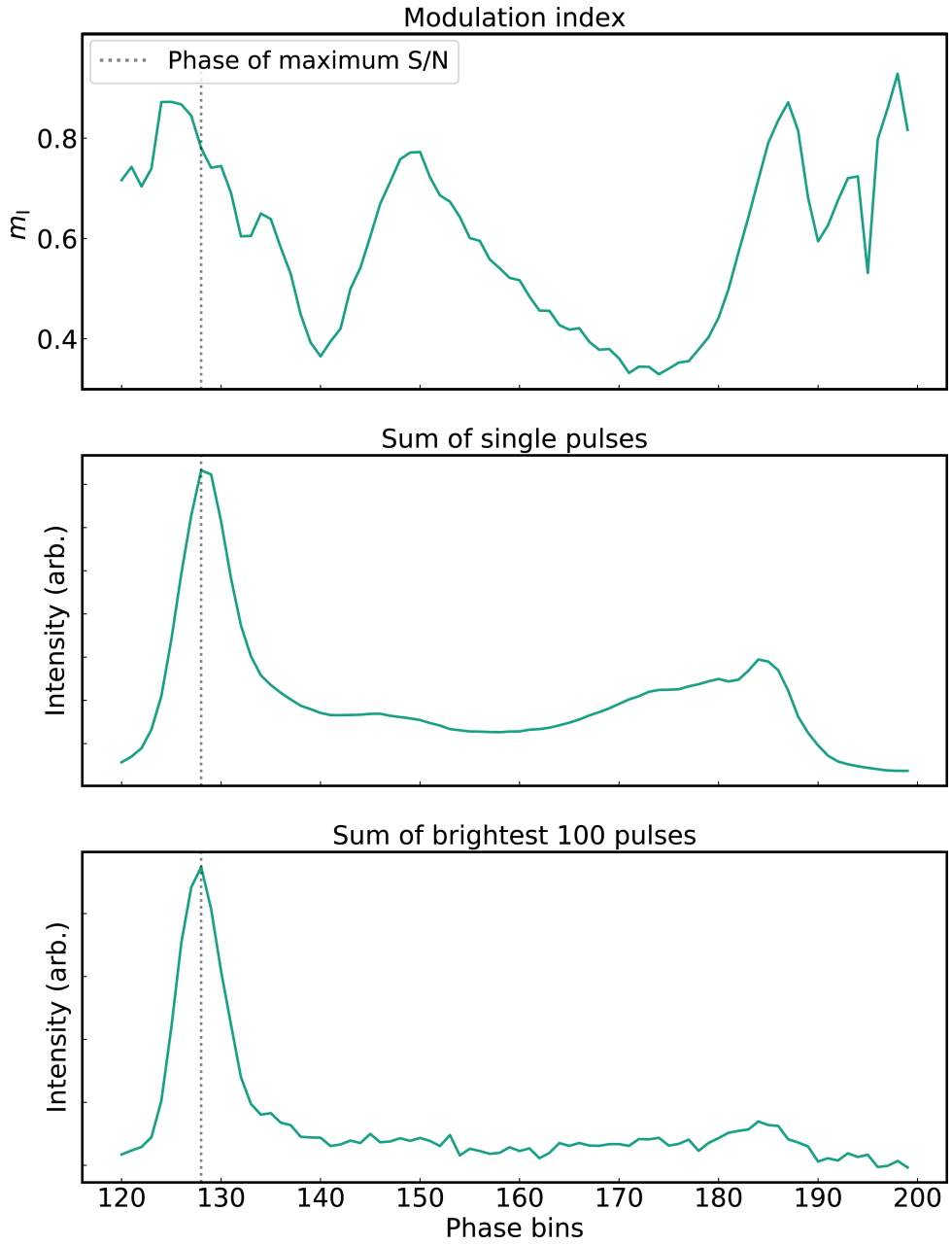

Figure 5.34 Phase-resolved modulation index for PSR J2145–0750 shown across the on-pulse region in the upper panel. The middle panel shows the integrated profile from 16000 single pulses and the lower panel shows the mean profile from 100 brightest pulses. The vertical grey dashed line represents the phase of maximum S/N for the profile shown in the lower panel.

The S/N histograms of the two components (C1 and C2) and the full on-pulse window show log-normal distributions. An integrated profile formed from the brightest 100 pulses is shown in the sub-plot, in which the second component is much weaker than the first. The wide variability in phase and amplitude exhibited by the single pulses results in large levels of jitter noise. We estimate a $\sigma_{\rm J}$ value of 200±20 ns in an hour and find that jitter scales as $1/\sqrt{N_{\rm p}}$.

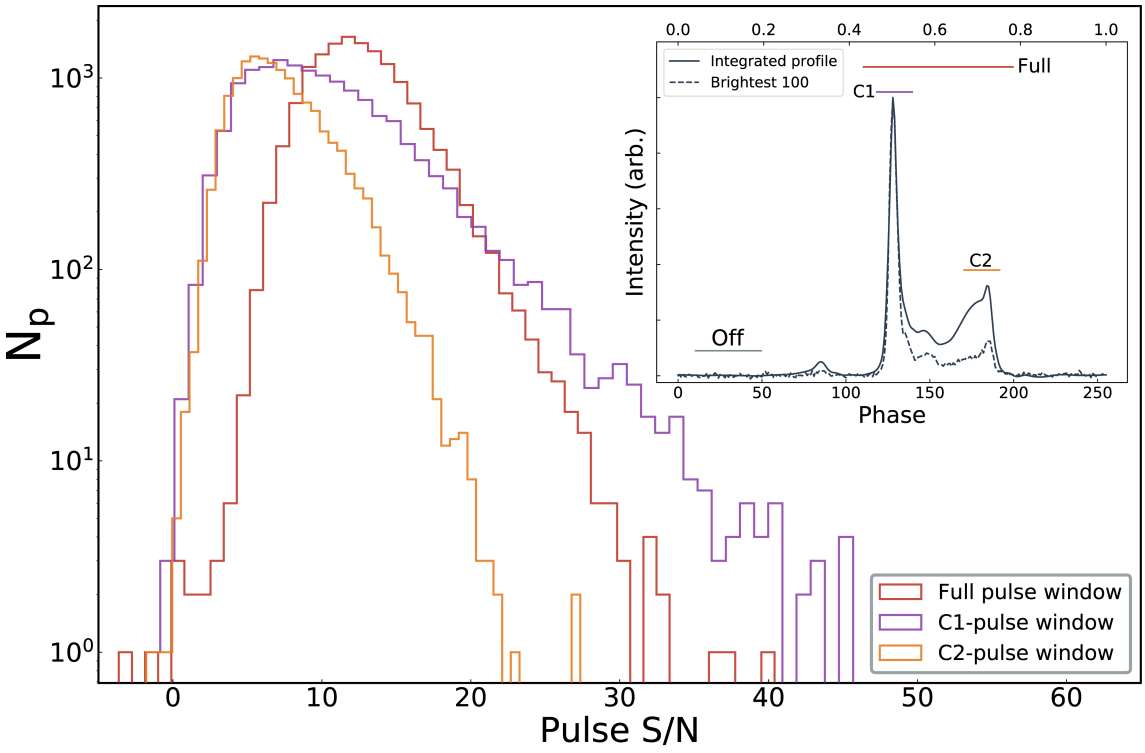

Figure 5.35 Single pulse S/N histograms for PSR J2145–0750. The off-pulse distribution, which is Gaussian and centered at zero is not shown here to preserve clarity. See Figure 5.12 caption for further details.

5.6.8 PSR J2241–5236

PSR J2241–5236 has a spin period of $\sim$ 2.2 ms and is in a 3.5 hour orbit with a low mass companion (Keith et al. 2011). The higher flux density, low dispersion measure and rotational stability makes it an excellent candidate for high precision timing experiments. Consecutive single pulses from PSR J2241–5236 are shown in Figure 5.36, which exhibit very high levels of stability in phase variations. The pulse profile of this pulsar at 20cm wavelengths has a narrow main component with an interpulse, similar to PSR J1909–3744.

We did not detect single pulses from the interpulse in our observations. We analysed $\sim$ 24000 pulses with a maximum S/N of $\sim$ 15.

The phase resolved modulation index across the on-pulse window is shown in the upper panel of Figure 5.37 along with the integrated profile formed from averaging the single pulses and the mean profile from averaging the brightest 1000 pulses in the bottom two panels. The modulation index is the weakest towards the peak of the pulse profile indicative of low levels of amplitude modulation. The brightest pulses largely resemble the integrated profile and so the ToAs of the brightest pulses might be expected to have similar arrival times as the average S/N pulses. This is shown in Figure 5.38, in which the median value of the brightest pulses (S/N $>$ 7) ToAs coincides with the median value of the rest of the pulses (5 $<$ S/N $<$ 7). We did not observe any correlation between ToAs and their S/N.

The S/N histograms of the single pulses follow an appoximately Gaussian distribution as shown in Figure 5.39. The Gaussian distribution implies low variability in pulse amplitudes, as also seen from the low modulation index near the peak component, suggestive of low levels of jitter noise. This pulsar exhibits the lowest levels of jitter relative to any pulsar to date of just 3.8$\pm$0.8 ns in an hour.

The S/N of single pulses were not sufficient to estimate the scaling relation of jitter. The observation that was used to measure jitter from the folded archives (in Section 5.4) had an estimated median single pulse S/N of $\sim$ 10. However, there was no search mode recorded for that particular observation. In comparison, the median single pulse S/N that are presented here are only $\sim$ 4. Analysis of single pulses during scintillation maxima would prove very interesting for precision timing analysis.

5.7 Discussions and Conclusions

We have presented the first short-term high-precision pulsar timing results using the MeerKAT radio telescope including a study of single pulse phenomenology of MSPs. We find that in the highest S/N observations, stochastic pulse shape and amplitude variations cause excess scatter in the ToAs, which is higher than that expected from radiometer noise alone. Out of the 25 MSPs in our sample, we detected new jitter levels for 5 pulsars and placed new upper limits on 8 more. For the remaining 12 pulsars, we find that our measurements are either consistent with previously reported values or have tighter upper limits. PSR J2241–5236 has the lowest levels of jitter hitherto reported in any pulsar of just $\sim$ 4 ns in an hour followed by PSR J1909–3744 with a jitter level of $\sim$ 9 ns in the same time. The upper limit on PSRs J1017–7156 and J2129–5721 are $<$ 11 ns in an hour, which

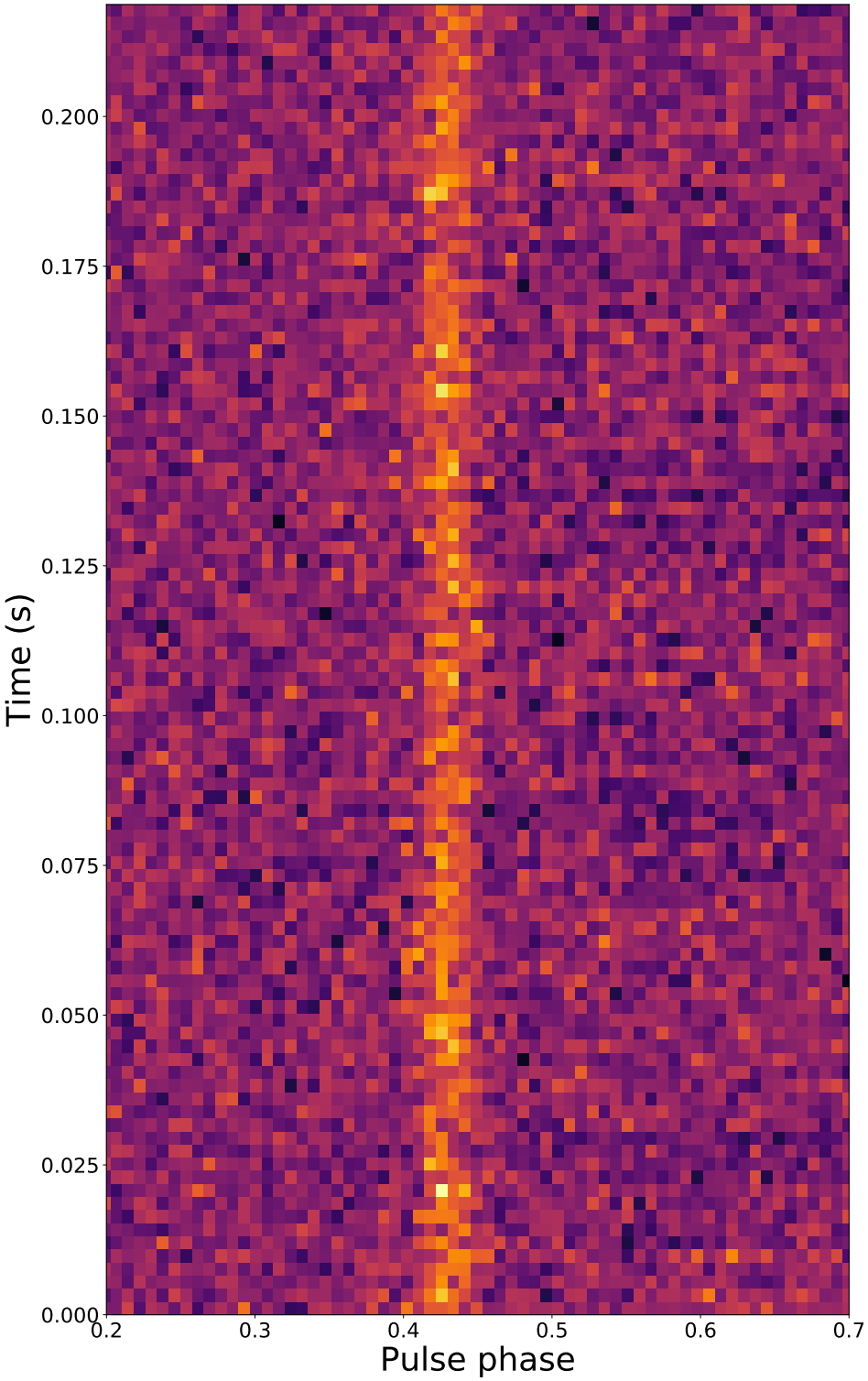

Figure 5.36 Consecutive single pulses of PSR J2241–5236 shown across the on-pulse region of pulse phase.

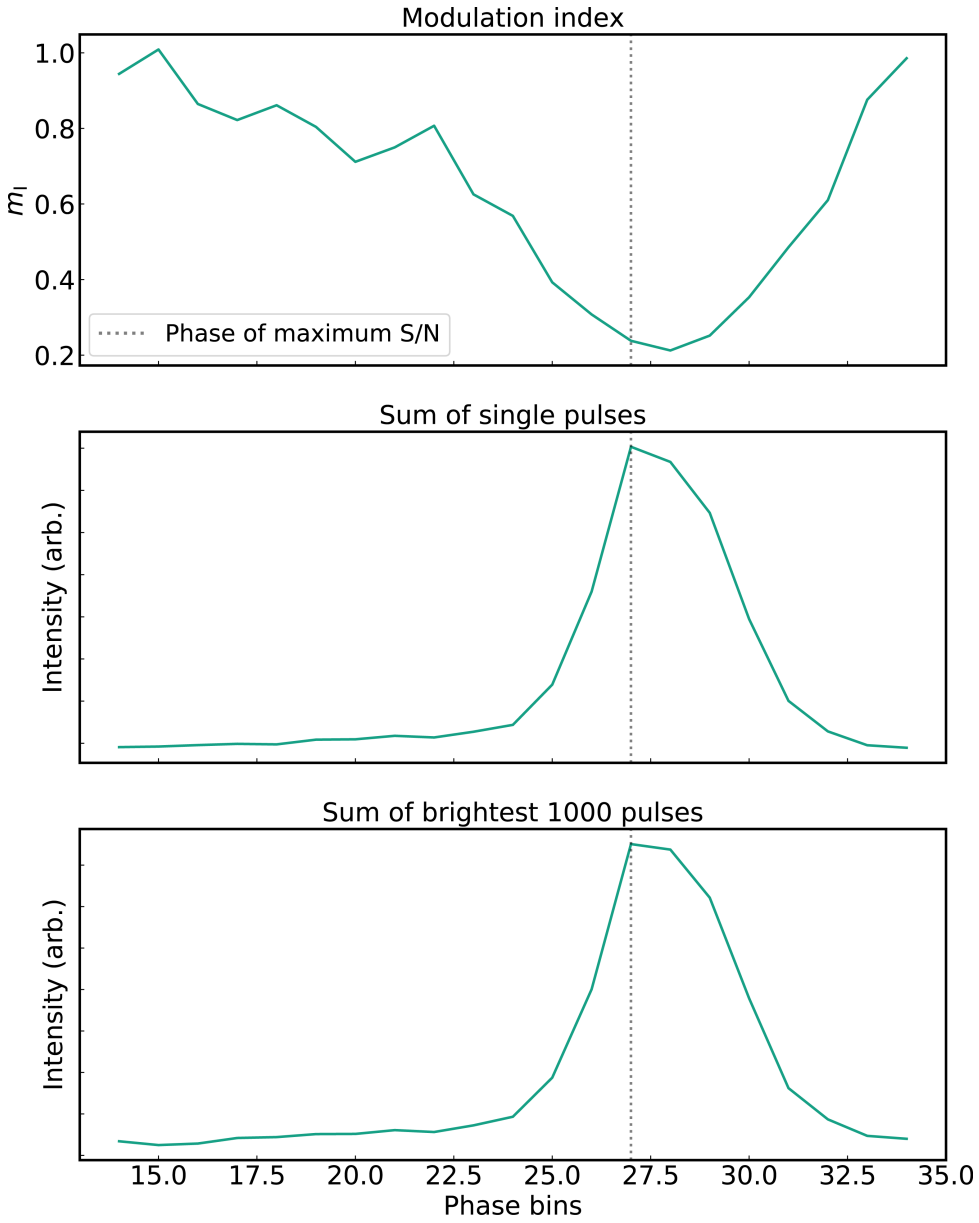

Figure 5.37 Phase-resolved modulation index for PSR J2241–5236 shown across the on-pulse region in the top panel. The middle panel shows the integrated profile from 24000 single pulses and the lower panel shows the integrated profile from 1000 brightest pulses. The vertical grey dashed line represents the phase of maximum S/N for the profile shown in the lower panel.

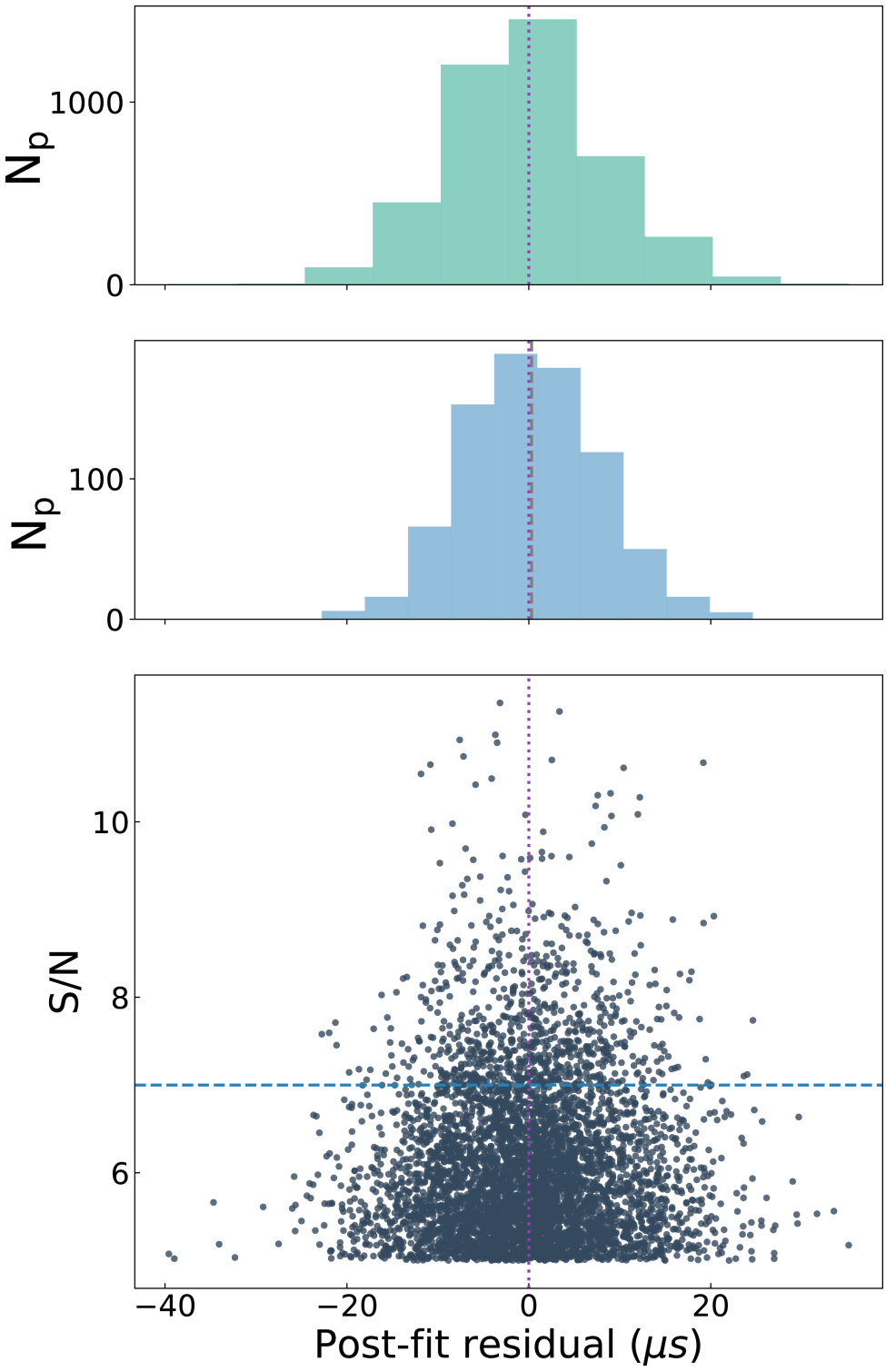

Figure 5.38 ToAs computed from a randomly chosen subset of ∼ 10000 single pulses plotted against their corresponding S/N for PSR J2241–5236. The distribution of ToAs for pulses with $5 < \mathrm{S/N} < 7$ are shown in the top panel and for the brightest pulses with $\mathrm{S/N} > 7$ are shown in the middle panel. The blue dashed horizontal line represents the S/N threshold for selecting the brightest pulses. The vertical dashed line in the middle panel represents the median of the histogram, while the vertical dotted line across all three panels is at zero μs.

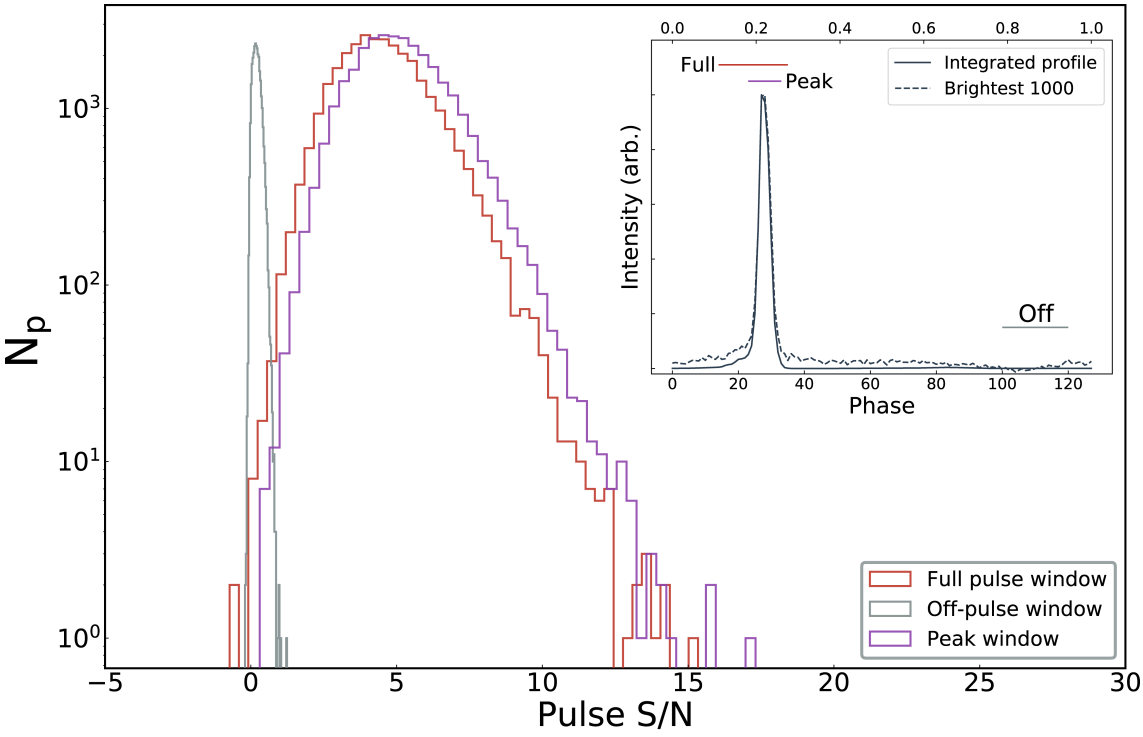

Figure 5.39 Single pulse S/N histograms for PSR J2241–5236. See Figure 5.12 caption for further details.

promise to be excellent pulsars for high-precision timing experiments. The new detections of jitter in MSPs clearly indicate that jitter is a generic property in all pulsars and our ability to detect jitter in many more pulsars will grow with increasing sensitivity of radio telescopes.

We find evidence of the frequency dependence of jitter in PSR J0437–4715 and show that jitter decreases only moderately with increasing observing frequency. We also find that jitter decorrelates over the observing bandwidth of MeerKAT which suggests that the pulse emission statistics will become increasingly independent to each other with wider bandwidths. The decorrelated nature of emission suggests that each individual pulse will have a varying spectral index and owing to the very high S/N of each pulse across the band, we detect this effect in the pulsar timing residuals as time-varying frequency dependence on very short timescales. These time-varying frequency-dependent features are prominent even after modelling the frequency evolution of the pulse profile using wideband templates. Measurements of the DM on short-timescales are thus dominated by the varying spectral index of integrated profiles which places a fundamental limit on the precision with which the pulsars' DM can be measured. We speculate that with more sensitive radio telescopes and in high S/N observations, this phenomena will also contribute in limiting the attainable timing precision.

Although the MeerKAT MSP data set is not yet sensitive to gravitational wave radiation due to its short timing baselines, there are a number of ways in which it can contribute to high precision pulsar timing and PTA experiments. Limitations in precision timing experiments are typically due to an incomplete understanding of systematics in both the instrument and analysis methodologies or due to lack of sensitivity. Precise estimates of DM variations are crucial for PTA experiments, which can be improved by conducting near simultaneous global observing campaigns of a few MSPs with telescopes like MeerKAT, GBT, Parkes, Effelsberg and FAST. Such campaigns not only place a strong constraint on DM variations but also help characterize the instrumental response and post-processing pipelines. With new upcoming receivers such as the Ultra High Frequency (UHF) receiver (580 MHz to 1015 MHz) and the S-band receiver (1750 MHz to 3500 MHz) (Kramer et al. 2016) at MeerKAT, high sensitivity can be achieved owing to steep spectral indices of pulsars and by observing pulsars at their scintillation maxima.

The study of single-pulse phenomenology is important to characterise jitter and its effect on precision pulsar timing. Single pulse statistics also provide valuable insights into pulsar emission models. Using our high S/N observations, we reported the first single pulse study of 8 MSPs from our sample using MeerKAT. Single pulse statistics

for PSRs J0125-2327 and J2241–5236 have not been previously reported. We also report the first observation of pulse nulling in PSR J1909–3744. Using PCA we characterised the single pulse variability via an eigen-decomposition of the profile residual covariance matrix. The phase-space spanned by the linear combinations of significant eigenvectors define the variability in pulse shape morphology and thus, larger number of eigenvectors implies higher pulse shape and phase variability. However, the number of significant eigenvectors also depend on the S/N of each individual pulse. We found that in pulsars with a high S/N, increased jitter implies higher number of significant eigenvectors. Also, the fact that the number of detected significant eigenvectors is typically much lower than the number of phase bins used in the covariance matrix indicates that the total variability observed in single pulses can be fully characterised by a linear combination of the significant basis eigenvectors. Such an analysis was previously implemented by Osłowski et al. (2011) using single pulses from PSR J0437–4715 to mitigate the effects of jitter, who reported a reduction of 20% on the arrival time scatter. With high S/N and wider frequency coverage with MeerKAT, it is important to incorporate more advanced mitigation techniques which also model the frequency evolution of the profile into standard template ToA matching algorithms.

Most pulsars in our sample with detected single pulses show log-normal distributions consistent with previous such results with MSPs (Shannon et al. 2014b) and slow spinning pulsars (Burke-Spolaor et al. 2012). However, pulsars with the lowest levels of jitter noise, PSRs J2241–5236, J1909–3744 and J1744–1134 show approximately Gaussian distributions. Studying energy distributions enable us to distinguish between different models of plasma behaviour based upon theoretical predictions. For example, self-organised criticality (Bak 1996; Bak et al. 1988) describes self-consistent systems that interact without any preferred distance or timescales. It predicts a power-law distribution of pulse intensities. However, models based on stochastic growth theory (Robinson et al. 1992; Robinson 1995) describe interactions in an independent homogeneous medium with preferred distances and timescales. This model predicts a log-normal distribution of pulse intensities. Cairns et al. (2004) found Gaussian energy distributions at the edges of the pulse profile in slow spinning pulsars. They attribute this to either irregularities in the density of the plasma or a superposition of multiple weak emission components. Following from this, it can perhaps be speculated that for the three pulsars in our sample showing Gaussian energy distributions, our line of sight traverses the edge of the emission region. It is also interesting to note that all three pulsars have single component Gaussian profiles with an interpulse.

In pulsars which show high levels of jitter noise, we find that the phase-resolved modulation index increases towards the main emission component, such as in PSRs J0437–4715, J1022+1001, J1603–7202, whereas in pulsars with the lowest levels of jitter noise, the modulation index shows the opposite trend and approaches a minimum towards the main emission component, such as in PSRs J1744–1134, J1909–3744 and J2241–5236. These are consistent with the observations of approximately Gaussian pulse energy distributions in these three pulsars as opposed to log-normal distributions in the other pulsars indicating a tail of bright pulses, thus increasing the modulation index. The phase-resolved modulation index can be used to distinguish between pulsar emission models and previous theoretical work has suggested that the modulation index depends upon some function of the pulsar period and its period derivative. It is however, somewhat arbitrary to define a modulation index from the phase-resolved modulation index profile because it is highly dependent on the pulse phase. In this case, we choose a value that is representative of the modulation index near the main emission component of the integrated pulse profile. We used a Spearman correlation coefficient to determine the correlations between the modulation index and other pulsar parameters. We find moderate correlations of 0.62±0.08 and 0.54±0.03 between the period, period derivative and the modulation index of the pulsar respectively. These measurements are consistent with previous reports (Jenet & Gil 2003, 2004; Edwards & Stappers 2003) which suggest that such a relationship is a consequence of the 'sparking gap' model first theorized by Ruderman & Sutherland (1975). Future observations with more pulsars will enable us to identify correlations with the various 'complexity parameters' (Gil & Sendyk 2000; Lou 2001) that aid in distinguishing between different emission models which will prove powerful in probing deeper into understanding pulsar emission models. We also measure the correlation of $\sigma_{\rm j}$ with various estimates of the pulse width. We consider different measurements of the pulse widths at the 50% (W_{50}), 10% (W_{10}) and the effective pulse width ($W_{\rm eff}$) which is a measure of the sharpness of the pulse profile. We estimate the effective pulse width following the definition in Downs & Reichley (1983) and Cordes & Shannon (2010),

$$W_{\rm eff} = \frac{\Delta\phi}{\sum_i \left[P\left(\phi_{i+1}\right) - P\left(\phi_i\right)\right]^2}, \tag{5.9}$$

where $\Delta\phi$ is the phase resolution of the pulse profile in units of time and P is the pulse profile which is normalised to a peak intensity of unity. We find a moderate correlation of 0.64±0.09 with W_{50} and no significant relationship with $W_{\rm eff}$. This suggests that the level of pulse jitter does not significantly depend on the 'sharpness' of the pulse profile. We also measured the correlation between the DM and pulse jitter to study if uncertainties

due to scintillation noise biases our measurements and found no such relationship.

The results presented in this chapter are very relevant to current and future radio telescopes with regards to precision pulsar timing experiments and to optimizing observing strategies. As more pulsars in the timing campaign are limited by jitter, it is perhaps better to sub-array MeerKAT to observe multiple pulsars simultaneously over longer duration than use the full array to observe pulsars one by one. In the context of the IPTA, perhaps more sensitive telescopes should be used to observe the relatively fainter pulsars while observing the bright ones with small-aperture telescopes? The pulsar timing backend at MeerKAT will eventually have the potential to form up to four tied-array beams on the sky leading to a significant improvement in the efficiency of the timing program. Sub-arrays consisting of a small number of antennas ($\sim$ 4-8) could be deployed to scan the skies to look for pulsars in a scintillation maximum, which could enhance the sensitivity of pulsar timing observations aiding high precision pulsar timing experiments. High precision pulsar timing will greatly benefit from utilizing MeerKAT in conjunction with established radio telescopes and observing programs from around the globe.

6

Conclusions and future prospects

The work reported in this thesis focused on understanding the timing properties across the population of radio pulsars, from characterising the long-term red noise processes to short-term jitter and single pulse phenomenology. We built upon existing Bayesian pulsar timing frameworks to present the first robust characterisation of timing noise for a sample of 85 young high-$\dot{E}$ radio pulsars observed over a time span of $\sim$15 years and extended these results to discuss their long-term spin evolution via braking index measurements. Using the state-of-the-art SKA precursor MeerKAT radio telescope in South Africa, we presented short-term high precision pulsar timing results for 25 millisecond pulsars and studied their single pulse phenomenology. In this chapter we review the main findings of this thesis and discuss future directions for the work presented here.

6.1 Extending the Bayesian pulsar timing framework

In Chapters 3 and 4, we built upon the existing Bayesian pulsar timing framework, TEMPONEST, to characterise the timing properties of a large sample of young radio pulsars. We improved TEMPONEST by incorporating new models for low-frequency noise components and glitch recovery signals in timing data sets. Although this framework provides clear advantages over standard timing methods, it is based on the traditional pulsar timing paradigm of utilizing pulse times-of-arrival (ToAs) as the fundamental data product. The pulse ToA represents a single measurement for a number of integrated single pulse profiles (after folding). Although single pulses can show a high degree of variability in both amplitude and phase, the average profile formed after integrating just a few thousand pulses is usually remarkably stable. However, as the sensitivity of radio telescopes increase, single pulse stochasticity more obviously degrades the precision of pulsar timing experiments implemented through traditional pulsar timing techniques (Lentati &

Shannon 2015). In order to achieve the highest precision pulsar timing and to properly describe the timing uncertainties with state-of-the-art radio telescopes, it is imperative to incorporate information about profile stochasticity. Pulsar profiles also exhibit significant evolution as a function of observing frequency, which leads to biased estimates of ToA uncertainties if not properly modelled. This effect becomes more prominent and important to account for in modern radio receivers which have wider fractional bandwidths. As discussed in Chapter 5, the stochastic variability in pulse shape and amplitude causes excess scatter in the timing residuals known as jitter. Modelling this directly in the profile domain enables an in-depth study of single pulse emission statistics and allows us to obtain realistic uncertainties on pulsar parameters derived from timing models. Also, as the pulsar signal propagates through the ionised interstellar medium (IISM), it experiences a frequency-dependent delay along with more subtle effects like scatter broadening and intensity variations. These time-dependent effects also lead to biases in estimating ToAs and thus need to be incorporated into the pulsar timing paradigm. Although many currently used pulsar timing packages attempt to model these effects, they utilize ToAs and not the averaged profiles; also, most methods do not account for the covariances between the timing noise and deterministic pulsar parameters that lead to further biases in estimating timing model uncertainties.

The profile domain timing methodology was first introduced by Lentati et al. (2015a) who implemented a Bayesian inference framework to simultaneously model the stochastic signals such as timing noise and DM variations, as well as the stochasticity in the pulse profiles. Lentati & Shannon (2015), Lentati et al. (2017a) and Lentati et al. (2017b) in a series of papers further extended the profile domain timign framework to incorporate pulse jitter, wideband effects and profile scattering. They tested this framework on simulated data and on a few selected MSPs with high flux densities. However, this method has not been widely applied to larger data sets owing to computing constraints and the low S/N observations of many pulsars. With the increasing bandwidth of modern radio receivers, the effects of frequency-dependent profile evolution becomes significant when estimating the ToAs. It has also been shown via simulations that the timing noise induced in the residuals due to temporal profile variations is highly covariant with a gravitational wave background while using the traditional timing paradigm with ToAs (Lentati & Shannon 2015). With more sensitive radio telescopes, these effects will become even more dominant on pulse ToAs, making the profile domain approach a viable extension to the current Bayesian pulsar timing framework.

Correlated changes in pulse shape variations and pulsar period derivatives have been

observed in a handful of young radio pulsars (Lyne et al. 2010) and in a couple of MSPs excursions from the timing model have been witnessed, PSR J1643-1224 (Shannon et al. 2016a) and J0437–4715. Studying the origin of these changes have proven challenging owing to the difficulty in distinguishing between different theories that predict such behaviour; for example, in establishing a robust way of differentiating between the mode-changing phenomena that leads to distinct profile changes and pulsar precession that leads to more secular changes in the pulse profile. Through profile domain timing, more robust characterisation of the covariances between timing properties and profile variability can be established, while using Bayesian selection to compare different theoretical models. This framework will also prove very useful in modelling the geodetic precession of relativistic systems, such as PSR J1141–6545, enabling improved timing precision and leading to further constraints in tests of gravity. Also, an interesting prospect is modelling the profile variability during eclipses simultaneously with timing properties to gain credible insights into magnetospheric dynamics and relativistic winds surrounding the pulsar. The development and integration of this methodology into a standard timing package could prove fruitful in many areas of pulsar astrophysics especially with current and next-generation radio facilities like MeerKAT, FAST and the Square Kilometer Array (SKA).

6.2 Timing of young radio pulsars

Long-term monitoring and timing of young radio pulsars provides a unique opportunity to study timing noise, spin-evolution and glitches. In Chapters 3 and 4, we have characterised the timing noise properties of 85 young radio pulsars and have shown that they scale proportionally to $\nu^{1}\dot{\nu}^{-0.6\pm0.1}$, where ν and $\dot{\nu}$ are the spin-period and spin-period derivative. We also explored the long-term spin-evolution of a subset of these pulsars through their braking index measurements (n) and show that n can be significantly higher than the expected value of 3 when not being affected by exponential glitch recoveries. The phenomena of timing noise, spin-evolution and glitches are highly covariant and thus present interesting opportunities for further investigation.

The timing noise model that is widely used in pulsar timing is that of a power-law. However, there are competing models that describe timing noise as a quasi-periodic process or a power-law with a cut-off frequency. Hobbs et al. (2010b) argued that timing noise is a quasi-periodic process based on a timing analysis of a large sample of pulsars over $\sim$ 10 years. However, their timing methodology did not model the covariances between stochastic and deterministic pulsar parameters and was susceptible to measurement biases. A number of other phenomenological models arising from superfluid turbulence (Melatos

& Link 2014a) or due to asteroid belts (Shannon et al. 2013) predict that the spectrum of timing noise plateaus below a cut-off frequency. However, there have been no direct measurements to support this.

Robust timing analyses of large scale timing projects as described in Chapters 3 and 4 with the Parkes radio telescope and similar projects with the Jodrell Bank and Nancay radio telescopes with combined timing baselines of > 40 years hold the potential to provide further insights into the long-term characteristics of timing noise. Phenomenological models of timing noise can be incorporated into the young pulsar timing framework developed in this thesis, which can be tested on various timing datasets. The relation between glitch characteristics and timing noise is not well established. In this thesis we characterised the timing noise properties of pulsars with no known glitches (with few exceptions). A natural extension is to compare timing noise characteristics of glitching pulsars to non-glitching ones which might provide valuable insights into neutron star interior mechanisms and its relation to timing noise.

Observing cadence and long timing baselines are crucial for timing noise studies. Radio facilities like the MeerKAT telescope with its increased sensitivity and fast slew times can complement existing observing programs by providing high cadence and high S/N observations of weaker pulsars. Regular observations of weak southern pulsars for short integration times over a span of five years would not only complement existing timing programs with Parkes but also provide the unique ability to study potential links between profile changes, timing noise properties and glitches.

Palfreyman et al. (2018), reported the first ever detection of single pulses during a glitch in the Vela pulsar. Such observations provide a unique opportunity to measure the equation-of-state of the neutron star and study its internal superfluid dynamics. Ashton et al. (2019), used a novel Bayesian framework to further investigate these observations and concluded that the preferred model of the glitch was different from a simple step glitch and found evidence for an initial spin-down prior to the glitch, which has not been predicted. The large number of young pulsars currently being observed by the Parkes radio telescope and being complemented by the MeerKAT Thousand Pulsar Array program (TPA) (Johnston et al. submitted) with very high S/N and high-time resolution single pulse data, promises a detailed study of glitches and will provide a unique opportunity to quantitatively test various glitch models. The work presented in this thesis on glitches and glitch recovery can be readily extended to incorporate different glitch recovery models and study them in conjunction with high S/N single pulse profiles. This also strengthens the case for developing a profile domain timing framework to study such events.

6.3 A comprehensive study of jitter and single pulse phenomenology across the pulsar population

Official pulsar timing observations with the MeerKAT radio telescope commenced on February, 2019 and since then a total of 854 unique pulsars have been observed with a median S/N of ~ 180. The high sensitivity of MeerKAT and access to the southern skies provides a great opportunity to create a legacy data set to study a myriad of pulsar astrophysics. In Chapter 5, we reported jitter measurements for a sample of 25 MSPs observed with the MeerKAT radio telescope. These measurements help us access the limitations imposed by single pulse variability on precision timing experiments. We detected jitter in 12 MSPs, out of which three have jitter levels of < 30 ns in an hour while of those pulsars with measured upper limits, four have jitter limits of < 30 ns in an hour. From these estimates it would take a minimum of ~ 30 hours to get a 10 ns jitter limit on just seven pulsars. Of these seven pulsars, PSRs J1017–7156, J1909–3744, J2129–5721 and J2241–5236 are promising sources which have estimated jitter levels of ~ 10 ns. However, it must be noted that these estimates strongly depend on the S/N of the observation and the timing noise in the pulsar. For example, a jitter limit of ~ 4 ns for PSR J2241–5236 was obtained from an observation with a S/N of ~ 4900 in 512 s, whereas other observations of the same pulsar with integration times of ~ 4 hours resulted in S/N of just ~ 4000 and only upper limits on jitter. It is perhaps better to observe more pulsars with reasonably higher jitter levels to ensure sky coverage and variability in S/N. From our jitter measurements, we estimate that it would take at least 15 hours to get a 20 ns jitter limit on 10 MSPs and 17 hours to get a 100 ns limit on 20 MSPs. It is important to incorporate these results into observing strategies and the sensitivity of pulsar timing array experiments to gravitational waves. However, since the timing baseline of the MeerKAT data set is less than a year, it is not yet sensitive to low-frequency gravitational waves, but provides a number of unique opportunities to aid in the efforts of the IPTA.

A natural extension of the jitter analysis and single pulse phenomenology presented in Chapter 5, is to extend it to a large sample of young radio pulsars observed with MeerKAT. The last comprehensive large-scale analysis of single pulses was reported in Burke-Spolaor et al. (2012) using the Parkes radio telescope. With the improved sensitivity of MeerKAT, wider observing bandwidths and utilizing novel Bayesian techniques, there is a unique opportunity to study state-of-the-art, high S/N, broadband single pulse statistics across the pulsar population. To showcase the extensibility of the work presented in Chapter 5 to a younger population of pulsars and to highlight the promise of the MeerKAT data set,

we present a preliminary analysis of the single pulse properties of PSR J0904–4246.

This is a relatively young pulsar, with a spin-period of ~ 0.9 s. In the left panel of Figure 6.1, we show a ~ 900 s observation of this pulsar (using 8 s integrations), exhibiting significant mode-changing behaviour toward the start and end of the observation. Mode-changing is a phenomenon where pulsars switch between two or more quasi-stable states of emission (Backer 1970a; Wang et al. 2007). They are thought be due to a reconfiguration of current flow in the pulsar's magnetosphere (Kramer et al. 2006a) and could potentially be linked to the drifting subpulse phenomenon (Rankin 1986). The timing residuals shown in the right panel of Figure 6.1 show clear evidence of increased scatter when the pulsar switches between the two states. This is the first observation of mode-changing behaviour in this pulsar which clearly shows the potential of the MeerKAT young pulsar data set.

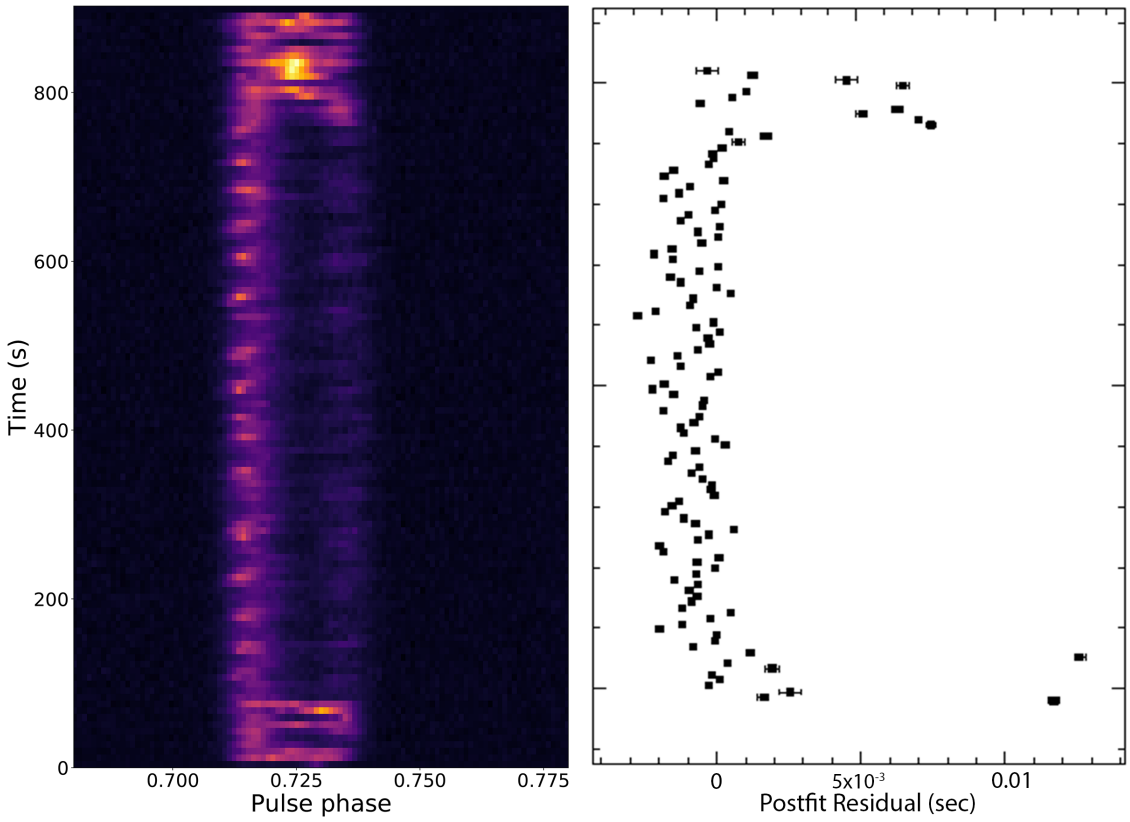

Figure 6.1 A ~ 900 s observation of PSR J0904–4246 exhibiting mode-changing behaviour as it switches between two different states of emission toward the start and end of the observation is shown in the left panel along with correlated changes in the timing residuals showing increased scatter during the state changes.

Using the framework developed in Chapter 5, we investigated the single pulse statistics of this pulsar. The integrated profile of the pulsar at 20cm wavelengths consists of two

peaks, with the first component being brighter than the second, as shown in Figure 6.2 as *Mode 1*. This is the dominant emission state of the pulsar, which occasionally switches to a different state with an integrated profile as shown in Figure 6.2 as *Mode 2*. In Figure 6.3, we show consecutive single pulses (left panel) and the brightest 30 pulses (right panel) exhibiting significant variability in phase and amplitude. The consecutive pulses shown here represent the more dominant of the two states of emission, which shows both the components of the profile. Although many of the brightest pulses show emission from the leading edge of the profile, the brightest two arise surprisingly from approximately the middle of the profile (phases of ~ 0.72), which suggests high amplitude modulation at this phase.

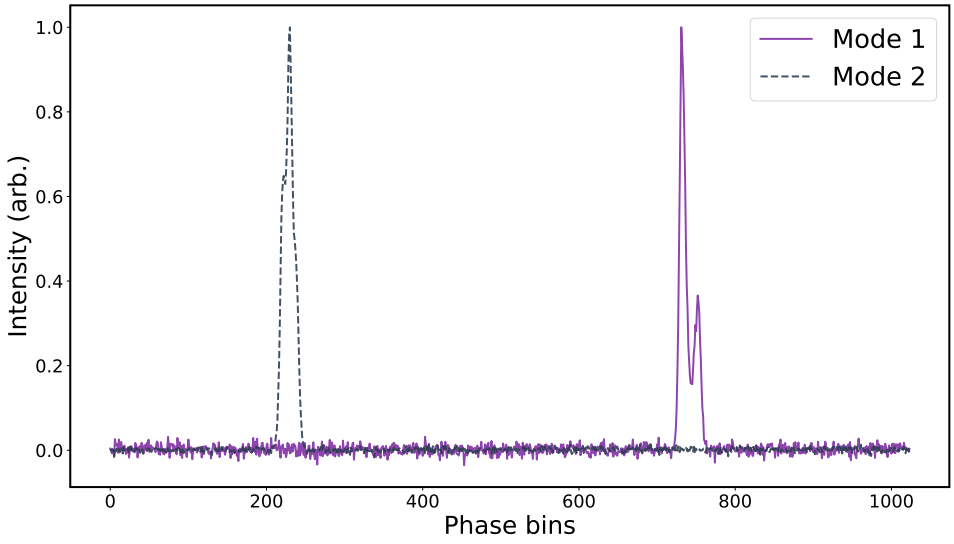

Figure 6.2 Integrated profiles for the two different emission states of PSR J0904–4246. The profile on the right side (solid line) is the dominant emission state with occasional changes to the profile shown in the left side (dashed line). Both the profiles are normalised to their peak intensities.

The nature of mode-changing can be studied in detail from the single pulses. In Figure 6.4 (left side), we show consecutive single pulses when the pulsar is switching between the emission states, exhibiting signs of pulse drifting at about ~ 15 s into the observation. Such phenomena can be used to probe pulsar emission physics and understand the relationships between pulse drifting, mode-changing and nulling.

To understand the nature of bright pulse emission statistics, we computed the phase-resolved modulation index of the profile as shown in the upper panel of Figure 6.4 (right

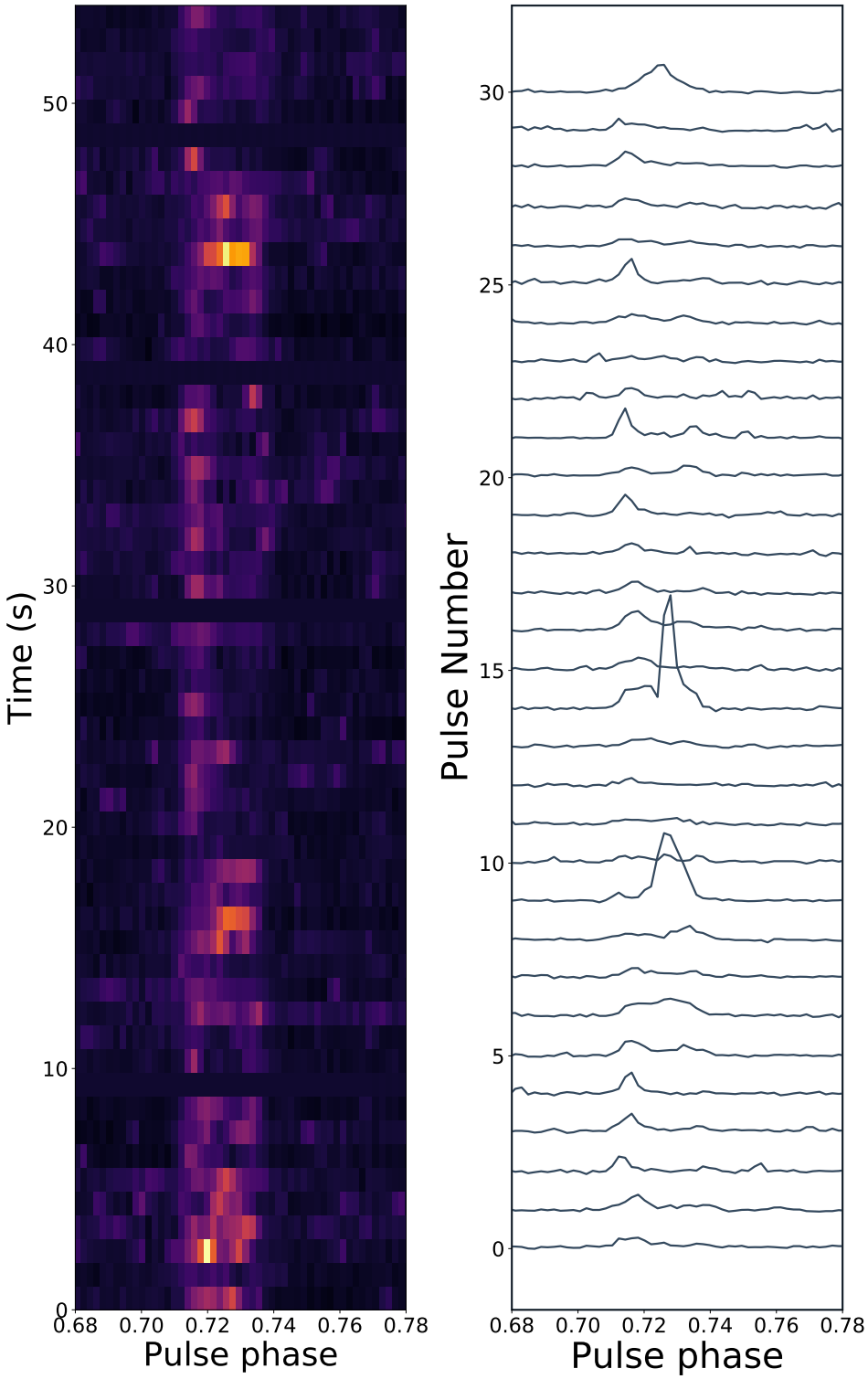

Figure 6.3 Consecutive pulses of PSR J0904–4246 (left panel) along with the brightest 30 pulses (right panel).

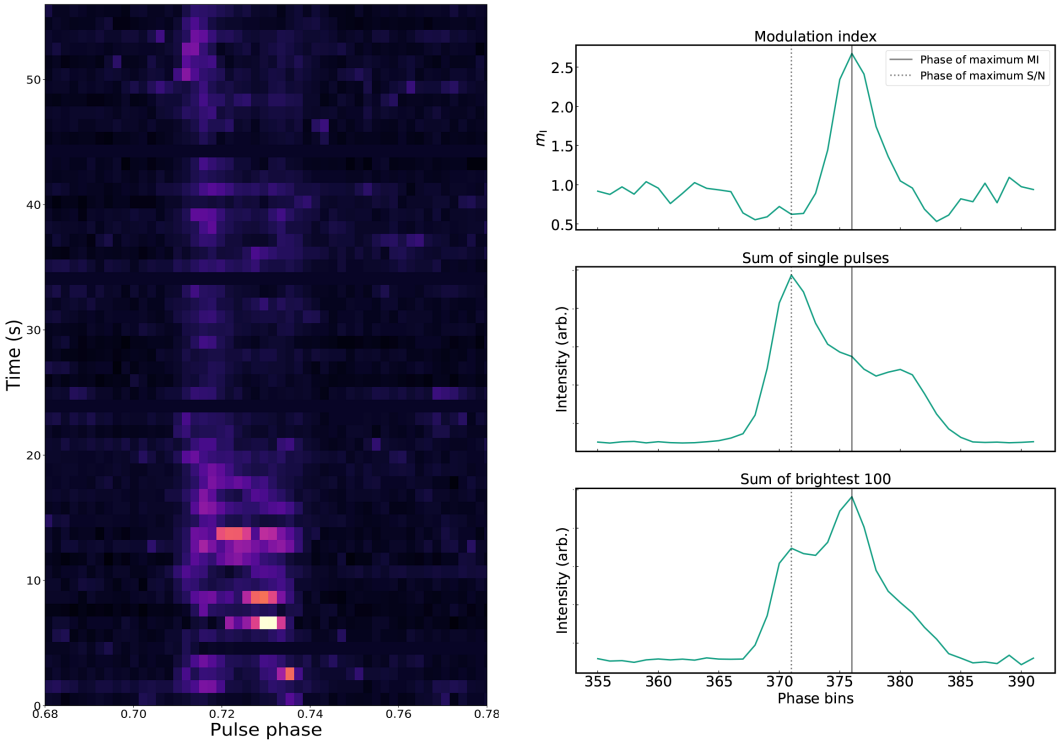

Figure 6.4 Consecutive pulses of PSR J0904–4246 exhibiting transition of one emission state to the other, showing signs of pulse drifting (left). Phase-resolved modulation index for PSR J0904–4246 shown on the right across the on-pulse region in the upper panel. The middle panel shows the integrated profile from 1000 single pulses and the bottom panel shows the mean profile from averaging the brightest 100 pulses. The vertical grey dashed line represents the phase of maximum S/N for the profile shown in the middle panel and the vertical solid line represent the phase of the strongest modulation index.

side). The integrated profile formed from the sum of the ~ 1000 single pulses is shown in the middle panel. The sum of the brightest 100 pulses shown in the lower panel is strikingly different to that of the integrated profile. The brightest pulses have strong emission corresponding to the middle of the integrated profile which also shows the strongest modulation. Detailed analysis of this pulsar and more such phenomena will complement the work presented in this thesis to study short-term jitter, single pulse phenomenology and pulsar emission mechanisms across the pulsar population using highly sensitive radio telescopes like MeerKAT and FAST.

In summary, this thesis has explored and implemented novel methodologies based on Bayesian inference to study timing properties on a large sample of young radio pulsars over decadal time scales. We have estimated scaling laws for timing noise, measured new proper motions and braking index values and have used these to characterise the long-term spin-evolution of young pulsars. The potential of extending this framework to study a wide range of astrophysical phenomena is promising. We also reported the first short-term high precision pulsar timing results using the MeerKAT radio telescope and characterised jitter noise and single pulse phenomenology in MSPs. MeeKAT is poised to be a key instrument in understanding single pulse phenomenology and in achieving sub-ns precision in pulsar timing. Both these avenues are natural extensions of the work presented in this thesis.

Bibliography

Abdo, A. A., Ajello, M., Allafort, A., Baldini, L., Ballet, J., Barbiellini, G., Baring, M. G., Bastieri, D., Belfiore, A., Bellazzini, R., Bhattacharyya, B., Bissaldi, E., Bloom, E. D., Bonamente, E., Bottacini, E., Brandt, T. J., Bregeon, J., Brigida, M., Bruel, P., Buehler, R., Burgay, M., Burnett, T. H., Busetto, G., Buson, S., Caliandro, G. A., Cameron, R. A., Camilo, F., Caraveo, P. A., Casandjian, J. M., Cecchi, C., Çelik, Ö., Charles, E., Chaty, S., Chaves, R. C. G., Chekhtman, A., Chen, A. W., Chiang, J., Chiaro, G., Ciprini, S., Claus, R., Cognard, I., Cohen-Tanugi, J., Cominsky, L. R., Conrad, J., Cutini, S., D'Ammando, F., de Angelis, A., DeCesar, M. E., De Luca, A., den Hartog, P. R., de Palma, F., Dermer, C. D., Desvignes, G., Digel, S. W., Di Venere, L., Drell, P. S., Drlica-Wagner, A., Dubois, R., Dumora, D., Espinoza, C. M., Falletti, L., Favuzzi, C., Ferrara, E. C., Focke, W. B., Franckowiak, A., Freire, P. C. C., Funk, S., Fusco, P., Gargano, F., Gasparrini, D., Germani, S., Giglietto, N., Giommi, P., Giordano, F., Giroletti, M., Glanzman, T., Godfrey, G., Gotthelf, E. V., Grenier, I. A., Grondin, M. H., Grove, J. E., Guillemot, L., Guiriec, S., Hadasch, D., Hanabata, Y., Harding, A. K., Hayashida, M., Hays, E., Hessels, J., Hewitt, J., Hill, A. B., Horan, D., Hou, X., Hughes, R. E., Jackson, M. S., Janssen, G. H., Jogler, T., Jóhannesson, G., Johnson, R. P., Johnson, A. S., Johnson, T. J., Johnson, W. N., Johnston, S., Kamae, T., Kataoka, J., Keith, M., Kerr, M., Knödlseder, J., Kramer, M., Kuss, M., Lande, J., Larsson, S., Latronico, L., Lemoine-Goumard, M., Longo, F., Loparco, F., Lovellette, M. N., Lubrano, P., Lyne, A. G., Manchester, R. N., Marelli, M., Massaro, F., Mayer, M., Mazziotta, M. N., McEnery, J. E., McLaughlin, M. A., Mehault, J., Michelson, P. F., Mignani, R. P., Mitthumsiri, W., Mizuno, T., Moiseev, A. A., Monzani, M. E., Morselli, A., Moskalenko, I. V., Murgia, S., Nakamori, T., Nemmen, R., Nuss, E., Ohno, M., Ohsugi, T., Orienti, M., Orlando, E., Ormes, J. F., Paneque, D., Panetta, J. H., Parent, D., Perkins, J. S., Pesce-Rollins, M., Pierbattista, M., Piron, F., Pivato, G., Pletsch, H. J., Porter, T. A., Possenti, A., Rainò, S., Rando, R., Ransom, S. M., Ray, P. S., Razzano, M., Rea, N., Reimer, A., Reimer, O., Renault, N., Reposeur, T., Ritz, S., Romani, R. W., Roth, M., Rousseau, R., Roy, J., Ruan, J., Sartori, A., Saz Parkinson, P. M., Scargle, J. D., Schulz, A., Sgrò, C., Shannon, R., Siskind, E. J., Smith, D. A., Spandre, G., Spinelli, P., Stappers, B. W., Strong, A. W., Suson, D. J., Takahashi, H., Thayer, J. G., Thayer, J. B., Theureau, G., Thompson, D. J., Thorsett, S. E., Tibaldo, L., Tibolla, O., Tinivella, M., Torres, D. F., Tosti, G., Troja, E., Uchiyama, Y., Usher, T. L., Vandenbroucke, J., Vasileiou, V., Venter, C., Vianello, G., Vitale, V., Wang, N., Weltevrede, P., Winer, B. L., Wolff, M. T., Wood, D. L., Wood, K. S., Wood, M., &

Yang, Z., *ApJS*, 208(2):17, Oct 2013.

Aggarwal, K., Arzoumanian, Z., Baker, P. T., Brazier, A., Brinson, M. R., Brook, P. R., Burke-Spolaor, S., Chatterjee, S., Cordes, J. M., Cornish, N. J., Crawford, F., Crowter, K., Cromartie, H. T., DeCesar, M., Demorest, P. B., Dolch, T., Ellis, J. A., Ferdman, R. D., Ferrara, E., Fonseca, E., Garver-Daniels, N., Gentile, P., Hazboun, J. S., Holgado, A. M., Huerta, E. A., Islo, K., Jennings, R., Jones, G., Jones, M. L., Kaiser, A. R., Kaplan, D. L., Kelley, L. Z., Key, J. S., Lam, M. T., Lazio, T. J. W., Levin, L., Lorimer, D. R., Luo, J., Lynch, R. S., Madison, D. R., McLaughlin, M. A., McWilliams, S. T., Mingarelli, C. M. F., Ng, C., Nice, D. J., Pennucci, T. T., Pol, N. S., Ransom, S. M., Ray, P. S., Siemens, X., Simon, J., Spiewak, R., Stairs, I. H., Stinebring, D. R., Stovall, K., Swiggum, J., Taylor, S. R., Turner, J. E., Vallisneri, M., van Haasteren, R., Vigeland , S. J., Witt, C. A., Zhu, W. W., & NANOGrav Collaboration, *ApJ*, 880(2):116, August 2019.

Akbal, O., Alpar, M. A., Buchner, S., & Pines, D., *MNRAS*, 469(4):4183–4192, Aug 2017.

Alpar, M. A., Nandkumar, R., & Pines, D., *ApJ*, 288:191–195, January 1985.

Alpar, M. A., Chau, H. F., Cheng, K. S., & Pines, D., *ApJ*, 409:345, May 1993.

Alpar, M. A. & Baykal, A., *MNRAS*, 372:489–496, Oct 2006.

Alvarez, L. W., *Physical Review*, 52(2):134–135, Jul 1937.

Anderson, P. W. & Itoh, N., *Nature*, 256:25–27, July 1975.

Andersson, N., Antonopoulou, D., Espinoza, C. M., Haskell, B., & Ho, W. C. G., *ApJ*, 864(2):137, Sep 2018.

Antoniadis, J., Freire, P. C. C., Wex, N., Tauris, T. M., Lynch, R. S., van Kerkwijk, M. H., Kramer, M., Bassa, C., Dhillon, V. S., Driebe, T., Hessels, J. W. T., Kaspi, V. M., Kondratiev, V. I., Langer, N., Marsh, T. R., McLaughlin, M. A., Pennucci, T. T., Ransom, S. M., Stairs, I. H., van Leeuwen, J., Verbiest, J. P. W., & Whelan, D. G., *Science*, 340:448, April 2013.

Antonopoulou, D., Espinoza, C. M., Kuiper, L., & Andersson, N., *MNRAS*, 473:1644–1655, Jan 2018.

Archibald, R. F., Gotthelf, E. V., Ferdman, R. D., Kaspi, V. M., Guillot, S., Harrison, F. A., Keane, E. F., Pivovaroff, M. J., Stern, D., Tendulkar, S. P., & Tomsick, J. A., *ApJ*, 819:L16, Mar 2016.

Armstrong, J. W., *Nature*, 307(5951):527–528, Feb 1984.

Armstrong, J. W., Rickett, B. J., & Spangler, S. R., *ApJ*, 443:209, Apr 1995.

Arzoumanian, Z., Nice, D. J., Taylor, J. H., & Thorsett, S. E., *ApJ*, 422:671, February 1994.

Arzoumanian, Z., Brazier, A., Burke-Spolaor, S., Chamberlin, S. J., Chatterjee, S., Christy, B., Cordes, J. M., Cornish, N. J., Demorest, P. B., Deng, X., Dolch, T., Ellis, J. A., Ferdman, R. D., Fonseca, E., Garver-Daniels, N., Jenet, F., Jones, G., Kaspi, V. M., Koop, M., Lam, M. T., Lazio, T. J. W., Levin, L., Lommen, A. N., Lorimer, D. R., Luo, J., Lynch, R. S., Madison, D. R., McLaughlin, M. A., McWilliams, S. T., Nice, D. J., Palliyaguru, N., Pennucci, T. T., Ransom, S. M., Siemens, X., Stairs, I. H., Stinebring, D. R., Stovall, K., Swiggum, J., Vallisneri, M., van Haasteren, R., Wang, Y., Zhu, W. W., & NANOGrav Collaboration, *ApJ*, 810:150, September 2015.

Arzoumanian, Z., Baker, P. T., Brazier, A., Burke-Spolaor, S., Chamberlin, S. J., Chatterjee, S., Christy, B., Cordes, J. M., Cornish, N. J., Crawford, F., Thankful Cromartie, H., Crowter, K., DeCesar, M., Demorest, P. B., Dolch, T., Ellis, J. A., Ferdman, R. D., Ferrara, E., Folkner, W. M., Fonseca, E., Garver-Daniels, N., Gentile, P. A., Haas, R., Hazboun, J. S., Huerta, E. A., Islo, K., Jenet, F., Jones, G., Jones, M. L., Kaplan, D. L., Kaspi, V. M., Lam, M. T., Lazio, T. J. W., Levin, L., Lommen, A. N., Lorimer, D. R., Luo, J., Lynch, R. S., Madison, D. R., McLaughlin, M. A., McWilliams, S. T., Mingarelli, C. M. F., Ng, C., Nice, D. J., Park, R. S., Pennucci, T. T., Pol, N. S., Ransom, S. M., Ray, P. S., Rasskazov, A., Siemens, X., Simon, J., Spiewak, R., Stairs, I. H., Stinebring, D. R., Stovall, K., Swiggum, J., Taylor, S. R., Vallisneri, M., Vigeland, S., & Zhu, W. W., *ArXiv e-prints*, January 2018a.

Arzoumanian, Z., Brazier, A., Burke-Spolaor, S., Chamberlin, S., Chatterjee, S., Christy, B., Cordes, J. M., Cornish, N. J., Crawford, F., Thankful Cromartie, H., Crowter, K., DeCesar, M. E., Demorest, P. B., Dolch, T., Ellis, J. A., Ferdman, R. D., Ferrara, E. C., Fonseca, E., Garver-Daniels, N., Gentile, P. A., Halmrast, D., Huerta, E. A., Jenet, F. A., Jessup, C., Jones, G., Jones, M. L., Kaplan, D. L., Lam, M. T., Lazio, T. J. W., Levin, L., Lommen, A., Lorimer, D. R., Luo, J., Lynch, R. S., Madison, D., Matthews, A. M., McLaughlin, M. A., McWilliams, S. T., Mingarelli, C., Ng, C., Nice, D. J., Pennucci, T. T., Ransom, S. M., Ray, P. S., Siemens, X., Simon, J., Spiewak, R., Stairs, I. H., Stinebring, D. R., Stovall, K., Swiggum, J. K., Taylor, S. R., Vallisneri,

M., van Haasteren, R., Vigeland, S. J., Zhu, W., & NANOGrav Collaboration, *ApJS*, 235(2):37, April 2018b.

Arzoumanian, Z., Brazier, A., Burke-Spolaor, S., Chamberlin, S., Chatterjee, S., Christy, B., Cordes, J. M., Cornish, N. J., Crawford, F., Thankful Cromartie, H., Crowter, K., DeCesar, M. E., Demorest, P. B., Dolch, T., Ellis, J. A., Ferdman, R. D., Ferrara, E. C., Fonseca, E., Garver-Daniels, N., Gentile, P. A., Halmrast, D., Huerta, E. A., Jenet, F. A., Jessup, C., Jones, G., Jones, M. L., Kaplan, D. L., Lam, M. T., Lazio, T. J. W., Levin, L., Lommen, A., Lorimer, D. R., Luo, J., Lynch, R. S., Madison, D., Matthews, A. M., McLaughlin, M. A., McWilliams, S. T., Mingarelli, C., Ng, C., Nice, D. J., Pennucci, T. T., Ransom, S. M., Ray, P. S., Siemens, X., Simon, J., Spiewak, R., Stairs, I. H., Stinebring, D. R., Stovall, K., Swiggum, J. K., Taylor, S. R., Vallisneri, M., van Haasteren, R., Vigeland, S. J., Zhu, W., & NANOGrav Collaboration, *ApJS*, 235(2):37, Apr 2018c.

Ashton, G., Lasky, P. D., Graber, V., & Palfreyman, J., *arXiv e-prints*, art. arXiv:1907.01124, Jul 2019.

Asseo, E. *Plasma Instabilities : Sources for Coherent Radio Emission.* In Johnston, S., Walker, M. A., & Bailes, M., editors, *IAU Colloq. 160: Pulsars: Problems and Progress*, volume 105 of *Astronomical Society of the Pacific Conference Series*, page 147, Jan 1996.

Asseo, E. & Porzio, A., *MNRAS*, 369(3):1469–1490, Jul 2006.

Baade, W. & Zwicky, F., *Contributions from the Mount Wilson Observatory*, 3:73–78, Jan 1934a.

Baade, W. & Zwicky, F., *Contributions from the Mount Wilson Observatory*, 3:79–83, Jan 1934b.

Baade, W. & Zwicky, F., *Physical Review*, 46(1):76–77, Jul 1934c.

Backer, D. C., *Nature*, 227(5259):692–695, Aug 1970a.

Backer, D. C., *Nature*, 228:1297–1298, December 1970b.

Backer, D. C., *Nature*, 228(5266):42–43, Oct 1970c.

Backer, D. C., Kulkarni, S. R., Heiles, C., Davis, M. M., & Goss, W. M., *Nature*, 300 (5893):615–618, Dec 1982.

Bailes, M. *Precision Timing at the Parkes 64-m Radio Telescope.* In Bailes, M., Nice, D. J., & Thorsett, S. E., editors, *Radio Pulsars*, volume 302 of *Astronomical Society of the Pacific Conference Series*, page 57, Jan 2003.

Bailes, M., Manchester, R. N., Kesteven, M. J., Norris, R. P., & Reynolds, J. E., *MNRAS*, 247:322, November 1990.

Bailes, M., Bates, S. D., Bhalerao, V., Bhat, N. D. R., Burgay, M., Burke-Spolaor, S., D'Amico, N., Johnston, S., Keith, M. J., Kramer, M., Kulkarni, S. R., Levin, L., Lyne, A. G., Milia, S., Possenti, A., Spitler, L., Stappers, B., & van Straten, W., *Science*, 333: 1717, September 2011.

Bailes, M., Barr, E., Bhat, N. D. R., Brink, J., Buchner, S., Burgay, M., Camilo, F., Champion, D. J., Hessels, J., Janssen, G. H., Jameson, A., Johnston, S., Karastergiou, A., Karuppusamy, R., Kaspi, V., Keith, M. J., Kramer, M., McLaughlin, M. A., Moodley, K., Oslowski, S., Possenti, A., Ransom, S. M., Rasio, F. A., Sievers, J., Serylak, M., Stappers, B. W., Stairs, I. H., Theureau, G., van Straten, W., Weltevrede, P., & Wex, N., *arXiv e-prints*, art. arXiv:1803.07424, Mar 2018.

Bak, P. *How nature works : the science of self-organized criticality.* 1996.

Bak, P., Tang, C., & Wiesenfeld, K., *Phys. Rev. A*, 38(1):364–374, Jul 1988.

Balanis, C. A. *Antenna theory : analysis and design.* 2005.

Bassa, C. G., Janssen, G. H., Stappers, B. W., Tauris, T. M., Wevers, T., Jonker, P. G., Lentati, L., Verbiest, J. P. W., Desvignes, G., Graikou, E., Guillemot, L., Freire, P. C. C., Lazarus, P., Caballero, R. N., Champion, D. J., Cognard, I., Jessner, A., Jordan, C., Karuppusamy, R., Kramer, M., Lazaridis, K., Lee, K. J., Liu, K., Lyne, A. G., McKee, J., Osłowski, S., Perrodin, D., Sanidas, S., Shaifullah, G., Smits, R., Theureau, G., Tiburzi, C., & Zhu, W. W., *MNRAS*, 460(2):2207–2222, Aug 2016.

Baym, G., Pethick, C., & Pines, D., *Nature*, 224:673–674, Nov 1969.

Belczynski, K., Kalogera, V., Rasio, F. A., Taam, R. E., Zezas, A., Bulik, T., Maccarone, T. J., & Ivanova, N., *ApJS*, 174(1):223–260, Jan 2008.

Beskin, V. S. & Nokhrina, E. E., *Ap&SS*, 308(1-4):569–573, Apr 2007.

Blandford, R. D., Applegate, J. H., & Hernquist, L., *MNRAS*, 204:1025–1048, Sep 1983.

Blandford, R. D. & Romani, R. W., *MNRAS*, 234:57P–60, Oct 1988.

Bolton, J. G., Stanley, G. J., & Slee, O. B., *Nature*, 164(4159):101–102, Jul 1949.

Bonanno, A. & Urpin, V., *MNRAS*, 451:2117–2122, August 2015.

Bothe, W. & Becker, H., *Zeitschrift fur Physik*, 66(5-6):289–306, May 1930.

Bowyer, S., Byram, E. T., Chubb, T. A., & Friedman, H., *Science*, 146(3646):912–917, Nov 1964.

Boynton, P. E., Groth, E. J., I., Partridge, R. B., & Wilkinson, D. T., *ApJ*, 157:L197, Sep 1969.

Boynton, P. E., Groth, E. J., Hutchinson, D. P., Nanos, G. P., J., Partridge, R. B., & Wilkinson, D. T., *ApJ*, 175:217, July 1972.

Brook, P. R., Karastergiou, A., Johnston, S., Kerr, M., Shannon, R. M., & Roberts, S. J., *MNRAS*, 456:1374–1393, Feb 2016.

Burgay, M., D'Amico, N., Possenti, A., Manchester, R. N., Lyne, A. G., Joshi, B. C., McLaughlin, M. A., Kramer, M., Sarkissian, J. M., Camilo, F., Kalogera, V., Kim, C., & Lorimer, D. R., *Nature*, 426(6966):531–533, Dec 2003.

Burke-Spolaor, S., Johnston, S., Bailes, M., Bates, S. D., Bhat, N. D. R., Burgay, M., Champion, D. J., D'Amico, N., Keith, M. J., Kramer, M., Levin, L., Milia, S., Possenti, A., Stappers, B., & van Straten, W., *MNRAS*, 423(2):1351–1367, Jun 2012.

Caballero, R. N., Lee, K. J., Lentati, L., Desvignes, G., Champion, D. J., Verbiest, J. P. W., Janssen, G. H., Stappers, B. W., Kramer, M., Lazarus, P., Possenti, A., Tiburzi, C., Perrodin, D., Osłowski, S., Babak, S., Bassa, C. G., Brem, P., Burgay, M., Cognard, I., Gair, J. R., Graikou, E., Guillemot, L., Hessels, J. W. T., Karuppusamy, R., Lassus, A., Liu, K., McKee, J., Mingarelli, C. M. F., Petiteau, A., Purver, M. B., Rosado, P. A., Sanidas, S., Sesana, A., Shaifullah, G., Smits, R., Taylor, S. R., Theureau, G., van Haasteren, R., & Vecchio, A., *MNRAS*, 457(4):4421–4440, Apr 2016.

Caballero, R. N., Guo, Y. J., Lee, K. J., Lazarus, P., Champion, D. J., Desvignes, G., Kramer, M., Plant, K., Arzoumanian, Z., Bailes, M., Bassa, C. G., Bhat, N. D. R., Brazier, A., Burgay, M., Burke-Spolaor, S., Chamberlin, S. J., Chatterjee, S., Cognard, I., Cordes, J. M., Dai, S., Demorest, P., Dolch, T., Ferdman, R. D., Fonseca, E., Gair, J. R., Garver-Daniels, N., Gentile, P., Gonzalez, M. E., Graikou, E., Guillemot, L., Hobbs, G., Janssen, G. H., Karuppusamy, R., Keith, M. J., Kerr, M., Lam, M. T., Lasky, P. D., Lazio, T. J. W., Levin, L., Liu, K., Lommen, A. N., Lorimer, D. R.,

Lynch, R. S., Madison, D. R., Manchester, R. N., McKee, J. W., McLaughlin, M. A., McWilliams, S. T., Mingarelli, C. M. F., Nice, D. J., Osłowski, S., Palliyaguru, N. T., Pennucci, T. T., Perera, B. B. P., Perrodin, D., Possenti, A., Ransom, S. M., Reardon, D. J., Sanidas, S. A., Sesana, A., Shaifullah, G., Shannon, R. M., Siemens, X., Simon, J., Spiewak, R., Stairs, I., Stappers, B., Stinebring, D. R., Stovall, K., Swiggum, J. K., Taylor, S. R., Theureau, G., Tiburzi, C., Toomey, L., van Haasteren, R., van Straten, W., Verbiest, J. P. W., Wang, J. B., Zhu, X. J., & Zhu, W. W., *MNRAS*, 481(4): 5501–5516, December 2018.

Cairns, I. H., Johnston, S., & Das, P., *MNRAS*, 353(1):270–286, Sep 2004.

Camilo, F., Ransom, S. M., Chatterjee, S., Johnston, S., & Demorest, P., *ApJ*, 746(1):63, Feb 2012.

Candy, B. N. & Blair, D. G., *ApJ*, 307:535, Aug 1986.

Carozzi, T. D. & Woan, G., *IEEE Transactions on Antennas and Propagation*, 59(6): 2058–2065, Jun 2011.

Chadwick, J., *Nature*, 129(3252):312, Feb 1932.

Chamberlin, S. J. & Siemens, X., *Phys. Rev. D*, 85(8):082001, April 2012.

Champion, D. J., Hobbs, G. B., Manchester, R. N., Edwards, R. T., Backer, D. C., Bailes, M., Bhat, N. D. R., Burke-Spolaor, S., Coles, W., Demorest, P. B., Ferdman, R. D., Folkner, W. M., Hotan, A. W., Kramer, M., Lommen, A. N., Nice, D. J., Purver, M. B., Sarkissian, J. M., Stairs, I. H., van Straten, W., Verbiest, J. P. W., & Yardley, D. R. B., *ApJ*, 720(2):L201–L205, Sep 2010.

Chandrasekhar, S., *ApJ*, 74:81, Jul 1931.

Cheng, K. S., *ApJ*, 321:799, Oct 1987a.

Cheng, K. S., *ApJ*, 321:805, October 1987b.

Cole, T. W., *Nature*, 223:487, August 1969.

Coles, W., Hobbs, G., Champion, D. J., Manchester, R. N., & Verbiest, J. P. W., *MNRAS*, 418:561–570, November 2011.

Collins, J. C. & Perry, M. J., *Phys. Rev. Lett.*, 34(21):1353–1356, May 1975.

Cordes, J. M., *ApJ*, 237:216–226, Apr 1980.

Cordes, J. M. & Downs, G. S., *ApJS*, 59:343–382, Nov 1985.

Cordes, J. M. & Greenstein, G., *ApJ*, 245:1060–1079, May 1981.

Cordes, J. M. & Helfand, D. J., *ApJ*, 239:640–650, Jul 1980.

Cordes, J. M. & Lazio, T. J. W., *arXiv e-prints*, art. astro-ph/0207156, July 2002.

Cordes, J. M. & Shannon, R. M., *ApJ*, 682(2):1152–1165, Aug 2008.

Cordes, J. M. & Shannon, R. M., *arXiv e-prints*, art. arXiv:1010.3785, Oct 2010.

Cordes, J. M., Kramer, M., Lazio, T. J. W., Stappers, B. W., Backer, D. C., & Johnston, S., , 48(11-12):1413–1438, Dec 2004.

Cornish, N. J., O'Beirne, L., Taylor, S. R., & Yunes, N., *Phys. Rev. Lett.*, 120(18):181101, May 2018.

Cromartie, H. T., Fonseca, E., Ransom, S. M., Demorest, P. B., Arzoumanian, Z., Blumer, H., Brook, P. R., DeCesar, M. E., Dolch, T., Ellis, J. A., Ferdman, R. D., Ferrara, E. C., Garver-Daniels, N., Gentile, P. A., Jones, M. L., Lam, M. T., Lorimer, D. R., Lynch, R. S., McLaughlin, M. A., Ng, C., Nice, D. J., Pennucci, T. T., Spiewak, R., Stairs, I. H., Stovall, K., Swiggum, J. K., & Zhu, W. W., *Nature Astronomy*, 4:72–76, January 2020.

Cui, X. H., Wang, H. G., Xu, R. X., & Qiao, G. J., *A&A*, 472:1–3, September 2007.

D'Alessandro, F., McCulloch, P. M., King, E. A., Hamilton, P. A., & McConnell, D., *MNRAS*, 261:883–894, Apr 1993a.

D'Alessandro, F., McCulloch, P. M., King, E. A., Hamilton, P. A., & McConnell, D., *MNRAS*, 261:883–894, Apr 1993b.

Damour, T. & Vilenkin, A., *Physical Review Letters*, 85:3761–3764, October 2000.

Damour, T. & Taylor, J. H., *Phys. Rev. D*, 45(6):1840–1868, Mar 1992.

Davies, J. G., Hunt, G. C., & Smith, F. G., *Nature*, 221:27–29, January 1969.

Demorest, P. B., Pennucci, T., Ransom, S. M., Roberts, M. S. E., & Hessels, J. W. T., *Nature*, 467(7319):1081–1083, Oct 2010.

Demorest, P. B., Ferdman, R. D., Gonzalez, M. E., Nice, D., Ransom, S., Stairs, I. H., Arzoumanian, Z., Brazier, A., Burke-Spolaor, S., Chamberlin, S. J., Cordes, J. M., Ellis, J., Finn, L. S., Freire, P., Giampanis, S., Jenet, F., Kaspi, V. M., Lazio, J., Lommen, A. N., McLaughlin, M., Palliyaguru, N., Perrodin, D., Shannon, R. M., Siemens, X., Stinebring, D., Swiggum, J., & Zhu, W. W., *ApJ*, 762(2):94, Jan 2013.

Detweiler, S., *ApJ*, 234:1100–1104, December 1979.

Dexter, J., Deller, A., Bower, G. C., Demorest, P., Kramer, M., Stappers, B. W., Lyne, A. G., Kerr, M., Spitler, L. G., Psaltis, D., Johnson, M., & Narayan, R., *MNRAS*, 471: 3563–3576, November 2017.

Dib, R. & Kaspi, V. M., *ApJ*, 784:37, March 2014.

Dowd, A., Sisk, W., & Hagen, J. *WAPP — Wideband Arecibo Pulsar Processor.* In Kramer, M., Wex, N., & Wielebinski, R., editors, *IAU Colloq. 177: Pulsar Astronomy - 2000 and Beyond*, volume 202 of *Astronomical Society of the Pacific Conference Series*, pages 275–276, Jan 2000.

Downs, G. S. & Reichley, P. E., *ApJS*, 53:169–240, Sep 1983.

Drake, F. D. & Craft, H. D., *Nature*, 220(5164):231–235, Oct 1968.

Duncan, J. C., *ApJ*, 89:482, May 1939.

Duncan, R. C. & Thompson, C., *ApJ*, 392:L9, Jun 1992.

Dunning, A., Bowen, M., Bourne, M., Hayman, D., & Smith, S. L. *An ultra-wideband dielectrically loaded quad-ridged feed horn for radio astronomy.* In *2015 IEEE-APS Topical Conference on Antennas and Propagation in Wireless Communications (APWC)*, pages 787–790, Sept 2015. doi: 10.1109/APWC.2015.7300180.

Eatough, R. P., Falcke, H., Karuppusamy, R., Lee, K. J., Champion, D. J., Keane, E. F., Desvignes, G., Schnitzeler, D. H. F. M., Spitler, L. G., Kramer, M., Klein, B., Bassa, C., Bower, G. C., Brunthaler, A., Cognard, I., Deller, A. T., Demorest, P. B., Freire, P. C. C., Kraus, A., Lyne, A. G., Noutsos, A., Stappers, B., & Wex, N., *Nature*, 501: 391–394, September 2013.

Eddington, A. S., *Nature*, 117(2948):25–32, May 1926.

Edwards, R. T. & Stappers, B. W., *A&A*, 407:273–287, Aug 2003.

Edwards, R. T., Hobbs, G. B., & Manchester, R. N., *MNRAS*, 372(4):1549–1574, Nov 2006.

Espinoza, C. M., Lyne, A. G., Kramer, M., Manchester, R. N., & Kaspi, V. M., *ApJ*, 741 (1):L13, Nov 2011a.

Espinoza, C. M., Lyne, A. G., Stappers, B. W., & Kramer, M., *MNRAS*, 414:1679–1704, June 2011b.

Espinoza, C. M., Lyne, A. G., & Stappers, B. W., *MNRAS*, 466:147–162, Apr 2017.

Esposito, P., Israel, G. L., Turolla, R., Mattana, F., Tiengo, A., Possenti, A., Zane, S., Rea, N., Burgay, M., Götz, D., Mereghetti, S., Stella, L., Wieringa, M. H., Sarkissian, J. M., Enoto, T., Romano, P., Sakamoto, T., Nakagawa, Y. E., Makishima, K., Nakazawa, K., Nishioka, H., & François-Martin, C., *MNRAS*, 416(1):205–215, Sep 2011.

Ferdman, R. D., Archibald, R. F., Gourgouliatos, K. N., & Kaspi, V. M., *ApJ*, 852(2): 123, Jan 2018.

Feroz, F., Hobson, M. P., & Bridges, M., *MNRAS*, 398:1601–1614, October 2009.

Feroz, F., Hobson, M. P., & Bridges, M. *MultiNest: Efficient and Robust Bayesian Inference*, Sep 2011.

Ferrari, A. & Ruffini, R., *ApJ*, 158:L71, Nov 1969.

Foster, G., Karastergiou, A., Paulin, R., Carozzi, T. D., Johnston, S., & van Straten, W., *MNRAS*, 453(2):1489–1502, Oct 2015.

Foster, R. S. & Backer, D. C., *ApJ*, 361:300–308, September 1990.

Fowler, R. H., *MNRAS*, 87:114–122, Dec 1926.

Frail, D. A., Goss, W. M., & Whiteoak, J. B. Z., *ApJ*, 437:781, Dec 1994.

Freire, P. *Super-Massive Neutron Stars*. In *American Astronomical Society Meeting Abstracts #211*, volume 211 of *American Astronomical Society Meeting Abstracts*, page 161.01, March 2008.

Freire, P. C. C., Kramer, M., & Wex, N., *Classical and Quantum Gravity*, 29(18):184007, Sep 2012.

Fuentes, J. R., Espinoza, C. M., Reisenegger, A., Shaw, B., Stappers, B. W., & Lyne, A. G., *A&A*, 608:A131, Dec 2017.

Gaensler, B. M. & Johnston, S., *MNRAS*, 275(4):L73–L75, Aug 1995.

Gair, J. R., Romano, J. D., & Taylor, S. R., *Phys. Rev. D*, 92(10):102003, November 2015.

Gavriil, F. P., Kaspi, V. M., & Woods, P. M., *Nature*, 419(6903):142–144, Sep 2002.

Gavriil, F. P., Gonzalez, M. E., Gotthelf, E. V., Kaspi, V. M., Livingstone, M. A., & Woods, P. M., *Science*, 319:1802, March 2008.

Gil, J. A. & Sendyk, M., *ApJ*, 541(1):351–366, Sep 2000.

Ginzburg, V. L. & Zhelezniakov, V. V., *ARA&A*, 13:511–535, Jan 1975.

Glampedakis, K. & Andersson, N., *Physical Review Letters*, 102(14):141101, April 2009.

Gold, T., *Nature*, 218(5143):731–732, May 1968.

Goldreich, P. & Julian, W. H., *ApJ*, 157:869, Aug 1969.

Granet, C., Zhang, H. Z., Forsyth, A. R., Graves, G. R., Doherty, P., Greene, K. J., James, G. L., Sykes, P., Bird, T. S., Sinclair, M. W., Moorey, G., & Manchester, R. N., *IEEE Antennas and Propagation Magazine*, 47(3):13–19, Jun 2005.

Greenstein, G., *Nature*, 227:791–794, Aug 1970.

Grishchuk, L. P., *Physics Uspekhi*, 48:1235–1247, December 2005.

Grishchuk, L. P. & Sidorov, I. V., *Classical and Quantum Gravity*, 6:L155–L160, September 1989.

Groth, E. J., *ApJS*, 29:453–465, Nov 1975.

Gunn, J. E. & Ostriker, J. P., *Nature*, 221:454–456, Feb 1969.

Guo, Y. J., Lee, K. J., & Caballero, R. N., *MNRAS*, 475(3):3644–3653, April 2018.

Hampson, G., Macleod, A., Beresford, R., Brothers, M., Brown, A., Bunton, J., Cantrall, C., Chekkala, R., Cheng, W., Forsyth, R., Gough, R., Hay, S., Kanapathippillai, J., Kiraly, D., Leach, M., Morison, N., Neuhold, S., Roberts, P., Shaw, R., Schinckel, A., Shields, M., & Tuthill, J. *ASKAP PAF ADE — Advancing an L-band PAF design towards SKA*. In *2012 International Conference on Electromagnetics in Advanced Applications*, pages 807–809, Sept 2012. doi: 10.1109/ICEAA.2012.6328742.

Hankins, T. H. & Rickett, B. J. *Pulsar signal processing*. In *Methods in Computational Physics. Volume 14 - Radio astronomy*, volume 14, pages 55–129, Jan 1975.

Harding, A. K., Contopoulos, I., & Kazanas, D., *ApJ*, 525:L125–L128, Nov 1999.

Harrison, E. R. & Tademaru, E., *ApJ*, 201:447–461, October 1975.

Haskell, B. & Melatos, A., *International Journal of Modern Physics D*, 24:1530008, Jan 2015.

Helfand, D. J., Manchester, R. N., & Taylor, J. H., *ApJ*, 198:661–670, June 1975.

Hellings, R. W. & Downs, G. S., *ApJ*, 265:L39–L42, February 1983.

Hess, V. F. & Steinmaurer, R., *Nature*, 135(3416):617–618, Apr 1935.

Hessels, J., Possenti, A., Bailes, M., Bassa, C., Freire, P. C. C., Lorimer, D. R., Lynch, R., Ransom, S. M., & Stairs, I. H. *Pulsars in Globular Clusters with the SKA*. In *Advancing Astrophysics with the Square Kilometre Array (AASKA14)*, page 47, Apr 2015.

Hessels, J. W. T., Ransom, S. M., Stairs, I. H., Freire, P. C. C., Kaspi, V. M., & Camilo, F., *Science*, 311(5769):1901–1904, Mar 2006.

Heuvel, E. P. J. V. D. *Compact stars and the evolution of binary systems*, pages 55–73. 2011.

Hewish, A., *Proceedings of the Royal Society of London Series A*, 209(1096):81–96, Oct 1951.

Hewish, A., *Proceedings of the Royal Society of London Series A*, 228(1173):238–251, Feb 1955.

Hewish, A. & Ryle, M., *MmRAS*, 67:97, Jan 1955.

Hewish, A., Bell, S. J., Pilkington, J. D. H., Scott, P. F., & Collins, R. A., *Nature*, 224 (5218):472, Nov 1969.

Ho, W. C. G. & Andersson, N., *Nature Physics*, 8:787–789, Nov 2012.

Hobbs, G., *ArXiv e-prints*, November 2009.

Hobbs, G., Lyne, A. G., Kramer, M., Martin, C. E., & Jordan, C., *MNRAS*, 353:1311–1344, October 2004.

Hobbs, G., Lorimer, D. R., Lyne, A. G., & Kramer, M., *MNRAS*, 360:974–992, July 2005.

Hobbs, G., Archibald, A., Arzoumanian, Z., Backer, D., Bailes, M., Bhat, N. D. R., Burgay, M., Burke-Spolaor, S., Champion, D., Cognard, I., Coles, W., Cordes, J., Demorest, P., Desvignes, G., Ferdman, R. D., Finn, L., Freire, P., Gonzalez, M., Hessels, J., Hotan, A., Janssen, G., Jenet, F., Jessner, A., Jordan, C., Kaspi, V., Kramer, M., Kondratiev, V., Lazio, J., Lazaridis, K., Lee, K. J., Levin, Y., Lommen, A., Lorimer, D., Lynch, R., Lyne, A., Manchester, R., McLaughlin, M., Nice, D., Oslowski, S., Pilia, M., Possenti, A., Purver, M., Ransom, S., Reynolds, J., Sanidas, S., Sarkissian, J., Sesana, A., Shannon, R., Siemens, X., Stairs, I., Stappers, B., Stinebring, D., Theureau, G., van Haasteren, R., van Straten, W., Verbiest, J. P. W., Yardley, D. R. B., & You, X. P., *Classical and Quantum Gravity*, 27(8):084013, Apr 2010a.

Hobbs, G., Lyne, A. G., & Kramer, M., *MNRAS*, 402(2):1027–1048, Feb 2010b.

Hobbs, G., Coles, W., Manchester, R. N., Keith, M. J., Shannon, R. M., Chen, D., Bailes, M., Bhat, N. D. R., Burke-Spolaor, S., Champion, D., Chaudhary, A., Hotan, A., Khoo, J., Kocz, J., Levin, Y., Oslowski, S., Preisig, B., Ravi, V., Reynolds, J. E., Sarkissian, J., van Straten, W., Verbiest, J. P. W., Yardley, D., & You, X. P., *MNRAS*, 427(4): 2780–2787, Dec 2012.

Hobbs, G., Guo, L., Caballero, R. N., Coles, W., Lee, K. J., Manchester, R. N., Reardon, D. J., Matsakis, D., Tong, M. L., Arzoumanian, Z., Bailes, M., Bassa, C. G., Bhat, N. D. R., Brazier, A., Burke-Spolaor, S., Champion, D. J., Chatterjee, S., Cognard, I., Dai, S., Desvignes, G., Dolch, T., Ferdman, R. D., Graikou, E., Guillemot, L., Janssen, G. H., Keith, M. J., Kerr, M., Kramer, M., Lam, M. T., Liu, K., Lyne, A., Lazio, T. J. W., Lynch, R., McKee, J. W., McLaughlin, M. A., Mingarelli, C. M. F., Nice, D. J., Osłowski, S., Pennucci, T. T., Perera, B. B. P., Perrodin, D., Possenti, A., Russell, C. J., Sanidas, S., Sesana, A., Shaifullah, G., Shannon, R. M., Simon, J., Spiewak, R., Stairs, I. H., Stappers, B. W., Swiggum, J. K., Taylor, S. R., Theureau, G., Toomey, L., van Haasteren, R., Wang, J. B., Wang, Y., & Zhu, X. J., *MNRAS*, 491(4):5951–5965, February 2020.

Hobbs, G. B., Edwards, R. T., & Manchester, R. N., *MNRAS*, 369(2):655–672, Jun 2006.

Hotan, A. W., Bailes, M., & Ord, S. M., *MNRAS*, 355(3):941–949, Dec 2004a.

Hotan, A. W., van Straten, W., & Manchester, R. N., , 21(3):302–309, Jan 2004b.

Hotan, A. W., Bailes, M., & Ord, S. M., *MNRAS*, 362(4):1267–1272, Oct 2005.

Hotan, A. W., Bailes, M., & Ord, S. M., *MNRAS*, 369(3):1502–1520, Jul 2006a.

Hotan, A. W., Bailes, M., & Ord, S. M., *MNRAS*, 369(3):1502–1520, Jul 2006b.

Hotan, A. W., Long, S. R., Dickey, J. M., & Dolley, T. J., *ApJ*, 668(1):449–455, Oct 2007.

Hubble, E. P., *Leaflet of the Astronomical Society of the Pacific*, 1(14):55, Jan 1928.

Hulse, R. A. & Taylor, J. H., *ApJ*, 195:L51–L53, January 1975.

Jackson, J. D. *Classical electrodynamics*. 1975.

Jaffe, A. H. & Backer, D. C., *ApJ*, 583:616–631, February 2003.

Janka, H.-T., *Annual Review of Nuclear and Particle Science*, 62:407–451, November 2012.

Jankowski, F., van Straten, W., Keane, E. F., Bailes, M., Barr, E. D., Johnston, S., & Kerr, M., *MNRAS*, 473(4):4436–4458, Feb 2018.

Janssen, G., Hobbs, G., McLaughlin, M., Bassa, C., Deller, A., Kramer, M., Lee, K., Mingarelli, C., Rosado, P., Sanidas, S., Sesana, A., Shao, L., Stairs, I., Stappers, B., & Verbiest, J. P. W. *Gravitational Wave Astronomy with the SKA*. In *Advancing Astrophysics with the Square Kilometre Array (AASKA14)*, page 37, Apr 2015.

Jenet, F. A. & Anderson, S. B., *PASP*, 110(754):1467–1478, Dec 1998.

Jenet, F. A., Cook, W. R., Prince, T. A., & Unwin, S. C., *PASP*, 109:707–718, Jun 1997.

Jenet, F. A., Anderson, S. B., Kaspi, V. M., Prince, T. A., & Unwin, S. C., *ApJ*, 498: 365–372, May 1998.

Jenet, F. A., Anderson, S. B., & Prince, T. A., *ApJ*, 546(1):394–400, Jan 2001a.

Jenet, F. A., Anderson, S. B., & Prince, T. A., *ApJ*, 546(1):394–400, Jan 2001b.

Jenet, F. A. & Gil, J., *ApJ*, 596(2):L215–L218, Oct 2003.

Jenet, F. A. & Gil, J., *ApJ*, 602(2):L89–L92, Feb 2004.

Jenet, F. A., Lommen, A., Larson, S. L., & Wen, L., *The Astrophysical Journal*, 606(2): 799, 2004.

Jenet, F. A., Hobbs, G. B., Lee, K. J., & Manchester, R. N., *ApJ*, 625(2):L123–L126, Jun 2005.

Johnston, S. & Galloway, D., *MNRAS*, 306:L50–L54, July 1999.

Johnston, S. & Karastergiou, A., *MNRAS*, 467:3493–3499, May 2017.

Johnston, S. & Karastergiou, A., *MNRAS*, 485(1):640–647, May 2019.

Johnston, S., Hobbs, G., Vigeland, S., Kramer, M., Weisberg, J. M., & Lyne, A. G., *MNRAS*, 364:1397–1412, December 2005.

Jonas, J. & MeerKAT Team. *The MeerKAT Radio Telescope*. In *Proceedings of MeerKAT Science: On the Pathway to the SKA. 25-27 May*, page 1, Jan 2016.

Jones, M. L., McLaughlin, M. A., Lam, M. T., Cordes, J. M., Levin, L., Chatterjee, S., Arzoumanian, Z., Crowter, K., Demorest, P. B., Dolch, T., Ellis, J. A., Ferdman, R. D., Fonseca, E., Gonzalez, M. E., Jones, G., Lazio, T. J. W., Nice, D. J., Pennucci, T. T., Ransom, S. M., Stinebring, D. R., Stairs, I. H., Stovall, K., Swiggum, J. K., & Zhu, W. W., *ApJ*, 841(2):125, Jun 2017.

Jones, P. B., *MNRAS*, 246:364, September 1990.

Kaplan, D. B. & Nelson, A. E., *Physics Letters B*, 175(1):57–63, Jul 1986.

Kaplan, D. L., Kupfer, T., Nice, D. J., Irrgang, A., Heber, U., Arzoumanian, Z., Beklen, E., Crowter, K., DeCesar, M. E., Demorest, P. B., Dolch, T., Ellis, J. A., Ferdman, R. D., Ferrara, E. C., Fonseca, E., Gentile, P. A., Jones, G., Jones, M. L., Kreuzer, S., Lam, M. T., Levin, L., Lorimer, D. R., Lynch, R. S., McLaughlin, M. A., Miller, A. A., Ng, C., Pennucci, T. T., Prince, T. A., Ransom, S. M., Ray, P. S., Spiewak, R., Stairs, I. H., Stovall, K., Swiggum, J., & Zhu, W., *ApJ*, 826(1):86, Jul 2016.

Karastergiou, A., Johnston, S., Karastergiou, A., Johnston, S., Andersson, N., Breton, R., Brook, P., Gwinn, C., Lewandowska, N., Keane, E., Kramer, M., Macquart, J. P., Serylak, M., Shannon, R., Stappers, B., van Leeuwen, J., Verbiest, J., Weltevrede, P., & Wright, G. *Understanding pulsar magnetospheres with the SKA*. In *Advancing Astrophysics with the Square Kilometre Array (AASKA14)*, page 38, Apr 2015.

Kaspi, V. M., *Proceedings of the National Academy of Science*, 107:7147–7152, April 2010.

Kaspi, V. M., Manchester, R. N., Siegman, B., Johnston, S., & Lyne, A. G., *ApJ*, 422: L83, February 1994a.

Kaspi, V. M., Taylor, J. H., & Ryba, M. F., *ApJ*, 428:713, Jun 1994b.

Kaspi, V. M., *Ap&SS*, 308(1-4):1–11, Apr 2007.

Kaspi, V. M. & Beloborodov, A. M., *ARA&A*, 55(1):261–301, Aug 2017.

Keane, E., Bhattacharyya, B., Kramer, M., Stappers, B., Keane, E. F., Bhattacharyya, B., Kramer, M., Stappers, B. W., Bates, S. D., Burgay, M., Chatterjee, S., Champion, D. J., Eatough, R. P., Hessels, J. W. T., Janssen, G., Lee, K. J., van Leeuwen, J., Margueron, J., Oertel, M., Possenti, A., Ransom, S., Theureau, G., & Torne, P. *A Cosmic Census of Radio Pulsars with the SKA*. In *Advancing Astrophysics with the Square Kilometre Array (AASKA14)*, page 40, Apr 2015.

Keane, E. F. & Kramer, M., *MNRAS*, 391(4):2009–2016, Dec 2008.

Keith, M. J., Johnston, S., Ray, P. S., Ferrara, E. C., Saz Parkinson, P. M., Çelik, Ö., Belfiore, A., Donato, D., Cheung, C. C., Abdo, A. A., Camilo, F., Freire, P. C. C., Guillemot, L., Harding, A. K., Kramer, M., Michelson, P. F., Ransom, S. M., Romani, R. W., Smith, D. A., Thompson, D. J., Weltevrede, P., & Wood, K. S., *MNRAS*, 414 (2):1292–1300, Jun 2011.

Keith, M. J., Coles, W., Shannon, R. M., Hobbs, G. B., Manchester, R. N., Bailes, M., Bhat, N. D. R., Burke-Spolaor, S., Champion, D. J., Chaudhary, A., Hotan, A. W., Khoo, J., Kocz, J., Osłowski, S., Ravi, V., Reynolds, J. E., Sarkissian, J., van Straten, W., & Yardley, D. R. B., *MNRAS*, 429(3):2161–2174, Mar 2013.

Kerr, M., Johnston, S., Hobbs, G., & Shannon, R. M., *ApJ*, 809:L11, August 2015.

Kerr, M., Hobbs, G., Johnston, S., & Shannon, R. M., *MNRAS*, 455(2):1845–1854, Jan 2016.

Kiziltan, B., Kottas, A., De Yoreo, M., & Thorsett, S. E., *ArXiv e-prints*, September 2013.

Kramer, M. *Fundamental Physics with the SKA: Strong-Field Tests of Gravity Using Pulsars and Black Holes*, page 87. 2007.

Kramer, M., Backer, D. C., Cordes, J. M., Lazio, T. J. W., Stappers, B. W., & Johnston, S., , 48(11-12):993–1002, Dec 2004.

Kramer, M., Lyne, A. G., O'Brien, J. T., Jordan, C. A., & Lorimer, D. R., *Science*, 312 (5773):549–551, Apr 2006a.

Kramer, M., Stairs, I. H., Manchester, R. N., McLaughlin, M. A., Lyne, A. G., Ferdman, R. D., Burgay, M., Lorimer, D. R., Possenti, A., D'Amico, N., Sarkissian, J. M., Hobbs, G. B., Reynolds, J. E., Freire, P. C. C., & Camilo, F., *Science*, 314:97–102, October 2006b.

Kramer, M., Stairs, I., Manchester, R., McLaughlin, M., Lyne, A., Ferdman, R., Burgay, M., Lorimer, D., Possenti, A., D'Amico, N., Sarkissian, J., Joshi, B., Freire, P., & Camilo, F., *Annalen der Physik*, 15(1-2):34–42, 2006. ISSN 1521-3889.

Kramer, M., Menten, K., Barr, E. D., Karuppusamy, R., Kasemann, C., Klein, B., Ros, E., Wieching, G., & Wucknitz, O. *The MeerKAT Max-Planck S-band System.* In *Proceedings of MeerKAT Science: On the Pathway to the SKA. 25-27 May*, page 3, Jan 2016.

Kramer, M., Lange, C., Lorimer, D. R., Backer, D. C., Xilouris, K. M., Jessner, A., & Wielebinski, R., *ApJ*, 526(2):957–975, Dec 1999.

Lai, D. *Neutron Star Kicks and Asymmetric Supernovae.* In Blaschke, D., Glendenning, N. K., & Sedrakian, A., editors, *Physics of Neutron Star Interiors*, volume 578 of *Lecture Notes in Physics, Berlin Springer Verlag*, page 424, 2001.

Lai, D. & Goldreich, P., *ApJ*, 535:402–411, May 2000.

Lai, D. & Qian, Y.-Z., *ApJ*, 505:844–853, October 1998.

Lam, M. T., Cordes, J. M., Chatterjee, S., Arzoumanian, Z., Crowter, K., Demorest, P. B., Dolch, T., Ellis, J. A., Ferdman, R. D., Fonseca, E., Gonzalez, M. E., Jones, G., Jones, M. L., Levin, L., Madison, D. R., McLaughlin, M. A., Nice, D. J., Pennucci, T. T., Ransom, S. M., Shannon, R. M., Siemens, X., Stairs, I. H., Stovall, K., Swiggum, J. K., & Zhu, W. W., *ApJ*, 834(1):35, Jan 2017.

Lam, M. T., McLaughlin, M. A., Arzoumanian, Z., Blumer, H., Brook, P. R., Cromartie, H. T., Demorest, P. B., DeCesar, M. E., Dolch, T., Ellis, J. A., Ferdman, R. D., Ferrara, E. C., Fonseca, E., Garver-Daniels, N., Gentile, P. A., Jones, M. L., Lorimer, D. R., Lynch, R. S., Ng, C., Nice, D. J., Pennucci, T. T., Ransom, S. M., Spiewak, R., Stairs, I. H., Stovall, K., Swiggum, J. K., Vigeland, S. J., & Zhu, W. W., *ApJ*, 872(2):193, Feb 2019.

Lampland, C. ., 1921.

Landau, L., *Nature*, 141(3564):333–334, Feb 1938.

Landau, L. D., *Phys. Zs. Sowjet*, 1:285, Dec 1932.

Lasky, P. D., Mingarelli, C. M. F., Smith, T. L., Giblin, J. T., Thrane, E., Reardon, D. J., Caldwell, R., Bailes, M., Bhat, N. D. R., Burke-Spolaor, S., Dai, S., Dempsey,

J., Hobbs, G., Kerr, M., Levin, Y., Manchester, R. N., Osłowski, S., Ravi, V., Rosado, P. A., Shannon, R. M., Spiewak, R., van Straten, W., Toomey, L., Wang, J., Wen, L., You, X., & Zhu, X., *Physical Review X*, 6(1):011035, January 2016.

Lattimer, J. M. & Prakash, M., *Science*, 304(5670):536–542, Apr 2004.

Lattimer, J. M. *Neutron Stars as a Probe of the Equation of State.* In *22nd Texas Symposium on Relativistic Astrophysics*, page 42, Jan 2004.

Lattimer, J. M. & Prakash, M., *Phys. Rep.*, 442(1-6):109–165, Apr 2007.

Lazarus, P., Karuppusamy, R., Graikou, E., Caballero, R. N., Champion, D. J., Lee, K. J., Verbiest, J. P. W., & Kramer, M., *MNRAS*, 458(1):868–880, May 2016.

Lazio, T. J. W., *Classical and Quantum Gravity*, 30(22):224011, Nov 2013.

Lee, K. J., Jenet, F. A., & Price, R. H., *ApJ*, 685:1304-1319, October 2008.

Lentati, L. & Shannon, R. M., *MNRAS*, 454:1058–1072, November 2015.

Lentati, L., Alexander, P., Hobson, M. P., Feroz, F., van Haasteren, R., Lee, K. J., & Shannon, R. M., *MNRAS*, 437:3004–3023, January 2014.

Lentati, L., Alexander, P., & Hobson, M. P., *MNRAS*, 447:2159–2168, March 2015a.

Lentati, L., Taylor, S. R., Mingarelli, C. M. F., Sesana, A., Sanidas, S. A., Vecchio, A., Caballero, R. N., Lee, K. J., van Haasteren, R., Babak, S., Bassa, C. G., Brem, P., Burgay, M., Champion, D. J., Cognard, I., Desvignes, G., Gair, J. R., Guillemot, L., Hessels, J. W. T., Janssen, G. H., Karuppusamy, R., Kramer, M., Lassus, A., Lazarus, P., Liu, K., Osłowski, S., Perrodin, D., Petiteau, A., Possenti, A., Purver, M. B., Rosado, P. A., Smits, R., Stappers, B., Theureau, G., Tiburzi, C., & Verbiest, J. P. W., *MNRAS*, 453(3):2576–2598, Nov 2015b.

Lentati, L., Shannon, R. M., Coles, W. A., Verbiest, J. P. W., van Haasteren, R., Ellis, J. A., Caballero, R. N., Manchester, R. N., Arzoumanian, Z., Babak, S., Bassa, C. G., Bhat, N. D. R., Brem, P., Burgay, M., Burke-Spolaor, S., Champion, D., Chatterjee, S., Cognard, I., Cordes, J. M., Dai, S., Demorest, P., Desvignes, G., Dolch, T., Ferdman, R. D., Fonseca, E., Gair, J. R., Gonzalez, M. E., Graikou, E., Guillemot, L., Hessels, J. W. T., Hobbs, G., Janssen, G. H., Jones, G., Karuppusamy, R., Keith, M., Kerr, M., Kramer, M., Lam, M. T., Lasky, P. D., Lassus, A., Lazarus, P., Lazio, T. J. W., Lee, K. J., Levin, L., Liu, K., Lynch, R. S., Madison, D. R., McKee, J., McLaughlin,

M., McWilliams, S. T., Mingarelli, C. M. F., Nice, D. J., Osłowski, S., Pennucci, T. T., Perera, B. B. P., Perrodin, D., Petiteau, A., Possenti, A., Ransom, S. M., Reardon, D., Rosado, P. A., Sanidas, S. A., Sesana, A., Shaifullah, G., Siemens, X., Smits, R., Stairs, I., Stappers, B., Stinebring, D. R., Stovall, K., Swiggum, J., Taylor, S. R., Theureau, G., Tiburzi, C., Toomey, L., Vallisneri, M., van Straten, W., Vecchio, A., Wang, J. B., Wang, Y., You, X. P., Zhu, W. W., & Zhu, X. J., *MNRAS*, 458:2161–2187, May 2016a.

Lentati, L., Shannon, R. M., Coles, W. A., Verbiest, J. P. W., van Haasteren, R., Ellis, J. A., Caballero, R. N., Manchester, R. N., Arzoumanian, Z., Babak, S., Bassa, C. G., Bhat, N. D. R., Brem, P., Burgay, M., Burke-Spolaor, S., Champion, D., Chatterjee, S., Cognard, I., Cordes, J. M., Dai, S., Demorest, P., Desvignes, G., Dolch, T., Ferdman, R. D., Fonseca, E., Gair, J. R., Gonzalez, M. E., Graikou, E., Guillemot, L., Hessels, J. W. T., Hobbs, G., Janssen, G. H., Jones, G., Karuppusamy, R., Keith, M., Kerr, M., Kramer, M., Lam, M. T., Lasky, P. D., Lassus, A., Lazarus, P., Lazio, T. J. W., Lee, K. J., Levin, L., Liu, K., Lynch, R. S., Madison, D. R., McKee, J., McLaughlin, M., McWilliams, S. T., Mingarelli, C. M. F., Nice, D. J., Osłowski, S., Pennucci, T. T., Perera, B. B. P., Perrodin, D., Petiteau, A., Possenti, A., Ransom, S. M., Reardon, D., Rosado, P. A., Sanidas, S. A., Sesana, A., Shaifullah, G., Siemens, X., Smits, R., Stairs, I., Stappers, B., Stinebring, D. R., Stovall, K., Swiggum, J., Taylor, S. R., Theureau, G., Tiburzi, C., Toomey, L., Vallisneri, M., van Straten, W., Vecchio, A., Wang, J. B., Wang, Y., You, X. P., Zhu, W. W., & Zhu, X. J., *MNRAS*, 458(2):2161–2187, May 2016b.

Lentati, L., Kerr, M., Dai, S., Hobson, M. P., Shannon, R. M., Hobbs, G., Bailes, M., Bhat, N. D. R., Burke-Spolaor, S., Coles, W., Dempsey, J., Lasky, P. D., Levin, Y., Manchester, R. N., Osłowski, S., Ravi, V., Reardon, D. J., Rosado, P. A., Spiewak, R., van Straten, W., Toomey, L., Wang, J., Wen, L., You, X., & Zhu, X., *MNRAS*, 466: 3706–3727, April 2017a.

Lentati, L., Kerr, M., Dai, S., Shannon, R. M., Hobbs, G., & Osłowski, S., *MNRAS*, 468 (2):1474–1485, Jun 2017b.

Lentati, L., Alexander, P., Hobson, M. P., Taylor, S., Gair, J., Balan, S. T., & van Haasteren, R., *Phys. Rev. D*, 87:104021, May 2013.

Li, L., Wang, N., Yuan, J. P., Wang, J. B., Hobbs, G., Lentati, L., & Manchester, R. N., *MNRAS*, 460:4011–4017, August 2016.

Liao, Y.-W., Chang, T.-C., Kuo, C.-Y., Masui, K. W., Oppermann, N., Pen, U.-L., & Peterson, J. B., *ApJ*, 833(2):289, Dec 2016.

Lindegren, L., Hernández, J., Bombrun, A., Klioner, S., Bastian, U., Ramos-Lerate, M., de Torres, A., Steidelmüller, H., Stephenson, C., Hobbs, D., Lammers, U., Biermann, M., Geyer, R., Hilger, T., Michalik, D., Stampa, U., McMillan, P. J., Castañeda, J., Clotet, M., Comoretto, G., Davidson, M., Fabricius, C., Gracia, G., Hambly, N. C., Hutton, A., Mora, A., Portell, J., van Leeuwen, F., Abbas, U., Abreu, A., Altmann, M., Andrei, A., Anglada, E., Balaguer-Núñez, L., Barache, C., Becciani, U., Bertone, S., Bianchi, L., Bouquillon, S., Bourda, G., Brüsemeister, T., Bucciarelli, B., Busonero, D., Buzzi, R., Cancelliere, R., Carlucci, T., Charlot, P., Cheek, N., Crosta, M., Crowley, C., de Bruijne, J., de Felice, F., Drimmel, R., Esquej, P., Fienga, A., Fraile, E., Gai, M., Garralda, N., González-Vidal, J. J., Guerra, R., Hauser, M., Hofmann, W., Holl, B., Jordan, S., Lattanzi, M. G., Lenhardt, H., Liao, S., Licata, E., Lister, T., Löffler, W., Marchant, J., Martin-Fleitas, J. M., Messineo, R., Mignard, F., Morbidelli, R., Poggio, E., Riva, A., Rowell, N., Salguero, E., Sarasso, M., Sciacca, E., Siddiqui, H., Smart, R. L., Spagna, A., Steele, I., Taris, F., Torra, J., van Elteren, A., van Reeven, W., & Vecchiato, A., *A&A*, 616:A2, Aug 2018.

Link, B., *MNRAS*, 422:1640–1647, May 2012.

Link, B. & Epstein, R. I., *ApJ*, 556:392–398, July 2001.

Liu, K., Keane, E. F., Lee, K. J., Kramer, M., Cordes, J. M., & Purver, M. B., *MNRAS*, 420(1):361–368, Feb 2012.

Livingstone, M. A. & Kaspi, V. M., *ApJ*, 742(1):31, Nov 2011.

Livingstone, M. A., Kaspi, V. M., Gavriil, F. P., & Manchester, R. N., *ApJ*, 619:1046–1053, Feb 2005.

Livingstone, M. A., Kaspi, V. M., Gavriil, F. P., Manchester, R. N., Gotthelf, E. V. G., & Kuiper, L., *Ap&SS*, 308(1-4):317–323, Apr 2007.

Lockyer, W. J. S., 1900.

Lorimer, D. R. & Kramer, M. *Handbook of Pulsar Astronomy.* December 2004.

Lou, Y.-Q., *ApJ*, 563(2):L147–L150, Dec 2001.

Luan, J. & Goldreich, P., *ApJ*, 790:82, July 2014.

Lundmark, K., *PASP*, 33(195):225, Oct 1921.

Lyne, A. G. & Lorimer, D. R., *Nature*, 369:127–129, May 1994.

Lyne, A. G. & Rickett, B. J., *Nature*, 219(5161):1339–1342, Sep 1968.

Lyne, A. G. & Smith, F. G., *Nature*, 218:124–126, April 1968.

Lyne, A. G., Manchester, R. N., & Taylor, J. H., *MNRAS*, 213:613–639, Apr 1985.

Lyne, A. G., Jordan, C. A., Graham-Smith, F., Espinoza, C. M., Stappers, B. W., & Weltevrede, P., *MNRAS*, 446:857–864, Jan 2015a.

Lyne, A. G., Stappers, B. W., Keith, M. J., Ray, P. S., Kerr, M., Camilo, F., & Johnson, T. J., *MNRAS*, 451(1):581–587, Jul 2015b.

Lyne, A. G., Stappers, B. W., Freire, P. C. C., Hessels, J. W. T., Kaspi, V. M., Allen, B., Bogdanov, S., Brazier, A., Camilo, F., Cardoso, F., Chatterjee, S., Cordes, J. M., Crawford, F., Deneva, J. S., Ferdman, R. D., Jenet, F. A., Knispel, B., Lazarus, P., van Leeuwen, J., Lynch, R., Madsen, E., McLaughlin, M. A., Parent, E., Patel, C., Ransom, S. M., Scholz, P., Seymour, A., Siemens, X., Spitler, L. G., Stairs, I. H., Stovall, K., Swiggum, J., Wharton, R. S., & Zhu, W. W., *ApJ*, 834(1):72, Jan 2017.

Lyne, A., Hobbs, G., Kramer, M., Stairs, I., & Stappers, B., *Science*, 329(5990):408, Jul 2010.

Lyne, A., Graham-Smith, F., Weltevrede, P., Jordan, C., Stappers, B., Bassa, C., & Kramer, M., *Science*, 342(6158):598–601, Nov 2013.

Manchester, R. N., *Science*, 304:542–547, April 2004.

Manchester, R. N. *Pulsar timing and its applications*. In *Journal of Physics Conference Series*, volume 932 of *Journal of Physics Conference Series*, page 012002, December 2017. doi: 10.1088/1742-6596/932/1/012002.

Manchester, R. N. & Taylor, J. H., *AJ*, 86:1953–1973, Dec 1981.

Manchester, R. N., Durdin, J. M., & Newton, L. M., *Nature*, 313:374–376, January 1985.

Manchester, R. N., Hobbs, G. B., Teoh, A., & Hobbs, M., *AJ*, 129(4):1993–2006, Apr 2005.

Manchester, R. N., Hobbs, G., Bailes, M., Coles, W. A., van Straten, W., Keith, M. J., Shannon, R. M., Bhat, N. D. R., Brown, A., Burke-Spolaor, S. G., Champion, D. J., Chaudhary, A., Edwards, R. T., Hampson, G., Hotan, A. W., Jameson, A., Jenet, F. A., Kesteven, M. J., Khoo, J., Kocz, J., Maciesiak, K., Oslowski, S., Ravi, V., Reynolds, J. R., Sarkissian, J. M., Verbiest, J. P. W., Wen, Z. L., Wilson, W. E., Yardley, D., Yan, W. M., & You, X. P., , 30:e017, Jan 2013.

Manchester, R. N. & Taylor, J. H. *Pulsars*. 1977.

Marshall, F. E., Guillemot, L., Harding, A. K., Martin, P., & Smith, D. A., *ApJ*, 827:L39, Aug 2016.

Matthews, A. M., Nice, D. J., Fonseca, E., Arzoumanian, Z., Crowter, K., Demorest, P. B., Dolch, T., Ellis, J. A., Ferdman, R. D., Gonzalez, M. E., Jones, G., Jones, M. L., Lam, M. T., Levin, L., McLaughlin, M. A., Pennucci, T. T., Ransom, S. M., Stairs, I. H., Stovall, K., Swiggum, J. K., & Zhu, W., *ApJ*, 818(1):92, Feb 2016.

Mayall, N. U., *PASP*, 49(288):101, Apr 1937.

McKee, C. F. & Ostriker, J. P., *ApJ*, 218:148–169, Nov 1977.

McKinney, J. C., *MNRAS*, 368(1):L30–L34, May 2006.

McLaughlin, M. A., *Classical and Quantum Gravity*, 30(22):224008, Nov 2013.

McLaughlin, M. A., Lyne, A. G., Lorimer, D. R., Kramer, M., Faulkner, A. J., Manchester, R. N., Cordes, J. M., Camilo, F., Possenti, A., Stairs, I. H., Hobbs, G., D'Amico, N., Burgay, M., & O'Brien, J. T., *Nature*, 439(7078):817–820, Feb 2006.

Melatos, A. & Warszawski, L., *ApJ*, 700(2):1524–1540, Aug 2009.

Melatos, A., Peralta, C., & Wyithe, J. S. B., *ApJ*, 672:1103–1118, Jan 2008.

Melatos, A. & Link, B., *MNRAS*, 437(1):21–31, Jan 2014a.

Melatos, A. & Link, B., *MNRAS*, 437:21–31, Jan 2014b.

Melrose, D. B., *Journal of Astrophysics and Astronomy*, 16:137–164, Jun 1995.

Messenger, C., Lommen, A., Demorest, P., & Ransom, S., *Classical and Quantum Gravity*, 28(5):055001, Mar 2011.

Messier, C., 1771.

Messier, C., 1774.

Michel, F. C., *ApJ*, 158:727, Nov 1969a.

Michel, F. C., *ApJ*, 157:1183, Sep 1969b.

Middleditch, J., Marshall, F. E., Wang, Q. D., Gotthelf, E. V., & Zhang, W., *ApJ*, 652: 1531–1546, Dec 2006.

Minkowski, R., *ApJ*, 96:199, Sep 1942.

Mitra, D., Wielebinski, R., Kramer, M., & Jessner, A., *A&A*, 398:993–1005, February 2003.

Namkham, N., Jaroenjittichai, P., & Johnston, S., *MNRAS*, 487(4):5854–5861, Aug 2019.

Narayan, R., *Philosophical Transactions of the Royal Society of London Series A*, 341 (1660):151–165, Oct 1992.

Navarro, J., Kulkarni, S. R., Thorsett, S. E., & Phillips, J. A. *Pulsar observations with the Caltech Fast Pulsar Timing Machine*. In *American Astronomical Society Meeting Abstracts*, volume 181, page 99.03, Dec 1992.

Ng, C. Y., Ho, W. C. G., Gotthelf, E. V., Halpern, J. P., Coe, M. J., Stappers, B. W., Lyne, A. G., Wood, K. S., & Kerr, M., *ApJ*, 880(2):147, Aug 2019.

Noutsos, A., Johnston, S., Kramer, M., & Karastergiou, A., *MNRAS*, 386:1881–1896, June 2008.

O'Beirne, L., Cornish, N. J., Vigeland, S. J., & Taylor, S. R., *Phys. Rev. D*, 99(12):124039, June 2019.

Oppenheimer, J. R. & Volkoff, G. M., *Physical Review*, 55(4):374–381, Feb 1939.

Osłowski, S., van Straten, W., Hobbs, G. B., Bailes, M., & Demorest, P., *MNRAS*, 418 (2):1258–1271, Dec 2011.

Osłowski, S., van Straten, W., Bailes, M., Jameson, A., & Hobbs, G., *MNRAS*, 441: 3148–3160, July 2014.

Pacini, F., *Nature*, 219(5150):145–146, Jul 1968.

Pacini, F., *Nature*, 216(5115):567–568, Nov 1967.

Palfreyman, J., Dickey, J. M., Hotan, A., Ellingsen, S., & van Straten, W., *Nature*, 556 (7700):219–222, Apr 2018.

Pandharipande, V. R., Pines, D., & Smith, R. A., *ApJ*, 208:550–566, Sep 1976.

Parthasarathy, A., Shannon, R. M., Johnston, S., Lentati, L., Bailes, M., Dai, S., Kerr, M., Manchester, R. N., Osłowski, S., Sobey, C., van Straten, W., & Weltevrede, P., *MNRAS*, 489(3):3810–3826, Nov 2019.

Parthasarathy, A., Johnston, S., Shannon, R. M., Lentati, L., Bailes, M., Dai, S., Kerr, M., Manchester, R. N., Osłowski, S., van Straten, C. S. W., & Weltevrede, P., *arXiv e-prints*, art. arXiv:2003.13303, March 2020.

Pennucci, T. T., *ApJ*, 871(1):34, Jan 2019.

Perera, B. B. P., DeCesar, M. E., Demorest, P. B., Kerr, M., Lentati, L., Nice, D. J., Osłowski, S., Ransom, S. M., Keith, M. J., Arzoumanian, Z., Bailes, M., Baker, P. T., Bassa, C. G., Bhat, N. D. R., Brazier, A., Burgay, M., Burke-Spolaor, S., Caballero, R. N., Champion, D. J., Chatterjee, S., Chen, S., Cognard, I., Cordes, J. M., Crowter, K., Dai, S., Desvignes, G., Dolch, T., Ferdman, R. D., Ferrara, E. C., Fonseca, E., Goldstein, J. M., Graikou, E., Guillemot, L., Hazboun, J. S., Hobbs, G., Hu, H., Islo, K., Janssen, G. H., Karuppusamy, R., Kramer, M., Lam, M. T., Lee, K. J., Liu, K., Luo, J., Lyne, A. G., Manchester, R. N., McKee, J. W., McLaughlin, M. A., Mingarelli, C. M. F., Parthasarathy, A. P., Pennucci, T. T., Perrodin, D., Possenti, A., Reardon, D. J., Russell, C. J., Sanidas, S. A., Sesana, A., Shaifullah, G., Shannon, R. M., Siemens, X., Simon, J., Spiewak, R., Stairs, I. H., Stappers, B. W., Swiggum, J. K., Taylor, S. R., Theureau, G., Tiburzi, C., Vallisneri, M., Vecchio, A., Wang, J. B., Zhang, S. B., Zhang, L., Zhu, W. W., & Zhu, X. J., *MNRAS*, page 2468, Oct 2019.

Petit, G. & Tavella, P., *A&A*, 308:290–298, Apr 1996.

Petroff, E., Keith, M. J., Johnston, S., van Straten, W., & Shannon, R. M., *MNRAS*, 435: 1610–1617, October 2013.

Pines, D. & Alpar, M. A., *Nature*, 316(6023):27–32, Jul 1985.

Radhakrishnan, V. & Srinivasan, G., *Current Science*, 51:1096–1099, Dec 1982.

Rajagopal, M. & Romani, R. W., *ApJ*, 446:543, June 1995.

Rankin, J. M., *ApJ*, 301:901, Feb 1986.

Ransom, S. M., Stairs, I. H., Archibald, A. M., Hessels, J. W. T., Kaplan, D. L., van Kerkwijk, M. H., Boyles, J., Deller, A. T., Chatterjee, S., Schechtman-Rook, A., Berndsen, A., Lynch, R. S., Lorimer, D. R., Karako-Argaman, C., Kaspi, V. M., Kondratiev, V. I., McLaughlin, M. A., van Leeuwen, J., Rosen, R., Roberts, M. S. E., & Stovall, K., *Nature*, 505:520–524, January 2014.

Reardon, D. J., Hobbs, G., Coles, W., Levin, Y., Keith, M. J., Bailes, M., Bhat, N. D. R., Burke- Spolaor, S., Dai, S., Kerr, M., Lasky, P. D., Manchester, R. N., Osłowski, S., Ravi, V., Shannon, R. M., van Straten, W., Toomey, L., Wang, J., Wen, L., You, X. P., & Zhu, X. J., *MNRAS*, 455:1751–1769, January 2016.

Reardon, D. J., Coles, W. A., Hobbs, G., Ord, S., Kerr, M., Bailes, M., Bhat, N. D. R., & Venkatraman Krishnan, V., *MNRAS*, 485(3):4389–4403, May 2019.

Rickett, B. J., *ARA&A*, 28:561–605, Jan 1990.

Rickett, B. J., *ApJ*, 197:185–191, April 1975.

Rigoselli, M., Mereghetti, S., Suleimanov, V., Potekhin, A. Y., Turolla, R., Taverna, R., & Pintore, F., *A&A*, 627:A69, Jul 2019.

Ritchings, R. T., *MNRAS*, 176:249–263, Aug 1976.

Robinson, P. A., *Physics of Plasmas*, 2(5):1466–1479, May 1995.

Robinson, P. A., Cairns, I. H., & Gurnett, D. A., *ApJ*, 387:L101, Mar 1992.

Rohlfs, K. & Wilson, T. L. *Tools of radio astronomy*. 2000.

Romani, R. W. *Timing a Millisecond Pulsar Array*, pages 113–117. Springer Netherlands, Dordrecht, 1989. ISBN 978-94-009-2273-0.

Rookyard, S. C., Weltevrede, P., & Johnston, S., *MNRAS*, 446(4):3367–3388, Feb 2015.

Rudak, B. & Ritter, H., *MNRAS*, 267:513, Apr 1994.

Ruderman, M., *Nature*, 223:597–598, August 1969.

Ruderman, M. A. & Sutherland, P. G., *ApJ*, 196:51–72, February 1975.

Sandhu, J. S., Bailes, M., Manchester, R. N., Navarro, J., Kulkarni, S. R., & Anderson, S. B., *ApJ*, 478(2):L95–L98, Apr 1997.

Sanidas, S. A., Battye, R. A., & Stappers, B. W., *ApJ*, 764:108, February 2013.

Sazhin, M. V., *Soviet Ast.*, 22:36–38, February 1978.

Schmidt, M., *Nature*, 197(4872):1040, Mar 1963.

Schnitzeler, D. H. F. M., *MNRAS*, 427:664–678, November 2012.

Seymour, A. D. & Lorimer, D. R., *MNRAS*, 428:983–998, Jan 2013.

Shannon, R. M., Cordes, J. M., Metcalfe, T. S., Lazio, T. J. W., Cognard, I., Desvignes, G., Janssen, G. H., Jessner, A., Kramer, M., Lazaridis, K., Purver, M. B., Stappers, B. W., & Theureau, G., *ApJ*, 766(1):5, Mar 2013.

Shannon, R. M., Johnston, S., & Manchester, R. N., *MNRAS*, 437:3255–3264, February 2014a.

Shannon, R. M., Osłowski, S., Dai, S., Bailes, M., Hobbs, G., Manchester, R. N., van Straten, W., Raithel, C. A., Ravi, V., Toomey, L., Bhat, N. D. R., Burke-Spolaor, S., Coles, W. A., Keith, M. J., Kerr, M., Levin, Y., Sarkissian, J. M., Wang, J. B., Wen, L., & Zhu, X. J., *MNRAS*, 443(2):1463–1481, Sep 2014b.

Shannon, R. M., Ravi, V., Lentati, L. T., Lasky, P. D., Hobbs, G., Kerr, M., Manchester, R. N., Coles, W. A., Levin, Y., Bailes, M., Bhat, N. D. R., Burke-Spolaor, S., Dai, S., Keith, M. J., Osłowski, S., Reardon, D. J., van Straten, W., Toomey, L., Wang, J. B., Wen, L., Wyithe, J. S. B., & Zhu, X. J., *Science*, 349(6255):1522–1525, Sep 2015.

Shannon, R. M., Lentati, L. T., Kerr, M., Bailes, M., Bhat, N. D. R., Coles, W. A., Dai, S., Dempsey, J., Hobbs, G., Keith, M. J., Lasky, P. D., Levin, Y., Manchester, R. N., Osłowski, S., Ravi, V., Reardon, D. J., Rosado, P. A., Spiewak, R., van Straten, W., Toomey, L., Wang, J.-B., Wen, L., You, X.-P., & Zhu, X.-J., *ApJ*, 828:L1, September 2016a.

Shannon, R. M., Lentati, L. T., Kerr, M., Johnston, S., Hobbs, G., & Manchester, R. N., *MNRAS*, 459:3104–3111, Jul 2016b.

Shannon, R. M. & Cordes, J. M., *ApJ*, 725:1607–1619, December 2010.

Shannon, R. M. & Cordes, J. M., *ApJ*, 761(1):64, Dec 2012.

Shao, L., Stairs, I., Antoniadis, J., Deller, A., Freire, P., Hessels, J., Janssen, G., Kramer, M., Kunz, J., Laemmerzahl, C., Perlick, V., Possenti, A., Ransom, S., Stappers, B., & van Straten, W. *Testing Gravity with Pulsars in the SKA Era.* In *Advancing Astrophysics with the Square Kilometre Array (AASKA14)*, page 42, Apr 2015.

Shapiro, I. I., *Phys. Rev. Lett.*, 13(26):789–791, Dec 1964.

Shklovskii, I. S., *Soviet Ast.*, 10:6, Aug 1966.

Siemens, X., Ellis, J., Jenet, F., & Romano, J. D., *Classical and Quantum Gravity*, 30 (22):224015, Nov 2013.

Simon, J. & Burke-Spolaor, S., *ApJ*, 826:11, July 2016.

Smith, D. A., Guillemot, L., Camilo, F., Cognard, I., Dumora, D., Espinoza, C., Freire, P. C. C., Gotthelf, E. V., Harding, A. K., Hobbs, G. B., Johnston, S., Kaspi, V. M., Kramer, M., Livingstone, M. A., Lyne, A. G., Manchester, R. N., Marshall, F. E., McLaughlin, M. A., Noutsos, A., Ransom, S. M., Roberts, M. S. E., Romani, R. W., Stappers, B. W., Theureau, G., Thompson, D. J., Thorsett, S. E., Wang, N., & Weltevrede, P., *A&A*, 492(3):923–931, Dec 2008.

Spitkovsky, A., *ApJ*, 648(1):L51–L54, Sep 2006.

Spruit, H. & Phinney, E. S., *Nature*, 393(6681):139–141, May 1998.

Staelin, D. H. & Reifenstein, E. C., *Science*, 162 3861:1481–3, 1968.

Stairs, I. H., Lyne, A. G., & Shemar, S. L., *Nature*, 406(6795):484–486, Aug 2000.

Stairs, I. H., Lyne, A. G., Kramer, M., Stappers, B. W., van Leeuwen, J., Tung, A., Manchester, R. N., Hobbs, G. B., Lorimer, D. R., & Melatos, A., *MNRAS*, page 628, Mar 2019.

Staveley-Smith, L., Wilson, W. E., Bird, T. S., Disney, M. J., Ekers, R. D., Freeman, K. C., Haynes, R. F., Sinclair, M. W., Vaile, R. A., Webster, R. L., & Wright, A. E., , 13(3):243–248, Nov 1996.

Tauris, T. M. & Konar, S., *A&A*, 376:543–552, Sep 2001.

Tauris, T. M. & Manchester, R. N., *MNRAS*, 298(3):625–636, Aug 1998.

Tauris, T. M., Kaspi, V. M., Breton, R. P., Deller, A. T., Keane, E. F., Kramer, M., Lorimer, D. R., McLaughlin, M. A., Possenti, A., Ray, P. S., Stappers, B. W., & Weltevrede, P. *Understanding the Neutron Star Population with the SKA*. In *Advancing Astrophysics with the Square Kilometre Array (AASKA14)*, page 39, Apr 2015.

Tauris, T. M., Kramer, M., Freire, P. C. C., Wex, N., Janka, H. T., Langer, N., Podsiadlowski, P., Bozzo, E., Chaty, S., Kruckow, M. U., van den Heuvel, E. P. J., Antoniadis, J., Breton, R. P., & Champion, D. J., *ApJ*, 846(2):170, Sep 2017.

Taylor, J. H., *Philosophical Transactions of the Royal Society of London*, 341:117–134, Jan 1992.

Taylor, J. H. & Cordes, J. M., *ApJ*, 411:674, Jul 1993.

Taylor, J. H. & Weisberg, J. M., *ApJ*, 253:908–920, Feb 1982a.

Taylor, J. H. & Weisberg, J. M., *ApJ*, 253:908–920, Feb 1982b.

Taylor, J. H. & Weisberg, J. M., *ApJ*, 345:434–450, October 1989.

Taylor, J. H. & Weisberg, J. M., *ApJ*, 253:908–920, Feb 1982c.

Taylor, J. H., Manchester, R. N., & Huguenin, G. R., *ApJ*, 195:513–528, Jan 1975.

Taylor, S. R., Simon, J., & Sampson, L., *Phys. Rev. Lett.*, 118(18):181102, May 2017.

Thorsett, S. E., Arzoumanian, Z., & Taylor, J. H., *ApJ*, 412:L33, Jul 1993.

Turolla, R. *Isolated Neutron Stars: The Challenge of Simplicity.* In Becker, W., editor, *Astrophysics and Space Science Library*, volume 357, page 141, Jan 2009. doi: 10.1007/978-3-540-76965-1_7.

Vallisneri, M., Taylor, S. R., Simon, J., Folkner, W. M., Park, R. S., Cutler, C., Ellis, J. A., Lazio, T. J. W., Vigeland, S. J., Aggarwal, K., Arzoumanian, Z., Baker, P. T., Brazier, A., Brook, P. R., Burke-Spolaor, S., Chatterjee, S., Cordes, J. M., Cornish, N. J., Crawford, F., Cromartie, H. T., Crowter, K., DeCesar, M., Demorest, P. B., Dolch, T., Ferdman, R. D., Ferrara, E. C., Fonseca, E., Garver-Daniels, N., Gentile, P., Good, D., Hazboun, J. S., Holgado, A. M., Huerta, E. A., Islo, K., Jennings, R., Jones, G., Jones, M. L., Kaplan, D. L., Kelley, L. Z., Key, J. S., Lam, M. T., Levin, L., Lorimer, D. R., Luo, J., Lynch, R. S., Madison, D. R., McLaughlin, M. A., McWilliams, S. T., Mingarelli, C. M. F., Ng, C., Nice, D. J., Pennucci, T. T., Pol, N. S., Ransom, S. M., Ray, P. S., Siemens, X., Spiewak, R., Stairs, I. H., Stinebring, D. R., Stovall, K., Swiggum, J. K., van Haasteren, R., Witt, C. A., & Zhu, W. W., *ApJ*, 893(2):112, April 2020.

van Haasteren, R. & Levin, Y., *MNRAS*, 428:1147–1159, January 2013.

van Straten, W., *ApJS*, 152(1):129–135, May 2004.

van Straten, W., *ApJS*, 204(1):13, Jan 2013.

van Straten, W., *ApJ*, 642(2):1004–1011, May 2006.

van Straten, W. & Bailes, M., , 28(1):1–14, Jan 2011.

van Straten, W. & Bailes, M. *Annual-orbital Parallax and Nearby Binary Pulsars.* In Bailes, M., Nice, D. J., & Thorsett, S. E., editors, *Radio Pulsars*, volume 302 of *Astronomical Society of the Pacific Conference Series*, page 65, Jan 2003.

van Straten, W., Manchester, R. N., Johnston, S., & Reynolds, J. E., , 27(1):104–119, Mar 2010.

van Straten, W., Britton, M., Bailes, M., Anderson, S., & Kulkarni, S. *Pulsar Applications of the Caltech Parkes Swinburne Baseband Processing System.* In Kramer, M., Wex, N., & Wielebinski, R., editors, *IAU Colloq. 177: Pulsar Astronomy - 2000 and Beyond*, volume 202 of *Astronomical Society of the Pacific Conference Series*, page 283, Jan 2000.

Verbiest, J. P. W., Bailes, M., van Straten, W., Hobbs, G. B., Edwards, R. T., Manchester, R. N., Bhat, N. D. R., Sarkissian, J. M., Jacoby, B. A., & Kulkarni, S. R., *ApJ*, 679(1): 675–680, May 2008.

Verbiest, J. P. W., Lentati, L., Hobbs, G., van Haasteren, R., Demorest, P. B., Janssen, G. H., Wang, J. B., Desvignes, G., Caballero, R. N., Keith, M. J., Champion, D. J., Arzoumanian, Z., Babak, S., Bassa, C. G., Bhat, N. D. R., Brazier, A., Brem, P., Burgay, M., Burke-Spolaor, S., Chamberlin, S. J., Chatterjee, S., Christy, B., Cognard, I., Cordes, J. M., Dai, S., Dolch, T., Ellis, J. A., Ferdman, R. D., Fonseca, E., Gair, J. R., Garver-Daniels, N. E., Gentile, P., Gonzalez, M. E., Graikou, E., Guillemot, L., Hessels, J. W. T., Jones, G., Karuppusamy, R., Kerr, M., Kramer, M., Lam, M. T., Lasky, P. D., Lassus, A., Lazarus, P., Lazio, T. J. W., Lee, K. J., Levin, L., Liu, K., Lynch, R. S., Lyne, A. G., Mckee, J., McLaughlin, M. A., McWilliams, S. T., Madison, D. R., Manchester, R. N., Mingarelli, C. M. F., Nice, D. J., Osłowski, S., Palliyaguru, N. T., Pennucci, T. T., Perera, B. B. P., Perrodin, D., Possenti, A., Petiteau, A., Ransom, S. M., Reardon, D., Rosado, P. A., Sanidas, S. A., Sesana, A., Shaifullah, G., Shannon, R. M., Siemens, X., Simon, J., Smits, R., Spiewak, R., Stairs, I. H., Stappers, B. W., Stinebring, D. R., Stovall, K., Swiggum, J. K., Taylor, S. R., Theureau, G.,

Tiburzi, C., Toomey, L., Vallisneri, M., van Straten, W., Vecchio, A., Wang, Y., Wen, L., You, X. P., Zhu, W. W., & Zhu, X. J., *MNRAS*, 458(2):1267–1288, May 2016.

Verbiest, J. P. W., *arXiv e-prints*, art. arXiv:0906.4246, Jun 2009.

Viganò, D., Rea, N., Pons, J. A., Perna, R., Aguilera, D. N., & Miralles, J. A., *MNRAS*, 434(1):123–141, Sep 2013.

Vigeland, S. J. & Vallisneri, M., *MNRAS*, 440(2):1446–1457, May 2014.

Wang, H., Taylor, S. R., & Vallisneri, M., *MNRAS*, 487(3):3644–3649, Aug 2019.

Wang, N., Manchester, R. N., & Johnston, S., *MNRAS*, 377(3):1383–1392, May 2007.

Weisberg, J. M., Romani, R. W., & Taylor, J. H., *ApJ*, 347:1030, Dec 1989.

Weisberg, J. M., Siegel, M. H., Frail, D. A., & Johnston, S., *ApJ*, 447:204, Jul 1995.

Weltevrede, P., Johnston, S., Manchester, R. N., Bhat, R., Burgay, M., Champion, D., Hobbs, G. B., Kızıltan, B., Keith, M., Possenti, A., Reynolds, J. E., & Watters, K., , 27(1):64–75, Mar 2010.

Weltevrede, P., Johnston, S., & Espinoza, C. M., *MNRAS*, 411:1917–1934, March 2011.

Weltevrede, P. & Johnston, S., *MNRAS*, 387(4):1755–1760, Jul 2008.

Wick, G. C., *Zeitschrift fur Physik*, 84(11-12):799–800, Nov 1933.

Wolszczan, A. & Frail, D. A., *Nature*, 355:145–147, January 1992.

Xie, Y.-W., Wang, J.-B., Hobbs, G., Kaczmarek, J., Li, D., Zhang, J., Dai, S., Cameron, A., Zhang, L., Miao, C.-C., Yuan, M., Wang, S., Zhang, S.-B., Xu, H., & Xu, R.-X., *Research in Astronomy and Astrophysics*, 19(7):103, Jul 2019.

Yao, J. M., Manchester, R. N., & Wang, N., *ApJ*, 835:29, January 2017.

Young, M. D., Manchester, R. N., & Johnston, S., *Nature*, 400(6747):848–849, Aug 1999.

Young, M. D. T., Chan, L. S., Burman, R. R., & Blair, D. G., *MNRAS*, 402(2):1317–1329, Feb 2010.

Yu, M., Manchester, R. N., Hobbs, G., Johnston, S., Kaspi, V. M., Keith, M., Lyne, A. G., Qiao, G. J., Ravi, V., Sarkissian, J. M., Shannon, R., & Xu, R. X., *MNRAS*, 429(1): 688–724, Feb 2013.

Yunes, N. & Siemens, X., *Living Reviews in Relativity*, 16(1):9, Nov 2013.

Zhu, W. W., Stairs, I. H., Demorest, P. B., Nice, D. J., Ellis, J. A., Ransom, S. M., Arzoumanian, Z., Crowter, K., Dolch, T., Ferdman, R. D., Fonseca, E., Gonzalez, M. E., Jones, G., Jones, M. L., Lam, M. T., Levin, L., McLaughlin, M. A., Pennucci, T., Stovall, K., & Swiggum, J., *ApJ*, 809(1):41, Aug 2015.

Zou, W. Z., Hobbs, G., Wang, N., Manchester, R. N., Wu, X. J., & Wang, H. X., *MNRAS*, 362:1189–1198, October 2005.

Zwicky, F., *Physical Review*, 55(8):726–743, Apr 1939.